UNIVERSITY OF SOUTHAMPTON

Faculty of Social, Human and Mathematical Sciences

School of Mathematical Sciences, Applied Mathematics

Modelling ion migration and charge carrier transport in planar perovskite solar cells

by

Nicola Elizabeth Courtier

ORCID iD 0000-0002-5714-1096

A thesis submitted for the degree of
Doctor of Philosophy

April 2019

UNIVERSITY OF SOUTHAMPTON

ABSTRACT

FACULTY OF SOCIAL, HUMAN AND MATHEMATICAL SCIENCES
SCHOOL OF MATHEMATICAL SCIENCES, APPLIED MATHEMATICS

Doctor of Philosophy

by Nicola Elizabeth Courtier

Perovskite solar cells (PSCs) have significant potential for success in the global market, as both a thin-film technology and as part of perovskite-on-silicon tandem devices. The latter technology is currently in the early stages of commercialisation. The record efficiencies of some types of PSC are close to their theoretical maximum; however, their long-term stability remains an area of concern. Rapid degradation caused by the external environment can be avoided via careful encapsulation of the device. However, cells also show an unforeseen internal behaviour, the effects of which have been termed current-voltage hysteresis by the research field. It is now widely accepted that ion migration via vacancies in the perovskite is the origin of hysteresis, and hence that this behaviour is intrinsic to every PSC. Modelling ion migration in PSCs, and its effect on both their transient and steady-state performance, is the topic of this project. A combination of numerical techniques and asymptotic analysis is used to investigate a three-layer drift-diffusion model for ion vacancy migration and charge carrier transport within a PSC. For realistic values of the parameters, such a model displays both temporal and spatial stiffness and hence requires tailored numerical methods of solution. In addition, a simplified surface polarisation model is derived using the method of matched asymptotic expansions. The form of this model reveals how ion vacancy migration controls the evolution of the electric field across the three layers of a PSC and that this is the key to explaining its behaviour. The influence of two important properties of the transport layers, which adjoin the perovskite layer of a PSC, on the distribution of the electric field is highlighted and explained for the first time. Simulations are used to reproduce a number of experimentally observed trends, including why PSCs with organic transport layers tend to display reduced hysteresis. Strategies for determining the dominant charge carrier recombination mechanism, and reducing the associated performance loss, are also discussed.

Contents

Nomenclature **xi**

List of Publications **xv**

DECLARATION OF AUTHORSHIP **xvii**

Acknowledgements **xix**

1 Introduction **1**
1.1 Motivation 1
1.2 Thesis outline 3
1.3 Contributions 4

2 Background **7**
2.1 Perovskite-based solar cells 7
2.2 Hysteresis in perovskite solar cells 12
2.3 Pre-existing models of ion migration 19
2.4 Summary 24

3 The Charge Transport Model **27**
3.1 Operational principles of a perovskite solar cell 27
3.2 Model formulation 29
3.3 Charge carrier generation and recombination 38
3.4 Parameter estimates 43
3.5 The dimensionless model 46

4 Numerical Methods of Solution **53**
4.1 Review of methods used in the literature 54
4.2 Reduction of the problem to a single-layer model 58
4.3 Finite element scheme 62
4.4 Finite difference scheme 70
4.5 Verification of methods and comparison to alternative numerical methods 74
4.6 Comparison to and validation of published single-layer asymptotic results 81
4.7 Summary 86

5 Asymptotic Analysis of the Charge Transport Model **89**
5.1 The asymptotic limits 90

5.2 Analysis of the decoupled model 94
5.3 Evolution of the charge density stored within the Debye layers 101
5.4 Determination of the generated current density 105
5.5 Verification against numerical solutions 109
5.6 Discussion and summary 114

6 Effects of Key Physical Properties on Cell Performance 117
6.1 Review of experimentally observed trends in cell performance 118
6.2 Physical description of the asymptotic results 123
6.3 Modelling hysteresis as an effect of iodide ion vacancy migration 126
6.4 Modelling the effects of variation in the transport layer properties 129
6.5 Summary 141

7 An Analytic Expression for the Current Density 143
7.1 Review of the diode theory for perovskite solar cells 144
7.2 Analysis based on monomolecular recombination rates 146
7.3 Simplified expressions for the current density 151
7.4 Summary and outlook 158

8 Conclusions and Future Directions 161

A Ion flux with volume exclusion effects 165
A.1 Lattice hopping model 165
A.2 Thermodynamic approach 170
A.3 Modified Possion-Nernst-Planck equations 172

B Extension of Numerical Schemes to the Three-Layer Model 175
B.1 Finite difference scheme 175
B.2 Finite element scheme 178
B.3 Initial conditions 180

References 181

List of Figures

1.1 Structure of a planar PSC. 2

2.1 Crystal structure of $MAPbI_3$. 9
2.2 Determination of J-V curve metrics. 13
2.3 Schematic explanation for how ion accumulation could cause hysteresis. . 22

3.1 Three layers of a planar PSC. 28
3.2 Band diagram of a PSC. 30
3.3 Variable domains. 33
3.4 Model equations. 36
3.5 Recombination mechanisms. 40

4.1 Electric potential distribution across the perovskite layer. 56
4.2 The computational grid. 66
4.3 Finite element mass matrix and Jacobian. 69
4.4 Finite difference mass matrix and Jacobian. 73
4.5 Pointwise convergence of numerical schemes. 77
4.6 Comparison of the errors and run times of all numerical schemes. 79
4.7 Asymptotic and numerical results for a current decay transient. 83
4.8 Comparison of asymptotic and numerical solutions. 84
4.9 Asymptotic and numerical results for a current-voltage curve. 85

5.1 Locations of asymptotic boundary layers. 93
5.2 Debye layer charge density-potential relation. 102
5.3 Verification of asymptotic solutions for a slow current transient. 111
5.4 Verification of asymptotic solutions for a fast current transient. 112
5.5 Verification of asymptotic solutions for a current transient into forward bias. 113
5.6 Verification of asymptotic solutions for a set of J-V curves. 114

6.1 Band energy diagram of a PSC. 124
6.2 Debye layer capacitance relation. 125
6.3 An example J-V curve with corresponding evolution of the electric potential. 127
6.4 The definition of the hysteresis factor and an example curve. 128
6.5 Hysteresis versus scan rate for three sets of ETL properties. 131
6.6 Evolution of the charge density during a voltage transient. 132

6.7 Effects of varying the TL doping densities on the evolution of the electric potential. . . . 133
6.8 Hysteresis factor versus scan rate for different TL doping densities for a cell with bulk-dominated recombination. . . . 134
6.9 Hysteresis factor versus scan rate for different TL doping densities for a cell with interface-dominated recombination. . . . 135
6.10 Simulated J-V curves and evolution of the bulk electric field. . . . 137
6.11 Steady-state electric potential and ion vacancy distributions and recombination losses for different TL doping densities. . . . 139

7.1 Verification of the uniformly-valid carrier concentrations in the perovskite layer against numerical solutions. . . . 150
7.2 Verification of the simplified current density for monomolecular recombination rates. . . . 151
7.3 Comparison of the simplified current density against numerical solution for varying illumination. . . . 156
7.4 Comparison of the simplified current density against numerical solution for varying parameter values. . . . 157

A.1 One-dimensional lattice of ion sites. . . . 166
A.2 Probability of each possible arrangement of ions. . . . 166
A.3 The ionic potential energy landscape. . . . 167
A.4 Lattice of ion sites partially filled by ions. . . . 170

List of Tables

3.1 Standard semiconductor notation and definitions. 29
3.2 Physical parameter definitions and estimates. 44
3.3 Recombination parameter definitions and estimates. 45
3.4 Dimensionless parameter estimates and descriptions. 51
3.5 Dimensionless recombination parameter estimates and descriptions. . . . 51

Nomenclature

Abbreviations

AM1.5G	The global standard solar spectrum (Air Mass 1.5 - global)
DAE	Differential algebraic equation
DFT	Density functional theory
DoS	Density of states
ETL	Electron transport layer
FF	Fill factor
HTL	Hole transport layer
HF	Hysteresis factor
I-V	Current-voltage
J-V	Current density-voltage
J_{SC}	Short-circuit current
$MAPbI_3$	Methyl ammonium lead iodide, $CH_3NH_3PbI_3$
ODE	Ordinary differential equation
PDE	Partial differential equation
PCBM	Phenyl-C61-butyric acid methyl ester
PCE	Power conversion efficiency
PEDOT:PSS	Poly(3,4-ethylenedioxythiophene):poly(styrenesulfonate)
PL	Photo-luminescence
PSC	Perovskite solar cell
Spiro-OMeTAD	2,2',7,7'-tetrakis-(N,N-di-p-methoxyphenyl-amine)- 9,9'-spirobi-fluorene
SRH	Shockley-Read-Hall (recombination)
SnO_2	Tin oxide
TiO_2	Titania, or titanium dioxide
TL	Transport layer
V_{OC}	Open-circuit voltage

Symbols

α	Absorption coefficient
β	Radiative recombination coefficient

γ	SRH recombination parameter
δ	Ratio between the ETL doping and mean ion vacancy densities
ε	Permittivity
ε_0	Permittivity of free space
κ	Dimensionless diffusion coefficient
λ	Dimensionless Debye length
μ_n	Electron mobility
μ_p	Hole mobility
ν_n	Electron SRH recombination velocity
ν_p	Hole SRH recombination velocity
ρ	Charge density
ς	Relative timescale of electron motion
τ	SRH recombination parameter
τ_{ion}	Timescale of iodide ion vacancy migration
Υ	Product of the absorption coefficient and perovskite width
ϕ	Electric potential
Φ	Dimensionless applied voltage
Φ_{bi}	Dimensionless built-in voltage
χ	Ratio between the TL doping densities
Ω	Dimensionless parameter
b	Layer width
c	SRH recombination parameter
d	Effective doping density
D_E	Electron diffusion coefficient in the ETL
D_H	Hole diffusion coefficient in the HTL
D_I	Iodide ion vacancy diffusion coefficient
D_n	Electron diffusion coefficient in the perovskite
D_p	Hole diffusion coefficient in the perovskite
E	Electric field
E_a	Activation energy
E_C	Energy of conduction band edge
E_{f_E}	Fermi level of the ETL
E_{f_H}	Fermi level of the HTL
E_g	Band gap
E_i	Intrinsic potential energy
E_t	Trap state energy level
E_V	Energy of valence band edge
F_{ph}	Incident photon flux at 1 Sun
F^P	Iodide ion vacancy flux

G	Charge carrier generation rate
G_0	Mean charge carrier generation rate
$\bar{G}_l$	Charge carrier generation parameter
H	Hysteresis factor
I_s	Intensity of incident light
j^n	Electron current density
j^p	Hole current density
k_B	Boltzmann constant
k_E	Band offset factor at the ETL/perovskite interface
k_H	Band offset factor at the perovskite/HTL interface
l	Parameter indicating the direction of light
n	Electron concentration
n_i	Intrinsic carrier concentration
N_0	Mean ion vacancy density
N_C	Effective conduction band DoS
N_V	Effective valence band DoS
p	Hole concentration
P	Iodide ion vacancy density
q	Elementary charge
R	Charge carrier recombination rate
R_l	Recombination rate across the ETL/perovskite interface
R_r	Recombination rate across the perovskite/HTL interface
t	Time
T	Temperature
V	Applied voltage
V_{bi}	Built-in voltage
V_T	Thermal voltage
x	Distance from the ETL/perovskite interface

List of Publications

1. N. E. Courtier, J. M. Foster, S. E. J. O'Kane, A. B. Walker, and G. Richardson. Systematic derivation of a surface polarisation model for planar perovskite solar cells. *European Journal of Applied Mathematics*, **30**(3), 427 - 457, 2019.

2. N. E. Courtier, G. Richardson, and J. M. Foster. A fast and robust numerical scheme for solving models of charge transport and ion vacancy motion in perovskite solar cells. *Applied Mathematical Modelling*, **63**, 329 - 348, 2018.

3. N. E. Courtier, J. M. Cave, J. M. Foster, A. B. Walker, and G. Richardson. How transport layer properties affect perovskite solar cell performance: Insights from a coupled charge transport/ion migration model. *Energy & Environmental Science*, **12**, 396 - 409, 2019.

4. J. Idígoras, L. Contreras-Bernal, J. M. Cave, N. E. Courtier, Á. Barranco, A. Borras, J. R. Sánchez-Valencia, J. A. Anta, and A. B. Walker. The role of surface recombination on the performance of perovskite solar cells: Effect of morphology and crystalline phase of TiO_2 contact. *Advanced Materials Interfaces*, **5**, 1801076, 2018.

Conference Presentations

1. British Applied Mathematics Colloquium. Oxford, UK, 7th April 2016.

2. 3rd International Conference on Perovskite Solar Cells and Optoelectronics. Oxford, UK, 19th September 2017.

3. CDT-PV Showcase. Liverpool, UK, 9th November 2017.

4. 4th International Conference on Perovskite Solar Cells and Optoelectronics. Lausanne, Switzerland, 2nd October 2018.

DECLARATION OF AUTHORSHIP

I, **Nicola Elizabeth Courtier**, declare that the thesis entitled **Modelling ion migration and charge carrier transport in planar perovskite solar cells** and the work presented in the thesis are both my own, and have been generated by me as the result of my own research. I confirm that:

- this work was done wholly in candidature for a research degree at this University;
- if any part of this thesis has previously been submitted for a degree or any other qualification at this University or any other institution, this has been clearly stated;
- where I have consulted the published work of others, this is always clearly attributed;
- where I have quoted from the work of others, the source is always given. With the exception of such quotations this thesis is entirely my own work;
- I have acknowledged all main sources of help;
- where the thesis is based on work done by myself jointly with others, I have made clear exactly what was done by others and what I have contributed myself;
- parts of this work have been published as listed in the List of Publications.

Signed:

Date:

Acknowledgements

First and foremost, I would like to thank my supervisor Dr Giles Richardson for his continuous encouragement and ambition for the project. I would also like to thank Dr Jamie M. Foster for his friendly guidance and support throughout the last four years. In addition, I am grateful for having had the advantage of working with Prof. Alison Walker, James Cave and others from the University of Bath, with whom we have had many interesting and fruitful discussions. Thank you also to my examiners Prof. Peter Howell and Dr Giampaolo D'Alessandro for their kind and constructive comments.

This project was supported by an EPSRC funded studentship from the CDT in New and Sustainable Photovoltaics (reference EP/L01551X/1). I would like to thank all involved with the CDT for providing me with a fantastic and diverse set of experiences, particularly in the first year, as well as the knowledge I needed to become an interdisciplinary researcher. I feel lucky to have shared these experiences with the unique and wonderful other members of C1.

Thank you to all my friends, from home, Oxford and now Southampton, who have kept in touch during these busy years and provided me with opportunities to escape from the challenges of academia. Special thanks go to Roxana for kindly sharing her valuable advice. My successes in the last few years are also undoubtedly thanks to the selfless support of Sam. Last but certainly not least, I thank my amazing family for all the encouragement, entertainment and assistance that has enabled me to get to this point.

Chapter 1

Introduction

In order to meet the global energy demand of the future with low-carbon and renewable technology, there is a need to produce solar panels that are cheaper, more lightweight and/or more efficient than the conventional silicon panels. Perovskite solar cells are one of the most promising, emerging photovoltaic technologies. Significant research interest has fuelled an unprecedented rise in their power conversion efficiency from 14% to 22.7% within the last 5 years [94] and the technology has entered the early stages of commercialisation [100]. However, for perovskite solar cells to reach their potential, significant improvements are still needed in terms of the stability and longevity of the cells. This work focuses on the development of a detailed charge transport model for a perovskite solar cell that is able to capture and explain the distinctive features of their unusual transient behaviour.

1.1 Motivation

Wider context. Solar energy, alongside other forms of renewable energy, is an increasingly important resource needed to meet a growing global energy demand and to ease our unsustainable reliance on fossil fuels [90]. Despite the successes of the conventional silicon-based solar cells, the search continues for lightweight, low-cost alternatives. A number of emerging thin-film photovoltaic (PV) technologies, including perovskite solar cells, have the potential to fulfil these requirements.

A simplified description of a solar cell is a device that generates electricity by absorbing photons. In a perovskite solar cell (PSC), it is the perovskite layer in which light is absorbed and charge carriers (conduction electrons and holes) are generated. To create an electric current, charge carriers must be separated to different contacts. The key processes

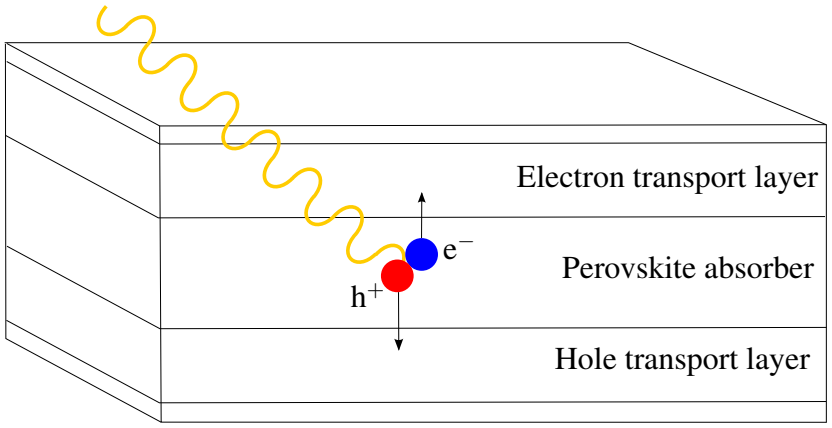

FIGURE 1.1: A diagram showing the structure of a planar PSC and highlighting the key processes of photo-generation and the separation of an electron (e^-) and a hole (h^+).

of charge carrier photo-generation and separation are shown schematically in Figure 1.1 on a diagram of a typical planar PSC. The power conversion efficiency (PCE) of a solar cell is defined as the amount of power generated by the cell as a proportion of the power of the incident light. This single value, the PCE, provides an effective way to rate one type of solar cell against another as it represents how much energy can be produced per unit area and hence, given the cost of manufacture and lifetime of the cell, the cost of the electricity. The PCE depends on the amount of light absorbed as well as the amount of photo-generated charge lost via charge-carrier recombination. A common target for any emerging photovoltaic technology is therefore to achieve the highest possible PCE, by maximising light absorption and minimising recombination.

Unique challenges. Metal halide PSCs have sparked interest among researchers and a remarkable rise in their PCE has been achieved in just a few years [94]. A major challenge for the continued development of PSCs into a commercially viable technology is in extending their promising PCE results into long-term performance. The cells are susceptible to rapid degradation resulting from exposure to ultra-violet light, oxygen and/or moisture. The mechanisms responsible for degradation depend on the composition of each material layer of a PSC, though experimental work indicates that issues arising from external factors can be prevented via careful encapsulation of the device [80]. However, the performance of PSCs has also been found to vary as a result of internal processes.

In 2014, Snaith *et al.* [128] showed that PSCs exhibit hysteresis, an unusual phenomenon that does not affect the performance of other types of solar cell. In the field of PSC research, the term hysteresis refers to a dependence of the power output of a cell on the history of previous conditions applied to the cell, for example the applied voltage. Established solar cell simulators, designed to model conventional solar cells, are not able to

capture the unusual transient behaviour displayed by PSCs. This is because the underlying computational models consider only the motion of electronic charge carriers, which move far too quickly to be responsible for the transient behaviour that has been observed to occur on a timescale of seconds or longer. Several theories were initially proposed for the origin of the hysteresis [128], as discussed in Section 2.2. Of the suggested theories, ion vacancy migration is considered the most plausible mechanism and is now widely accepted as the underlying cause. *Ab initio* calculations performed by Eames *et al.* [45] among others support the theory that ion vacancy migration occurs within PSCs. However, a better understanding of the internal process of ion vacancy migration and how it affects the performance of a cell is required. Charge transport modelling, alongside experimentation, can be a powerful tool to acquire this understanding.

Applications of modelling in the literature prior to 2017 are described in Section 2.3. However, no simplified model has been able to reproduce the full range of experimental behaviour measured in the laboratory. One reason for this is the mathematical difficulties associated with determining accurate solutions to physically relevant models; this is discussed in detail in Section 4.1. Another difficulty in reproducing experimental data is that a large number of parameters and possible mechanisms have not been measured independently by experiment. Indeed, this provides significant motivation for developing a detailed physical model with which the effect of each parameter can be investigated independently. In this work, a combined approach is taken in which both numerical and asymptotic methods are employed to study the effects of ion vacancy migration on the internal state and performance of a PSC.

1.2 Thesis outline

Chapter 2 reviews the development of metal halide PSCs to date and the issues facing researchers in this rapidly expanding field of research. The properties of metal halide perovskite materials are described, to highlight their suitability as the light-absorbing layer of a high-efficiency and low-cost photovoltaic technology. The discovery and experimentally-observed effects of hysteresis are discussed. Then, the theory of ion vacancy migration and the first models used to study this mechanism as the underlying cause of hysteresis are described. Further short reviews of the literature relevant to topics within each chapter are given at the start of the chapter to avoid repetition.

Chapter 3 presents in detail a charge transport model for the operation of a PSC which incorporates ion vacancy migration within the perovskite layer. Estimates for each of the physical parameters are given and used to obtain an appropriate dimensionless model.

Chapter 4 investigates two different numerical schemes, namely a finite difference and a finite element scheme, which both reduce the model to a time-dependent problem which can be solved using the method of lines. The performance of the two schemes, in terms of speed and accuracy, is benchmarked against a previously-used alternative on two tailored non-uniform spatial grids. The contents of this chapter have been published in [35]. Results obtained using the finite difference method have been published in [67].

Chapter 5 contains an asymptotic analysis of the three-layer charge transport model for a PSC. The analysis reveals how ion vacancy motion in the perovskite layer is able to affect the performance of a PSC. The resulting uniformly-valid solutions are shown to give very good agreement to numerical solutions of the full model within realistic operating regimes.

Chapter 6 studies the physical effects of two key dimensionless parameters that are highlighted by the asymptotic analysis. A theory is put forward to explain the experimental observation that, in general, PSCs with organic layers adjoining the perovskite layer exhibit reduced effects of hysteresis compared to the original reports of hysteresis. Crucially, the theory addresses the cause, and not just the effects, of hysteresis. Distinctive features of hysteresis are reproduced and explained.

Chapter 7 investigates the theoretical potential of planar PSCs. The steady-state performance of a solar cell is typically assessed in terms of the diode ideality factor, however the standard diode theory does not accurately describe the performance of a PSC in which ion vacancy migration occurs. A modified expression for the current density as a function of the applied voltage is found via a systematic approximation of the asymptotic results presented in Chapter 5.

Chapter 8 summarises the conclusions of this work and suggests future avenues for research.

1.3 Contributions

The contents of Chapter 4 have been published as a standalone work in Applied Mathematical Modelling [35]. In particular, Sections 4.3-4.6 are reproduced almost exactly from the published paper. This work was supervised by Dr Jamie M. Foster and Dr Giles Richardson. The manuscript was written mainly by myself and Dr Jamie M. Foster.

The contents of Chapter 6 have been published as a standalone work in Energy & Environmental Science. In particular, Sections 6.2-6.4 (excluding 6.3.3) are reproduced

almost exactly from the published paper. This work was produced mainly in collaboration with Dr Giles Richardson, alongside numerous useful discussions with Prof. Alison B. Walker, James M. Cave, and Dr Jamie M. Foster. All authors contributed to editing the manuscript.

The results, rather than the content, of the other publications on which I am a co-author are included in this thesis with appropriate citations.

Chapter 2

Background

2.1 Perovskite-based solar cells

This chapter provides an overview of the development, properties and first models of perovskite solar cells (PSCs). In this first section, the development of PSCs is documented, from the first use of a perovskite material in a photovoltaic device, through their unprecedented rise in power conversion efficiency (PCE) to the high-performance devices of recent years. The rapid rise in PCE has been possible due to the many desirable physical properties of perovskite materials and has led the field of PSC development to become a very active area of research. The latest PCE records demonstrate the potential of PSCs to compete with established photovoltaic technologies [94]. Here, the term perovskite is used to refer specifically to the group of metal halide perovskite materials, named after their chemical structure (see Figure 2.1).

2.1.1 A brief history

The discovery of the promising potential of metal-halide perovskite materials came as a result of experimentation on their use as the sensitiser in a dye-sensitised solar cell (DSSC) [77]. In such a device, the perovskite is incorporated solely to enhance the absorption of light in the visible range of wavelengths. In this capacity, the perovskite is termed a light-harvester. The first perovskite-based DSSCs were reported in 2009 and recorded a maximum PCE of 3.8% [77]. In 2012, the cell architecture of a DSSC was adapted to make use of a solid-state hole conductor, namely the organic material abbreviated as Spiro-OMeTAD, in place of the electrolyte solution used to separate charges in the DSSC [75]. This led to improved device stability as well as a higher PCE.

The next development was to incorporate the perovskite as an extremely thin absorber layer on top of (as well as infiltrated into) the mesoporous titanium dioxide (TiO_2) scaffold [79]. This work led to the finding that the perovskite layer provided fast electron transport, in addition to its light harvesting abilities. The first certified PCE (measured under standard illumination conditions at an accredited laboratory) for a mesoporous PSC was recorded as 14.14% in 2013 [21]. To date, all subsequent PSC PCE records have also been achieved using a mesoporous TiO_2 layer. The latest record is 22.7%, compared to stabilised PCEs of 22.3% for conventional multicrystalline silicon solar cells and 26.1% for higher-cost monocrystalline silicon solar cells, as verified by the National Renewable Energy Laboratory in the US (NREL) [94].

2.1.2 Thin film architecture

Soon after the development of mesoporous cell architectures and the discovery that perovskite has both good charge transport and light absorption properties [79], the desire for more easily processable layers (without a complex mesostructure) led to perovskite being deposited as a planar absorber layer directly on top of a planar layer of TiO_2. Planar cells are simpler, and therefore potentially cheaper, to fabricate. Liu *et al.* [86] were the first to demonstrate the possibility of obtaining PCEs of over 15% using a planar architecture with a 125-500 nm thick perovskite absorber layer formed by vapour-deposition. In comparison, conventional silicon solar cells employ absorber layers that are around a hundred to a thousand times thicker; it is for this reason that planar PSCs are classified as thin-film. In 2014, the first report was made of a PCE greater than 10% for a planar PSC formed using the technique of solution-processing [47]. Both techniques of vapour deposition and solution-processing can be scaled-up to industrial scale production lines, which is crucial for the future viability of these cells.

Significant improvements in PCE came as a result of controlling the formation of the perovskite layer to obtain larger crystal grains for a more uniform morphology [97] and adjusting the other material layers for compatibility with the perovskite [165]. Reviews of the early stages of PSC development were written by Miyasaka [93], Stranks and Snaith [133], and Sum *et al.* [134]. Then, in 2015, the replacement of TiO_2 by a layer of SnO_2 was found to increase both performance and stability [31]. Such cells also showed remarkably high open-circuit voltages (V_{OC}) of 1.19 V, close to their thermodynamic limit of approximately 1.32 V [139].

Further incremental increases in PCE were quick to emerge due to experimental advances in both processing techniques and cell design [121, 156, 166]. Recently, PCEs in excess of 20% have been achieved using planar thin film architectures [6, 7, 129]. At present, the

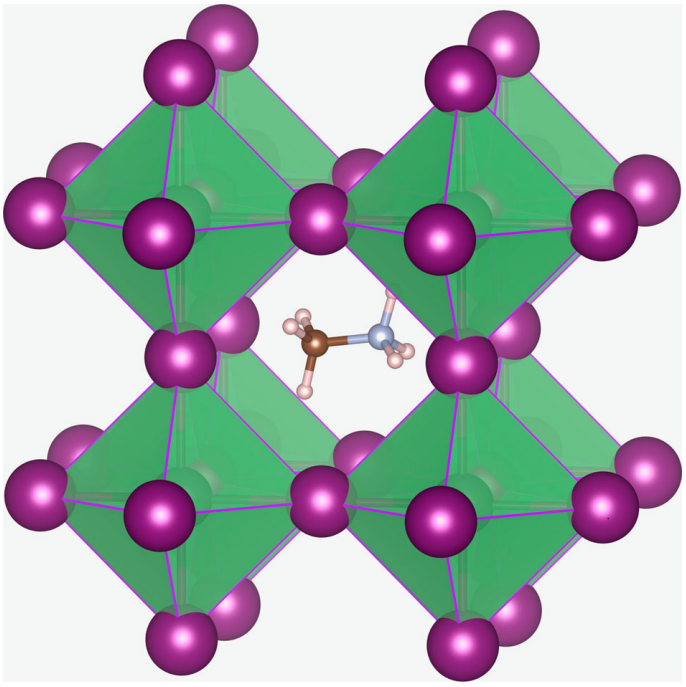

FIGURE 2.1: Cubic crystal structure of methyl ammonium lead iodide ($MAPbI_3$), reproduced from Eames *et al.* [45]. Iodide (I^-) ions (purple circles) surround lead (Pb^{2+}) ions (encased in green, corner-sharing octahedra) and the central methyl ammonium (MA^+) cation.

highest published certified efficiency for a PSC is 22.6% as reported in [70]. A review of the rapid rise in PCE of both mesoporous and planar PSCs has been published by Correa-Baena *et al.* [30].

2.1.3 Favourable properties of lead halide perovskite materials

There are a number of physical properties exhibited by metal halide perovskite materials that make them an ideal choice for photovoltaic applications. The class of materials is named after its perovskite crystal structure, which has the chemical formula ABX_3 where A and B are cations and X is an anion. The most studied perovskite composition in the field of PSCs is that of methyl ammonium lead iodide ($CH_3NH_3PbI_3$ or $MAPbI_3$) in which the A cation is methyl ammonium ($CH_3NH_3^+$ or MA^+ for short), B is lead (Pb^{2+}) and X is iodide (I^-) [69]. The ideal cubic phase of the $MAPbI_3$ perovskite structure is shown in Figure 2.1. At room temperature, $MAPbI_3$ exists in a tetragonal phase (in which the corner-sharing tetrahedra are tilted), but undergoes a reversible phase transition from tetragonal to cubic at approximately 57°C [8, 107].

Alternative perovskite materials that have been successfully incorporated as the absorber in a PSC have been formed by substituting either all or some of the methyl ammonium with formamidinium (FA^+) and/or cesium (Cs^+), some or all of the lead with tin (Sn^{2+})

and/or some or all of the iodide with other halides (Cl^- or Br^-) [85, 101, 115]. Mixed-formulation perovskite devices frequently show improved performance and stability compared to $MAPbI_3$ devices. Recently, the addition of rubidium (Rb^+) or potassium (K^+) (cations that are too small to form the perovskite structure alone) into the mixture has led to further improvements in device stability [19, 114]. However, as the most common and thoroughly investigated perovskite formulation for PSCs, the focus of this work is $MAPbI_3$.

The defining property that enables perovskite to be an efficient light-harvester is its semiconductor band gap. Under illumination, incident photons with energies greater than the band gap are absorbed by the perovskite. The band gap of $MAPbI_3$ has been determined using UV-visible spectroscopy to be 1.51 eV [8]. This value is close to the ideal band gap of around 1.4 eV for solar radiation absorption [95]. The absorption spectrum of $MAPbI_3$ shows that it is a panchromatic absorber with a high absorption coefficient across the visible part of the electromagnetic spectrum and a particularly sharp absorption onset corresponding to the band gap [38]. The sharp onset signifies that $MAPbI_3$ has a well-ordered structure with a low density of electronic defects.

Alongside the desirable light-harvesting properties of $MAPbI_3$, it has also been revealed as a good ambipolar charge-transporter. The absorption of photons with energies above the band gap leads to the generation of excitons. In $MAPbI_3$, these excitons are so weakly bound (with a binding energy of $\sim$50 meV [78]) that they rapidly dissociate into a free electron in the conduction band and a hole in the valence band. The function of a photovoltaic cell is to then separate these charge carriers (electrons and holes) and transport them to opposite contacts to enable the flow of current. The typical distance that a charge carrier diffuses before it recombines with a carrier of the opposite charge is termed the diffusion length. Stranks *et al.* [132] estimated from photoluminescence (PL) decay data that, in $MAPbI_3$, the charge carrier diffusion lengths are on the order of 100 nm. Such long diffusion lengths demonstrate the intrinsic ability of $MAPbI_3$ to transport charge with relatively low losses to recombination. Even greater potential was shown in this regard by the mixed-halide perovskite $MAPbI_{3-x}Cl_x$, in which charge carrier diffusion lengths were estimated to be an order of magnitude higher than in $MAPbI_3$ (> 1 μm) [132].

In a solar cell design, selecting the optimal thickness for an absorber layer is necessarily a balance between increasing the thickness in order to absorb a higher fraction of the incident light and decreasing the thickness to reduce the distance that charge carriers need to be transported. Notably, for perovskite, the two relevant lengthscales are of comparable magnitude. Both the absorption depth (given by the inverse of the absorption coefficient) and the charge carrier diffusion lengths are on the order of a hundred nanometres. This

characteristic lengthscale aligns well with the range of experimentally-optimised planar perovskite layer thicknesses reported in the literature.

Findings on the topic of the fundamental, and favourable, properties of perovskite have been reviewed by Herz [66] and Brenner *et al.* [14], with the former focussing on light-harvesting properties and the latter on the charge-transport characteristics of perovskite. Discussion of the physical properties of appropriate materials for the other layers of a PSC is deferred to the beginning of Chapter 6.

2.1.4 Challenges and outlook

A significant obstacle to the development of PSCs into a competitive commercial product is their instability. Current PSC architectures show signs of both long- and short-term stability issues. The target device lifetime for any emerging photovoltaic technology is the 25-year market standard set by crystalline silicon solar cells. The record to date for PSCs is just one year under controlled standard conditions [62]. However, the performance losses exhibited by high-efficiency PSCs are much greater.

Experimental studies have shown that PSCs can display a myriad of different electrical behaviours in response to external stimuli such as humidity, atmosphere, temperature, illumination intensity, and applied voltage and which also depend on cell architecture, perovskite composition and fabrication method, as reviewed in [12, 98]. Different mechanisms have been suggested to explain the observations however it is proving difficult to disentangle how each mechanism affects PSC performance. The situation is made more complicated by the fact that PSCs suffer from both reversible and irreversible degradation mechanisms. Irreversible degradation can be a result of chemical reactivity or structural instabilities, caused or exacerbated by the external environment [98]. Anomalous reversible behaviours have been reported to occur on timescales of a few seconds [128, 143] up to a period of days [40, 135]; these slow (in comparison to the timescale of electronic motion) but short-term variations in performance are the topic of Section 2.2. The interplay between reversible and irreversible degradation mechanisms is considered in Section 6.1.4.

Since PSCs have already demonstrated the potential to obtain high PCEs, research efforts must now focus on improving the stability of these devices. Some issues, such as chemical degradation due to extrinsic water and oxygen, can be prevented via careful encapsulation of the device [42, 80, 92]. However, experiments performed on incomplete device architectures (*e.g.* just the perovskite film on glass) have shown that some performance loss is due to a mechanism intrinsic to the perovskite layer [59, 128]. Therefore

it is necessary to investigate the effects of intrinsic, and therefore unavoidable, mechanisms on PSC performance and to develop strategies to minimise any associated losses. A comprehensive theoretical understanding of PSC behaviours from the microscopic to macroscopic level is currently lacking and advances are needed to guide future developments. Advances are also needed in the processing techniques required for large-scale production, to ensure the fabrication of consistently high quality material layers while at the same time decreasing costs to achieve commercial viability.

In practise, the most feasible route for perovskite to break into the established silicon-dominated solar cell industry may be as a second absorber layer in a perovskite-silicon tandem cell [149]. An attractive feature of perovskite materials for use in a tandem configuration is their tunable semiconductor band gap, which can be modified via the choice of ionic composition to maximise the light absorption spectrum of the complete device. In doing so, it is possible to obtain PCEs beyond the single-junction Shockley-Queisser limit, in exchange for the costs of processing one additional layer. However, at present, the design and optimisation of perovskite-silicon tandem cells are similarly limited by unresolved issues of stability. The steps for this type of device to become a reality have been set out in [137]. Other potential applications for perovskite materials include use in light emitting diodes [89, 133], photodetectors [41] and resistance-switching memories ("memristors") [155].

The focus of this work is on the unusual reversible behaviours exhibited by $MAPbI_3$ PSCs with a planar architecture that occur on the timescale of seconds to minutes. Then, in Chapter 8, the conclusions of this work are presented along with a discussion of their relevance to the wider range of PSC architectures and experimental observations. In the next section, the first observations of reversible variations in PSC performance are described and then the theories proposed to explain the findings are reviewed.

2.2 Hysteresis in perovskite solar cells

In the field of PSC research, the term hysteresis is used to refer to the anomalous, reversible variations in electrical performance exhibited by PSCs. The term was coined by Snaith *et al.* [128] upon providing the first article on this unexpected feature of PSCs. This article along with many subsequent reports of hysteresis have motivated both experimental and theoretical investigations of the underlying physical process(es) responsible for hysteresis.

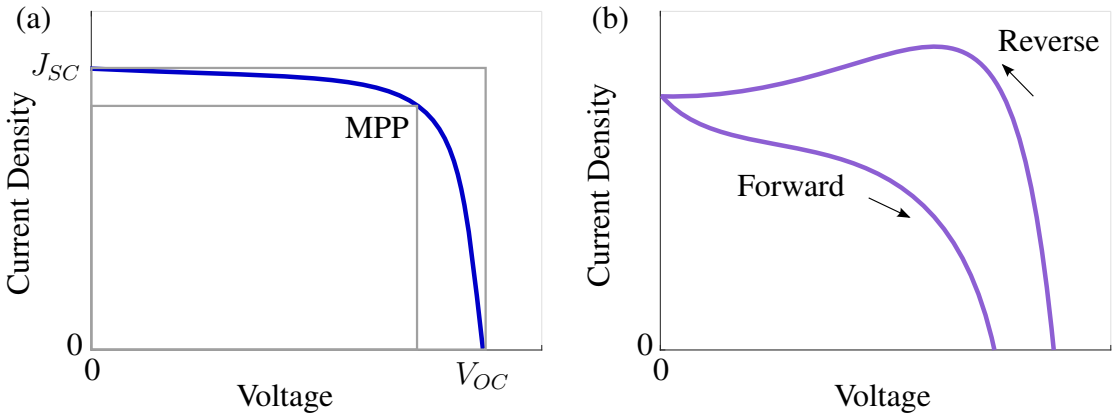

FIGURE 2.2: a) Diagram of a J-V curve for a typical silicon solar cell, with labels indicating the following performance metrics: the short-circuit current density (J_{SC}), the open-circuit voltage (V_{OC}) and the maximum power point (MPP), *i.e.* the point on the curve that gives the maximum product of J and V. The fill factor (FF) is the ratio between the value of the maximum power density and the product of J_{SC} and V_{OC}, *i.e.* the proportion of the large grey rectangle filled by the smaller grey rectangle. b) An illustration of how J-V hysteresis can complicate the determination of PSC performance metrics, with labelled arrows indicating the direction of the voltage scan.

2.2.1 Experimental discovery and observations

The issue of current density-voltage (J-V) hysteresis was first brought to light in 2014 [44, 128]. The standard method for determining the relative performance of a solar cell is to measure the current density (J) output as a function of the voltage (V) applied across the cell under standard environmental test conditions, and then to calculate its PCE, defined as follows, from the maximum power point (MPP) on the resulting J-V curve.

$$\mathrm{PCE} = \frac{P_{max}}{P_S}\,, \tag{2.1}$$

where P_{max} is the maximum power output of the cell per unit area and P_S is the incident light power density (typically that of the standard AM1.5 spectrum, approximately 100 mW/cm^2). The PCE can equivalently be calculated from three properties of a J-V curve as follows [95].

$$\mathrm{PCE} = \frac{J_{\mathrm{SC}} V_{\mathrm{OC}} FF}{P_S}\,, \tag{2.2}$$

in which the three J-V curve properties (illustrated in Figure 2.2 (a)) are: J_{SC}, the short-circuit current; V_{OC}, the open-circuit voltage; and, FF, the fill factor (a measure of the "squareness of the J-V curve").

Snaith *et al.* [128] were the first to show, however, that J-V measurements of PSCs

display a strong dependence on the history of external conditions (such as the applied voltage) to which the cell has been subjected, *i.e.* that PSCs display J-V hysteresis. It was found that the effects of hysteresis can cause both an over- or underestimation of a cell's PCE and other performance metrics [143]; see Figure 2.2 (b). This observation opened up the question of how to accurately determine the genuine performance of a PSC and casts doubt on earlier PCE reports. The conditions under which J-V measurements have been performed and the degree of hysteresis exhibited in the results are now reported as a matter of course [27].

The original paper by Snaith *et al.* [128] demonstrates that J-V measurements of both mesostructured and planar PSCs are dependent on the voltage scan rate and scan direction. It is found that hysteresis persists even for impractically slow scan rates (as low as 1 mV/s), preventing the accurate determination of a cell's PCE from its J-V curve. PSC architecture, in addition to the conditions of measurement, is shown to be a contributing factor to the extent of J-V hysteresis. In order to probe the location of the cause of hysteresis in the cell architecture, J-V measurements of PSCs lacking one or other of the charge transporting layers are taken and found to also exhibit hysteresis.

In a similar vein, Xiao *et al.* [154] study a PSC that lacks a hole transport layer (HTL) while Zhang *et al.* [162] compare PSCs with and without a compact TiO_2 electron transport layer (ETL). A layer of $MAPbI_3$ placed directly between two metal contacts is also shown to exhibit hysteresis [60]. Hence it is deduced, by elimination, that the origin of the hysteresis must lie within the perovskite absorber layer, though the extent of hysteresis is strongly affected by the contact materials.

Hysteresis can also be observed in other, previously standard characterisation measurements. For example, alongside J-V hysteresis, Unger *et al.* [143] present reversible changes in current transients, external quantum efficiency (EQE) spectra and J-V scans measured after different periods of light-soaking at forward or reverse bias. Current transients, in which a PSC is held at a fixed voltage before the applied voltage is abruptly switched to another value and the current density response is measured [99, 143], indicate that the process behind J-V hysteresis occurs on a timescale on the order of seconds. There is also some evidence of a second, even slower process.

Impedance spectroscopy measurements provide additional evidence that one or more anomalous processes, particular to PSCs, take place on the timescale of seconds or longer [5, 25, 104, 116]. In particular, an unexpected capacitance appears in the impedance spectra at a lower frequency (*i.e.* on a slower timescale) than that associated with charge carrier transport.

The phenomenon of J-V hysteresis has previously been reported for other photovoltaic

technologies [53, 136] however the topic has far from dominated research and development the way it has for PSCs in the past few years. In such cases, the hysteresis occurs only on much shorter timescales (micro-milliseconds) and has been attributed to internal capacitances due to charge carrier accumulation.

2.2.2 Discussion of suggested causes

From the initial observations of J-V hysteresis described above, it can be deduced that its origin is a process, or a combination of processes, that:

- generates an electric field-dependent charge density distribution that can both increase or decrease the photo-current from its steady-state value;
- is intrinsic to the perovskite, though strongly affected by the type of contact; and,
- occurs on the timescale of seconds.

After noting some of the factors contributing to J-V hysteresis, Snaith *et al.* [128] hypothesised three possible origins for the anomalous characteristics. The three suggested causes are (i) slow trapping/de-trapping of charge carriers, (ii) formation of ferroelectric domains and (iii) ion migration. In this section, the three theories are discussed in turn before a convincing case is put forward for the mechanism deemed the most likely cause of hysteresis.

(i). Slow trapping/de-trapping of charge carriers. Trap states are energy states that can trap, or remove, a free electron from the conduction band or a hole from the valence band. Trapped charges can act as recombination centres by attracting and recombining with a carrier of the opposite charge, resulting in a loss of photo-generated charge. Perovskite films are reported to have a low density of sub-gap trap states [38], *i.e.* trap states that lie within the ideally unoccupied semiconductor band gap that form as a result of defects in the crystalline structure. However, high densities of trap states could exist at the interfaces between the perovskite and the adjoining transport layers (TLs) due to dangling bonds and lattice mismatch. In particular, a high density of trap states is expected to exist at the interface between a layer of TiO_2 and the perovskite layer deposited on top [135, 157].

In a scenario in which recombination between trapped charges and the opposite type of charge carrier is limited (*e.g.* if there is a very low concentration of minority charge carriers), the presence of trap states could lead to an accumulation of trapped charge at the interface. As the applied voltage is varied, this could lead to a variable density of trapped charge at the interface that either enhances or reduces charge extraction into the

TLs and, in turn, the photo-current. Hence, a slow trapping/de-trapping of charge carriers could give rise to a J-V hysteresis that has a strong dependence on the quality and type of contact.

Shao *et al.* [125] were the first to demonstrate a reduction in the effects of hysteresis for a cell incorporating organic TLs, by including the organic material phenyl-C61-butyric acid methyl ester (PCBM) as an ETL. Control devices made without PCBM show a significant J-V hysteresis that is suppressed by the addition of a layer of PCBM into the device architecture. The suppression of hysteresis is attributed to the ability of the PCBM to either passivate or inhibit the formation of interfacial trap states. Thermal admittance spectroscopy analysis is used to confirm that the addition of PCBM leads to a significant reduction in the density of interfacial trap states. A similar effect is found to result from the inclusion of a self-assembled fullerene (C_{60}) monolayer between the perovskite and an inorganic TiO_2 ETL [152]. However, although the passivation of trap states reduces the effects of hysteresis, it does not prove the hypothesis that the trap states are the cause of hysteresis.

An equivalent circuit model for a planar solar cell with a high density of interfacial trap states is presented by Cojocaru *et al.* [28]. The existence of interfacial trap states is described by a capacitor at each interface. The model is extended, by addition of a diode, inductor and resistor, to include a Schottky barrier capable of creating a reverse current in order to reproduce more features of J-V hysteresis. However, in a comment by Tada, it is claimed that the equivalent circuit may not accurately describe the fundamental causes of hysteresis.

(ii). Formation of ferroelectric domains. Previous to the discovery of hysteresis, Brivio *et al.* [17] suggested that the ferroelectric properties of $MAPbI_3$ could affect the charge carrier dynamics and hence performance of a $MAPbI_3$-based PSC. The possibility of a "photoferroic" effect is mentioned, *i.e.* an effect that is based upon a ferroelectric ordering of the methyl ammonium (MA^+) cations caused by a light-induced electric field. Using density functional theory (DFT), it is found that the MA^+ cation has only a low energy barrier for rotation, meaning that reorientation of its dipole can take place rapidly at room temperature. It is proposed that the presence of an electric field can lead to a slow ferroelectric polarisation of the perovskite layer via the alignment of the MA^+ cations [54]. Qualitative explanations of how ferroelectric polarisation could cause experimentally observed trends in J-V hysteresis are presented in [26, 148].

However, a further study suggests that ferroelectric polarisation cannot produce a surface charge density larger than 1 $\mu C/cm^2$ and so cannot be the origin of the charge density in excess of 1000 $\mu C/cm^2$ measured by impedance spectroscopy [10]. More recently, it has been shown that a layer of $MAPbI_3$ is not ferroelectric at room temperature [113]. The

large surface charge densities recorded in both of these works are instead attributed to an accumulation of ionic charge resulting from the third hypothesis.

(iii). Ion migration. In an operating PSC, mobile charges in the perovskite layer are subject to an electric field that encourages them to drift towards one of the contacts. Hence, assuming that the contact materials present a barrier to the movement of ions, any mobile ionic charge that exists in the perovskite would accumulate at the interfaces. A redistribution of ionic charge (particularly an accumulation or depletion of charge at the interfaces) could either aid or hinder the extraction of electronic charge into the contacts and hence increase or decrease the photo-current.

Xiao *et al.* [154] show that it is possible to reverse the direction of photo-current in a PSC architecture with symmetric properties by varying the applied voltage. This behaviour can be explained by a field-driven ion migration that creates an effective p-i-n or n-i-p homojunction within the perovskite layer. A compositional change near the edges of the $MAPbI_3$ layer is also observed and adds support to the theory of ion migration.

DFT calculations performed by Walsh *et al.* [145] indicate that a significant percentage of ion sites (in excess of 0.4% at room temperature) in the crystal structure of $MAPbI_3$ may be left vacant after synthesis of the perovskite layer. The proposed mechanism is therefore that ions can hop to neighbouring ion vacancies and hence migrate via a hopping process through the material. Results from Eames *et al.* [45] (discussed in Section 2.3.1) confirm that vacancy-assisted ion migration is a feasible origin for the J-V hysteresis. Vacancy-assisted ion migration can equivalently be described as a migration of mobile ion vacancies, in an analogous way to how the motion of electrons in the valence band of a semiconductor is expressed as the motion of holes. Using the estimate from the work of Walsh *et al.* [145], the ion vacancy density is predicted to be around 1.6×10^{19} cm^{-3} [45]. As well as mobile ion vacancies, other mobile ionic species in perovskite could include interstitial defects (*i.e.* excess ions that remain in the perovskite after its formation) or extrinsic ions that enter from the contact layers (*e.g.* dopant Li^+ ions from Spiro-OMeTAD) [84].

Although the first two suggested causes, *(i)* and *(ii)*, have not been completely ruled out, evidence has been growing most strongly in support of *(iii)*, the theory of ion migration. In terms of the three criteria set out at the beginning of this discussion, the simplest argument in favour of ion migration is the timescale on which hysteresis occurs. The observed timescale of seconds is considered a particularly slow timescale for both *(i)*, the trapping/de-trapping of charge carriers and *(ii)*, the formation of ferroelectric domains, whereas it is the expected timescale for ion migration according to DFT calculations.

Tress *et al.* [140] presented a discussion of J-V hysteresis in 2015 which similarly con-

cludes that ion migration is its more plausible origin. The origin is deemed to be of an ionic, rather than electronic, nature due to the observation that hysteresis occurs independently of illumination intensity, which implies that the exceptionally large surface charge densities are not likely to be formed from an accumulation of photo-generated charge carriers. Six supporting reasons for the conclusion that the ionic mechanism is that of ion migration are given, including the characteristic timescale of seconds. Additionally, a qualitative explanation is given for how a slow, field-induced mechanism that tends to cancel the electric field (such as ion migration) leads to the observed effects of hysteresis, see Section 2.3.2. Tress *et al.* [140] bolster their argument with proof-of-concept device simulation, based on drift-diffusion theory, which is outlined in Section 2.3.3 along with details of the progress made, prior to 2017, in drift-diffusion modelling of PSCs.

In 2016, experimental work identified iodide ions as the mobile ionic species responsible for J-V hysteresis. Li *et al.* [82] used X-ray photo-emission spectroscopy to determine the ratio of iodide (I^-) to lead (Pb^{2+}) ions near one electrode. It is found that, after applying a potential difference across the perovskite for 30 minutes, the ratio grows from an intrinsic value of 3 to around 5.6. This indicates that the applied voltage causes a significant accumulation of iodide ions near the electrode. After 6 hours with no applied voltage, the ratio is found to return to near 3, implying that the iodide ions diffuse back to a uniform distribution. De Quilettes *et al.* [37] were the first to publish visual evidence of ion migration. Specifically, time-of-flight secondary-ion-mass spectrometry (ToF-SIMS) measurements of $MAPbI_3$ were taken after an area of the sample had been subjected to pulses of light. Spatial profiles show a depletion of iodide ions in the centre of the light-soaked area, with a ring of displaced ions around it. It is shown that for double the photon dose, the iodide ions displace further both laterally and vertically through the perovskite.

The consensus among researchers is therefore that iodide ion migration plays a significant role in $MAPbI_3$-based PSC behaviour [160], although quantitative simulation of J-V hysteresis from a coupled ionic-electronic model is still lacking from the literature. It is also not yet clear how other mechanisms and properties of both the perovskite and transport layers interact with ion migration to affect the charge carrier dynamics of a PSC. The goal of this work is to investigate to what extent the observed features of J-V hysteresis can be reproduced by assuming its sole origin is the migration of iodide ions, via vacancies in the perovskite structure.

2.2.3 Reduced hysteresis and "hysteresis-free" cells

The first published method for suppressing hysteresis was the passivation of interface trap states, resulting from the inclusion of an organic ETL [125, 152]. Since 2014, there

have been other reports of reduced hysteresis and even apparently hysteresis-free cells [50, 65, 158]. Such reduced-hysteresis cells have been fabricated using advances in the choice of deposition techniques or material layers [31, 74, 161]. However, until the causes of hysteresis are fully understood, it is difficult to deduce whether observations of reduced hysteresis result from either a reduction in the cause or a reduction in the appearance of hysteresis. For example, some apparently hysteresis-free cells have been shown to exhibit hysteresis at low temperature [18, 81], indicating that the underlying physical origin of hysteresis has not been eliminated. Therefore, in this work, the discussion of reduced hysteresis is postponed to Chapter 6, after a model for the migration of iodide ions within the perovskite layer has been set out and analysed.

2.3 Pre-existing models of ion migration

A range of approaches exist for modelling PSC characteristics, extending from fundamental, atomistic DFT calculations to macroscopic, equivalent circuit device models, *e.g.* that of Cojocaru *et al.* [28, 29]. Drift-diffusion modelling offers a macroscopic description of dynamic behaviour that is linked directly to microscopic properties, which can be obtained either from DFT calculations or from experimental measurements. Heuristic models also play an important role in advancing our understanding of a physical theory such as ion vacancy migration. In this section, findings from a number of different approaches that have been used in the context of PSCs are described.

2.3.1 Atomistic models

Density functional theory (DFT) is a valuable tool that is used extensively for calculating, from first principles, the values of microscopic properties of materials such as perovskite, including quantities relating to its electronic structure and ionic migration. A review of progress in this area has been provided by Frost and Walsh [55]. The challenges for atomistic modelling presented by the complexities of perovskite materials are described in [151].

Eames *et al.* [45] obtained estimates from DFT for the activation energy associated with a vacancy-assisted hopping process for different ionic species. Only the iodide (I^-) ion vacancies are deemed to exhibit a sufficiently low activation energy (0.58 eV) to allow for facile migration through the perovskite layer. Higher activation energies are found for the MA^+ and Pb^{2+} cation vacancies (0.84 eV and 2.31 eV, respectively). Hence the cations are believed to be immobile on the timescale of J-V hysteresis. The mechanism of

interstitial defect migration is dismissed due to spatial restrictions imposed by the close-packed perovskite structure. In support of the theory of ion vacancy migration as the origin of hysteresis, good agreement is demonstrated between the theoretical activation energy for iodide ion vacancy migration and experimentally-derived activation energies (0.60-0.68 eV) calculated from photo-current transients measured over a range of realistic operating temperatures.

An important limitation of microscopic models is the huge computational cost required to simulate more than a few unit cells of the perovskite crystal structure (see Figure 2.1). Thus, such models cannot be used to reproduce the dynamic behaviour of an entire PSC under varying external conditions. However, an activation energy (E_A) calculated from first principles can act as an input for a macroscopic, drift-diffusion model via the diffusion coefficient, which, for a hopping process such as iodide ion vacancy migration, is given by the Arrhenius relation:

$$D = D_\infty \exp\left(-E_A/k_B T\right) , \tag{2.3}$$

in which D_∞ is the high-temperature limit of the diffusion coefficient and $k_B T$ is the thermal voltage (approximately 25 meV at room temperature). Eames *et al.* [45] calculate a diffusion coefficient on the order of 10^{-12} cm^2/s for iodide ion vacancies at a temperature of 320 K. A value that is four orders of magnitude smaller (10^{-16} cm^2/s) is estimated for the MA^+ ion vacancies, which confirms that negligible diffusion of this ionic species can be expected.

Subsequent to the work of Eames *et al.* [45], a range of values for the E_A associated with the slow process of hysteresis (0.42-0.55 eV) have been deduced from experimental observations [41, 105]. Recently, a novel experimental technique has been used to estimate an activation energy of 0.48 eV and a diffusion coefficient of 1.6×10^{-14} cm^2/s for iodide ion vacancy migration in $MAPbI_3$ at a temperature of 300 K [49].

2.3.2 Heuristic models

Heuristic models can provide key insights into how a microscopic, physical phenomenon can affect overall PSC performance. A qualitative explanation of how a slow, field-induced process, such as ion vacancy migration, can cause hysteresis is given by Tress *et al.* [140]. The theory is that a potential difference across the cell causes a slow accumulation/depletion of charge at the interfaces between the perovskite and the transport layers (TLs). The amount of ionic charge accumulation lags behind the application of the potential difference, and affects the photo-current by modifying the carrier collection

efficiency of each of the TLs. The theory can explain the shape of a typical hysteretic J-V curve as follows.

It is common practice to precondition a PSC, to ensure that it has reached steady state, before performing a J-V measurement. An example protocol for a J-V scan is to precondition the cell at open-circuit (*i.e.* at the applied voltage at which no net current flows) before scanning the applied voltage down to zero and back up to open-circuit at a constant voltage scan rate. The result of this protocol is a J-V curve, see Figure 2.2. Under illumination, the open-circuit voltage for a typical PSC is close to the value of its built-in voltage (around 1 V). Hence, at the start of the example J-V scan, the steady-state ionic charge distribution is close to being uniform across the perovskite layer. As the applied voltage is scanned down from the value of the built-in voltage to zero, a potential difference of increasing magnitude is applied to the device which results in a positive electric field across the perovskite layer. A positive electric field aids the separation and transport of photo-generated charges within the perovskite, encouraging electrons towards the ETL and holes towards the HTL. However the positive electric field also encourages the migration of any mobile ionic species in the perovskite towards one of the contacts. During the reverse scan, a slow build-up of ionic charge at the interfaces between the perovskite and the TLs (which are assumed to be impermeable to ions) progressively screens the electric field, see Figure 2.3. A reduced/negative internal electric field is detrimental to the performance of a cell which relies on the efficient separation of charges resulting from a positive electric field. As the ionic charge accumulation lags behind the scan, this slow screening of the electric field can explain why the photo-current is typically lower on the forward scan, compared to the reverse scan.

Ionic charge accumulation at the interfaces also modifies the efficiency of charge carrier extraction into the TLs [61]. However, the interplay between electronic and ionic motion, for different cell architectures, material properties and experimental protocols, is too complex to be described heuristically. Therefore it is necessary to explore and refine the proposed explanation of hysteresis, via the use of quantitative simulation, in order to find out to what extent the unusual behaviour of PSCs can be attributed to ion vacancy migration. Models based on drift-diffusion theory offer the advantage of directly linking properties of the microscopic device physics to the performance of an entire PSC.

2.3.3 Models based on drift-diffusion theory

Prior to the realisation of the importance of mobile ions in PSCs, a drift-diffusion model for the electronic charge carriers was presented by Foster *et al.* [52]. The motion of the charge carriers is considered in one spatial dimension (perpendicular to the material inter-

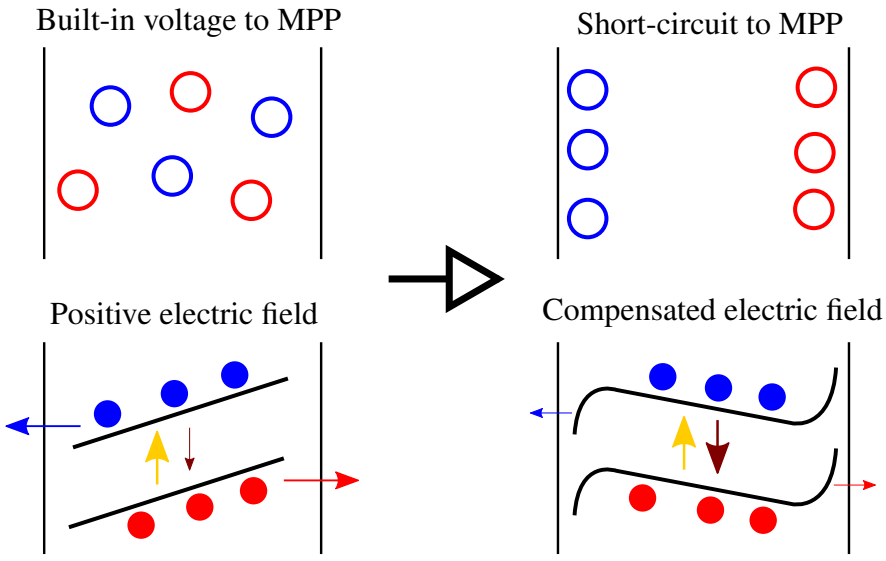

FIGURE 2.3: Schematic diagrams to demonstrate how a slow build-up of ionic charge could cause J-V hysteresis. Left: the internal state of a cell after a rapid change in the applied voltage from the built-in voltage (around 1 V) to MPP (typically around 0.8 V). Right: internal state of a cell after a rapid change in the applied voltage from near short-circuit (0 V) to MPP. The top panels show the distribution of ionic charges (open circles) while the bottom panels show the corresponding band energy diagram for electronic charges (filled circles) with arrows indicating the processes of photo-generation (yellow), bulk recombination (dark red) and charge carrier extraction (blue and red).

faces and in the direction of the photo-current) across three layers of a PSC, namely, the electron transport layer (ETL), the perovskite absorber layer and the hole transport layer (HTL). These three layers are sandwiched between metal contacts described by Ohmic boundary conditions. The model consists of partial differential equations (PDEs) for the conservation of charge carriers (electrons and holes) coupled with Poisson's equation for the electric potential. The model is analysed using both a numerical technique and the method of matched asymptotic expansions. Good agreement is demonstrated between the two approaches but, without mobile ions, the model cannot reproduce the dynamic behaviour of a PSC.

Tress *et al.* [140] performed proof-of-concept simulations for ion migration as the origin of hysteresis by adapting a drift-diffusion model designed for a standard (non-ionic) p-i-n heterojunction solar cell. The proposed theory suggests that, at a steady applied voltage, ionic charge accumulates to fully or partially screen the electric field and reduce the magnitude of the electric field across the bulk of the perovskite layer to zero. This effect is captured in the electronic model by setting the value of the cell's built-in voltage to the negative of the preconditioning voltage. J-V scans are then simulated at a scan rate (100 V/s) that is assumed to be sufficiently fast that the ions do not have time to redistribute during the measurement.

The first drift-diffusion models for the operation of a PSC that include both electronic and ionic motion were provided by van Reenen *et al.* [144] and Richardson *et al.* [109]. Simulations by van Reenen *et al.* [144] indicate that the inclusion of a mobile ionic species, at a mean density of 10^{18} cm^{-3}, in the perovskite layer can cause the type of J-V hysteresis observed experimentally. However, only the results of simulations that make use of unrealistically high ion mobilities and voltage scan rates are included, due to prohibitively long calculation times for more realistic values. A second, simpler approach is adopted based on the assumption that a sufficiently fast J-V scan can be simulated by decoupling the charge carrier dynamics from the relatively slow motion of ions. Following the experimental procedure, the numerical technique is two-step: firstly, the steady-state ion distribution is calculated as a function of the preconditioning voltage, then the charge carrier dynamics are simulated for a varying voltage while the ion distribution is held fixed. Using this approach, the model is shown to qualitatively reproduce the experimental trend, published by Tress *et al.* [140], on the preconditioning voltage-dependence of the photo-current measured at the very fast scan rate of 100 V/s. However, the numerical method of solution is shown to be unable to resolve the solution accurately in space; this is discussed in detail in Section 4.1. The same approach has subsequently been used by Levine *et al.* [81] to investigate the effects of temperature-dependent charge carrier dynamics on the extent of J-V hysteresis.

A different approach is taken by Richardson *et al.* [109, 112] who perform an asymptotic analysis of a single layer model for just the perovskite layer that includes mobile iodide ion vacancies at a mean density of 1.6×10^{19} cm^3. The use of asymptotic approximations leads to a decoupling of the ion vacancy dynamics from the evolution of the charge carrier distributions, which are quasi-steady on the timescales of interest and obtained numerically. Full details of the asymptotic method are given in [34]. Simulations using a diffusion coefficient on the order of that predicted by atomistic models ($\sim 10^{-12}$ cm^2/s) show qualitative agreement with experimental J-V curves measured over a range of scan rates. The same method of solution is used by O'Kane *et al.* [99] to simulate dark current transient measurements.

A time-dependent drift-diffusion model, that describes a p-i-n homojunction with mobile ions included in the intrinsic perovskite layer, is investigated by Calado *et al.* [22]. The approximation of a PSC as a p-i-n homojunction means that differences in the material properties (such as the permittivity and band energy levels) of the ETL and HTL compared to the perovskite layer are neglected. Such approximations lead to significant differences between their simulations and the results of other models, as described in Section 4.1. The mobile ionic species is assumed to be positively charged (*e.g.* iodide ion vacancies), to exist at a mean density of 10^{19} cm^{-3} within the perovskite layer and to be balanced by an equal density of static negative charge. The work addresses the unre-

solved issue of how the extent of J-V hysteresis can depend so strongly on the choice of contact layers if the origin of hysteresis is ion vacancy migration, a mechanism intrinsic to the perovskite layer. Transient measurements of the open-circuit voltage and photocurrent are simulated and it is shown that electric field screening, consistent with ion migration, can be observed in both cells that exhibit significant J-V hysteresis at room temperature and those that do not. The model equations are solved numerically using one of MATLAB's built-in solvers, namely `pdepe`, however it is noted that a compromise was required between numerical accuracy and calculation time. This method of solution is reviewed and used as a benchmark for comparison in Chapter 4.

2.4 Summary

In summary, anomalous hysteresis has been observed in the J-V curves and other transient measurements of perovskite solar cells. This phenomenon is an obstacle to the development of PSCs into a viable thin-film technology as it prevents accurate measurement of the PCE of a cell and, more importantly, its causes are likely linked to the rapid degradation of the devices. Even during steady-state operation, the underlying cause of hysteresis affects a cell's behaviour and so it is crucial to determine its fundamental origin. Three possible causes were initially suggested to explain hysteresis but a consensus has since been reached that only one of these mechanisms is capable of explaining the growing amount of experimental data. A combination of experimental and computational research has shown that iodide ion vacancy migration within the perovskite layer of a PSC is the most feasible origin of hysteresis.

However, findings from models of ion vacancy migration have thus far been limited due to long calculation times and difficulties associated with obtaining accurate solutions to drift-diffusion models within realistic parameter regimes. The numerical difficulties are related to the spatial and temporal stiffness inherent to the model and reveal why many of the solution attempts to date have had to use unrealistic parameters. Prior to 2017, the only study to obtain solutions within physically relevant parameter regimes is that of Richardson *et al.* [109] who make use of the stiffness of the problem to simplify the model. In 2017, further work on the drift-diffusion modelling of PSCs was presented by colleagues of Richardson [40, 99] amongst others [68, 96, 108, 126]. A detailed review of the technical limitations and flaws of the different methods of solution used in the literature is given in Section 4.1. Advances in the methods used to obtain solutions to drift-diffusion models of PSCs are thus required in order to improve the (so far only qualitative) agreement between simulation and experimental results. Detailed investigation of the interplay between ion vacancy migration and other mechanisms that take place within

a PSC, such as charge carrier recombination, is also needed to further our understanding and guide the development of PSCs.

In the next chapter, a drift-diffusion model for the transport of iodide ion vacancies and charge carriers across the perovskite layer and both transport layers of a planar PSC is set out, assumptions of the model are justified and physically relevant values of the model parameters are provided. Numerical and asymptotic methods of solution of this model are the subjects of Chapters 4 and 5, respectively.

Chapter 3

The Charge Transport Model

The aim of this chapter is to present a comprehensive but tractable model for the operation of a planar perovskite solar cell (PSC). In this context, a "good" model is one that reproduces the important features of PSC behaviour by capturing the interplay of all relevant device physics, whilst depending only on key physical quantities and the minimum number of fitting parameters. In particular, the principal focus of this work is on investigating the motion of iodide ion vacancies as the origin of the anomalous J-V characteristics exhibited by PSCs on the timescale of seconds.

Firstly, the operation of a PSC is described. In the second section, a model is formulated based upon the theory of drift and diffusion and the model assumptions are discussed. A summary of the model is displayed in Figure 3.4. The rates of charge carrier generation and recombination are the topic of Section 3.3. A set of estimates for each of the physical parameters is given in Section 3.4. Then, based upon these estimates, a suitable non-dimensionalisation of the model is presented in Section 3.5.

3.1 Operational principles of a perovskite solar cell

The structure of a planar PSC is shown in Figure 3.1. The illustration shows a cell with a standard architecture, in which the light enters through the ETL, however cells can also be fabricated with an inverted architecture in which the light enters though the HTL. When the cell is under illumination, charge-carrier pairs (electrons in the conduction band and holes in the valence band) are generated within the perovskite absorber layer. These photo-generated charge carriers drift and diffuse across the perovskite layer. When the cell is operating in a power-generating regime, electrons are extracted into the adjacent electron transport layer (ETL) and holes are extracted into the hole transport layer (HTL).

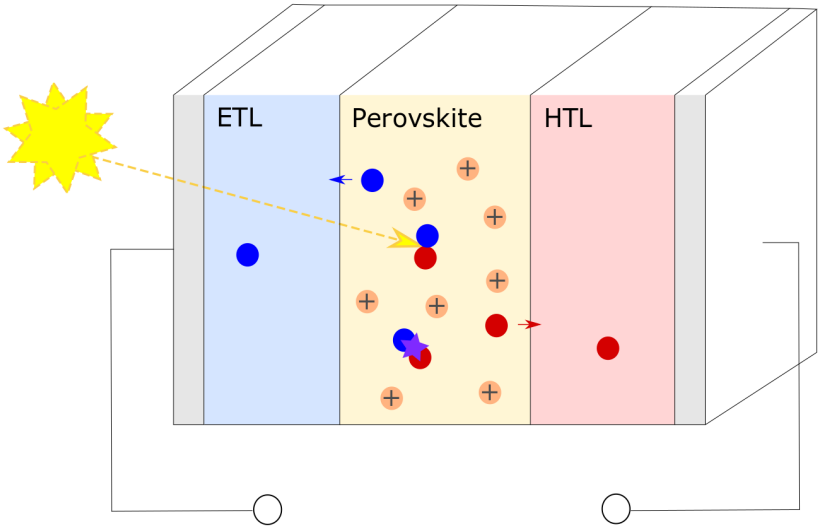

FIGURE 3.1: An illustration of a three-layer planar perovskite solar cell, indicating the processes of charge carrier photo-generation, recombination and extraction within a PSC and the locations of the different mobile charge species in the model. Electrons (blue) exist in the ETL and perovskite, positively-charged iodide ion vacancies (orange) are restricted to the perovskite layer and holes (red) exist in the perovskite and HTL.

These transport layers (TLs), due to their material properties, selectively transport either electrons or holes, and block the opposite type of carrier. The resulting separation of charge generates an electric current (or photo-current). In an efficient cell, only a minimal proportion of the photo-current is lost due to charge carrier recombination. It is not possible to eliminate recombination entirely according to the laws of thermodynamics. Descriptions of the photo-generation profile and the different types of electron-hole recombination in a PSC are given in Section 3.3.

A feature peculiar to PSCs is that the perovskite material (most commonly $MAPbI_3$) contains ion vacancies that enable the migration of ions across the perovskite layer. This migration takes place on a timescale that is slower than that of the charge carrier dynamics. A changing ion vacancy distribution within the perovskite layer has a large effect on the electric field across the device (tending to screen the built-in field) and hence the ability of the cell to separate and extract charge. The result is that the photo-current, and therefore the power output, of a PSC depends upon the history of external conditions to which the cell has been subjected. The reversible effects of this dependence are, in the field of PSC research, simply referred to as hysteresis.

The effects of the motion of iodide ion vacancies on PSC performance can be unravelled via a thorough investigation of an appropriate charge-transport model. It turns out that the screening of the electric field by the ion vacancy distribution is not only significant for transient behaviour, such as hysteresis, but also influences steady-state performance. Therefore, it is necessary to consider an ion migration model not only for the purpose of

reproducing transient behaviour but also to predict the true theoretical potential of PSCs operating at steady-state.

Charge-transport modelling based on the theory of drift and diffusion is the appropriate framework for this investigation. The physical parameters in a drift-diffusion model, relating to the microscopic properties of a PSC, can be derived either from experimental measurements or from first principles via DFT calculations. Hence, simulations of such a model can reveal how microscopic properties affect the power output of an entire device. In the next section, drift-diffusion theory is used to write down a system of equations and boundary conditions that describe the movement of both iodide ion vacancies and charge carriers in a PSC.

3.2 Model formulation

As illustrated in Figure 3.1, a planar PSC is comprised of three semiconducting material layers sandwiched between two metal contacts. The transport of charge is assumed to predominantly occur in one spatial dimension across the cell, in the direction perpendicular to the material interfaces, for the following reasons. Firstly, there is a significant disparity in lengthscales between the width of the perovskite layer between the ETL and HTL ($\sim$100-500 nm) and the dimensions of the surface area of the cell ($\sim 1 \times 1$ cm^2). Secondly, any potential difference between the two metal contacts is applied uniformly across the area of the cell, with its gradient in the direction perpendicular to the contacts. Hence, a model in one spatial dimension (x) and time (t) is assumed to be able to capture the dynamic behaviour of a PSC. In addition, the three material layers are each assumed to be compositionally invariant. In particular, this assumption neglects any possible influence on overall PSC performance of the spatial distribution of grain boundaries that exists within a polycrystalline perovskite layer, including any effects that may result from grain boundaries acting as preferential channels for ion vacancy migration [124].

TABLE 3.1: Table of model variables.

Symbol	Description	Unit	Symbol	Description	Unit
$n(x,t)$	Electron concentration	m^{-3}	$j^n(x,t)$	Electron current density	Am^{-2}
$p(x,t)$	Hole concentration	m^{-3}	$j^p(x,t)$	Hole current density	Am^{-2}
$P(x,t)$	Iodide ion density	m^{-3}	$F^P(x,t)$	Iodide ion flux	$\mathrm{m}^{-2}\mathrm{s}^{-1}$
$\phi(x,t)$	Electric potential	V	$E(x,t)$	Electric field	Vm^{-1}
$G(x,t)$	Photo-generation rate	$\mathrm{m}^{-3}\mathrm{s}^{-1}$	$R(n,p)$	Recombination rate	$\mathrm{m}^{-3}\mathrm{s}^{-1}$

The operation of a solar cell, in terms of the generation/recombination and transport of electronic charge carriers, is well-described within the standard framework of semiconductor device physics [95]. In this work, standard semiconductor terminology and nota-

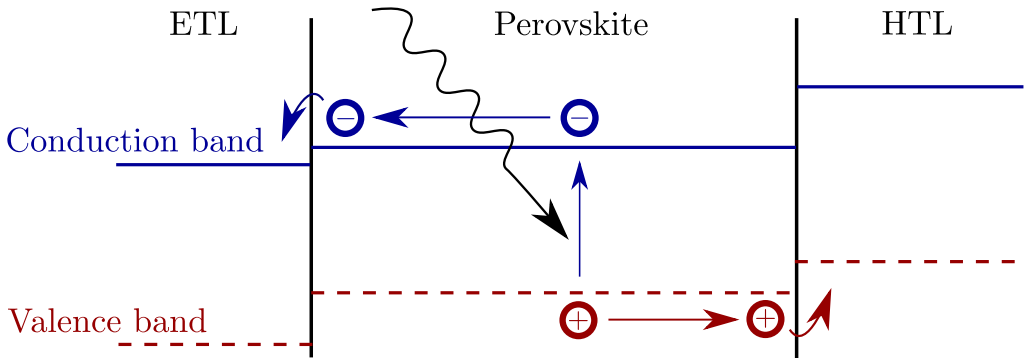

FIGURE 3.2: Sketch of a planar PSC showing the structure of the conduction (blue solid lines) and valence (red dashed lines) bands and the flow of electrons and holes, reproduced from the work of Courtier *et al.* [35].

tion is used. A list of the model variables is given in Table 3.1, while a list of the device parameters, along with typical values estimated from the literature, is given in Table 3.2. A diagram of the process of photo-current generation in a PSC is shown in Figure 3.2. The important features of this schematic band energy diagram are:

- a suitable band gap (between the conduction and valence bands) of the perovskite to allow for efficient absorption of sunlight;
- favourable alignment of the conduction band across the ETL/perovskite interface and the valence band across the perovskite/HTL interface to allow for efficient extraction of electrons into the ETL and holes in the HTL; and,
- large offsets in the valence band across the ETL/perovskite interface and the conduction band across the perovskite/HTL interface that create energy barriers which prevent entry of the opposite type of charge carrier into the TLs.

Electrons in the conduction band and holes in the valence band move under the influences of thermally-induced diffusion and electronically-induced drift. The electron and hole current equations in terms of diffusion (the first term) and drift (the second term), from [95] Section 3.7.1, are

$$j^n = qD_n\frac{\partial n}{\partial x} + q\mu_n nE\,, \qquad j^p = -qD_p\frac{\partial p}{\partial x} + q\mu_p pE\,, \tag{3.1}$$

in which $j^n(x,t)$ and $j^p(x,t)$ are, respectively, the electron and hole current densities in the direction of x; q is the elementary charge; $n(x,t)$ is the electron concentration; $p(x,t)$ is the hole concentration; $E(x,t)$ is the electric field in the direction of x; and D and μ are, respectively, the diffusion coefficient and the mobility of the charge carrier indicated by the subscript. The charge carrier mobilities can be related to their respective diffusion

coefficients via the Einstein relation:

$$\mu = \frac{D}{V_T}\,, \tag{3.2}$$

where V_T is the thermal voltage and is given by $k_B T/q$, in which k_B is Boltzmann's constant and T is absolute temperature.

The dynamics and conservation of the charge carriers are described by the semiconductor transport equations. From [95] Sections 4.1-4.2, these are

$$\frac{\partial n}{\partial t} - \frac{1}{q}\frac{\partial j^n}{\partial x} = G - R\,, \qquad \frac{\partial p}{\partial t} + \frac{1}{q}\frac{\partial j^p}{\partial x} = G - R\,, \tag{3.3}$$

where G and R are the volume rates of charge carrier generation and recombination, respectively. See Section 3.3 for details on the functional forms of these rates.

The theory of ion vacancy migration in PSCs suggests that the perovskite layer should be treated as a mixed electronic-ionic conductor [138]. In all pre-existing ion migration models of PSCs [22, 109, 144], this treatment has been accomplished via the inclusion of an additional drift-diffusion equation, analogous to those for the charge carriers, for the motion of each mobile ionic species. However, due to the physical size of the ions/ion vacancies in the perovskite structure, compared to the smaller charge carriers, it is worth considering whether this description is valid. In Appendix A, an expression for the flux of ion vacancies within the perovskite layer is derived using both a hopping model and a thermodynamic approach that include steric effects. It is found that, in the case of one mobile ionic species, the standard drift-diffusion equation is indeed a good approximation. However, a recent investigation of a model for a single layer of perovskite, between metal contacts, that includes both mobile cation and anion vacancies [146] shows that if two mobile ionic species exist within the perovskite, the limit of close-packing can easily be exceeded, when using the standard description. In this case, the drift-diffusion equations for ion vacancies can be modified as described in Appendix A to take account of steric effects [*work in preparation by J. M. Foster, N. E. Courtier, and G. Richardson*].

In this study, it is assumed that the only mobile ionic species in $MAPbI_3$ is the iodide ion vacancies and that the number of ion vacancies is fixed, *i.e.* that ion vacancies cannot be generated or recombine with an ion. It is possible that thermal or field-driven generation/recombination of ion vacancies may take place within the perovskite layer, as a result of the low value of the Schottky formation energy (0.14 eV) predicted by DFT calculations [145]. However, the inclusion of this additional mechanism is beyond the scope of this study. Therefore, the conservation of positively charged iodide ion vacancies, with

density $P(x,t)$ and flux $F^P(x,t)$ in the direction of x, is described by

$$\frac{\partial P}{\partial t} + \frac{\partial F^P}{\partial x} = 0\,, \qquad F^P = -D_I\left(\frac{\partial P}{\partial x} - \frac{PE}{V_T}\right)\,, \tag{3.4}$$

where D_I is the diffusion coefficient relating to the iodide ion vacancies.

Finally, the electric field E must obey Gauss's law, *i.e.*

$$\frac{\partial E}{\partial x} = \frac{1}{\varepsilon_s}\left(\rho + \rho_{\text{fixed}}\right)\,, \tag{3.5}$$

where ε_s is the permittivity of the semiconductor, $\rho(n,p,P)$ is the total charge density resulting from the mobile charges (electrons, holes and iodide ion vacancies) and $\rho_{\text{fixed}}(x)$ is the local density of static charge resulting from static dopants or immobile ion vacancies.

In equations (3.1), (3.4) and (3.5), it is often useful to rewrite the electric field in terms of the electric potential $\phi(x,t)$ as follows.

$$E = -\frac{\partial \phi}{\partial x}\,. \tag{3.6}$$

In particular, the substitution of ϕ into (3.5) results in Poisson's equation for the electric potential:

$$\frac{\partial^2 \phi}{\partial x^2} = -\frac{1}{\varepsilon_s}\left(\rho + \rho_{\text{fixed}}\right)\,. \tag{3.7}$$

Poisson's equation couples to the appropriate set of conservation and current/flux equations for the electrons, holes and/or iodide ion vacancies to form a complete description of charge transport within each layer of a PSC.

In the following three subsections, the model equations for the perovskite layer and two TLs of a PSC are set out along with appropriate boundary and continuity conditions. All continuity conditions are given together in Section 3.2.3. The equations are written in terms of the four dependent variables: n, p, P and ϕ. The domains of each of these variables are shown schematically in Figure 3.3. The widths of the ETL, perovskite layer and HTL are denoted by b_E, b and b_H, respectively.

3.2.1 Perovskite layer

The perovskite layer contains all three species of mobile charge. The existence of iodide ion vacancies, each with charge q, at a mean density denoted by N_0 is assumed

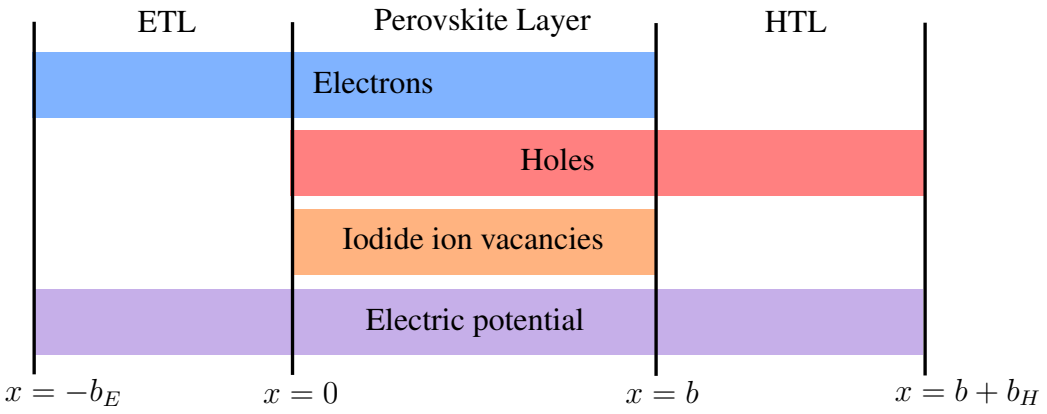

FIGURE 3.3: A sketch showing the domains for the different variables across the three layers of a PSC. Each coloured bar represents the domain of a second-order equation (namely, conservation equations for the electrons, holes and iodide ion vacancies and Poisson's equation for the electric potential).

to be compensated by the existence of a static and uniformly distributed density of negatively charged cation vacancies. Note that this static charge density ($-qN_0$) could include contributions from any lead (Pb^{2+}) vacancies as well as the methyl ammonium (MA^+) vacancies. In addition, it is assumed that the perovskite is not doped. Therefore, the total mobile charge density ρ is formed from the electron, hole and iodide ion vacancy densities, while ρ_{fixed} equals the static charge density due to the cation vacancies ($-qN_0$). Hence, ion vacancy motion and charge carrier transport in the interval $0 < x < b$ is described by three conservation equations coupled to Poisson's equation as follows.

$$\frac{\partial n}{\partial t} - \frac{1}{q}\frac{\partial j^n}{\partial x} = G - R\,, \qquad j^n = qD_n\left(\frac{\partial n}{\partial x} - \frac{n}{V_T}\frac{\partial \phi}{\partial x}\right)\,, \tag{3.8}$$

$$\frac{\partial p}{\partial t} + \frac{1}{q}\frac{\partial j^p}{\partial x} = G - R\,, \qquad j^p = -qD_p\left(\frac{\partial p}{\partial x} + \frac{p}{V_T}\frac{\partial \phi}{\partial x}\right)\,, \tag{3.9}$$

$$\frac{\partial P}{\partial t} + \frac{\partial F^P}{\partial x} = 0\,, \qquad F^P = -D_I\left(\frac{\partial P}{\partial x} + \frac{P}{V_T}\frac{\partial \phi}{\partial x}\right)\,, \tag{3.10}$$

$$\frac{\partial^2 \phi}{\partial x^2} = -\frac{q}{\varepsilon_p}(P - N_0 + p - n)\,, \tag{3.11}$$

where ε_p is the permittivity of the perovskite.

This system of equations is eighth-order and so requires the application of eight boundary/continuity conditions. Poisson's equation, (3.11), is supplemented by two continuity conditions for the electric potential, at $x = 0$ (the interface with the ETL) and $x = b$ (the interface with the HTL). The conservation equations for the electrons and holes, (3.8)-(3.9), are each supplemented by a continuity condition (on the electron or hole concentration, respectively) at the interface with the corresponding TL and a boundary condition (on the electron or hole current density, respectively) at the other. The remaining two

conditions are boundary conditions for the distribution of iodide ion vacancies. For the continuity conditions, see Section 3.2.3. The four perovskite layer boundary conditions are as follows.

At the interface between the ETL and the perovskite, the energy band offset between the valence bands of the two materials (as shown in Figure 3.2) is such that it prevents the transport of holes out of the perovskite. However, holes may "leak out" of the perovskite via trap-assisted recombination with an electron from the ETL. Similarly, at the interface between the perovskite and the HTL, the conduction band offset prevents the transport of electrons out of the perovskite but electrons may recombine via trap states with a hole from the HTL. Hence, the appropriate boundary conditions on the electron and hole currents are

$$j^p|_{x=0} = -qR_l\,, \qquad\qquad j^n|_{x=b} = -qR_r\,, \tag{3.12}$$

where R_l and R_r are the recombination rates at the left (ETL/perovskite) and right (perovskite/HTL) interface respectively. See Section 3.3 for more details.

It is assumed that the material interfaces also act as barriers to the motion of ions. Therefore, the following zero-flux conditions are imposed on the iodide ion vacancies.

$$F^P|_{x=0} = 0\,, \qquad\qquad F^P|_{x=b} = 0\,. \tag{3.13}$$

3.2.2 Transport layers

In this model, it is assumed that the ETL has a sufficiently large band gap and is sufficiently highly doped, with a doping density d_E, that the concentration of holes is negligible (*i.e.* $p \equiv 0$) and that no generation or recombination of charge carriers takes place within this layer (*i.e.* $G \equiv R \equiv 0$). These assumptions imply that the only mobile charge species to be considered in the ETL is the electrons. Therefore, charge transport in the interval $-b_E < x < 0$ is described by the conservation of electrons coupled to Poisson's equation as follows.

$$\frac{\partial n}{\partial t} - \frac{1}{q}\frac{\partial j^n}{\partial x} = 0\,, \qquad\qquad j^n = qD_E\left(\frac{\partial n}{\partial x} - \frac{n}{V_T}\frac{\partial \phi}{\partial x}\right)\,, \tag{3.14}$$

$$\frac{\partial^2 \phi}{\partial x^2} = \frac{q}{\varepsilon_E}(n - d_E)\,, \tag{3.15}$$

where ε_E and D_E are, respectively, the permittivity and the electron diffusion coefficient associated with the ETL.

Equations (3.14)-(3.15) are both subject to two continuity conditions at $x = 0$ (the ETL/perovskite interface) and one boundary condition at $x = -b_E$ (the metal contact). The ETL is assumed to form an Ohmic contact with the adjoining metal layer. Therefore, the following Dirichlet conditions, from *e.g.* [119] Section 6.4, are used.

$$n|_{x=-b_E} = d_E\,, \qquad\qquad \phi|_{x=-b_E} = \frac{V_{bi} - V}{2}\,, \tag{3.16}$$

in which $V_{bi} - V(t)$ is the total potential difference across the cell, where V_{bi} is the cell's built-in voltage and $V(t)$ is the applied voltage. The built-in voltage is determined by the difference in work-function across the device, which is equal to the difference between the Fermi levels of the ETL and HTL at equilibrium [95]. Hence,

$$V_{bi} = \frac{1}{q}(E_{f_E} - E_{f_H})\,, \tag{3.17}$$

where E_{f_E} and E_{f_H} are the Fermi levels of the ETL and HTL, respectively.

An analogous set of assumptions for the HTL (*i.e.* that $n \equiv 0$ and $G \equiv R \equiv 0$) imply that charge transport in the interval $b < x < b + b_H$ is described by the conservation of holes coupled to Poisson's equation as follows.

$$\frac{\partial p}{\partial t} + \frac{1}{q}\frac{\partial j^p}{\partial x} = 0\,, \qquad\qquad j^p = -qD_H\left(\frac{\partial p}{\partial x} + \frac{p}{V_T}\frac{\partial \phi}{\partial x}\right)\,, \tag{3.18}$$

$$\frac{\partial^2 \phi}{\partial x^2} = \frac{q}{\varepsilon_E}(d_H - p)\,, \tag{3.19}$$

where d_H, ε_H and D_H are, respectively, the doping density, permittivity and the hole diffusion coefficient associated with the HTL.

The boundary conditions for the Ohmic metal contact at $x = b + b_H$ are

$$p|_{x=b+b_H} = d_H\,, \qquad\qquad \phi|_{x=b+b_H} = -\frac{V_{bi} - V}{2}\,, \tag{3.20}$$

while the remaining four continuity conditions for (3.18)-(3.19) are included in the complete set of continuity conditions given in the next subsection.

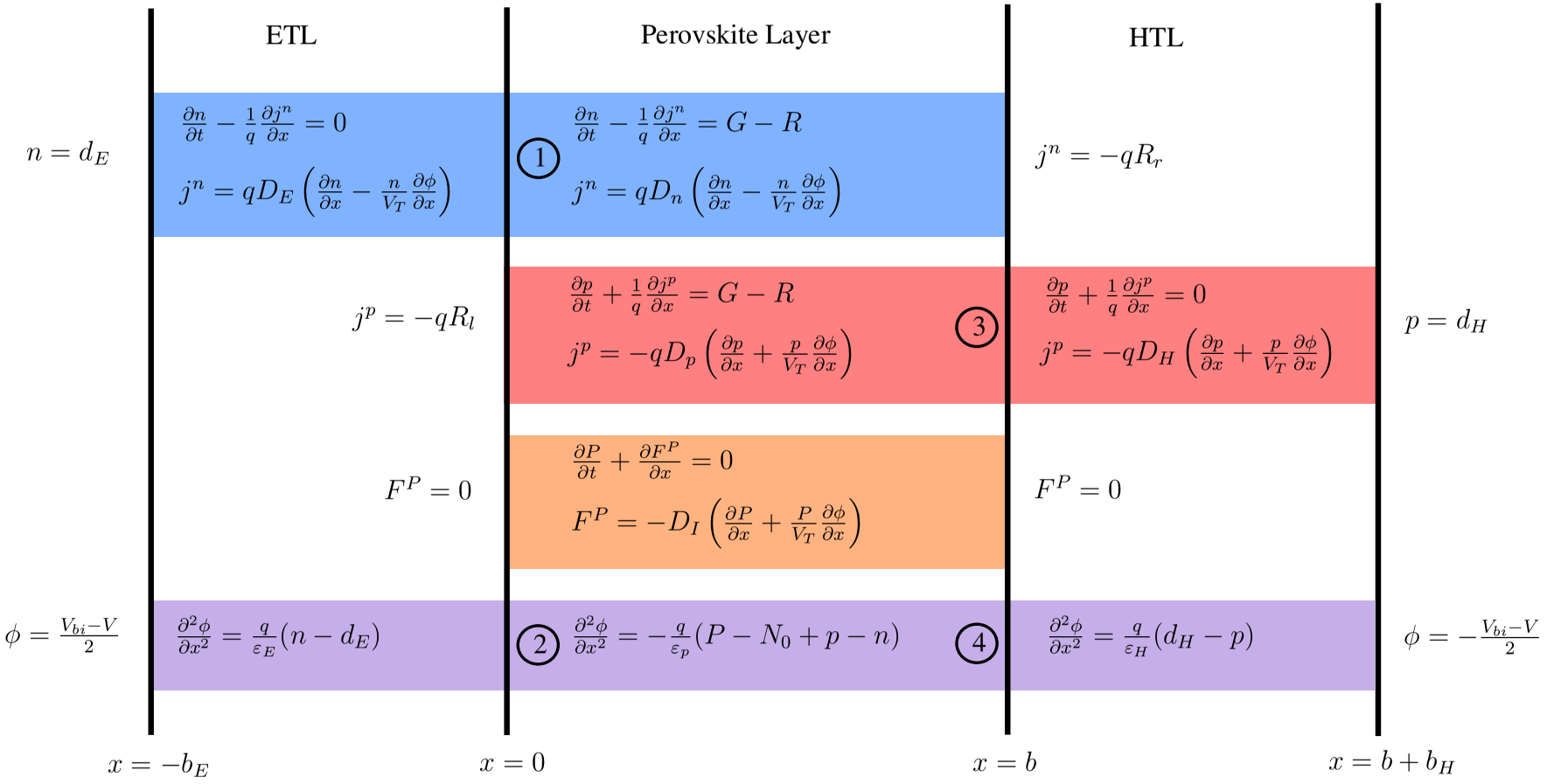

FIGURE 3.4: Model equations in terms of the electrons (with concentration n, current density j^n), holes (concentration p, current density j^p), iodide ion vacancies (density P, flux F^P) and electric potential (ϕ). Coloured bars show the domains of each equation. Boundary conditions are included alongside while the continuity equations at (1-4) are given together in Section 3.2.3. Definitions and estimates for the parameters are given in Table 3.2.

3.2.3 Continuity conditions at the interfaces

At each interface, the majority current density is conserved taking account of the loss of charge due to interface recombination. The electric potential and the electric displacement field (which, in this model, is equivalent to the product of the permittivity and the electric field) are both continuous across an interface. Therefore, at the interface between the ETL and the perovskite,

$$j^n|_{x=0^-} = j^n|_{x=0^+} - R_l\,, \quad \phi|_{x=0^-} = \phi|_{x=0^+}\,, \quad \varepsilon_E \frac{\partial\phi}{\partial x}\Big|_{x=0^-} = \varepsilon_p \frac{\partial\phi}{\partial x}\Big|_{x=0^+}\,. \tag{3.21}$$

Similarly, at the interface between the perovskite and HTL,

$$j^p|_{x=b^-} - R_r = j^p|_{x=b^+}\,, \quad \varepsilon_p \frac{\partial\phi}{\partial x}\Big|_{x=b^-} = \varepsilon_H \frac{\partial\phi}{\partial x}\Big|_{x=b^+}\,, \quad \phi|_{x=b^-} = \phi|_{x=b^+}\,. \tag{3.22}$$

In addition, the majority carrier concentration in each TL is related to the corresponding carrier concentration in the perovskite by a factor depending on the relevant band offset, as in [52, 112].

$$k_E n|_{x=0^-} = n|_{x=0^+}\,, \qquad\qquad p|_{x=b^-} = k_H p|_{x=b^+}\,, \tag{3.23}$$

where k_E and k_H are the following constants of proportionality.

$$k_E = \frac{N_{C,p}}{N_{C,E}} \exp\left(-\frac{E_{C,p} - E_{C,E}}{k_B T}\right)\,, \quad k_H = \frac{N_{V,p}}{N_{V,H}} \exp\left(\frac{E_{V,p} - E_{V,H}}{k_B T}\right)\,, \tag{3.24}$$

where N_C is the effective conduction band density of states (DoS), N_V is the effective valence band DoS, E_C is the energy of the conduction band edge and E_V is the energy of the valence band edge, each for the material indicated by the second subscript (E, p or H for ETL, perovskite or HTL, respectively). In this work, the values of $N_{C,E}$ and $N_{V,H}$ are approximated by the doping densities in the relevant TL (d_E and d_H, respectively). Also, due to the high levels of TL doping used in practice, the conduction band edge of the ETL and valence band edge of the HTL are here approximated by the Fermi levels of the respective TL. Hence, the following approximate definitions, in which the subscript p for perovskite has been dropped, are used in place of (3.24).

$$k_E = \frac{N_C}{d_E} \exp\left(-\frac{E_C - E_{f_E}}{k_B T}\right)\,, \qquad k_H = \frac{N_V}{d_H} \exp\left(\frac{E_V - E_{f_H}}{k_B T}\right)\,. \tag{3.25}$$

3.3 Charge carrier generation and recombination

The opposing processes of charge carrier generation and recombination take place within the perovskite absorber layer and at the interfaces between the perovskite and the TLs. High PSC performance relies on efficient photo-generation, provided by the desirable panchromatic absorption properties of perovskite, combined with minimal recombination, obtained via high quality material deposition and cell design. In this section, descriptions and models are given for the different types of generation and recombination within a PSC.

3.3.1 Thermal generation and recombination

In a semiconductor, such as perovskite, an electron can be thermally excited from the valence band to the conduction band via a transfer of vibrational energy from a phonon [95]. This process is termed thermal generation and there is an equivalent process for the relaxation of a conduction electron down to the valence band. In thermal equilibrium, the rates of thermal generation and recombination are equal, meaning that the net rate of change in the charge carrier concentrations due to thermal processes is zero. From [95] Section 3.4.3, the equilibrium product of the carrier concentration can be expressed as

$$np = n_i^2 = N_C N_V \mathrm{e}^{-E_g/k_B T}\,, \tag{3.26}$$

where n_i is the intrinsic carrier concentration and E_g is the magnitude of the band gap. As a result, the rate of thermal generation is not included in the generation rate G, but is instead included implicitly in the form of the recombination rate R. Specifically, rates of recombination are chosen to be proportional to $(np - n_i^2)$ in order to ensure that there is zero net recombination when the device is in thermal equilibrium.

3.3.2 Photo-generation

The absorption of a photon with an energy exceeding that of the band gap results in the generation of an exciton. At ambient temperatures, excitons in perovskite rapidly dissociate into an electron-hole pair due to their low binding energy of $\sim$50 meV [78]. Therefore it is assumed that the absorption of a photon with sufficient energy corresponds directly to the photo-generation of an electron-hole pair.

In this work, the rate of photo-generation within the perovskite layer is assumed to follow the Beer-Lambert law of light absorption for a uniform material. In a standard-

architecture PSC, in which light enters through the ETL (from the left), the generation rate therefore takes the form

$$G(x,t) = I_s(t) F_{\text{ph}} \alpha \mathrm{e}^{-\alpha x} \,, \tag{3.27}$$

where I_s is the intensity of light (as a multiple of 1 Sun), F_{ph} is the flux of photons incident on the light-facing perovskite surface (after accounting for reflection) when the cell is under the equivalent of 1 Sun illumination and α is the light absorption coefficient of the perovskite. In an inverted-architecture PSC, in which light enters through the HTL (from the right),

$$G(x,t) = I_s(t) F_{\text{ph}} \alpha \mathrm{e}^{-\alpha(b-x)} \,. \tag{3.28}$$

Hence the photo-generation rate, valid for both types of PSC architecture, is given by

$$G(x,t) = I_s(t) F_{\text{ph}} \alpha \mathrm{e}^{-\alpha\left(lx + \frac{1-l}{2} b\right)} \,, \qquad l = \begin{cases} 1 & \text{for standard architecture,} \\ -1 & \text{for inverted architecture.} \end{cases} \tag{3.29}$$

A more detailed model of light absorption is used by Walter *et al.* [146].

3.3.3 Bulk recombination

In order to minimise photo-current losses due to charge carrier recombination, it is vital to determine the main recombination pathways in a PSC. According to the thermodynamic principle of detailed balance, losses due to radiative recombination (the opposite process to photo-generation) cannot be eliminated [95]. However, any additional losses due to non-radiative recombination prevent the PSC from achieving its theoretical maximum. The term non-radiative recombination refers to the annihilation of a conduction electron and a hole in which the energy is released in the form of a phonon or via a transfer of kinetic energy to another carrier, rather than as a photon. The principal mechanisms through which recombination can take place are shown schematically in Figure 3.5.

Radiative recombination is a band-to-band process, which depends on the availability of one of each type of charge carrier and is therefore modelled using a bimolecular recombination rate:

$$R_{\text{bim}}(n,p) = \beta(np - n_i^2) \,, \tag{3.30}$$

where β is the radiative recombination coefficient associated with the perovskite.

In perovskite, the dominant form of non-radiative recombination is believed to be trap-assisted [109, 131]. The study by Stranks *et al.* [131] investigates the recombination kinetics of a layer of perovskite (with the mixed halide formulation $CH_3NH_3PbI_{3-x}Cl_x$)

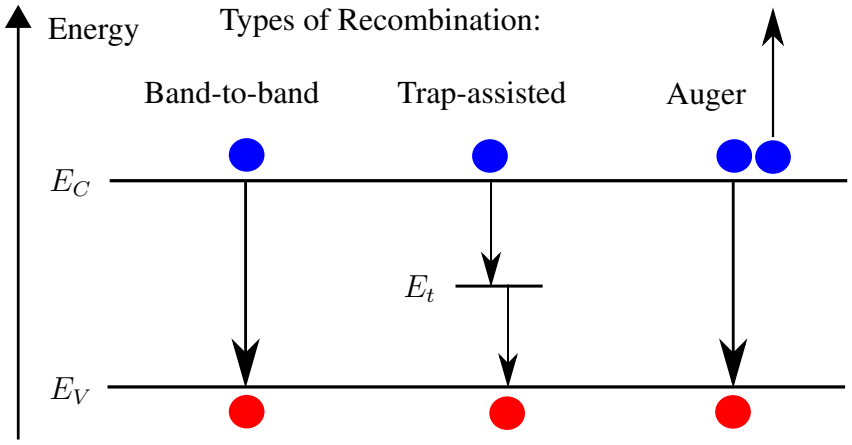

FIGURE 3.5: A diagram showing the three different mechanisms for recombination: a) band-to-band, b) trap-assisted and c) Auger recombination.

deposited on glass. A time-dependent model is presented that takes both bimolecular and trap-assisted recombination into account. It is deduced from PL measurements that, at the light intensities associated with sunlight, recombination is predominantly trap-assisted, while bimolecular recombination only becomes significant at higher light intensities.

Trap-assisted recombination is a two-step process involving the capture of an electron by a trap state followed by the annihilation of the trapped electron and a hole. The model by Stranks *et al.* [131] assumes that there is a constant density of trap states (although it is postulated that the density varies with temperature) and explicitly includes the evolution of the number of traps which are filled. In this work, it is assumed that the density of trap states is uniform across the perovskite layer and, as the focus is on the timescale and effects of ion vacancy migration, that the proportion of traps that are filled is in quasi-equilibrium with the free charge carrier densities. Hence, recombination via trap states is modelled using the Shockley-Read-Hall (SRH) recombination rate. Unlike the expressions in [131], the SRH recombination rate (R_{SRH}) includes contributions from the (small) intrinsic concentrations of free and trapped charge carriers that result from the balance between thermal generation and recombination. From [95] Section 4.5.5,

$$R_{\text{SRH}}(n,p) = \frac{np - n_i^2}{\tau_n(p + p_t) + \tau_p(n + n_t)}\,, \tag{3.31}$$

where τ_n and τ_p are, respectively, the electron and hole pseudo-lifetimes, and p_t and n_t are, respectively, the values that the hole and electron concentrations would take if the Fermi level were equal to the trap state energy level (or, in other words, if exactly half the

traps are filled) using the Boltzmann approximation, *i.e.*

$$p_t = n_i \mathrm{e}^{(E_i - E_t)/k_B T}, \qquad n_t = n_i \mathrm{e}^{(E_t - E_i)/k_B T}, \tag{3.32}$$

where E_i is the intrinsic potential energy (equal to the Fermi level of the semiconductor in equilibrium) and E_t is the energy level of the trap states. The derivation of R_{SRH} is extended to include a distribution of trap state energy levels throughout the band gap in [76]. Here, it is assumed that there is a single (most effective or most common) trap state energy level and that it lies near the centre of the band gap. Therefore it is approximately true that $E_t = E_i$ and hence,

$$R_{\text{SRH}}(n,p) = \frac{np - n_i^2}{\tau_n p + \tau_p n + (\tau_n + \tau_p) n_i}, \tag{3.33}$$

The negligible size of the approximate term $(\tau_n + \tau_p)n_i$ relative to the other terms in the denominator implies that this expression is appropriate for a range of trap state energy levels close to E_i.

Stranks *et al.* [131] estimate the values of their model parameters at 300 K via the fitting of experimental PL data. The estimated rates of electron-trapping and trapped charge recombination can be used to calculate electron and hole pseudo-lifetimes of $\tau_n = 2 \times 10^{-7}$ s and $\tau_p = 5 \times 10^{-6}$ s. From these estimates, it is clear that $\tau_p \gg \tau_n$ which indicates that the bulk SRH recombination rate is most likely dominated by the hole concentration (*i.e.* $R_{SRH} \approx p/\tau_p$). The density of trap states is estimated to be as low as 2.5×10^{16} cm^3, which corresponds to approximately one trap state in every 10^6 perovskite unit cells. Similar estimates of $1.2 - 6.7 \times 10^{16}$ cm^3 are reported in [156]. It should be noted, however, that the density and distribution of trap states may depend strongly on the presence of grain boundaries. It has been shown that recombination within perovskite occurs predominantly at grain boundaries [36], which implies that the magnitude of bulk recombination is strongly dependent upon the quality of the perovskite layer. Well formed perovskite layers with large crystals therefore have lower rates of bulk recombination [97]. However, it has also been claimed that the density of grain boundaries has little effect on the recombination dynamics in highly efficient PSCs [32]. Furthermore, advances in perovskite deposition techniques have enabled the formation of large perovskite crystals that span the width of the perovskite layer [121]. So, here, consistent with the assumption of uniform material layers, it is assumed that the recombination parameters are a bulk property of the perovskite layer. Within this assumption, poor quality layers (with small grains and hence a high density of grain boundaries) correspond to comparatively short SRH pseudo-lifetimes and hence high rates of recombination.

Auger recombination involves the collision of three particles (two electrons and a hole).

Therefore, at the charge carrier concentrations associated with typical illumination intensities, this type of recombination is relatively rare and so it is assumed to have a negligible effect on cell performance.

The total bulk recombination rate is equal to the sum of the rates of radiative and non-radiative recombination, *i.e.*

$$R(n,p) = R_{bim} + R_{SRH} = \beta(np - n_i^2) + \frac{np - n_i^2}{\tau_n p + \tau_p n + (\tau_n + \tau_p)n_i}\,. \tag{3.34}$$

In this work, it is assumed from the findings of [109, 131] that the rate of bimolecular recombination is negligible in comparison to the rate of SRH recombination and therefore β is set equal to zero. Estimates for the SRH parameters are given in Table 3.3.

3.3.4 Interface recombination

Interface recombination (also referred to as interfacial or surface recombination) is often attributed as the limiting factor in PSC performance. High densities of interfacial trap states have been identified in all types of PSC architecture, including at interfaces between the perovskite and metal oxide ETLs [102, 135, 153, 157] and between the perovskite and organic HTLs [32, 142]. Successful strategies to reduce the interfacial trap state density have involved modifying/exchanging the TL material [32, 142, 157] or inserting a thin layer of another material (often fullerene, first used in [125], or a fullerene derivative) between the perovskite and the TL [102, 135, 153]. In each case, improved PSC performance has been attributed to lower densities of interfacial trap states leading to reduced rates of recombination. However, each strategy is tailored to the specific device architecture under investigation. These recent studies show that determining the rates of recombination at both the ETL/perovskite and perovskite/HTL interfaces is crucial to enable researchers to identify and reduce losses in performance.

Trap-assisted interface recombination is modelled using the interface SRH recombination rate from [95] Section 4.5.6, in which reciprocal recombination velocities take the place of the pseudo-lifetimes.

$$R_{l,r}(n^-, p^+) = \frac{n^- p^+ - n_i^- n_i^+}{\frac{1}{\nu_n^-}(p^+ + p_t^+) + \frac{1}{\nu_p^+}(n^- + n_t^-)}, \tag{3.35}$$

where superscripts indicate whether a quantity is associated with the left ($-$) or right ($+$) side of the interface, and ν_p and ν_n are the hole and electron recombination velocities towards the relevant interface.

Using the charge carrier density (n and p) continuity conditions in (3.23) and an equivalent "deep-trap" approximation as that used to obtain the bulk SRH recombination rate in (3.33), the expressions for interface recombination at the left (ETL/perovskite) and right (perovskite/HTL) interfaces become

$$R_l(n|_{x=0^+}, p|_{x=0^+}) = \frac{n|_{x=0^+}p|_{x=0^+} - n_i^2}{\frac{k_E}{\nu_{n,E}}p|_{x=0^+} + \frac{1}{\nu_{p,E}}n|_{x=0^+} + \left(\frac{k_E}{\nu_{n,E}} + \frac{1}{\nu_{p,E}}\right)n_i}\,, \tag{3.36}$$

$$R_r(n|_{x=b^-}, p|_{x=b^-}) = \frac{n|_{x=b^-}p|_{x=b^-} - n_i^2}{\frac{1}{\nu_{n,H}}p|_{x=b^-} + \frac{k_H}{\nu_{p,H}}n + |_{x=b^-}\left(\frac{1}{\nu_{n,H}} + \frac{k_H}{\nu_{p,H}}\right)n_i}\,. \tag{3.37}$$

Within this SRH model for interface recombination, high densities of interfacial trap states correspond to high values of the limiting recombination velocities (up to a physical maximum on the order of 10^5 ms^{-1}).

3.4 Parameter estimates

A complete set of estimates for the model parameters is given in Tables 3.2 and 3.3. These estimates are made in line with values provided in the literature that are deduced from either experimental measurement or theoretical predictions.

The model parameters describe a cell which is held under standard illumination conditions, *i.e.* 1000 Wm^{-2} of AM1.5G illumination. The flux of photons incident on the cell with energies above the band gap is calculated from the AM1.5G spectrum to be 2.0×10^{21} m^{-2}s^{-1}. However, a fraction of the incident light is reflected or absorbed before reaching the perovskite layer, so the value of F_{ph} takes a lower value that is selected to give good agreement to the maximum obtainable photo-current of $23 - 23.8$ mAcm^{-2} for a $MAPbI_3$-based PSC [9]. The perovskite absorption coefficient α is calculated from Loper *et al.* [87] based on a light wavelength of 515 nm, a value that is within the range of wavelengths absorbed most efficiently by the perovskite layer.

The perovskite conduction and valence band energy levels have been chosen in line with [120], although it has been found that the values vary depending on the processing technique used to form the perovskite layer [46]. The corresponding value of the band gap (E_g) is

$$E_g = E_C - E_V = 1.7 \text{ eV}\,. \tag{3.38}$$

The ion vacancy parameters D_I and N_0 are set equal to values predicted by DFT calcu-

TABLE 3.2: Parameter table in which the abbreviation DoS denotes the density of states. A single value or the value given in square brackets is the representative value used in this work unless otherwise stated. Fundamental physical constants are given to 3 significant figures. Note that $V_T = k_B T/q$ is calculated using a room temperature of 25°C.

Symbol	Description	Value(s) [Default]	Unit	Reference(s)
ε_0	Permittivity of free space	8.85×10^{-12}	Fm^{-1}	
q	Elementary charge	1.60×10^{-19}	C	
V_T	Thermal voltage	25.7	mV	
F_{ph}	Incident photon flux at 1 Sun	1.4×10^{21}	$\mathrm{m}^{-2}\mathrm{s}^{-1}$	
I_s	Intensity of incident light	1	Sun	
	Perovskite Properties			
α	Absorption coefficient	1.3×10^{7}	m^{-1}	[87]
b	Width	400-600 [400]	nm	
ε_p	Permittivity	24.1	ε_0	[16]
D_n	Electron diffusion coefficient	1.7×10^{-4}	$\mathrm{m}^2\mathrm{s}^{-1}$	[130]
D_p	Hole diffusion coefficient	1.7×10^{-4}	$\mathrm{m}^2\mathrm{s}^{-1}$	[130]
E_C	Conduction band minimum	-3.7	eV	[120]
E_V	Valence band maximum	-5.4	eV	[120]
N_C	Conduction band DoS	8.1×10^{24}	m^{-3}	[16]
N_V	Valence band DoS	5.8×10^{24}	m^{-3}	[16]
D_I	I^- vacancy diffusion coefficient	10^{-16}	$\mathrm{m}^2\mathrm{s}^{-1}$	[45, 109]
N_0	Mean density of ion vacancies	1.6×10^{25}	m^{-3}	[145]
	ETL Properties			
b_E	Width	100	nm	
d_E	Doping density	5×10^{24}	m^{-3}	
D_E	Electron diffusion coefficient	10^{-5}	$\mathrm{m}^2\mathrm{s}^{-1}$	
ε_E	Permittivity	3-60 [10]	ε_0	
E_{f_E}	Fermi level	-4.0	eV	
	HTL Properties			
b_H	Width	200	nm	
d_H	Doping density	5×10^{24}	m^{-3}	
D_H	Hole diffusion coefficient	10^{-6}	$\mathrm{m}^2\mathrm{s}^{-1}$	
ε_H	Permittivity	3	ε_0	
E_{f_H}	Fermi level	-5.1	eV	

lations, as in the work of Richardson *et al.* [109] in which simulations of a drift-diffusion model are first used to reproduce the dependence of J-V hysteresis on scan rate and verify the mechanism of vacancy-assisted ion migration as a plausible cause of J-V hysteresis. In reality, the values of D_I and N_0 may depend on the quality of the perovskite morphology, in particular the granularity [97]. In [109], it is shown that ionic charge accumulates within very narrow layers adjacent to the interfaces. As is standard in electrochemistry, these narrow layers of charge are termed Debye layers. A characteristic width for such layers, called the Debye length, arises from Poisson's equation for the electric potential and depends on the mean density of the majority mobile charge species. Hence, the perovskite Debye length (L_D) is defined with respect to the mean density of iodide ion

vacancies N_0 as follows.

$$L_D = \sqrt{\frac{V_T \varepsilon_p}{q N_0}} \quad \left[\approx 1.5 \text{ nm} \right]. \tag{3.39}$$

This value of L_D corresponds to the width of around 2.4 unit cells of the $MAPbI_3$ lattice, calculated using an average lattice parameter of 6.28 Å as given in [45].

Common materials for the ETL include titania (TiO_2), tin oxide (SnO_2) and the organic material PCBM, usually highly n-doped to contain an abundance of conduction electrons. Common materials for the HTL are p-doped organic materials such as Spiro-OMeTAD and PEDOT:PSS. Values for the ETL and HTL properties in Table 3.2 are not selected based on any of these materials in particular but to represent the types of material able to function as TLs in a PSC. The effects of varying these parameters are studied in Chapter 6. One of the most notable differences in parameter values for different TL materials is between the permittivities of the ETL which vary from $3\varepsilon_0$ for the organic PCBM, to $10\varepsilon_0$ for SnO_2 and up to $60\varepsilon_0$ for TiO_2. The chosen values of the TL Fermi levels give a built-in voltage of

$$V_{bi} = 1.1 \text{ V}, \tag{3.40}$$

which is in agreement with experimental reports [120].

Three types of recombination are included in all numerical simulations of the three-layer model (in Chapters 5-7) with parameters given in Table 3.3. The values in Set (a) are chosen such that bulk recombination is the dominant recombination mechanism, while those in Set (b) cause a combination of the two types of interface recombination to limit the performance of the cell.

TABLE 3.3: Table of recombination (rec.) parameters.

Symbol	Description	Set (a)	Set (b)	Unit
τ_n	Electron pseudo-lifetime in perovskite	3×10^{-11}	3×10^{-9}	s
τ_p	Hole pseudo-lifetime in perovskite	3×10^{-9}	3×10^{-7}	s
v_{n_E}	Electron rec. velocity at ETL interface	10^5	10^5	ms^{-1}
v_{p_E}	Hole rec. velocity at ETL interface	1	10	ms^{-1}
v_{n_H}	Electron rec. velocity at HTL interface	0.01	0.1	ms^{-1}
v_{p_H}	Hole rec. velocity at HTL interface	10^5	10^5	ms^{-1}

3.5 The dimensionless model

In this section, the model is non-dimensionalised for both simplicity of solution and in order to highlight the key dimensionless parameters that characterise the system of equations.

3.5.1 Non-dimensionalisation

The non-dimensionalisation consists of scaling the perpendicular distance across the cell (x) with the width of the perovskite layer (b); the time (t) with the characteristic timescale for ion migration (τ_{ion}), see (3.48); the iodide ion vacancy density (P) with its mean value (N_0); the electric potential (ϕ) with the thermal voltage (V_T); the charge carrier current densities (j^n, j^p) with the charge density generated per unit area per second under the equivalent of 1 Sun illumination; the electron concentration in the ETL (n^E) with the ETL doping density (d_E); and, the hole concentration in the HTL (p^H) with the HTL doping density (d_H).

For the charge carrier concentrations in the perovskite, there is a choice of scalings. One option is to scale the concentrations with a typical concentration of photo-generated charge under 1 Sun illumination (see Section 4.2.1). A second option is to scale the concentrations of electrons and holes in proportion to the concentrations of electrons in the ETL and holes in the HTL, respectively. In Chapters 5, 6 and 7, the effects of the transport layers are investigated and found to significantly influence cell performance. Therefore, the second option is taken here. Specifically, the electron concentration in the perovskite (n) is non-dimensionalised with respect to the concentration at the ETL/perovskite interface when there is no electric field ($d_E k_E$) and the hole concentration in the perovskite (p) is scaled with the concentration at the perovskite/HTL interface when there is no electric field ($d_H k_H$).

Note that, as the charge carrier concentrations are rescaled separately for the perovskite layer and for the relevant transport layer, superscripts are introduced to differentiate between the perovskite layer and the electron (E) and hole (H) transport layers.

Hence, dimensionless variables (denoted by a star) are defined with respect to the relevant

quantities as follows.

$$\begin{gathered} x = bx^*\,, \qquad t = \tau_{ion}t^*\,, \qquad n = d_E k_E n^*\,, \qquad p = d_H k_H p^*\,, \\ P = N_0 P^*\,, \qquad \phi = V_T\phi^*\,, \quad n^E = d_E(n^E)^*\,, \quad p^H = d_H(p^H)^*\,, \\ F^P = \frac{D_I N_0}{b}(F^P)^*\,, \quad E = \frac{V_T}{b}E^*\,, \quad j^n = qG_0 b(j^n)^*\,, \quad j^p = qG_0 b(j^p)^*\,, \end{gathered} \tag{3.41}$$

where τ_{ion} is the characteristic timescale for ion migration (see 3.48) and G_0 is the mean[1] rate of charge carrier photo-generation per unit volume when the cell is under the equivalent of 1 Sun illumination (*i.e.* when $I_s = 1$ in (3.29)) given by

$$G_0 = \frac{\int_0^b G\,\mathrm{d}x}{b} = \frac{F^{ph}}{b}(1 - \mathrm{e}^{-\alpha b}) \quad \left[\approx 3.5 \times 10^{27}\ \mathrm{m^{-3}s^{-1}}\right]. \tag{3.42}$$

Correspondingly, the voltages, widths, permittivities and diffusion coefficients are non-dimensionalised as follows.

$$\begin{gathered} V = V_T\Phi\,, \quad x_E = \frac{b_E}{b}\,, \quad r_E = \frac{\varepsilon_E}{\varepsilon_p}\,, \quad \kappa_n = \frac{d_E k_E}{b^2 G_0}D_n\,, \quad \kappa_E = \frac{d_E}{b^2 G_0}D_E\,, \\ V_{bi} = V_T\Phi_{bi}\,, \quad x_H = \frac{b_H}{b}\,, \quad r_H = \frac{\varepsilon_H}{\varepsilon_p}\,, \quad \kappa_p = \frac{d_H k_H}{b^2 G_0}D_p\,, \quad \kappa_H = \frac{d_H}{b^2 G_0}D_H\,. \end{gathered} \tag{3.43}$$

The bulk charge carrier generation and recombination rates and rate parameters are non-dimensionalised as follows.

$$\begin{gathered} G = G_0 G^*\,, \qquad I_s = I_s^*\,(\text{Suns})\,, \qquad \Upsilon = \alpha b\,, \qquad R = G_0 R^*\,, \\ \gamma = \frac{d_H k_H}{\tau_p G_0}\,, \quad n_i = \sqrt{d_E d_H k_E k_H}\,n_i^*\,, \quad \tau = \frac{\tau_n d_H k_H}{\tau_p d_E k_E}\,, \quad c_3 = \frac{(\tau_n + \tau_p)n_i}{\tau_p d_E k_E}\,. \end{gathered} \tag{3.44}$$

The interface recombination rates and rate parameters are rescaled in an analogous way.

$$\begin{gathered} R_l = bG_0 R_l^*\,, \quad \gamma_l = \frac{d_H k_H \nu_{p,E}}{bG_0}\,, \quad \tau_E = \frac{d_H k_H \nu_{p,E}}{d_E \nu_{n,E}}\,, \quad c_E = \left(\frac{1}{k_E} + \frac{\nu_{p,E}}{\nu_{n,E}}\right)\frac{n_i}{d_E}\,, \\ R_r = bG_0 R_r^*\,, \quad \gamma_r = \frac{d_E k_E \nu_{n,H}}{bG_0}\,, \quad \tau_H = \frac{d_E k_E \nu_{n,H}}{d_H \nu_{p,H}}\,, \quad c_H = \left(\frac{1}{k_H} + \frac{\nu_{n,H}}{\nu_{p,H}}\right)\frac{n_i}{d_H}\,. \end{gathered} \tag{3.45}$$

The following dimensionless parameters (key to the asymptotic analysis performed in Chapter 5) are also introduced: ς_E, ς, ς_H, the timescales of electronic motion in each material layer relative to the timescale of ion migration (within the perovskite layer); χ, the ratio between the hole and electron concentrations within the perovskite; δ, the

[1] This definition of G_0 is used throughout the work except in Sections 4.3-4.6, in which it is temporarily redefined as the maximum, rather than the mean, rate for consistency with publications, see (4.6).

ratio between the perovskite electron concentration and the mean ion vacancy density; λ, the dimensionless perovskite Debye length; and λ_E, λ_H, the dimensionless TL Debye lengths in terms of the two dimensionless ratios Ω_E and Ω_H. The definitions of these dimensionless parameters are:

$$\begin{aligned} \varsigma_E &= \frac{d_E}{G_0\tau_{ion}}\,, \qquad \varsigma = \frac{d_E k_E}{G_0\tau_{ion}}\,, \qquad \varsigma_H = \frac{d_H}{G_0\tau_{ion}}\,, \qquad \chi = \frac{d_H k_H}{d_E k_E}\,, \\ \delta &= \frac{d_E k_E}{N_0}\,, \qquad \lambda = \frac{1}{b}\sqrt{\frac{V_T\varepsilon_p}{qN_0}}\,, \quad \lambda_E = \frac{1}{b}\sqrt{\frac{V_T\varepsilon_E}{qd_E}}\,, \quad \lambda_H = \frac{1}{b}\sqrt{\frac{V_T\varepsilon_H}{qd_H}}\,, \\ \Omega_E &= \sqrt{\frac{\varepsilon_p N_0}{\varepsilon_E d_E}}\,, \quad \Omega_H = \sqrt{\frac{\varepsilon_p N_0}{\varepsilon_H d_H}}\,. \end{aligned} \tag{3.46}$$

A pertinent choice for the dimensional timescale τ_{ion} can be made by considering the non-dimensional form of the conservation and flux of iodide ion vacancies from (3.10),

$$\frac{N_0}{\tau_{ion}}\frac{\partial P^*}{\partial t^*} + \frac{D_I N_0}{b^2}\frac{\partial (F^P)^*}{\partial x^*} = 0\,, \qquad (F^P)^* = -\left(\frac{\partial P^*}{\partial x^*} + P^*\frac{\partial \phi^*}{\partial x^*}\right)\,. \tag{3.47}$$

The timescale of interest is that on which the iodide ion vacancies migrate into and out of the perovskite Debye layers. At a distance of one Debye length from the ETL/perovskite interface (*i.e.* when $x^* = \lambda \ll 1$), the value of the flux $(F^P)^*$ is on the order of $1/\lambda$. The definition of τ_{ion} is therefore chosen in order to obtain a first-order balance between the two terms in the conservation equation when $(F^P)^* = O(1/\lambda)$. Hence, the relevant choice of τ_{ion} for the investigation of iodide ion vacancy migration is

$$\tau_{ion} = \frac{b^2\lambda}{D_I} = \frac{bL_D}{D_I} \quad \left[\approx 5.9\ \mathrm{s}\right]. \tag{3.48}$$

This value aligns well with the typical timescale of hysteresis observed by experiment.

Henceforth, the star superscript is dropped.

3.5.2 The dimensionless model

The following provides a statement of the charge transport model described by equations (3.8)-(3.16), (3.18)-(3.23), (3.29), (3.34), (3.36)-(3.37) in dimensionless form.

Perovskite Layer In $0 < x < 1$,

$$\varsigma\frac{\partial n}{\partial t} - \frac{\partial j^n}{\partial x} = G - R(n,p)\,, \qquad j^n = \kappa_n\left(\frac{\partial n}{\partial x} - n\frac{\partial \phi}{\partial x}\right)\,, \tag{3.49}$$

$$\varsigma\chi\frac{\partial p}{\partial t} + \frac{\partial j^p}{\partial x} = G - R(n,p)\,, \qquad j^p = -\kappa_p\left(\frac{\partial p}{\partial x} + p\frac{\partial \phi}{\partial x}\right)\,, \tag{3.50}$$

$$\frac{\partial P}{\partial t} + \lambda\frac{\partial F^P}{\partial x} = 0\,, \qquad F^P = -\left(\frac{\partial P}{\partial x} + P\frac{\partial \phi}{\partial x}\right)\,, \tag{3.51}$$

$$\lambda^2\frac{\partial^2\phi}{\partial x^2} = 1 - P + \delta(n - \chi p)\,, \tag{3.52}$$

with eight continuity conditions (stated together on the next page) and the boundary conditions

$$j^p|_{x=0} = -R_l\,, \qquad F^P|_{x=0} = 0\,, \qquad j^n|_{x=1} = -R_r\,, \qquad F^P|_{x=1} = 0\,. \tag{3.53}$$

Electron transport layer In $-x_E < x < 0$,

$$\varsigma_E\frac{\partial n^E}{\partial t} - \frac{\partial j^n}{\partial x} = 0\,, \qquad j^n = \kappa_E\left(\frac{\partial n^E}{\partial x} - n^E\frac{\partial \phi}{\partial x}\right)\,, \tag{3.54}$$

$$\lambda_E^2\frac{\partial^2\phi}{\partial x^2} = n^E - 1\,, \tag{3.55}$$

with four continuity conditions and

$$n^E|_{x=-x_E} = 1\,, \qquad \phi|_{x=-x_E} = \frac{\Phi_{bi} - \Phi}{2}\,. \tag{3.56}$$

Hole transport layer In $1 < x < 1 + x_H$,

$$\varsigma_H\frac{\partial p^H}{\partial t} + \frac{\partial j^p}{\partial x} = 0\,, \qquad j^p = -\kappa_H\left(\frac{\partial p^H}{\partial x} + p^H\frac{\partial \phi}{\partial x}\right)\,, \tag{3.57}$$

$$\lambda_H^2\frac{\partial^2\phi}{\partial x^2} = 1 - p^H\,, \tag{3.58}$$

with four continuity conditions and

$$p^H|_{x=1+x_H} = 1\,, \qquad \phi|_{x=1+x_H} = -\left(\frac{\Phi_{bi} - \Phi}{2}\right)\,. \tag{3.59}$$

Continuity between layers At the ETL/perovskite interface at $x = 0$,

$$\phi|_{x=0^-} = \phi|_{x=0^+}\,, \qquad r_E \frac{\partial \phi}{\partial x}\Big|_{x=0^-} = \frac{\partial \phi}{\partial x}\Big|_{x=0^+}\,, \tag{3.60}$$

$$n^E|_{x=0^-} = n|_{x=0^+}\,, \qquad j^n|_{x=0^-} = j^n|_{x=0^+} - R_l\,, \tag{3.61}$$

At the perovskite/HTL interface at $x = 1$,

$$\phi|_{x=1^-} = \phi|_{x=1^+}\,, \qquad \frac{\partial \phi}{\partial x}\Big|_{x=1^-} = r_H \frac{\partial \phi}{\partial x}\Big|_{x=1^+}\,, \tag{3.62}$$

$$p|_{x=1^-} = p^H|_{x=1^+}\,, \qquad j^p|_{x=1^-} - R_r = j^p|_{x=1^+}\,. \tag{3.63}$$

Generation Rate In $0 < x < 1$,

$$G(x,t) = I_s(t)\bar{G}_l \mathrm{e}^{-l\Upsilon x}\,, \qquad \bar{G}_l = \frac{\Upsilon \mathrm{e}^{-\Upsilon(1-l)/2}}{1-\mathrm{e}^{-\Upsilon}}\,, \tag{3.64}$$

in which the parameter l is set equal to $+1$ to model a standard-architecture cell and -1 for an inverted-architecture cell.

Recombination Rates In $0 < x < 1$,

$$R(n,p) = \frac{\gamma(np - n_i^2)}{n + \tau p + c_3}\,. \tag{3.65}$$

At $x = 0^+$ and $x = 1^-$, respectively,

$$R_l(n,p) = \frac{\gamma_l(np - n_i^2)}{n + \tau_E p + c_E}\,, \qquad R_r(n,p) = \frac{\gamma_r(np - n_i^2)}{p + \tau_H n + c_H}\,. \tag{3.66}$$

3.5.3 Dimensionless parameter estimates

Parameter estimates for the dimensionless model are given in Tables 3.4 and 3.5. All the parameters are given except the dimensionless recombination parameters n_i, c_3, c_E and c_H, which are all very small ($< 10^{-9}$). Therefore, for simplicity, it can be considered that these parameters have a negligible effect on the results and so they are left out of Table 3.5 (though their non-zero values are used in all numerical simulations of the three-layer model).

The dimensionless parameter estimates in Tables 3.4 and 3.5 complete the dimensionless model. The next chapter is concerned with an investigation into the capabilities of different numerical methods with respect to obtaining solutions to this dimensionless problem.

TABLE 3.4: Table of dimensionless parameter estimates, corresponding to the dimensional values given in Table 3.2.

Symbol	Estimate	Description
Φ_{bi}	43	Dimensionless built-in voltage
I_s	1	Dimensionless intensity of incident light
		Perovskite Properties
Υ	5.2	Dimensionless absorption coefficient
κ_n	21	Dimensionless electron diffusion coefficient
κ_p	15	Dimensionless hole diffusion coefficient
ς	3.4×10^{-9}	Ratio between the timescales of electron and ion vacancy motion
χ	0.72	Ratio between the electron and hole concentrations
δ	4.3×10^{-6}	Ratio between the electron concentration and ion vacancy density
λ	3.7×10^{-3}	Dimensionless Debye length
		ETL Properties
x_E	0.25	Width relative to the perovskite
r_E	0.41	Permittivity relative to the perovskite
κ_E	9.0×10^{4}	Dimensionless electron diffusion coefficient
ς_E	2.5×10^{-4}	Ratio between the timescales of electron and ion vacancy motion
Ω_E	2.8	Product of permittivity and doping density relative to the perovskite
λ_E	4.2×10^{-3}	Dimensionless Debye length
		HTL Properties
x_H	0.5	Width relative to the perovskite
r_H	0.12	Permittivity relative to the perovskite
κ_H	9.0×10^{3}	Dimensionless hole diffusion coefficient
ς_H	2.5×10^{-4}	Ratio between the timescales of hole and ion vacancy motion
Ω_H	5.2	Product of permittivity and doping density relative to the perovskite
λ_H	2.3×10^{-3}	Dimensionless Debye length

TABLE 3.5: Table of dimensionless parameter estimates, corresponding to the two sets of dimensional values given in Table 3.3. Set (a) corresponds to a cell limited by the rate of bulk recombination R, whereas Set (b) corresponds to a cell limited by a combination of the rates of interface recombination R_l and R_r.

Symbol	Estimate Set (a)	Estimate for Set (b)	Description
γ	4.7	0.047	Typical magnitude of R
τ	7.2×10^{-3}	7.2×10^{-3}	Parameter for R
γ_l	0.035	0.35	Typical magnitude of R_l
τ_E	9.9×10^{-11}	9.9×10^{-10}	Parameter for R_l
γ_r	5.0×10^{-4}	5.0×10^{-3}	Typical magnitude of R_r
τ_H	1.4×10^{-12}	1.4×10^{-11}	Parameter for R_r

The progress made and challenges faced by previous works on the drift-diffusion modelling of PSCs are described at the start of the chapter. A finding of this study is that the small size of some of the dimensionless parameters gives rise to severe numerical stiffness, which renders fast and accurate solution of the model a challenging task. On the other hand, the extreme size of these parameters motivates taking an asymptotic approach to the problem, following the analysis performed by Richardson *et al.* [34, 109]

of a model that explicitly describes only the perovskite layer. Solution of the three-layer dimensionless model, as described above, using the method of matched asymptotic expansions is the subject of Chapter 5.

Chapter 4

Numerical Methods of Solution

The charge transport model laid out in Chapter 3 for the motion of ion vacancies and the motion, generation and recombination of charge carriers within a PSC presents a challenging numerical problem. The difficulties arise from a combination of the spatial and temporal stiffness inherent to the model for realistic values of the parameters, as predicted by microscopic DFT calculations and experimental measurements. The primary cause of spatial stiffness is the short Debye length ($L_D \approx 1.5$ nm) which, when compared to a typical perovskite layer width of 400-600 nm, corresponds to a dimensionless Debye length of $\lambda = O(10^{-3})$. The non-dimensionalisation carried out in Section 3.5.1 enables the mathematical origin of the spatial stiffness to be identified, as it can be seen that a factor of λ^2 multiplies the highest derivative of Poisson's equation given in (3.52). The physical outcome of such a short Debye length is that mobile ionic charge accumulates in very narrow boundary layers, termed Debye layers, adjacent to the perovskite/TL interfaces in which the solution varies extremely rapidly (see Figure 4.1). Numerical solution of the system of PDEs therefore requires a very fine spatial grid local to the internal interfaces in order that the large gradients in the electric potential, ion vacancy density and charge carrier concentrations are properly resolved. As a result, a high floating-point precision is required to maintain accuracy. When computing time-dependent solutions, the numerical difficulties are further compounded by a temporal stiffness resulting from the large disparity between the timescales of ion vacancy migration (on the order of seconds) and the much faster charge carrier dynamics.

In this chapter, two numerical methods that can effectively cope with both the spatial and temporal stiffness are presented and contrasted. Spatial stiffness is addressed via the choice of an appropriate non-uniform grid, that allows the solution to be computed accurately within the Debye layers, and a tailored finite element or finite difference discretisation of the PDEs. Both methods employ the use of an adaptive time step, provided

by MATLAB's built-in ODE solver `ode15s`, in order to combat the second source of stiffness, due to the disparity in timescales between the motion of the ion vacancies and charge carriers. It is found that the finite element scheme provides significantly higher accuracy, in a given computation time, than both the finite difference scheme and some previously used alternatives (Chebfun and `pdepe`). A typical transient sweep of a J-V curve can be computed using the finite element scheme in only a few seconds on a standard personal computer.

The chapter is set out as follows. In the first section, a review of the literature describes previous attempts to obtain solutions to drift-diffusion models for PSCs that include ion motion. In Section 4.2, the charge transport model is reduced to a single-layer model, that only explicitly describes the perovskite layer, by making the approximation that the TLs function as "quasi-metals" (an assumption previously made by Richardson and co-workers [34, 109]). In Section 4.3, the spatial discretisation and implementation of a finite element scheme in MATLAB [91] is described. Then in Section 4.4, the equivalent description is given for a finite difference scheme whose implementation (also in MATLAB) uses the Advanpix Multi-Precision Toolbox [1]. In Section 4.5, the pointwise convergence of the two methods is demonstrated, as well as the importance of the choice of spatial grid on both accuracy and computation time. The two schemes are benchmarked against MATLAB's built-in solver `pdepe`, previously used on a uniform spatial grid by Calado *et al.* [22]. There is also a brief discussion of how the various approaches compare to attempts made using spectral methods, previously employed by Richardson *et al.* [109]. In Section 4.6, solutions obtained using the finite element scheme are compared to the asymptotically-derived results from [34] for some experimentally motivated test cases. Finally, in Section 4.7, a summary of the results and notes on the extension of the numerical schemes to the full three-layer model are given.

4.1 Review of methods used in the literature

The first publications to use drift-diffusion models incorporating ion motion to study the behaviour of PSCs are those by van Reenen *et al.* [144] and Richardson *et al.* [109]. It is found that the incorporation of ion dynamics into the standard electronic description of a solar cell leads to a model that is computationally challenging to solve, owing to severe spatial and temporal stiffness. The origins of the numerical stiffness are the disparity between the timescales of ion migration (slow) and charge carrier dynamics (fast) and the very narrow width of the Debye layers (see Figure 4.1). In the dimensionless model stated in Section 3.5.2, the disparity in timescales is manifested in the small size of the dimensionless parameter ς, while the narrow Debye layers are characterised by the small

size of the dimensionless perovskite Debye length λ.

In the work of van Reenen *et al.* [144], simulations for the main text are performed on a grid of evenly spaced points, 4 nm apart. However, using their parameter estimates, the perovskite Debye length is just 3 nm (corresponding to a dimensionless Debye length of $\lambda = 6.4 \times 10^{-3}$) and therefore simulations on a 4 nm grid cannot accurately resolve the key physical features, namely the Debye layers, that result from ion vacancy migration. Indeed, in the Supporting Information of [144], it is shown that a simulation performed on a grid with 2 nm spacing produces a visibly different result, indicating that their numerical method has not converged. However, it is reported that long calculation times prohibit the use of a sufficiently refined grid.

The temporal stiffness is tackled by van Reenen *et al.* [144] in two different ways, which are tailored to the experimental protocol under investigation. Firstly, J-V curves measured at a scan rate of 100 V/s by Tress *et al.* [140] are assumed to be sufficiently fast that the ions are unable to move from their initial distribution during the measurement. As a result, simulations in which the ion dynamics are decoupled from that of the charge carriers are performed by first calculating the stationary ion distribution and then setting the ion mobility to zero during the scan. Secondly, simulations of J-V curves including time-dependent ion dynamics are obtained by splitting the voltage scan into a series of voltage steps and choosing unrealistically high values for both the ionic mobility and voltage scan rate. Despite these amendments, the simulations are shown to qualitatively reproduce some important features of the J-V hysteresis exhibited by PSCs.

In order to circumvent the numerical difficulties associated with the two sources of stiffness, Richardson *et al.* [109] employ the method of matched asymptotic analysis to simplify the model. This method, though approximate, is shown to be capable of capturing the dynamics of the ionic charge accumulation in the Debye layers within the parameter regimes of interest (including a short Debye length corresponding to $\lambda = 2.4 \times 10^{-3}$). In particular, this method allows for the time-dependent simulation of a set of J-V curves measured over a range of scan rates, between 50 mV/s and 1 V/s. The results of the simulations are close to giving quantitative agreement with the experimental data.

The main assumptions of the asymptotic analysis performed by Richardson *et al.* [109] are that the TLs are sufficiently highly doped that they can be considered to be "quasi-metals"; that the iodide ion vacancy density is significantly greater than the charge carrier concentrations (such that the contributions of the charge carriers to Poisson's equation can be neglected); and, that ion vacancy migration takes place on a much slower timescale than the charge carrier dynamics. The first assumption reduces the model to a single-layer problem for just the perovskite layer of a PSC. The latter assumptions are used to reduce the system of PDEs to a single ordinary differential equation (ODE), for the evo-

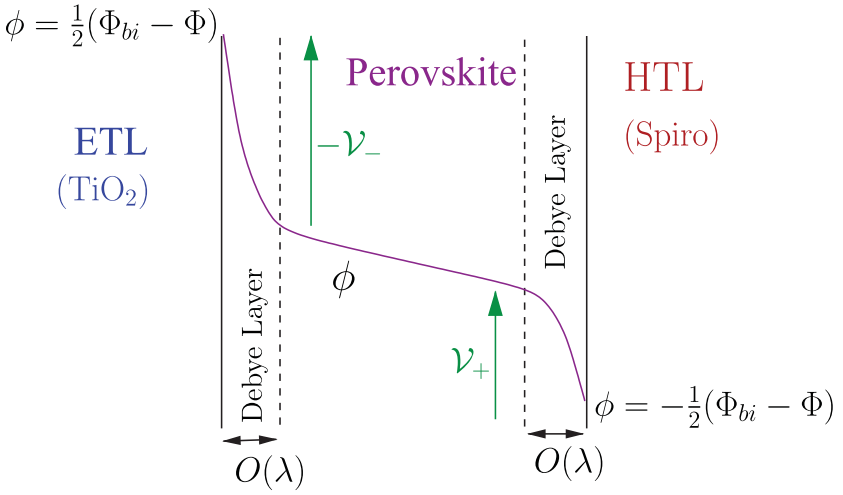

FIGURE 4.1: A diagram showing the positions of narrow Debye layers within the perovskite layer and their effect on the distribution of the dimensionless electric potential ϕ for applied voltages less than the built-in voltage ($\Phi < \Phi_{bi}$) , reproduced from [34]. Note that the ion vacancy density and the charge carrier concentrations depend approximately exponentially on the electric potential within the Debye layers. The Debye layers form as a result of an accumulation or depletion of mobile iodide ion vacancies adjacent to the interfaces. The dimensionless Debye length $\lambda = O(10^{-3})$, in units of the perovskite layer width. Not to scale.

lution of the charge density stored within the Debye layers, and a non-stiff quasi-steady state boundary value problem (BVP) which consists of the conservation equations for the electrons and holes across the perovskite bulk (excluding the Debye layers). Uniformly-valid solutions for the electric potential and ion vacancy density are calculated in terms of the Debye layer charge density. The charge carrier concentrations are then calculated from the known electric potential via the numerical solution of the non-stiff BVP. The numerical method makes use of the Chebfun package for MATLAB. Full details of the asymptotic analysis, as well as verification against numerical solutions of the single-layer model (obtained using the finite difference scheme presented in this chapter and in [35]) are provided in [34].

The combined asymptotic/numeric, single-layer approach has subsequently been used by the same group to simulate other transient behaviour exhibited by PSCs. O'Kane *et al.* [99] simulate current transients, measured in the dark at a range of temperatures, that occur on a timescale of seconds. Domanski *et al.* [40] investigate a model that includes a second, less mobile ionic species (assumed to be the MA^+ cation vacancies) in order to simulate experimental measurements that demonstrate the reversibility of losses in performance sustained by operating PSCs on a timescale of hours.

Following the works of van Reenen *et al.* [144] and Richardson *et al.* [109], the next work to use a drift-diffusion model including both ionic and electronic motion was that by Cal-

ado *et al.* [22]. In order to avoid the spatial stiffness associated with the Debye layers, Calado *et al.* [22] make use of a number of simplifying approximations to the physical system under investigation. The three layers of PSC are modelled as a p-i-n homojunction, rather than a p-i-n heterojunction, meaning that the material properties of the TLs (such as the permittivity and band energy levels) are assumed to be identical to those of the perovskite. Hence, the band offsets across the perovskite/TL interfaces and resulting changes in charge carrier concentrations are neglected. As a result, unrealistically high concentrations of the charge carriers can exist across the device and act to screen any accumulation of ionic charge within the perovskite layer. This screening produces an approximately linear electric potential across the perovskite and thus the spatial stiffness associated with narrow Debye layers is reduced. However, the lack of physically realistic Debye layers is a significant source of error because the J-V characteristics of a PSC strongly depend on the behaviour of the Debye layers.

A further simplifying approximation made by Calado *et al.* [22] is that interface recombination is incorporated at all points that lie within 10 nm of the perovskite/TL interfaces, within the perovskite layer, rather than at the interfaces themselves. It is stated that this approximation is unrealistic but is needed to circumvent numerical inaccuracies in their method of solution. The numerical method in question is an application of MATLAB's built-in PDE solver for parabolic and elliptic equations, `pdepe`. The capabilities and limitations of this solver when applied to a single-layer model of a PSC are tested and discussed further in Section 4.5.4.

Jacobs *et al.* [68] investigate a p-i-n heterojunction model for a PSC in which ionic accumulation is incorporated via the addition of narrow layers of "doping" adjacent to the interfaces. Simulations rely on the assumption, previously made by van Reenen *et al.* [144], that for sufficiently fast J-V scans, the ion and charge carrier dynamics can be decoupled in time. Their method is therefore to first calculate the equilibrium density of charge stored within the "doping" layers (based on the preconditioning voltage) and then to simulate a fast (10 V/s) J-V scan with static "doping" layers using the SCAPS solar cell simulator (designed for standard, inorganic thin film solar cells without mobile ions). A similar doping-layer model is used in work by Shen *et al.* [126] to study possible causes for the "inverted" J-V hysteresis exhibited by some mesoporous PSCs.

A second model is developed by Shen *et al.* [126] that uses the COMSOL Multiphysics® semiconductor module, in which the ion vacancy distribution evolves according to a drift-diffusion equation. However, the difficulties associated with the spatial stiffness of the problem are avoided via the choice of a low value for the ion vacancy density (corresponding to a relatively large dimensionless Debye length of $\lambda = 0.015$). Neukom *et al.* [96] also only present results for a low ion vacancy density (corresponding to $\lambda = 0.018$).

In [96], fast J-V curves, in which ionic and electronic motion are decoupled as before, are simulated using the Setfos software created by Fluxim Inc. In addition, interface recombination is incorporated using the same simplifying approximation as Calado *et al.* [22] (this time using 3 nm thick regions adjacent to each of the perovskite/TL interfaces) and assumed to take place via a radiative recombination mechanism, rather than interfacial trap states.

Simplified models that focus on the effects of ion and carrier accumulation at the ETL/perovskite interface have been studied by Bisquert and co-workers [61, 108]. In the work by Gottesman *et al.* [61], solutions are obtained from a single-layer model that is independent of time. In contrast, Ravishankar *et al.* [108] propose a dynamic model for the polarisation of the ETL/perovskite interface, which they term a "surface polarisation" model. Results obtained from simplified models can provide useful physical insight, however such findings should be verified against simulations of a complete model of charge transport within a PSC.

In summary, although many physical models have been presented in the literature, thus far, concessions have had to be made when choosing a method of solution. This is due to the difficulty in obtaining solutions to a numerically stiff system of equations. The most common approach has been to decouple the ionic motion from that of the charge carriers, justified by the discernible difference in timescales. An exception is the work of Calado *et al.* [22] in which approximations are made to the physical system that is modelled. The method used in this work provides a benchmark against which the numerical methods described in this chapter are tested.

4.2 Reduction of the problem to a single-layer model

A sensible first step to take when testing and developing a numerical method is to attempt a reduced version of the problem that retains the key features of the original model. For the charge transport model described in Chapter 3, the key physical processes are the motion, generation and recombination of charge carriers (electrons and holes) and their interaction with mobile iodide ion vacancies that migrate on a timescale on the order of seconds. All these processes occur within the perovskite layer and, furthermore, photo-generation and ion vacancy migration are assumed to take place solely within the perovskite layer. Therefore it is possible to consider a single-layer model that explicitly describes only charge transport within the perovskite absorber layer [34, 109]. In this section, the dimensionless charge transport model for the perovskite and both transport layers of a planar PSC (from Section 3.5) is reduced to such a model. Notably, the

numerical schemes developed in Sections 4.3-4.4 for the single-layer model can easily be extended to more realistic multi-layer models, see Appendix B.

To reduce the problem to a single-layer model, it is assumed (as in previous work by Richardson and co-workers [34, 109]) that the high levels of transport layer doping allow these materials to be treated as "quasi-metals", through which the electric potential ϕ is uniform and equal to the value imposed at the adjoining metal contact. Hence, the majority charge carrier concentration is also uniform and equal in density to the transport layer doping. That is, in the ETL and the HTL, the solution to the dimensionless model satisfies

$$\phi \equiv \frac{\Phi_{bi} - \Phi(t)}{2}\,, \qquad n^E \equiv 1\,, \qquad \text{for } -x_E < x < 0\,, \tag{4.1}$$

$$\phi \equiv -\frac{\Phi_{bi} - \Phi(t)}{2}\,, \qquad p^H \equiv 1\,, \qquad \text{for } 1 < x < 1 + x_H\,, \tag{4.2}$$

respectively. Hence, the continuity conditions imposed on the ETL/perovskite interface (at $x = 0$) and the perovskite/HTL interface (at $x = 1$) in the dimensionless three-layer model, given in (3.60)-(3.63), are replaced with the following Dirichlet boundary conditions on the perovskite domain ($0 < x < 1$).

$$\phi|_{x=0} = \frac{\Phi_{bi} - \Phi(t)}{2}\,, \quad n|_{x=0} = 1\,, \quad \phi|_{x=1} = -\frac{\Phi_{bi} - \Phi(t)}{2}\,, \quad p|_{x=1} = 1\,. \tag{4.3}$$

The application of these boundary conditions, in place of the continuity conditions, leads to a single-layer model in which all the relevant physics takes place within the perovskite layer.

4.2.1 Rescaling of the charge carriers for the single-layer model

For the single-layer model, the non-dimensionalisation described in Section 3.5.1 is modified such that the charge carrier concentrations are scaled with respect to the characteristic carrier concentration (Π_0) required to remove the photo-generated charge in the absence of an electric field, defined by

$$\Pi_0 = \frac{F_{\text{ph}} b}{\hat{D}}\,, \tag{4.4}$$

where $\hat{D}$ is a typical carrier diffusivity and it is assumed here that $\hat{D} = D_n = D_p$. Hence, for the single-layer model only, the following transformation is applied to the dimensionless charge carrier concentrations, the ratio of the characteristic electron concentration to

the mean ion vacancy density (δ) and the ratio of the charge carrier concentrations (χ).

$$n \mapsto \frac{d_E k_E}{\Pi_0} n\,, \quad p \mapsto \frac{d_H k_H}{\Pi_0} p\,, \quad \delta \mapsto \hat{\delta} = \frac{\Pi_0}{N_0}\,, \quad \chi \mapsto 1\,. \tag{4.5}$$

One other modification is required in order to provide consistency with the published work of Courtier *et al.* [34, 35], namely that the definition of G_0 must be changed from the mean, as in (3.42), to the maximum rate of charge carrier photo-generation per unit volume when the cell is under the equivalent of 1 Sun illumination (*i.e.* when $I_s = 1$ in (3.29)). Hence, in Sections 4.3-4.6 only,

$$G_0 = \frac{F_p h}{b}\,. \tag{4.6}$$

In this scaling, the dimensionless diffusion coefficients κ_n and κ_p are set equal to one.

4.2.2 The single-layer model

The dimensionless single-layer model consists of the following conservation equations for anion vacancies, electrons and holes,

$$\frac{\partial P}{\partial t} + \lambda \frac{\partial F^P}{\partial x} = 0\,, \qquad F^P = -\left(\frac{\partial P}{\partial x} - PE\right)\,, \tag{4.7}$$

$$\varsigma \frac{\partial n}{\partial t} = \frac{\partial j^n}{\partial x} + G - R(n,p)\,, \qquad j^n = \frac{\partial n}{\partial x} + nE\,, \tag{4.8}$$

$$\varsigma \frac{\partial p}{\partial t} = -\frac{\partial j^p}{\partial x} + G - R(n,p)\,, \qquad j^p = -\left(\frac{\partial p}{\partial x} - pE\right)\,, \tag{4.9}$$

coupled to Poisson's equation for the electric potential,

$$\frac{\partial E}{\partial x} = \frac{1}{\lambda^2}\left(P - 1 + \hat{\delta}\,(p - n)\right)\,, \qquad E = -\frac{\partial \phi}{\partial x}\,. \tag{4.10}$$

In practice, the three dimensionless parameters λ (the ratio of the Debye length L_D to the perovskite layer width), ς (the ratio of the timescale for charge carrier motion to that for ion vacancy motion) and $\hat{\delta}$ (the ratio of typical carrier concentration to the mean ion vacancy density) are all very small, see (4.15).

Equations (4.7)-(4.10) hold within the perovskite layer, which is bounded by its interface with the ETL (at $x = 0$) and its interface with the HTL (at $x = 1$). From (3.53) and (4.3),

the non-dimensional boundary conditions are

$$F^P|_{x=0} = 0\,, \quad \phi|_{x=0} = \frac{\Phi_{bi} - \Phi(t)}{2}\,, \qquad n|_{x=0} = \bar{n}\,, \quad j^p|_{x=0} = -R_l(p)\,, \tag{4.11}$$

$$F^P|_{x=1} = 0\,, \quad \phi|_{x=1} = -\frac{\Phi_{bi} - \Phi(t)}{2}\,, \quad p|_{x=1} = \bar{p}\,, \quad j^n|_{x=1} = -R_r(n)\,, \tag{4.12}$$

where, given the rescaling given in (4.5),

$$\bar{n} = \frac{N_C}{\Pi_0} \exp\left(-\frac{E_C - E_{f_E}}{qV_T}\right)\,, \qquad \bar{p} = \frac{N_V}{\Pi_0} \exp\left(\frac{E_V - E_{f_H}}{qV_T}\right)\,. \tag{4.13}$$

The problem is closed by dimensionless initial conditions for the electron, hole and anion vacancy distributions which we denote as follows.

$$n|_{t=0} = n_{\text{init}}(x)\,, \quad p|_{t=0} = p_{\text{init}}(x)\,, \quad P|_{t=0} = P_{\text{init}}(x)\,. \tag{4.14}$$

4.2.3 Dimensionless parameter estimates

An analogous single-layer model and non-dimensionalisation (but for the case where the cation vacancies, as well as the anion vacancies, are mobile) is presented in Section 2 of [34]. In order to enable direct comparison with the results of this publication, the dimensionless parameter estimates for use in Sections 4.3-4.6 are taken to be

$$\begin{gathered} \varsigma = 5.8 \times 10^{-10}, \quad \lambda = 2.4 \times 10^{-3}, \quad \hat{\delta} = 2.1 \times 10^{-7}, \\ \bar{n} = 20, \qquad \bar{p} = 0.30, \qquad \Phi_{bi} = 40. \end{gathered} \tag{4.15}$$

These values correspond to a typical planar PSC formed by a 600 nm thick, $MAPbI_3$ absorber layer sandwiched between a TiO_2 ETL layer and a Spiro-OMeTAD HTL layer [34].

The difficulty in solving (4.7)-(4.14) arises from the extreme values of the parameters ς, λ and $\Phi_{bi} - \Phi(t)$. The very small value of ς reflects the large disparity in timescales for the electronic (fast) and ionic (slow) motion. This feature of the problem necessitates the use of an adaptive timestep since any fixed time stepping method would either be prohibitively slow or incapable of capturing the fast electronic dynamics. As is typical for many electrochemical problems (see *e.g.* [57]), the parameter characterising the ratio of the Debye length to the domain length, in this case λ, is also extremely small. This gives rise to appreciable stiffness in the system owing to the rapid changes in the solution across the narrow Debye layers. This issue is further exacerbated by the relatively large value of the dimensionless potential difference $\Phi_{bi} - \Phi(t)$. The dimensional built-in voltage

is typically around 1.1 V and standard experiments vary the dimensional applied voltage within the range of -0.5 to 2 V. Therefore the total dimensionless potential difference across the cell, $\Phi_{bi} - \Phi(t)$, measured in units of the thermal voltage ($V_T \approx 25.7$ mV at room temperature) can be quite large. The concentrations of the different charge species in the narrow Debye layers are approximately Boltzmann distributed, *i.e.* they vary exponentially with the potential. Therefore, a typical change in the dimensional potential difference across one of the two Debye layers of 0.5 V (corresponding to a dimensionless potential drop of around 20) results in a change in n, p or P by a factor of around $\exp(20) \approx O(10^9)$ across a region of dimensionless width $O(10^{-3})$. Therefore, what at first glance appears to be merely a stiff problem is actually an extremely stiff problem. Notably, depending on the approach to spatial discretisation, these very large changes in the magnitudes of the concentrations of the charged species can give rise to large condition numbers in the discrete counterparts of the PDEs leading to significant round off errors.

4.3 Finite element scheme

The central technique underlying both numerical schemes presented in this work is the method of lines. Since the equation governing the electric potential is elliptic, in contrast to those for the charge carrier densities which are parabolic, the discrete system takes the form of a system of coupled differential-algebraic equations (DAEs). As such, it requires a specialised algorithm for temporal integration. Here, we employ MATLAB's integrator `ode15s` [91] to evolve in time. In the physically relevant parameter regimes, typical solutions exhibit rapid changes in the narrow Debye (boundary) layers which gives rise to significant stiffness in the DAE system. This difficulty is overcome by employing a non-uniform grid spacing. Here we do not employ the Scharfetter-Gummel scheme [117], that is widely used in other semiconductor applications, to solve the conservation equations. We note that the Scharfetter-Gummel scheme is specifically designed to address issues of charge carrier transport rather than to deal with the difficulties associated with accurately resolving the solution in narrow Debye layers, which is the main issue here.

In this section, the spatial derivatives in (4.7)-(4.14) are discretised using a finite element scheme with second-order local accuracy. The computational grid is comprised of $N+1$ arbitrarily positioned grid points, denoted by $x = x_i$ for $i = 0, ..., N$, which partition the domain $x \in [0, 1]$ into N subintervals. The widths of the subintervals are denoted by $\Delta_{i+1/2} = x_{i+1} - x_i$, and we also introduce N half-points denoted by $x_{i+1/2} = (x_i + x_{i+1})/2$ for $i = 0, ..., N-1$. A sketch of the grid is shown in Figure 4.2. We employ a common approach in which the dependent variables are approximated as a

linear combination of piecewise linear basis functions (aka 'hat' or 'tent' functions). For a generic dependent variable, w say, we write

$$w(x,t) = \sum_{i=0}^{i=N} w_i(t)\varphi_i(x) \quad \text{where} \quad \varphi_i(x) = \begin{cases} \dfrac{x - x_{i-1}}{x_i - x_{i-1}} & \text{if } x \in (x_{i-1}, x_i) \\ \dfrac{x_{i+1} - x}{x_{i+1} - x_i} & \text{if } x \in (x_i, x_{i+1}) \\ 0 & \text{if } x \notin (x_{i-1}, x_{i+1}) \end{cases} \tag{4.16}$$

in which $\varphi_i(x)$ are referred to as the basis functions.

On eliminating the anion vacancy flux, F^P, and the electron and hole current densities, j^n and j^p, we derive three equations of the form

$$\alpha \frac{\partial w}{\partial t} = \beta \frac{\partial}{\partial x}\left(\frac{\partial w}{\partial x} \pm w\frac{\partial \phi}{\partial x}\right) + S(x, v, w)\,, \tag{4.17}$$

in which α and β are constants and the source term S is a function of x, w and another generic dependent variable denoted by v. Eliminating the electric field, E, between equations (4.10) leads to

$$\frac{\partial^2 \phi}{\partial x^2} = \frac{1}{\lambda^2}\left(1 - P - \hat{\delta}\,(p - n)\right)\,. \tag{4.18}$$

The spatially discretised equations are derived by multiplying both (4.17) and (4.18) through by each of the test functions $\varphi_j(x)$ (for $j = 0, ..., N$), integrating over the domain $x \in (0, 1)$ (using integration by parts where appropriate) and substituting the form (4.16) for each of the dependent variables. On doing so we arrive at

$$\alpha \sum_{i=0}^{i=N} \frac{\mathrm{d}w_i}{\mathrm{d}t} \int_0^1 \varphi_i \varphi_j \,\mathrm{d}x = \beta \left(\frac{\partial w}{\partial x} \pm w\frac{\partial \phi}{\partial x}\right)\varphi_j\Big|_{x=0}^{x=1} \tag{4.19}$$

$$- \beta \left(\sum_{i=0}^{i=N} w_i \int_0^1 \varphi_i' \varphi_j' \,\mathrm{d}x \pm \sum_{i=0}^{i=N}\sum_{k=0}^{k=N} w_i \phi_k \int_0^1 \varphi_i \varphi_j' \varphi_k' \,\mathrm{d}x\right) + \int_0^1 S(x, v, w)\varphi_j \,\mathrm{d}x\,,$$

$$\frac{\partial \phi}{\partial x}\varphi_j\Big|_{x=0}^{x=1} - \sum_{i=0}^{i=N} \phi_i \int_0^1 \varphi_i' \varphi_j' \,\mathrm{d}x = \frac{1}{\lambda^2}\left(\int_0^1 \varphi_j dx - \sum_{i=0}^{i=N}(P_i + \hat{\delta}(p_i - n_i)) \int_0^1 \varphi_i \varphi_j \,\mathrm{d}x\right). \tag{4.20}$$

In the equations above, each of the integrals containing expressions that depend solely on the basis functions and/or their derivatives with respect to x (denoted by a prime) can be

computed exactly and are as follows.

$$\int_0^1 \varphi_i \varphi_j \,\mathrm{d}x = \begin{cases} \frac{1}{3}\left(\Delta_{j+1/2} + \Delta_{j-1/2}\right) & \text{if } i = j \text{ and } j = 1, ..., N-1 \\ \frac{1}{3}\Delta_{1/2} & \text{if } i = j \text{ and } j = 0 \\ \frac{1}{3}\Delta_{N-1/2} & \text{if } i = j \text{ and } j = N \\ \frac{1}{6}\Delta_{j+1/2} & \text{if } i = j+1 \text{ and } j = 0, ..., N-1 \\ \frac{1}{6}\Delta_{j-1/2} & \text{if } i = j-1 \text{ and } j = 1, ..., N \\ 0 & \text{otherwise} \end{cases} \tag{4.21}$$

$$\int_0^1 \varphi_i' \varphi_j' \,\mathrm{d}x = \begin{cases} \frac{1}{\Delta_{j+1/2}} + \frac{1}{\Delta_{j-1/2}} & \text{if } i = j \text{ and } j = 1, ..., N-1 \\ \frac{1}{\Delta_{1/2}} & \text{if } i = j \text{ and } j = 0 \\ \frac{1}{\Delta_{N-1/2}} & \text{if } i = j \text{ and } j = N \\ \frac{-1}{\Delta_{j+1/2}} & \text{if } i = j+1 \text{ and } j = 0, ..., N-1 \\ \frac{-1}{\Delta_{j-1/2}} & \text{if } i = j-1 \text{ and } j = 1, ..., N \\ 0 & \text{otherwise} \end{cases} \tag{4.22}$$

$$\int_0^1 \varphi_i \varphi_j' \varphi_k' \,\mathrm{d}x = \begin{cases} \frac{1}{2\Delta_{j+1/2}} + \frac{1}{2\Delta_{j-1/2}} & \text{if } i = j,\, k = j \text{ and } j = 1, ..., N-1. \\ \frac{1}{2\Delta_{1/2}} & \text{if } i = j,\, k = j \text{ and } j = 0 \\ \frac{1}{2\Delta_{N-1/2}} & \text{if } i = j,\, k = j \text{ and } j = N \\ -\frac{1}{2\Delta_{j+1/2}} & \text{if } i = j,\, k = j+1 \text{ and } j = 0, ..., N-1 \\ -\frac{1}{2\Delta_{j-1/2}} & \text{if } i = j,\, k = j-1 \text{ and } j = 1, ..., N \\ -\frac{1}{2\Delta_{j+1/2}} & \text{if } i = j+1,\, k = j+1 \text{ and } j = 0, ..., N-1 \\ \frac{1}{2\Delta_{j+1/2}} & \text{if } i = j+1,\, k = j \text{ and } j = 0, ..., N-1 \\ -\frac{1}{2\Delta_{j-1/2}} & \text{if } i = j-1,\, k = j-1 \text{ and } j = 1, ..., N \\ \frac{1}{2\Delta_{j-1/2}} & \text{if } i = j-1,\, k = j \text{ and } j = 1, ..., N \\ 0 & \text{otherwise} \end{cases} \tag{4.23}$$

$$\int_0^1 \varphi_j \,\mathrm{d}x = \begin{cases} \frac{1}{2}\left(\Delta_{j+1/2} + \Delta_{j-1/2}\right) & \text{if } j = 1, ..., N-1 \\ \frac{1}{2}\Delta_{1/2} & \text{if } j = 0 \\ \frac{1}{2}\Delta_{N-1/2} & \text{if } j = N \\ 0 & \text{otherwise} \end{cases} \tag{4.24}$$

where the indices $i, j, k = 0, ..., N$.

Likewise, terms containing quantities evaluated on the boundaries $x = 0, 1$ can be computed exactly using the boundary conditions (4.11)-(4.12), else the relevant equation is replaced by the corresponding Dirichlet condition. The one remaining term that is not so readily computed is the final integral in (4.19) that depends on the source terms S. For the anion vacancy conservation, $S \equiv 0$ and so this term is zero. However, for the electron and hole conservation equations, the source term comprises both the generation and recombination rates, G and $R(n, p)$, which are usually nonlinear. Moreover, until the physical processes in PSCs are better understood, it is desirable to maintain the flexibility to quickly alter the functional forms of these terms without necessitating significant alterations to the scheme so that, *e.g.*, trap-assisted recombination can be augmented by radiative bimolecular recombination.

In order that the integral contained in the final term of (4.19) can be integrated (at least approximately) regardless of the functional form of the source term, we make a further approximation. This approximation is to replace the dependent variables in the integrand by functions that are piecewise constant over each subinterval, $x \in (x_i, x_{i+1})$, and have a value equal to that of the full series (4.16) at the midpoint of that interval. In short, we make the additional approximation,

$$\int_0^1 (G - R(n,p))\varphi_j \,\mathrm{d}x \approx \begin{cases} \frac{\Delta_{j-1/2}}{2}\left(G|_{x=x_{j-1/2}} - R\left(n|_{x=x_{j-1/2}}, p|_{x=x_{j-1/2}}\right)\right) \\ \qquad + \frac{\Delta_{j+1/2}}{2}\left(G|_{x=x_{j+1/2}} - R\left(n|_{x=x_{j+1/2}}, p|_{x=x_{j+1/2}}\right)\right), \\ \qquad\qquad \text{if } j = 1, ..., N-1\,, \\ \frac{\Delta_{1/2}}{2}\left(G|_{x=x_{1/2}} - R\left(n|_{x=x_{1/2}}, p|_{x=x_{1/2}}\right)\right), \\ \qquad\qquad \text{if } j = 0\,, \\ \frac{\Delta_{N-1/2}}{2}\left(G|_{x=x_{N-1/2}} - R\left(n|_{x=x_{N-1/2}}, p|_{x=x_{N-1/2}}\right)\right), \\ \qquad\qquad \text{if } j = N\,. \end{cases} \tag{4.25}$$

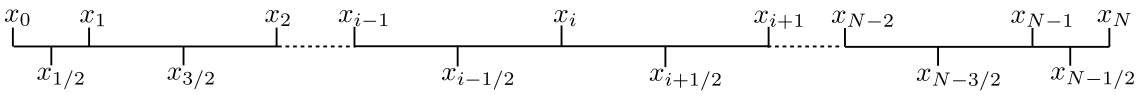

FIGURE 4.2: A schematic of the computational grid, reproduced from [35].

The additional error incurred as a result of this approximation is comparable to the error associated with the original piecewise linear approximation for the dependent variables. Thus, even though some additional error is introduced, the scheme retains its second order local accuracy. We note that this approach to dealing with the nonlinear source terms is a special case of the method used in the work of Skeel & Berzins [127], but we emphasise that, in contrast to their method, we only use this additional approximation for treatment of the source terms whilst the rest of the terms are integrated exactly. Once all the necessary integrals have been computed, the boundary conditions (4.11)-(4.12) can be imposed to form a system of DAEs which are closed by the initial conditions (4.14). It is this DAE system which is evolved in time using MATLAB's `ode15s`.

4.3.1 Spatial discretisation

In order to write down the spatially discretised system of equations in a concise form, we introduce three discrete operators: a difference operator $\mathfrak{D}_i$, an operator for evaluation of a dependent variables at a midpoint $\mathfrak{I}_i$ and a linear operator $\mathfrak{L}_i$. These act on a column vector $\mathbf{w}$ with the entries $w_i = w|_{x=x_i}$ $(i = 0, .., N)$ for a generic dependent variable w as follows:

$$\left.\frac{\partial w}{\partial x}\right|_{x=x_{i+1/2}} \approx \quad \mathfrak{D}_{i+1/2}(\mathbf{w}) = \frac{w_{i+1} - w_i}{\Delta_{i+1/2}}\,, \tag{4.26}$$

$$w|_{x=x_{i+1/2}} \approx \quad \mathfrak{I}_{i+1/2}(\mathbf{w}) = \frac{1}{2}(w_{i+1} + w_i)\,, \tag{4.27}$$

$$\mathfrak{L}_i(\mathbf{w}) = \frac{1}{6}\Delta_{i+1/2} w_{i+1} + \frac{1}{3}\left(\Delta_{i+1/2} + \Delta_{i-1/2}\right) w_i + \frac{1}{6}\Delta_{i-1/2} w_{i-1}\,. \tag{4.28}$$

We introduce $\mathbf{P}(t)$, $\mathbf{\Phi}(t)$, $\mathbf{n}(t)$ and $\mathbf{p}(t)$ as column vectors of length $N+1$ whose i'th entries are the functions $P_i(t)$, $\phi_i(t)$, $n_i(t)$ and $p_i(t)$, respectively. Using this notation we obtain discretised counterparts of the electric field, anion vacancy flux and carrier current

densities from (4.7(b)), (4.8(b)), (4.9(b)) and (4.10(b)) as follows,

$$E_{i+1/2} = -\mathfrak{D}_{i+1/2}(\mathbf{\Phi})\,, \tag{4.29}$$

$$F^P{}_{i+1/2} = -\left[\mathfrak{D}_{i+1/2}(\mathbf{P}) - \mathfrak{I}_{i+1/2}(\mathbf{P})E_{i+1/2}\right]\,, \tag{4.30}$$

$$j^n{}_{i+1/2} = \mathfrak{D}_{i+1/2}(\mathbf{n}) + \mathfrak{I}_{i+1/2}(\mathbf{n})E_{i+1/2}\,, \tag{4.31}$$

$$j^p{}_{i+1/2} = -\left[\mathfrak{D}_{i+1/2}(\mathbf{p}) - \mathfrak{I}_{i+1/2}(\mathbf{p})E_{i+1/2}\right]\,. \tag{4.32}$$

for $i = 0, ..., N-1$. We note that although the fluxes of the charged species and the field were eliminated in deriving the spatially discretised equations it is useful to reintroduce discrete versions of them here in the interests of brevity of notation and because it is often of interest to compute them for visualisation purposes after computations have been carried out.

The ODEs governing the evolution of the anion vacancy density, arising from (4.7), and ion flux boundary conditions, (4.11a) and (4.12a) are

$$\Delta_{1/2}\left[\frac{1}{3}\frac{\mathrm{d}P_0}{\mathrm{d}t} + \frac{1}{6}\frac{\mathrm{d}P_1}{\mathrm{d}t}\right] = -\lambda F^P{}_{1/2}\,, \tag{4.33}$$

$$\mathfrak{L}_i\left(\frac{\mathrm{d}\mathbf{P}}{\mathrm{d}t}\right) = -\lambda\left[F^P{}_{i+1/2} - F^P{}_{i-1/2}\right]\,, \qquad \text{for } i = 1, ..., N-1\,, \tag{4.34}$$

$$\Delta_{N-1/2}\left[\frac{1}{6}\frac{\mathrm{d}P_{N-1}}{\mathrm{d}t} + \frac{1}{3}\frac{\mathrm{d}P_N}{\mathrm{d}t}\right] = \lambda F^P{}_{N-1/2}\,. \tag{4.35}$$

The algebraic equations for the potential resulting from discretisation of (4.10) and the boundary conditions (4.11b) and (4.12b) are

$$0 = \phi_0 - \frac{\Phi - \Phi_{bi}}{2}\,, \tag{4.36}$$

$$\begin{aligned} 0 = \lambda^2\left[E_{i+1/2} - E_{i-1/2}\right] - \mathfrak{L}_i(\mathbf{P}) + \frac{1}{2}\left[\Delta_{i+1/2} + \Delta_{i-1/2}\right] \\ - \hat{\delta}\left[\mathfrak{L}_i(\mathbf{p}) - \mathfrak{L}_i(\mathbf{n})\right]\,, \qquad \text{for } i = 1, ..., N-1\,, \end{aligned} \tag{4.37}$$

$$0 = \phi_N + \frac{\Phi - \Phi_{bi}}{2}\,. \tag{4.38}$$

The ODEs for the electron and hole continuity equations, arising from (4.8) and (4.9),

and the remaining boundary conditions are

$$0 = n_0 - \bar{n}\,, \tag{4.39}$$

$$\varsigma\mathfrak{L}_i\left(\frac{\mathrm{d}\mathbf{n}}{\mathrm{d}t}\right) = {j^n}_{i+1/2} - {j^n}_{i-1/2} + \frac{\Delta_{i+1/2}}{2}\left[G_{i+1/2} - R_{i+1/2}\right] + \frac{\Delta_{i-1/2}}{2}\left[G_{i-1/2} - R_{i-1/2}\right]\,, \qquad \text{for } i = 1, ..., N-1\,, \tag{4.40}$$

$$\varsigma\Delta_{N-1/2}\left[\frac{1}{6}\frac{\mathrm{d}n_{N-1}}{\mathrm{d}t} + \frac{1}{3}\frac{\mathrm{d}n_N}{\mathrm{d}t}\right] = -{j^n}_{N-1/2} + \frac{\Delta_{N-1/2}}{2}\left[G_{N-1/2} - R_{N-1/2}\right] - R_r(n_N)\,, \tag{4.41}$$

$$\varsigma\Delta_{1/2}\left[\frac{1}{3}\frac{\mathrm{d}p_0}{\mathrm{d}t} + \frac{1}{6}\frac{\mathrm{d}p_1}{\mathrm{d}t}\right] = -{j^p}_{1/2} + \frac{\Delta_{1/2}}{2}\left[G_{1/2} - R_{1/2}\right] - R_l(p_0)\,, \tag{4.42}$$

$$\varsigma\mathfrak{L}_i\left(\frac{\mathrm{d}\mathbf{p}}{\mathrm{d}t}\right) = -\left[{j^p}_{i+1/2} - {j^p}_{i-1/2}\right] + \frac{\Delta_{i+1/2}}{2}\left[G_{i+1/2} - R_{i+1/2}\right] + \frac{\Delta_{i-1/2}}{2}\left[G_{i-1/2} - R_{i-1/2}\right]\,, \qquad \text{for } i = 1, ..., N-1\,, \tag{4.43}$$

$$0 = p_N - \bar{p}\,. \tag{4.44}$$

in which we have used the shorthand $G_{i+1/2} = G(\mathfrak{I}_{i+1/2}(\mathbf{x}))$ (in which $\mathbf{x}$ is a column vector of the values x_i, $i = 0, ..., N$) and $R_{i+1/2} = R(\mathfrak{I}_{i+1/2}(\mathbf{n}), \mathfrak{I}_{i+1/2}(\mathbf{p}))$.

4.3.2 Implementation

The system of DAEs formulated above is evolved forward in time using MATLAB's `ode15s` [122, 123] which is based on numerical differentiation formulae (of orders 1–5) or backward differentiation formulae [56] whose step size and order are automatically varied to ensure that the specified error tolerances are met. In order to minimise computational cost, by minimising the size of the system, we eliminate superfluous variables, namely F^P, j^n, j^p and E, and assemble the remaining $4N+4$ unknown functions of time into one column vector $\mathbf{u}(t)$ as follows:

$$\mathbf{u}(t) = \left[P_0, \cdots, P_N, \phi_0, \cdots, \phi_N, n_0, \cdots, n_N, p_0, \cdots, p_N\right]^{\mathrm{T}}\,, \tag{4.45}$$

$$\text{or equivalently,} \quad \mathbf{u}(t) = \left[\mathbf{P}(t)^{\mathrm{T}}\ \mathbf{\Phi}(t)^{\mathrm{T}}\ \mathbf{n}(t)^{\mathrm{T}}\ \mathbf{p}(t)^{\mathrm{T}}\right]^{\mathrm{T}}\,, \tag{4.46}$$

where a superscript T denotes a transpose. The problem to be solved can now be written in the form

$$\mathbf{M}\frac{\mathrm{d}\mathbf{u}}{\mathrm{d}t} = \mathbf{f}(\mathbf{u}) \quad \text{with} \quad \mathbf{u}|_{t=0} = \mathbf{u}_0\,, \tag{4.47}$$

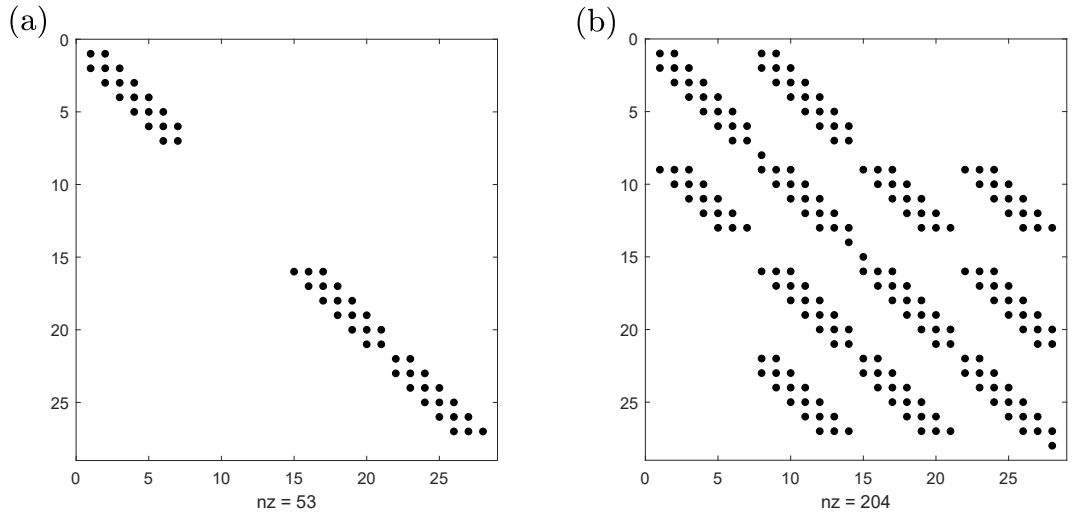

FIGURE 4.3: Plots to show the positions of the nonzero entries (black dots) in the mass matrix $\mathbf{M}$, panel (a), and the Jacobian matrix of $\mathbf{f}$, panel (b), for the finite element scheme in the case $N = 6$, reproduced from [35].

where $\mathbf{f}(\mathbf{u})$ is a nonlinear vector function of length $4N + 4$ whose entries are the right-hand sides of (4.33)-(4.44). The matrix $\mathbf{M}$ is a $(4N + 4) \times (4N + 4)$ diagonal mass matrix whose entries are the coefficients of the time derivative terms in the equations (4.33)-(4.44), see Figure 4.3 (a). Since the governing equations for the values of ϕ_i, (4.36)-(4.38), and the discrete boundary conditions (4.39) and (4.44) contain no temporal derivatives the corresponding entries on the diagonal of $\mathbf{M}$ are zero and hence the mass matrix is singular. It is this feature of the system that renders the problem a system of DAEs and motivates our choice of solver, namely `ode15s`, which is one of relatively few solvers that can handle problems of this type. Moreover, it offers an adaptive timestep which is able to deal with the numerical stiffness resulting from the disparity in timescales between the electronic and ionic motion.

The `ode15s` algorithm requires numerical evaluation of the Jacobian of $\mathbf{f}$ at each time step. For the general case, it is not possible to write down an analytic Jacobian. However, it is clear from the structure of the discrete system that many entries in the Jacobian are zero for all time. As a result, a heavy reduction in computational effort (around $0.005N^{3/2}$ in the convergence test case described in Section 4.5.1) can be achieved by exploiting the `jpattern` option for `ode15s`. This option allows the user to 'flag' the subset of entries in the Jacobian matrix that are not always zero, see Figure 4.3 (b). Only these entries then need to be approximated numerically at each time step (while the others are assumed to be zero).

4.4 Finite difference scheme

In this section we outline an alternative numerical scheme for solving the model (4.7)-(4.14), in which spatial derivatives are discretised using second order accurate finite differences on a 'staggered grid'. The resulting DAEs are again evolved forward in time using MATLAB's `ode15s`. The numerical stiffness arising from narrow Debye layers is tackled by (i) employing a non-uniform grid spacing, and (ii) using Advanpix's Multiprecision Computing Toolbox [1] to overload MATLAB's native commands with arbitrary-precision counterparts, thereby retaining good accuracy despite the large condition numbers of the underlying matrices.

We retain the computational grid, including the definition of the subinterval width and half points, defined at the beginning of Section 4.3. The anion vacancy profiles are determined subject to the Neumann conditions (4.11a) and (4.12a) which require zero flux of ions at each boundary. Thus, it is natural to compute the ion vacancy flux at the grid points and the ion vacancy density at the half points. Not only does this allow (4.11a) and (4.12a) to be imposed straightforwardly, it also ensures that the property of global conservation of anion vacancies is inherited by the discrete system[1]. The equation determining the electric potential is to be solved subject to the Dirichlet conditions (4.11b) and (4.12b) which motivates tracking the potential at the grid points and the electric field at the half points. Since the governing equations for electrons (holes) are solved subject to one Dirichlet and one Neumann condition, namely (4.11c) and (4.12d) ((4.11d) and (4.12c)), it is not obvious whether it is better to define the concentration or the flux on the grid points. Here, we elect to track the concentration on the grid points and the fluxes on the half-points so that evaluating the electron and hole contributions to the charge density on the right-hand side of Poisson's equation (4.10a) can be accomplished without interpolation, thereby avoiding additional errors. In summary we introduce discretised variables defined by

$$P_{i+1/2} = P|_{x=x_{i+1/2}}\,, \qquad {F^P}_i = F^P|_{x=x_i}\,, \tag{4.48}$$

$$\phi_i = \phi|_{x=x_i}\,, \qquad E_{i+1/2} = E|_{x=x_{i+1/2}}\,, \tag{4.49}$$

$$n_i = n|_{x=x_i}\,, \qquad {j^n}_{i+1/2} = j^n|_{x=x_{i+1/2}}\,, \tag{4.50}$$

$$p_i = p|_{x=x_i}\,, \qquad {j^p}_{i+1/2} = j^p|_{x=x_{i+1/2}}\,. \tag{4.51}$$

Note that this means that, in this section, $\mathbf{P}$ denotes a column vector of length N (rather than $N+1$ as in Section 4.3) that comprises the entries $P_{i+1/2}$, $i = 0, ..., N-1$. We also introduce three further column vectors, also of length N, namely $\mathbf{E}$, $\mathbf{j^n}$ and $\mathbf{j^p}$ as well as

[1] Global conservation of anion vacancy concentrations in the discrete system, up to second order, is reflected in the property that $d/dt\left(\sum_{i=0}^{N-1} P_{i+1/2}\right) = 0$, see equation (4.59).

one column vector of length $N+1$ namely $\mathbf{F^P}$. These have entries $E_{i+1/2}(t)$, ${j^n}_{i+1/2}(t)$, ${j^p}_{i+1/2}(t)$ for $i = 0, ..., N-1$ and ${F^P}_{i+1/2}(t)$ for $i = 0, ..., N$ respectively.

4.4.1 Spatial discretisation

Spatial discretisation is carried out using the discrete operators $\mathfrak{D}_{i+1/2}$ and $\mathfrak{I}_{i+1/2}$ defined in (4.26) and (4.27). We also introduce $\mathfrak{D}_i$ which approximates the first derivative at a grid point in terms of data at adjacent half points, and $\mathfrak{I}_i$ which linearly interpolates data at adjacent half points to return an approximation of a quantity at a grid point. These are defined as follows:

$$\left.\frac{\partial w}{\partial x}\right|_{x=x_i} \approx \quad \mathfrak{D}_i(\mathbf{w}) = \frac{w_{i+1/2} - w_{i-1/2}}{x_{i+1/2} - x_{i-1/2}}\,, \tag{4.52}$$

$$w|_{x=x_i} \approx \quad \mathfrak{I}_i(\mathbf{w}) = \frac{w_{i+1/2}(x_i - x_{i-1}) + w_{i-1/2}(x_{i+1} - x_i)}{x_{i+1} - x_{i-1}}\,. \tag{4.53}$$

A standard error analysis indicates that these both have second order local accuracy.

The discrete operators defined by (4.26), (4.27), (4.52) and (4.53) can be used to approximate the electric field, and electron and hole current densities at the half-points. The discretised versions of equations (4.10b), (4.8b) and (4.9b) are

$$E_{i+1/2} = -\mathfrak{D}_{i+1/2}(\mathbf{\Phi})\,, \tag{4.54}$$

$${j^n}_{i+1/2} = \mathfrak{D}_{i+1/2}(\mathbf{n}) + \mathfrak{I}_{i+1/2}(\mathbf{n})E_{i+1/2}\,, \tag{4.55}$$

$${j^p}_{i+1/2} = -\left[\mathfrak{D}_{i+1/2}(\mathbf{p}) - \mathfrak{I}_{i+1/2}(\mathbf{p})E_{i+1/2}\right]\,, \tag{4.56}$$

$$\text{for} \quad i = 0, ..., N-1\,.$$

The anion vacancy flux can then be computed on both the internal and boundary grid points by discretising equation (4.7b) and its boundary conditions (4.11a) and (4.12a). We have

$${F^P}_0 = {F^P}_N = 0\,, \tag{4.57}$$

$${F^P}_i = -\mathfrak{D}_i(\mathbf{P}) - \mathfrak{I}_i(\mathbf{P})\mathfrak{I}_i(\mathbf{E})\,, \quad \text{for } i = 1, .., N-1\,. \tag{4.58}$$

The ODEs governing the evolution of the anion vacancy density, arising from (4.7a), are

$$\frac{\mathrm{d}P_{i+1/2}}{\mathrm{d}t} = -\lambda\mathfrak{D}_{i+1/2}(\mathbf{F^P})\,, \quad \text{for } i = 0, ..., N-1\,. \tag{4.59}$$

The algebraic equations for the potential resulting from discretisation of (4.10a) and the

boundary conditions (4.11b) and (4.12b) are

$$\phi_0 - \frac{\Phi - \Phi_{bi}}{2} = 0\,, \tag{4.60}$$

$$\lambda^2 \mathfrak{D}_i(\mathbf{E}) + 1 - \mathfrak{I}_i(\mathbf{P}) + \hat{\delta}(n_i - p_i) = 0\,, \quad \text{for } i = 1, .., N-1\,, \tag{4.61}$$

$$\phi_N + \frac{\Phi - \Phi_{bi}}{2} = 0\,. \tag{4.62}$$

It is straightforward to discretise (4.8) to derive a set of $N-1$ ODEs governing the evolution of the electron density on the internal grid points

$$n_0 - \bar{n} = 0\,, \tag{4.63}$$

$$\varsigma \frac{\mathrm{d}n_i}{\mathrm{d}t} = \mathfrak{D}_i(\mathbf{j^n}) + G(x_i) - R(n_i, p_i)\,, \quad \text{for } i = 1, .., N-1\,, \tag{4.64}$$

$$j^n{}_{N-1/2} + \mathfrak{D}_{N-1}(\mathbf{j^n})(1 - x_{N-1/2}) + R_r(n_N) = 0\,. \tag{4.65}$$

Here the conditions (4.63) and (4.65) arise from the imposition of the Dirichlet boundary condition (4.11c) on $x = 0$ and the flux condition (4.12d) on $x = 1$, respectively. Notice that the latter is imposed by linear extrapolation of the electron current density to the boundary $x = 0$. Similarly, discretisation of (4.9) leads to a set of $N-1$ ODEs governing the evolution of the hole density on the internal grid points

$$j^p{}_{1/2} - \mathfrak{D}_1(\mathbf{j^P})x_{1/2} + R_l(p_0) = 0\,, \tag{4.66}$$

$$\varsigma \frac{\mathrm{d}p_i}{\mathrm{d}t} = -\mathfrak{D}_i(\mathbf{j^P}) + G(x_i) - R(n_i, p_i)\,, \quad \text{for } i = 1, .., N-1\,, \tag{4.67}$$

$$p_N - \bar{p} = 0\,. \tag{4.68}$$

Here the conditions (4.66) and (4.68) are derived from the flux condition (4.11d) on $x = 0$ and the Dirichlet boundary condition (4.12c), respectively. We note that the boundary conditions (4.65) and (4.66) are the only conditions that are not imposed exactly. However, the extrapolation involved only introduces second order errors, and therefore the scheme as a whole is still locally second order accurate as demonstrated by Figure 4.5 (a).

4.4.2 Implementation

The finite difference scheme is implemented using `ode15s` in the same way as the finite element scheme described in Section 4.3, except that in (4.46), $\mathbf{P}(t)$ is a vector of length N whose entries are the functions of time $P_{i+1/2}(t)$ for $i = 0, ..., N-1$. The problem to be solved can again be written in the form (4.47) where $\mathbf{f}(\mathbf{u})$ is now a nonlinear vector function of length $4N + 3$. Its first N entries are the right-hand sides of (4.59); the

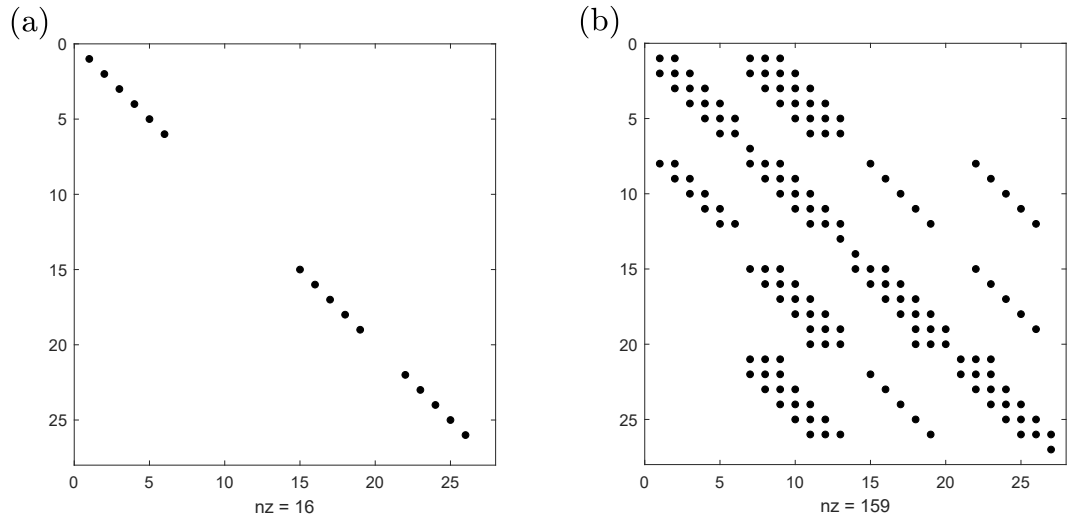

FIGURE 4.4: Plots to show the positions of the nonzero entries (black dots) in the mass matrix $\mathbf{M}$, panel (a), and the Jacobian matrix of $\mathbf{f}$, panel (b), for the finite difference scheme in the case $N = 6$, reproduced from [35].

subsequent $N + 1$ entries are the right-hand sides of (4.60)-(4.62); these are followed by the $N + 1$ right-hand sides of (4.63)-(4.65); and finally the $N + 1$ right-hand sides of (4.66)-(4.68). The matrix $\mathbf{M}$ is a $(4N + 3) \times (4N + 3)$ diagonal mass matrix whose entries are the coefficients of the time derivative terms in the equations (4.59)-(4.68), see Figure 4.4 (a). The sparse structure of the Jacobian of $\mathbf{f}$ is shown in Figure 4.4 (b).

When simulating many of the regimes of physical interest, we find that the condition number of the Jacobian is large, sometimes $O(10^{16})$ or greater, which has the potential to severely hamper the accuracy of matrix inversions performed by the solver, `ode15s`. To overcome this difficulty we make use of a third-party toolbox, Advanpix, which extends MATLAB's functionality to work with floating point numbers of higher precision. The use of quadruple precision results in a loss in the speed of computation for simple cases (those which can be computed accurately on a small number of grid points) for which runtimes, originally of a few seconds on a standard personal computer, are typically 15-30 times longer. However, we find the higher precision offered by Advanpix's Multiprecision Computing Toolbox [1] is crucial in allowing this finite difference scheme to cope with the spatial stiffness due to narrow Debye layers.

4.5 Verification of methods and comparison to alternative numerical methods

Here, we demonstrate the convergence properties of our two schemes and benchmark their performance via comparison to two alternative methods. One of these alternatives has appeared in the literature [22] and makes use of MATLAB's `pdepe` solver with a piecewise constant spatial grid; the other is an adaptation of the `pdepe`-based method to the non-uniform grids introduced below in Section 4.5.2. In order to perform the benchmarking we apply the methods to a physically pertinent test case with appropriate physical parameters, as given in (4.15). We examine the schemes' accuracy during a transient protocol, not just near steady state, and rate the performance in terms of numerical accuracy and computation time. We also discuss the shortcomings of previously used methods of solution including those based upon `pdepe` and the Chebfun package [43].

4.5.1 Choice of test case

We choose the particular scenario in which an illuminated cell is initially operating at an applied voltage equal to the built-in voltage $\Phi = \Phi_{bi} = 40$, so that the potential drop across the perovskite layer is zero. The applied voltage is then rapidly decreased to $\Phi = \Phi_{bi}/2$ so that the device is running in its power generating regime. We accomplish this by defining

$$\Phi(t) = \Phi_{bi}\left(1 - \frac{\tanh(\beta t)}{2\tanh(\beta t_{\text{end}})}\right) \quad \text{with} \quad \beta = 10^2\,, \quad t_{end} = 1\,. \tag{4.69}$$

Here β characterises the timescale for altering the applied voltage and t_{end} is the dimensionless time at which the simulation is terminated.

As is typical in such applications, we assume that the photo-generation rate, G, obeys the Beer-Lambert law, which has the dimensionless form

$$G(x) = \Upsilon \exp(-\Upsilon x)\,, \tag{4.70}$$

in which $1/\Upsilon$ is the dimensionless absorption length. The estimate given in Section 2 of [34] is

$$\Upsilon = 3.7\,. \tag{4.71}$$

We also choose the bulk recombination rate, $R(n,p)$, to take the form of the Shockley-Read-Hall (SRH) recombination rate (see [95] Section 4.5.5) and the interface recombi-

nation rates, $R_l(p)$ and $R_r(n)$, to both be zero, *i.e.*

$$R(n,p) = \gamma \left(\frac{np - n_i^2}{n + \tau p + c_3} \right) , \quad R_l(p) = R_r(n) = 0 , \tag{4.72}$$

where γ, n_i, τ and c_3 are dimensionless constants, defined and estimated in [34] Section 2 to be:

$$\gamma = 2.4, \qquad n_i = 8.6 \times 10^{-9}, \qquad \tau = 3.3 \times 10^{-3}, \qquad c_3 = 8.6 \times 10^{-9}. \tag{4.73}$$

All other dimensionless parameter values are also as in [34] Section 2 and listed in (4.15).

A simple choice of initial conditions that satisfies Poisson's equation (with $\phi|_{t=0} \equiv 0$) and six out of the eight boundary conditions (those for the carrier current densities are not satisfied) is

$$P_{\text{init}}(x) = 1 , \quad n_{\text{init}}(x) = p_{\text{init}}(x) = \bar{p}x + \bar{n}(1-x) . \tag{4.74}$$

In practice, the choice of initial conditions is not particularly important for the modelling of PSCs as, in any experimental procedure, it is standard practice to include a pre-conditioning step. This step involves holding the applied potential constant for a sufficiently long time such that any initial transients associated with charge carrier and ion vacancy motion decay towards zero.

4.5.2 Choice of spatial grid

We find that the choice of spatial grid can have a large impact on performance; this impact is shown in Figure 4.6. In anticipation of the fact that the largest gradients in the solution appear in narrow Debye layers adjacent to the domain boundaries, we compare two spatial grids in which points are concentrated near the domain boundaries. Using this approach, we are able to achieve good resolution in the Debye layers without wasting computational effort by over-resolving in the bulk where the solution varies more slowly. The first grid is comprised of Chebyshev nodes on the interval $[0, 1]$ and defined by

$$x_i = \frac{1}{2} \left(1 + \cos \left[\pi \left(\frac{i}{N} - 1 \right) \right] \right) , \quad \text{for} \quad i = 0, ..., N . \tag{4.75}$$

We term this the Chebyshev grid. We define a second grid, also with points clustered toward the domain boundaries, by

$$x_i = \frac{1}{2}\left(\frac{\tanh\left[\sigma\left(\frac{2i}{N}-1\right)\right]}{\tanh(\sigma)}+1\right), \quad \text{for} \quad i = 0, ..., N\,. \tag{4.76}$$

We term this the tanh grid. Here, the parameter σ represents the degree to which points are concentrated in the Debye layers, near $x = 0$ and $x = 1$, with large values of σ giving denser clustering of points in these layers. It is possible to relate σ to the fraction X of grid points lying within a dimensionless Debye length, λ, of each domain boundary (*i.e.* in the interval $x \in [0, \lambda]$, or equivalently in the interval $x \in [1-\lambda, 1]$) as follows

$$\lambda = \frac{1}{2}\left(\frac{\tanh\left[\sigma\left(2X-1\right)\right]}{\tanh(\sigma)}+1\right). \tag{4.77}$$

Based on our numerical tests we found that good results could be obtained by concentrating 20% (*i.e.* $X = 0.2$) of the grid points within each layer (the remaining 60% span the bulk region). This entailed taking $\sigma = 5$ for a dimensionless Debye length of $\lambda = 2.4 \times 10^{-3}$. We note that suitable values of σ depend strongly on the potential difference as well as the Debye length and so optimal values of σ may vary. In Section 4.5.3, we show the convergence of each of our schemes using the tanh grid. Then, in Section 4.5.4, we quantify the improvements made over the only previously used published method and, in Section 4.5.5, we compare all schemes considered in this work using a measure of accuracy (defined in Section 4.5.3) versus run time. Our results, shown in Figure 4.6, demonstrate that a significant gain in performance is achieved using the tanh grid as opposed to the Chebyshev grid, regardless of the choice of scheme.

4.5.3 Convergence

Here we demonstrate the expected second order spatial convergence of the schemes using the test case described in Section 4.5.1. Due to the choice of non-uniform spatial grid, namely the tanh grid defined in (4.76) with $\sigma = 5$, we chose to monitor the values of the following five variables. This is because, independent of the number of grid points used $(N + 1)$, they are available immediately following the temporal integration without the need for an additional interpolation step, thereby allowing a direct interrogation of the scheme.

$$\phi|_{x=1/2}\,, \quad n|_{x=1/2}\,, \quad n|_{x=1}\,, \quad p|_{x=0}\,, \quad p|_{x=1/2}\,. \tag{4.78}$$

Due to the lack of exact solutions to the model, it is necessary to verify convergence by

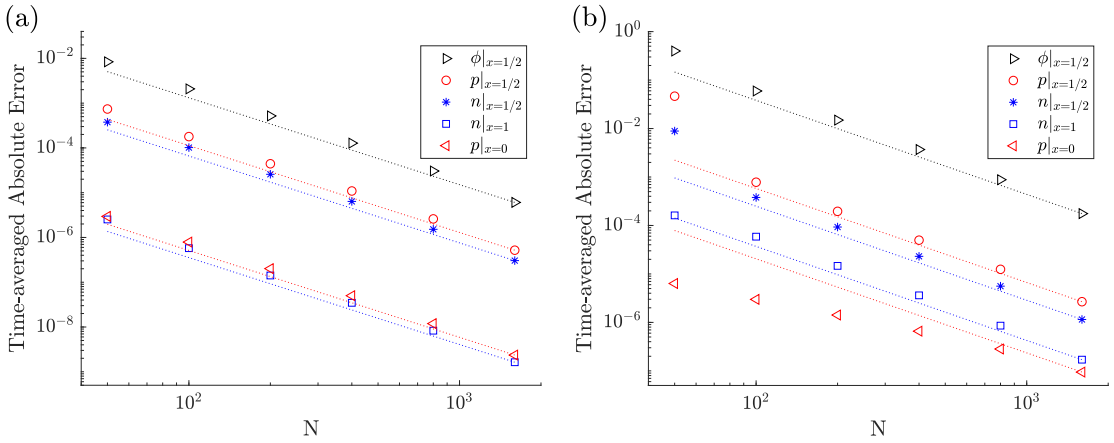

FIGURE 4.5: The pointwise convergence of (a) the finite element scheme and (b) the finite difference scheme demonstrated by plots of the time-averaged error $\bar{\mathcal{E}}$ for each of the five variables listed in (4.78) versus the number of subintervals, N. Markers show errors for computations with $N = 100, 200, 400, 800, 1600$ estimated against a numerical solution with $N_M = 3200$. Dotted lines show the expected second order convergence.

measuring the error relative to a solution computed on a highly refined grid. For some scalar quantity v (which could be any of those defined in (4.78)) computed using the scheme on $N + 1$ grid points with N subintervals, denoted by $v^{(N)}$, we can define the absolute error at time $t = T$ of the simulation as

$$\mathcal{E}(N)|_{t=T} = \left| v^{(N)}|_{t=T} - v^{(N_M)}|_{t=T} \right| , \tag{4.79}$$

for some $N_M \gg N$. Henceforth we take $N_M = 3200$. In order to quantify the total error involved in a computation, we use this absolute error to define a time-averaged error, averaged over all but the first time point of the evolution, as follows

$$\bar{\mathcal{E}}(N) = \frac{1}{M} \sum_{i=1}^{i=M} \mathcal{E}(N)|_{t=T_i} , \tag{4.80}$$

where T_i are M equally-spaced dimensionless time points in the interval $[1/M, 1]$, *i.e.*, $1/M$, $2/M$, ..., $(M-1)/M$, 1. This time-averaged error, for the case $M = 100$, for each of the quantities in (4.78) is shown in Figure 4.5 for both the finite element and finite difference methods described in Section 4.3 and Section 4.4 respectively. We find that these errors are representative of the error at each time-step and do not grow appreciably in time. Stability of each method with respect to time is confirmed in the next section in which the relative temporal tolerance is varied, but the resulting accuracy is maintained. The computations for Figure 4.5 were performed with temporal integration tolerances for `ode15s` controlled using the `RelTol` and `AbsTol` settings in MATLAB; the relative tolerance was 10^{-6} and the absolute tolerance was 10^{-8}. Both sets of results demonstrate

second order spatial convergence, as predicted by a naive analysis of the discrete operators (4.26)-(4.28) for the finite element scheme in Section 4.3 and (4.52)-(4.53) for the finite difference scheme in Section 4.4.

4.5.4 Comparison to pre-existing method based on MATLAB's `pdepe`

In order to benchmark our numerical schemes against an existing method, we turn to MATLAB's built-in solver `pdepe`, used by Calado *et al.* [22] to investigate a drift-diffusion model for PSCs. The `pdepe` solver is a routine which can provide numerical solution to systems of elliptic/parabolic PDEs, along with their associated boundary and initial conditions, in one spatial dimension and in time, provided that they can be cast in the 'standard form' accepted by the algorithm [127]. Temporal integration is provided by `ode15s` (like in our approaches) but for `pdepe` spatial discretisation is carried out autonomously by the solver and is based on the method presented by Skeel & Berzins [127].

Calado *et al.* [22] perform their simulations on a uniform grid with a spacing of 0.67 nm. In order to simulate on a grid with the same dimensional distance between adjacent grid points here would require $N = 900$. It is shown in the SI of [22] that appreciable differences were visible between the transient simulation results performed using a grid spacing of 0.67 nm and 0.5 nm (the smallest that was tried), indicating that numerical errors were non-negligible. It is stated in the main text that this choice was a "compromise between numerical accuracy and computation time". We find this method can be used to obtain solutions to the test case described in Section 4.5.1 (see Figure 4.6 and associated discussion in Section 4.5.5) however our measure of the error (the sum of the time-averaged error $\bar{\mathcal{E}}$ defined in (4.80) for the five variables listed in (4.78)) is as large as 0.3 for $N = 900$. Hence this method is prone to failure when attempting to simulate longer experimental protocols such as J-V scans.

Additionally, an important disadvantage of using `pdepe` in the context of PSC simulation is that the restriction that equations must be cast in its standard form prevents the extension of the method to a three-layer model incorporating charge carrier transport in the ETL and the HTL. In particular, `pdepe` is unable to accept jump conditions posed on internal boundaries such as those occurring at the ETL/perovskite and the perovskite/HTL interfaces. Such jump conditions are used to model the discontinuities in carrier current densities resulting from surface recombination. In order to circumvent this technical limitation, Calado *et al.* [22] artificially smeared the surface recombination across "diffuse" interface regions, however it is acknowledged that this approach is physically unrealistic. In contrast, the tailored numerical schemes detailed in this work can be readily extended

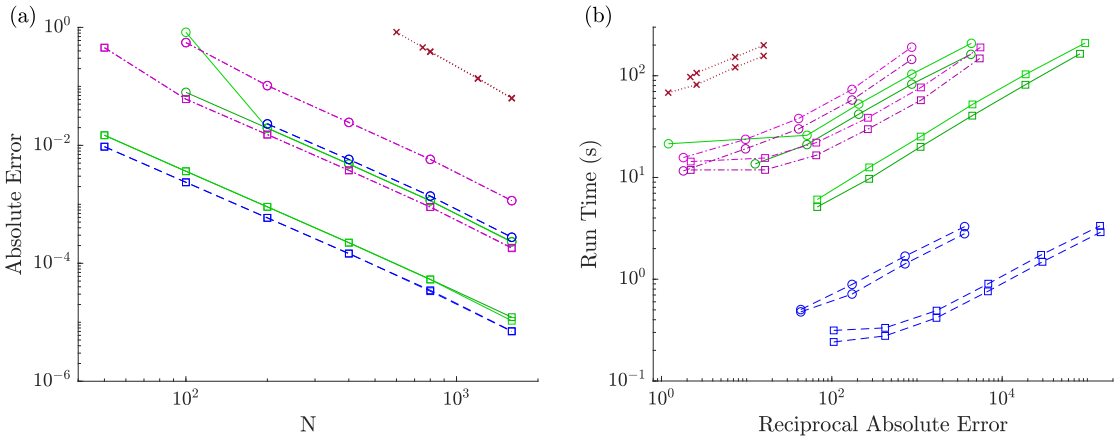

FIGURE 4.6: (a) The sum of the five time-averaged errors (as defined in (4.80) and plotted in Figure 4.5) for each of the five variables listed in (4.78) versus the number of subintervals, N. Results are for `pdepe` (green lines), the finite difference scheme (pink dot-dashed lines) and the finite element scheme (blue dashed lines) on either the Chebyshev (circles) or tanh (squares) grid (as defined in Section 4.5.2). Red dotted lines with crosses represent results from the previously used method of `pdepe` on a uniform grid as discussed in Section 4.5.4. Lines for simulations with relative temporal tolerance of 10^{-4} and 10^{-5} are almost indistinguishable on these scales. (b) The run times for each of the simulations in (a) plotted against the reciprocal of the sum of the time-averaged errors. The higher (slower) of each pair of lines corresponds to the stricter relative temporal tolerance of 10^{-5} compared to 10^{-4}. Reproduced from [35].

to include more layers and incorporate any necessary type of interface condition.

4.5.5 Comparison between all numerical methods

Here, we compare the performance of our methods against one another as well as MATLAB's built-in solver `pdepe` using the test case described in Section 4.5.1. In Figure 4.6 (a), the sum of the five time-averaged absolute errors (defined in Section 4.5.3) for each of the three schemes is shown versus the number of subintervals N on each of the nonlinear grids defined in Section 4.5.2. We show results down to the lowest multiple of 50 for N for which the solver returns a solution. Second-order pointwise convergence is found in all cases, however it is notable that there is a significant decrease (improvement) in the size of the error for simulations performed on the tanh grid over those performed on the Chebyshev grid, irrespective of the method used. Figure 4.6 (a) also illustrates that the methods based upon the technique of finite elements, namely the scheme presented in Section 4.3 and `pdepe`, significantly outperform the finite difference scheme presented in Section 4.4, although, unlike `pdepe`, it can be readily extended to a three-layer device with interface recombination.

For both panels in Figure 4.6, we apply relative temporal tolerances of 10^{-4} and 10^{-5}

(applied via the `RelTol` settings in MATLAB) while the absolute tolerance is kept at 10^{-8}. In Figure 4.6 (a), these results almost entirely overlap, indicating that the methods are stable in time. We find that all methods become unstable for relative temporal tolerances larger than 10^{-3}.

Figure 4.6 (b) shows the computational time required for simulation in regimes where the numerical integration was stable. We use the term "run time" to mean only the length of time taken during the simulation by the call to either `ode15s` or to `pdepe`. We choose to exclude the set-up time on grounds that this is a one-off cost that does not scale with the simulation protocol and can be avoided when running repeated simulations. Run times were recorded on a computer with a 2.40 GHz Intel processor. From the results for this test case, we conclude that computations carried out using our finite element scheme require roughly 50 times less processing time than their counterparts. These results demonstrate the increased accuracy versus run time afforded by our finite element scheme over both the finite difference scheme computed with quadruple precision and MATLAB's `pdepe`. Such improved accuracy versus run time is highly desirable and confirms that our finite element scheme provides a fast and robust tool that can enable thorough investigation of the varied behaviour of PSCs.

4.5.6 Comments on using the Chebfun package

We also considered schemes based on the Chebfun package available for MATLAB. We note that this has previously been used to solve PSC models, or simplifications to such models, in [52, 99, 109]. Chebfun employs spectral methods which offer high spatial accuracy when using only a relatively small number of collocation points.

Included in the Chebfun package is one of its automatic PDE solvers, `pde15s`, which (like `pdepe`) offers automatic spatial and temporal treatment of systems of elliptic/-parabolic PDEs in a single spatial dimension and time. Unfortunately, it is unable to cope with the multiple sources of stiffness in this problem. We find that values of λ and/or ς below 0.25 cause the current version (at the time of writing v5.7.0) to fail. Moreover, this method is unable to deal with the nonlinearity introduced by the presence of the SRH recombination rate.

We find that it is possible to facilitate the solution of the PSC model with realistic parameter values by implementing a 'manual' timestep; we tried both straightforward backward Euler and a more complicated predictor-corrector strategy. The former approach could better cope with the extreme values of the parameters but still suffered from an inability to deal with an SRH recombination rate. The latter remedied this issue (by linearising

the recombination rate), but the overheads associated with the iterative correction process mean that computations took an impractical length of time (days).

4.6 Comparison to and validation of published single-layer asymptotic results

In this section, we compare numerical results from our finite element scheme to the asymptotic solution presented in [34] for two physically relevant voltage protocols. To make this comparison, we use the realistic parameter estimates given in (4.15). The first voltage protocol is similar to that of the test case described in Section 4.5.1. The second protocol describes the measurement of a current-voltage curve. A current-voltage scan under 1 Sun illumination is the standard experimental procedure used to determine the power conversion efficiency of a solar cell. However, in the case of PSCs, such a curve often displays hysteresis as a result of ion migration which prevents accurate characterisation of their performance [128, 143]. The model and methods of solution presented in this work are intended to enable thorough investigation of the hysteresis due to ion migration during current-voltage measurements, as well as other transient protocols, in order to more thoroughly elucidate the underlying operating principles of PSCs.

Although a significant amount of progress can be made using the asymptotic method even when a nonlinear SRH recombination rate is taken, separate analytic expressions for the charge carrier concentrations can only be obtained (see [34] Section 3.3) when a linear, monomolecular bulk recombination rate is used. In order to compare directly to an analytic solution, that depends only on the numerical solution of a single ODE (for the Debye layer ionic charge density), we choose to compare the methods using the case where the bulk recombination rate, $R(n,p)$, is monomolecular (depending solely on the local hole concentration p) and the surface recombination rates, $R_l(p)$ and $R_r(n)$ are both zero, such that

$$R(n,p) = \gamma p\,, \quad R_l(p) = R_r(n) = 0\,, \tag{4.81}$$

where, as before, we take $\gamma = 2.4$. As noted in [34], monomolecular hole-dominated bulk recombination is the limit of the SRH recombination law, given in (4.72), when the electron pseudo-lifetime is much less than the hole pseudo-lifetime. This is usually a good approximation for recombination in the perovskite material methyl ammonium lead tri-iodide [131], however it can break down where the electron density becomes very small. Note however that the numerical schemes presented in this work are readily able to deal with nonlinear recombination rates such as the full SRH law. For further analysis

of the single layer model and a comparison to results from a mixed asymptotic/numeric approach that uses the full SRH recombination law, see Section 4 of [34].

4.6.1 Calculation of current density from numerical solutions

An expression for the total current density generated by a PSC can be derived from the dimensionless model as follows. Subtracting equation (3.49a) from equation (3.50a) gives

$$\varsigma\frac{\partial}{\partial t}(\chi p - n) + \frac{\partial}{\partial x}\left(j^p + j^n\right) = 0\,. \tag{4.82}$$

Then, by substituting the difference in the carrier concentrations $(\chi p - n)$ using Poisson's equation given in (3.52), this becomes

$$\frac{\partial}{\partial x}\left(j^p + j^n\right) - \frac{\varsigma}{\delta}\frac{\partial}{\partial t}\left(\lambda^2\frac{\partial^2\phi}{\partial x^2} - (1-P)\right) = 0\,. \tag{4.83}$$

Applying the time-derivative to the last term in the brackets allows us to use the ion vacancy conservation equation in (3.51) to make a substitution for $\frac{\partial P}{\partial t}$, which leads to

$$\frac{\partial}{\partial x}\left(j^p + j^n\right) - \frac{\varsigma\lambda^2}{\delta}\frac{\partial}{\partial t}\left(\frac{\partial^2\phi}{\partial x^2}\right) + \frac{\varsigma\lambda}{\delta}\frac{\partial F^P}{\partial x} = 0\,. \tag{4.84}$$

After swapping the order of spatial and temporal differentiation, integrating with respect to x and applying the Ohmic boundary conditions at either metal contact, the current density is found to be

$$J(t) = j^n + j^p - \frac{\varsigma\lambda^2}{\delta}\frac{\partial}{\partial t}\left(\frac{\partial\phi}{\partial x}\right) + \frac{\varsigma\lambda}{\delta}F^P\,. \tag{4.85}$$

Note that the third term on the right-hand side is the (dimensionless) displacement current density.

The total dimensional current density $J^{(\text{dim.})}(t)$ is calculated from the non-dimensional output of the numerical codes via

$$\begin{aligned} J^{(\text{dim.})}(t) = {} & qG_0 b\left({j^n}_{k+1/2} + {j^p}_{k+1/2}\right) \\ & - \frac{\varepsilon_p V_T}{b\tau_{ion}\hat{t}}\left(\left.\frac{\phi_{k+1}-\phi_k}{\Delta_{k+1/2}}\right|_t - \left.\frac{\phi_{k+1}-\phi_k}{\Delta_{k+1/2}}\right|_{t-\hat{t}}\right) + \frac{qD_I N_0}{b}F^P\,, \end{aligned} \tag{4.86}$$

in which j^n, j^p and F^P are given by their definitions in (4.31), (4.32) and (4.30), respectively; $k = \text{ceil}\left(\frac{N+1}{2}\right)$ is the index of the grid point at (or nearest to) the midpoint of the perovskite layer; and, $\hat{t}$ denotes the length of time since the previous time point. Note

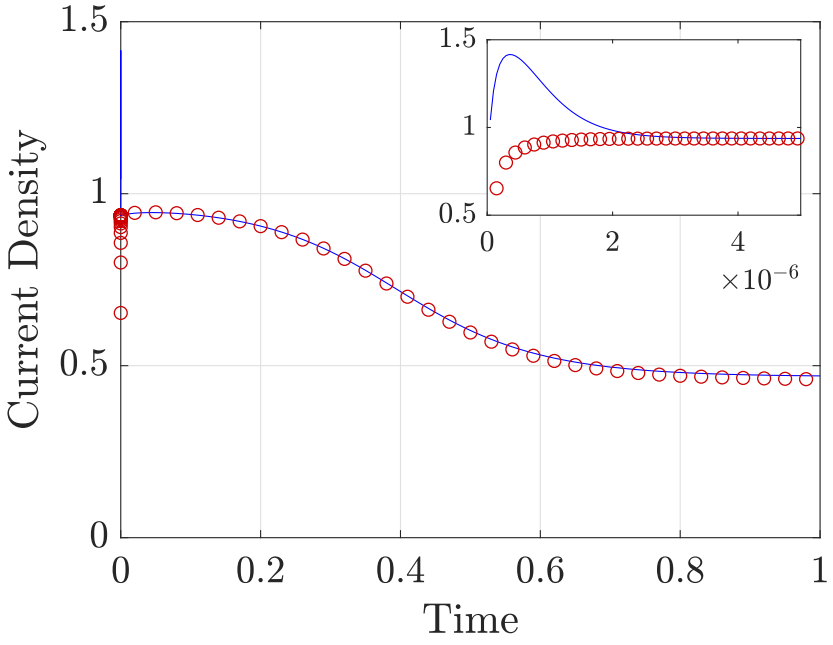

FIGURE 4.7: Current density as a function of time, in dimensionless units. Blue solid lines represent the full numerical solution and red circles represent the asymptotic result. Inset shows the extremely fast initial electronic transient which is not captured by the asymptotic solution. Reproduced from [35].

that both the displacement current density and the current density due to the ion vacancies (the third and fourth terms in (4.86), respectively) are usually very small compared to a typical value of the photo-current density of $O(10)$ mAcm^{-2}. In particular, the factor $\frac{\varepsilon_p V_T}{b\tau_{ion}} \approx 2.3 \times 10^{-7}$ mAcm^{-2} and the factor $\frac{qD_I N_0}{b} \approx 6.4 \times 10^{-5}$ mAcm^{-2} for the parameters in Table 3.2. Therefore, the total current density is, to a very good approximation, just given by the sum of the carrier current densities on the first line of (4.86).

4.6.2 A current decay transient

Here we simulate a cell that is preconditioned at $\Phi = \Phi_{bi} = 40$ for a sufficiently long time to eliminate transients, before undergoing a smooth but rapid decrease in applied bias from $\Phi = \Phi_{bi}$ at $t = 0$ to $\Phi = 0$ some short time later, obeying,

$$\Phi(t) = \Phi_{bi}\left(1 - \frac{\tanh(\beta t)}{\tanh(\beta t_{\text{end}})}\right) \quad \text{with} \quad \beta = 10^6\,, \quad t_{end} = 1\,. \tag{4.87}$$

For this simulation, we set the number of subintervals $N = 400$ and the temporal integration tolerances `RelTol` $= 10^{-6}$ and `AbsTol` $= 10^{-8}$.

A comparison between the photo-current calculated from the numerical solution and the asymptotic solution (as described in [34]) is made in Figure 4.7, showing remarkable

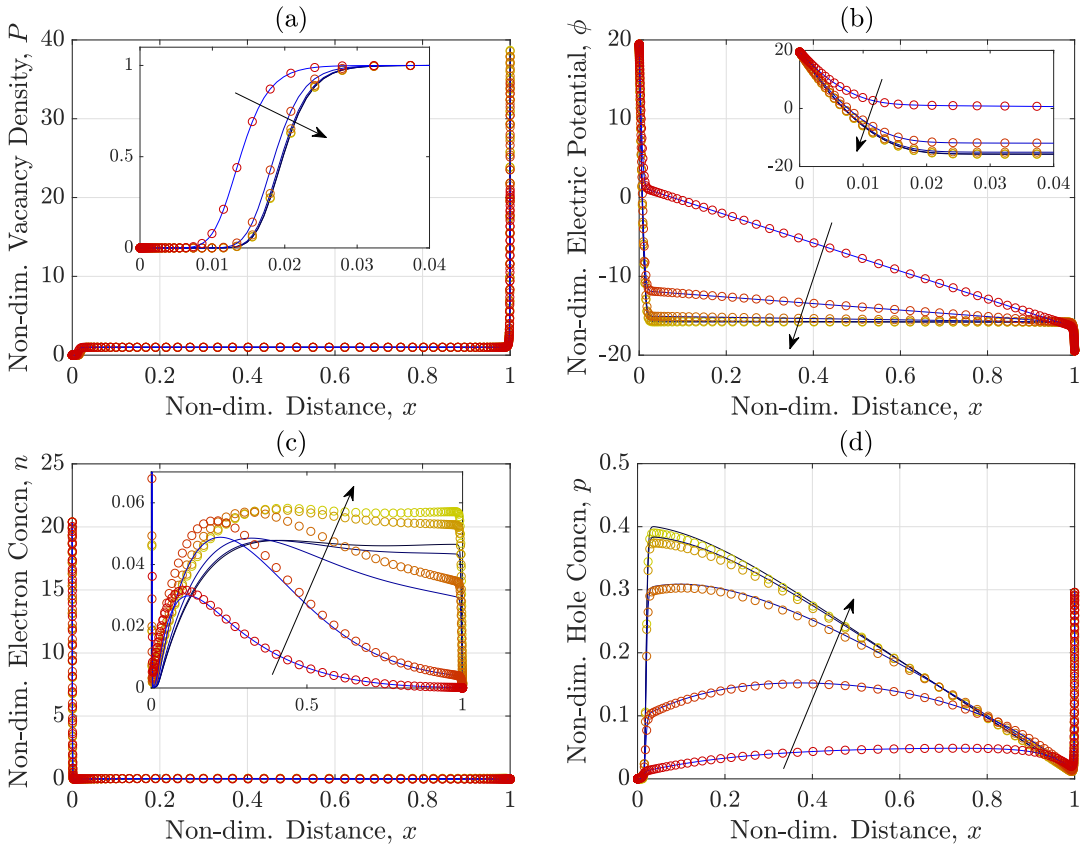

FIGURE 4.8: (a) Anion vacancy density, (b) electric potential, (c) electron concentration and (d) hole concentration profiles across the perovskite layer of a PSC at $t = 0.2, 0.4, 0.6, 0.8, 1$. Solid lines (blue to black for increasing time) represent the full numerical solutions and circles (red to yellow for increasing time) represent the uniformly-valid asymptotic expansions. Arrows indicate the direction of increasing time. Insets show magnified views of the distributions. Reproduced from [35].

agreement between the methods for all but very small times. The deviation in very short time behaviour is shown in the inset and represents a significant advantage of the numerical method over the asymptotic method. The numerical method is able fully capture the fast timescale transients associated with charge carrier motion. In contrast, the initial rise in current density is absent from the asymptotic solution. The ability of our numerical scheme to capture fast electronic transients is key for accurate simulation of many experimental protocols (such as time-of-flight measurements and high frequency impedance spectroscopy) and therefore crucial to the systematic investigation of certain properties of PSCs.

In Figure 4.8, we demonstrate good agreement between the numerical and asymptotic solutions, with the noticeable exception of panel (c) for the electron distribution in which the solutions vary in magnitude, but not shape. From a convergence check (increasing both spatial and temporal accuracy) and a check against an equivalent simulation using our finite difference scheme, it can be confirmed that the finite element scheme has indeed

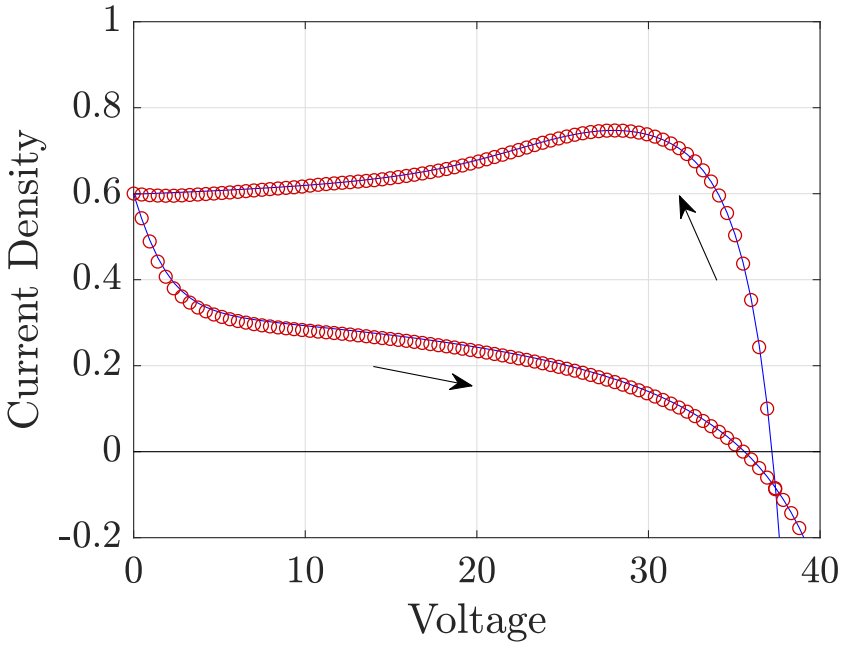

FIGURE 4.9: Current density as a function of applied voltage during the simulated 100 mV/s J-V scan, in dimensionless units. The blue line represents the full numerical solution and red circles represent the asymptotic approach. Arrows show the direction of the scan. Reproduced from [35].

converged. The discrepancy arises from a small $O(10^{-2})$ error in the asymptotic solution to the electric potential which in turn leads to the significant error in the asymptotic solution for electron density n, that can be seen in panel (c).

4.6.3 A current-voltage curve

Measurements of the current generated by a solar cell in response to a backwards and forwards sweep of the applied voltage are a common way of measuring cell properties and, in the case of PSCs, frequently result in significant sweep-rate dependent hysteresis [128, 143]. This hysteresis is a signature of the slow timescale ion motion in the cell. The standard experimental procedure for generating such a J-V hysteresis-curve, including a preconditioning step, is simulated as follows. The cell is preconditioned by increasing the applied voltage from the built-in voltage to 1.2 V (corresponding to $\Phi \approx 46.7$) over 5 seconds and held there for a further 5 seconds. Then the voltage is scanned smoothly from forward bias ($\Phi > \Phi_{bi}$) to short circuit ($\Phi = 0$) and back at a scan rate equivalent to 100 mV/s (corresponding to a rate of ≈ 7.1 in dimensionless units). This simulation was completed in approximately 6 seconds using our finite element scheme with $N = 400$ and `RelTol` = `AbsTol` $= 10^{-8}$. The resulting J-V curve is compared to the corresponding asymptotic solution from [34] in Figure 4.9. Once again excellent agreement between the

two approaches is observed.

4.7 Summary

In summary, two numerical schemes for solving a single-layer drift-diffusion model for a PSC, incorporating both ion vacancy motion and charge carrier transport, have been presented: one based on finite elements and the other based on finite differences. Both approaches use the method of lines to reduce the PDEs to a (large) system of ordinary DAEs with time as the independent variable. Even though the two methods are both capable of providing accurate solutions to the model in appropriate parameter regimes and use the same tool for temporal integration, the differences in their underlying spatial discretisations lead to some significant differences in their performance.

For realistic parameter values and in appropriate operating regimes, the model exhibits significant stiffness owing to (i) short Debye lengths that, in combination with large potential differences across the device, give rise to large and rapid changes in solution across the narrow Debye layers, and (ii) vastly different timescales for the transport of ion vacancies and electronic charge carriers. Both the finite element and finite difference schemes robustly cope with these difficulties by (a) using the adaptive timestep provided the `ode15s` MATLAB routine [91] and (b) utilising a non-uniform spatial grid to selectively concentrate grid points in the Debye layers in order to maintain accuracy without prohibitive computational cost. The choice of spatial grid proves to be a key ingredient for obtaining accurate solutions. We investigated two such grids, a Chebyshev grid and a tanh grid, both of which performed well in practice. Notably, computation in the relevant regime is not possible in a previously-used alternative, Chebfun, whose current version fails when realistic parameter values are taken.

The finite element approach presented in Section 4.3 distinguishes itself as the most apt when the speed of the two methods is benchmarked. We have shown that the finite element scheme not only outperforms the finite difference method, but also another well-known alternative in MATLAB's `pdepe`, taking around 50 times less computational effort (than either of the others) to achieve a given number of digits of accuracy. This speed increase is achieved even when `pdepe` is used together with the spatially non-uniform tanh grid proposed in this study. In particular, a typical experimental protocol for measuring a J-V curve can be simulated in only a few seconds on a standard personal computer. This tool therefore opens up the possibility to garner a deeper understanding of the principles that underpin the operation of PSCs.

To date, the finite element scheme described in Section 4.3 provides the fastest published

method [35] robust enough to furnish numerical solutions to a realistic charge transport model for a PSC. Although, Walter *et al.* [146] have also made significant progress in modelling the perovskite layer of a PSC, as shown by their recent publication that presents simulation results obtained using the Quokka3 solar cell simulator, originally developed to model silicon solar cells.

Further to the single-layer capabilities developed in this chapter, a complete description for the extension of the finite element discretisation to the full three-layer dimensionless model, outlined in Section 3.5.2, is included in the appendices in Section B.2. To allow the perovskite solar cell community to benefit from this latest advance in PSC modelling capabilities, it is the intention of the author to make the three-layer finite element code freely available online at `https://github.com/PerovskiteSCModelling/IonMaiden`, after the final submission of this thesis. However, as the finite element method was only developed towards the end of this project, it was not available for use in the following two chapters. For this work, a three-layer version of the (slower but still highly accurate) finite difference method is used to obtain numerical solutions. The extension of the finite difference scheme from the single- to the three-layer dimensionless model is also deferred to the appendices, see Section B.1.

Chapter 5

Asymptotic Analysis of the Charge Transport Model

In this chapter, an approximate approach is used to analyse the key mechanisms of ion migration and charge carrier transport that take place within a PSC. The use of an approximate approach is in contrast to that of the previous chapter, in which a high performance numerical method is developed to overcome the spatial and temporal stiffness intrinsic to the dimensionless charge transport model presented in Section 3.5.2. Here, the origins of the numerical stiffness, namely the extreme values of some of the dimensionless parameters, become advantageous properties that can be used to systematically approximate the system of PDEs using the method of matched asymptotic expansions. Such analysis can be used to garner a deeper understanding of the underlying mechanisms that cause J-V hysteresis and other anomalous transient behaviour exhibited by PSCs [40, 99, 109]. The validity of the approximate model is tested against numerical simulations of the full model in Section 5.5.

Asymptotic analysis has been used to study drift-diffusion models for a variety of solar cell applications. For example, in 1982, Please [103] presented an asymptotic analysis of a p-n junction. More recently, the technique has been used in the contexts of bipolar silicon devices [118], gallium arsenide solar cells [83], p-i-n heterojunctions (*i.e.* PSCs with no mobile ionic charge) [52] and organic solar cells [51, 110], including multidimensional models of bulk heterojunction solar cells [15, 111]. In the works of Foster *et al.* [51, 52] and Schmeiser & Unterreiter [118], the asymptotic derivations led to equivalent circuit models, which describe the characteristics of a device using a combination of ideal electrical components.

5.1 The asymptotic limits

The asymptotic approach taken in this chapter is a generalisation of the analysis of the single-layer model performed by Richardson for [99, 109], with full details presented in [34]. Good agreement between the asymptotic results and numerical solutions of the full single-layer model (stated in Section 4.2.2) has been demonstrated in Section 4.6 and in the work of Courtier *et al.* [34].

The key assumptions for the single-layer asymptotic derivation [34] are that:

- the TL materials are sufficiently highly doped that they may be considered to be "quasi-metals";
- the charge carrier concentrations are significantly smaller than the ion vacancy densities during relevant measurement protocols,
- the high density of mobile iodide ion vacancies corresponds to a short perovskite Debye length; and,
- the timescale of charge carrier transport is much faster than that of iodide ion vacancy migration.

Here, the asymptotic reduction of the single layer model, carried out in [34], is extended to the full three-layer model presented in Chapter 3 in order to properly account for the physical effects of the transport layers (TLs). For the three-layer asymptotic derivation, the first assumption is not used and, instead, the TLs are described by their material properties, namely their width, doping density, majority carrier diffusion coefficient, permittivity and Fermi level. The assumptions that are used are that:

- within the perovskite, the charge carrier concentrations are significantly smaller than the ion vacancy density during relevant measurement protocols (for illumination intensities up to 1 Sun), *i.e.* the ratio between the typical electron concentration and the mean ion vacancy density $\delta \ll 1$, while the ratio between the typical electron and hole concentrations $\chi = O(1)$;
- the high density of mobile iodide ion vacancies corresponds to a short ionic Debye length L_D compared to the width of the perovskite layer b, which leads to a small dimensionless Debye length $\lambda = L_D/b$ of $O(10^{-3})$;
- the high majority carrier concentrations in the TLs also correspond to short (electronic) Debye lengths, which similarly lead to small dimensionless ETL and HTL

Debye lengths (defined relative to the width of the perovskite layer) of λ_E, $\lambda_H = O(10^{-3})$; and,

- the timescales for equilibration of the charge carriers are much faster than that of ion vacancy migration, *i.e.* the ratios of the timescale of charge carrier transport in each layer relative to the timescale of ion vacancy motion ς, ς_E, $\varsigma_H \ll 1$.

In the single-layer derivation [34], it is shown that a good approximation of the electric potential can be found by neglecting the contributions of n and p in the perovskite to Poisson's equation. This approximation corresponds to the assumption that n, $p = O(\lambda^2)$ or smaller and leads to a model for the perovskite layer in which the equations for the ion vacancy density P and electric potential ϕ are decoupled from those for the charge carrier concentrations; the decoupled three-layer model is stated in full on the next page.

The following asymptotic reduction relies on the assumption that the charge carriers in the perovskite do not play a significant role in determining the electric potential. Thus, the electric potential is determined solely from the decoupled problem. Once the electric potential has been determined, a quasi-steady state BVP for the charge carrier distributions across the perovskite bulk remains to be solved, in which the potential appears as a known function. The solution of this problem allows the current density generated by the PSC to be calculated. The initial assumption that the charge carrier concentrations within the perovskite remain small throughout a realistic measurement protocol is verified once the asymptotic solution has been found; see Section 5.5.

To summarise, the following assumptions (which are consistent with the estimates given in Table 3.4) are made about the magnitudes of the dimensionless parameters of the model.

$$\delta \leq O(\lambda^2)\,, \quad \varsigma\,, \varsigma_E\,, \varsigma_H \leq O(\lambda)\,, \quad \kappa_E\,, \kappa_H \geq O(\lambda^{-1})\,, \quad \lambda_E\,, \lambda_H = O(\lambda)\,. \tag{5.1}$$

All other dimensionless parameters are assumed to be $O(1)$.

5.1.1 The decoupled dimensionless model

Due to the assumption that the contribution of the charge carrier concentrations to Poisson's equation for the perovskite layer (3.52) can be neglected, the equations for the electric potential ϕ and the iodide ion vacancies, with density P and flux F^P, decouple from those of the charge carrier concentrations within the perovskite layer. The decoupled model describing all three layers is as follows, in which $J(t)$ denotes the total current density generated by the PSC.

Perovskite Layer In $0 < x < 1$,

$$\frac{\partial P}{\partial t} + \lambda \frac{\partial F^P}{\partial x} = 0\,, \qquad F^P = -\left(\frac{\partial P}{\partial x} + P\frac{\partial \phi}{\partial x}\right), \tag{5.2}$$

$$\lambda^2 \frac{\partial^2 \phi}{\partial x^2} = 1 - P\,, \tag{5.3}$$

with boundary conditions on the ion vacancy flux,

$$F^P|_{x=0} = 0\,, \qquad F^P|_{x=1} = 0\,, \tag{5.4}$$

and continuity conditions on the electric potential,

$$\phi|_{x=0^-} = \phi|_{x=0^+} = \psi_a(t)\,, \qquad \phi|_{x=1^-} = \phi|_{x=1^+} = \psi_b(t)\,. \tag{5.5}$$

Here, the two functions of time, ψ_a and ψ_b, are introduced for clarity to denote the values of the electric potential at $x = 0$ (the ETL/perovskite interface) and $x = 1$ (the perovskite/HTL interface), respectively.

Electron transport layer In $-x_E < x < 0$,

$$\varsigma_E \frac{\partial n^E}{\partial t} - \frac{\partial j^n}{\partial x} = 0\,, \qquad j^n = \kappa_E\left(\frac{\partial n^E}{\partial x} - n^E\frac{\partial \phi}{\partial x}\right), \tag{5.6}$$

$$\lambda_E^2 \frac{\partial^2 \phi}{\partial x^2} = n^E - 1\,, \tag{5.7}$$

with the boundary conditions

$$n^E|_{x=-x_E} = 1\,, \quad \phi|_{x=-x_E} = \frac{\Phi_{bi} - \Phi}{2}\,, \quad j^n|_{x=-x_E} = J(t)\,, \quad r_E\frac{\partial \phi}{\partial x}\Big|_{x=0^-} = \frac{\partial \phi}{\partial x}\Big|_{x=0^+}. \tag{5.8}$$

Hole transport layer In $1 < x < 1 + x_H$,

$$\varsigma_H \frac{\partial p^H}{\partial t} + \frac{\partial j^p}{\partial x} = 0\,, \qquad j^p = -\kappa_H\left(\frac{\partial p^H}{\partial x} + p^H\frac{\partial \phi}{\partial x}\right), \tag{5.9}$$

$$\lambda_H^2 \frac{\partial^2 \phi}{\partial x^2} = 1 - p^H\,, \tag{5.10}$$

with the boundary conditions

$$j^p|_{x=1+x_H} = J(t)\,, \quad \frac{\partial \phi}{\partial x}\Big|_{x=1^-} = r_H\frac{\partial \phi}{\partial x}\Big|_{x=1^+}, \quad p^H|_{x=1+x_H} = 1\,, \quad \phi|_{x=1+x_H} = -\left(\frac{\Phi_{bi} - \Phi}{2}\right). \tag{5.11}$$

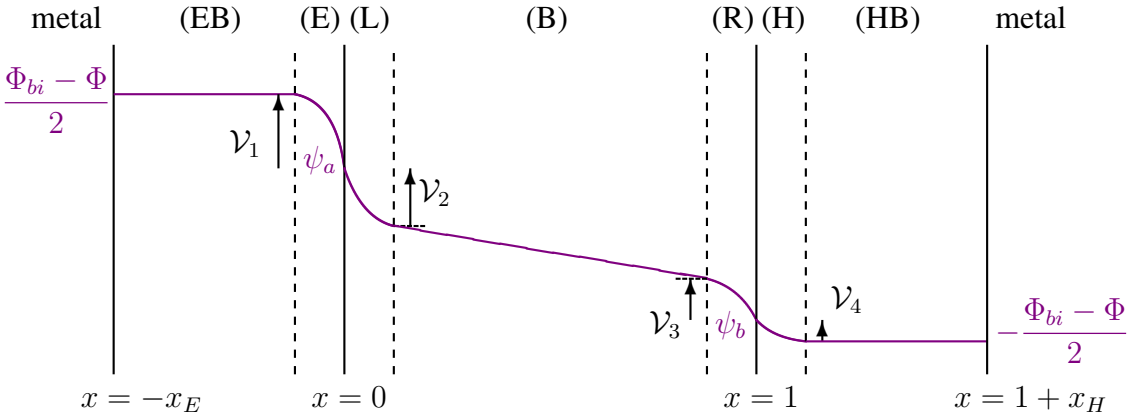

FIGURE 5.1: Diagram showing the 7 asymptotic regions: the ETL bulk, ETL Debye layer, left-hand perovskite Debye layer, perovskite bulk, right-hand perovskite Debye layer, HTL Debye layer and HTL bulk. The purple line shows an example solution for the electric potential ϕ with labels indicating the values at the material boundaries. The arrows illustrate the definitions of the potential differences $\mathcal{V}_1$, $\mathcal{V}_2$, $\mathcal{V}_3$ and $\mathcal{V}_4$.

5.1.2 Asymptotic boundary layers

As in the single layer model [34], it is found that the decoupled model (5.2)-(5.11) can be solved (approximately) with an asymptotic boundary layer analysis, performed in the limit $\lambda \to 0$. This analysis requires the solution to be subdivided into seven regions consisting of bulk (or outer) regions within each material layer, separated from the internal interfaces by four boundary layers, termed Debye layers, of width $O(\lambda)$. See Figure 5.1. The potential differences across the four Debye layers are denoted by $\mathcal{V}_1$, $\mathcal{V}_2$, $\mathcal{V}_3$ and $\mathcal{V}_4$.

In the next section, the method of matched asymptotic expansions is employed to find a uniformly-valid approximation for each variable in the decoupled model in terms of $\mathcal{V}_{1-4}$ and $J(t)$. The four as-yet-unknown functions of time $\mathcal{V}_{1-4}$ are then determined in Section 5.3 by considering the ionic charge density stored within each Debye layer.

To complete the analysis, in Section 5.4, the derived, uniformly-valid electric potential is substituted into the remaining quasi-steady BVP for the charge carrier concentrations within the perovskite layer in order to determine the photo-current density $J(t)$ generated by the PSC in terms of the ionic charge density stored within the Debye layers. In general, the distribution of holes and electrons within the perovskite layer must be found numerically, as described in Section 5.4.1. However, a particular choice of recombination rates that enables analytic analysis of the charge carrier concentrations is studied in Chapter 7.

5.2 Analysis of the decoupled model

This section details the asymptotic analysis of the decoupled dimensionless model (5.2)-(5.11) with the parameter value assumptions given in (5.1). The asymptotic regions in the perovskite layer are considered first, followed by those in the ETL and HTL.

5.2.1 Perovskite layer ($0 < x < 1$)

Bulk region (B). Away from the interfaces (*i.e.* for $x \gg \lambda$ and $1 - x \gg \lambda$), the perovskite layer variables P, F^P and ϕ can be expanded in powers of λ as follows.

$$P = P_0^{(\mathrm{B})} + \lambda P_1^{(\mathrm{B})} + \dots, \quad F^P = \mathcal{F}_0^{P(\mathrm{B})} + \lambda \mathcal{F}_1^{P(\mathrm{B})} \dots, \quad \phi = \phi_0^{(\mathrm{B})} + \lambda \phi_1^{(\mathrm{B})} \dots . \tag{5.12}$$

Hence, from Poisson's equation (5.3) and the conservation of iodide ion vacancies (5.2),

$$P_0^{(\mathrm{B})} = 1\,, \qquad P_1^{(\mathrm{B})} = 0\,, \qquad \mathcal{F}_0^{P(\mathrm{B})} = -\frac{\partial \phi_0^{(\mathrm{B})}}{\partial x}\,, \qquad \frac{\partial \mathcal{F}_0^{P(\mathrm{B})}}{\partial x} = 0\,. \tag{5.13}$$

Therefore

$$\frac{\partial^2 \phi_0^{(\mathrm{B})}}{\partial x^2} = -\frac{\partial \mathcal{F}_0^{P(\mathrm{B})}}{\partial x} = 0\,, \tag{5.14}$$

and so, at leading order, the electric potential is linear across the bulk of the perovskite, while the iodide ion vacancies are evenly distributed with a uniform flux, *i.e.*

$$\phi_0^{(\mathrm{B})} = \psi_L(1 - x) + \psi_R x\,, \qquad \mathcal{F}_0^{P(\mathrm{B})} = \psi_L - \psi_R\,, \tag{5.15}$$

where ψ_L and ψ_R denote the values of the electric potential at the left- and right-hand sides of the perovskite bulk, respectively. In terms of the notation used in Figure 5.1,

$$\psi_L = \psi_a - \mathcal{V}_2\,, \qquad \psi_R = \psi_b + \mathcal{V}_3\,. \tag{5.16}$$

Left-hand Debye layer (L). To obtain the asymptotic solution within this layer, space is rescaled using $x = \lambda z$ and the variables are expanded as follows.

$$P = P_0^{(\mathrm{L})} + \lambda P_1^{(\mathrm{L})} + \dots, \quad F^P = \mathcal{F}_0^{P(\mathrm{L})} + \lambda \mathcal{F}_1^{P(\mathrm{L})} + \dots, \quad \phi = \phi_0^{(\mathrm{L})} + \lambda \phi_1^{(\mathrm{L})} + \dots . \tag{5.17}$$

Substituting these asymptotic expansions into the rescaled versions of (5.2), (5.3), (5.4a) and (5.5a) gives, at leading order

$$\frac{\partial P_0^{(\mathrm{L})}}{\partial t} + \frac{\partial \mathcal{F}_0^{P(\mathrm{L})}}{\partial z} = 0\,, \qquad 0 = \frac{\partial P_0^{(\mathrm{L})}}{\partial z} + P_0^{(\mathrm{L})}\frac{\partial \phi_0^{(\mathrm{L})}}{\partial z}\,, \tag{5.18}$$

$$\frac{\partial^2 \phi_0^{(\mathrm{L})}}{\partial z^2} = 1 - P_0^{(\mathrm{L})}\,, \tag{5.19}$$

$$\text{with} \quad \mathcal{F}_0^{P(\mathrm{L})}|_{z=0} = 0\,, \qquad \phi_0^{(\mathrm{L})}|_{z=0} = \psi_a\,. \tag{5.20}$$

This problem is supplemented by a matching condition for each variable as $z \to \infty$. The first equation, (5.18a), leads to a solvability condition on the evolution of the charge density stored within the Debye layer, see Section 5.3. The second equation, (5.18b), can be integrated with respect to z to give the quasi-steady state solution for the leading order iodide ion vacancy density which, upon application of the matching condition $P_0^{(\mathrm{L})} \to 1$ as $\phi_0^{(\mathrm{L})} \to \psi_L$, is given by

$$P_0^{(\mathrm{L})} = \exp\left(\psi_L - \phi_0^{(\mathrm{L})}\right)\,. \tag{5.21}$$

Substituting this expression into the Poisson equation (5.19) gives a second-order equation for $\phi_0^{(\mathrm{L})}$ that is supplemented by a boundary condition at the interface and a far-field matching condition as follows.

$$\frac{\partial^2 \phi_0^{(\mathrm{L})}}{\partial z^2} = 1 - \exp\left(\psi_L - \phi_0^{(\mathrm{L})}\right)\,, \tag{5.22}$$

$$\text{with} \quad \phi_0^{(\mathrm{L})}|_{z=0} = \psi_a\,, \qquad \phi_0^{(\mathrm{L})} \to \psi_L \quad \text{as } z \to \infty\,. \tag{5.23}$$

By transforming from $\phi_0^{(\mathrm{L})}$ to $\theta = \phi_0^{(\mathrm{L})} - \psi_L$, the problem becomes

$$\frac{\partial^2 \theta}{\partial z^2} = 1 - \mathrm{e}^{-\theta}\,, \tag{5.24}$$

$$\text{with} \quad \theta|_{z=0} = \mathcal{V}_2\,, \qquad \theta \to 0 \quad \text{as } z \to \infty\,. \tag{5.25}$$

By multiplying (5.24) through by $\frac{\partial \theta}{\partial z}$, integrating and applying the far-field condition,

$$\frac{1}{2}\left(\frac{\partial \theta}{\partial z}\right)^2 = \mathrm{e}^{-\theta} + \theta - 1\,. \tag{5.26}$$

Assuming that the gradient of the electric potential is monotonic across the Debye layer, the sign of $\frac{\partial \theta}{\partial z}$ must take the opposite sign to the variable θ. Hence,

$$\frac{\partial z}{\partial \theta} = \frac{1}{\sqrt{2}}\,\mathrm{sign}(-\theta)\left(\mathrm{e}^{-\theta} + \theta - 1\right)^{-\frac{1}{2}}\,. \tag{5.27}$$

Integrating this equation with respect to θ and applying the boundary condition ($\theta|_{z=0} = \mathcal{V}_2$) leads to an implicit formula for $\theta(z;\mathcal{V}_2)$ given by

$$\begin{cases} z(\theta;\mathcal{V}_2) = \displaystyle\int_\theta^{\mathcal{V}_2} \frac{1}{\sqrt{2}}\,\mathrm{sign}(\Theta)\left(\mathrm{e}^{\Theta}+\Theta-1\right)^{-\frac{1}{2}}\,\mathrm{d}\Theta\,, \\ \qquad\qquad\qquad\qquad \text{for } 0<\theta\le\mathcal{V}_2\,, \text{ or for } \mathcal{V}_2\le\theta<0\,, \\ \text{otherwise,} \quad \theta(z;\mathcal{V}_2)=0\,. \end{cases} \tag{5.28}$$

Therefore, the leading-order electric potential and iodide ion vacancy distributions within the left-hand Debye layer are quasi-static and given in terms of $\mathcal{V}_2$ by

$$\phi_0^{(\mathrm{L})} = \theta\left(\frac{x}{\lambda};\mathcal{V}_2\right)+\psi_L\,, \qquad\qquad P_0^{(\mathrm{L})} = \exp\left[-\theta\left(\frac{x}{\lambda};\mathcal{V}_2\right)\right]\,. \tag{5.29}$$

The evolution of $\mathcal{V}_2$ depends on the flux of iodide ion vacancies into the Debye layer and is considered in Section 5.3.

Right-hand Debye layer (R). In order to derive corresponding results for the right-hand Debye layer, the spatial variable x is rescaled using $x = 1-\lambda\zeta$ and the dependent variables are similarly expanded in terms of λ. Substitution into (5.2), (5.3), (5.4b) and (5.5b) gives, at leading order

$$\frac{\partial P_0^{(\mathrm{R})}}{\partial t} - \frac{\partial \mathcal{F}_0^{P(\mathrm{R})}}{\partial\zeta} = 0\,, \qquad\qquad 0 = \frac{\partial P_0^{(\mathrm{R})}}{\partial\zeta} + P_0^{(\mathrm{R})}\frac{\partial\phi_0^{(\mathrm{R})}}{\partial\zeta}\,, \tag{5.30}$$

$$\frac{\partial^2\phi_0^{(\mathrm{R})}}{\partial\zeta^2} = 1-P_0^{(\mathrm{R})}\,, \tag{5.31}$$

$$\text{with} \quad \mathcal{F}_0^{P(\mathrm{R})}|_{\zeta=0} = 0\,, \qquad\qquad \phi_0^{(\mathrm{R})}|_{\zeta=0} = \psi_b\,. \tag{5.32}$$

The solution within the right-hand Debye layer can be found in an analogous way to that in the left-hand Debye layer. From (5.30b) and the matching condition $P_0^{(\mathrm{R})} \to 1$ as $\phi_0^{(\mathrm{R})} \to \psi_R$, it is found that the leading-order iodide ion vacancy density is given by

$$P_0^{(\mathrm{R})} = \exp\left(\psi_R - \phi_0^{(\mathrm{R})}\right)\,. \tag{5.33}$$

Then, from (5.31), the leading-order electric potential satisfies

$$\frac{\partial^2\phi_0^{(\mathrm{R})}}{\partial\zeta^2} = 1-\exp\left(\psi_R-\phi_0^{(\mathrm{R})}\right)\,, \tag{5.34}$$

$$\text{with} \quad \phi_0^{(\mathrm{R})}|_{\zeta=0} = \psi_b\,, \qquad \phi_0^{(\mathrm{R})} \to \psi_R \quad \text{as } \zeta\to\infty\,. \tag{5.35}$$

By transforming from $\phi_0^{(\mathrm{R})}$ to $\theta = \phi_0^{(\mathrm{R})} - \psi_R$, the problem becomes identical to (5.24)-(5.25) except that the potential difference $-\mathcal{V}_3$ takes the place of $\mathcal{V}_2$. Hence, the solution in the right-hand Debye layer can be expressed in terms of $\mathcal{V}_3$ and the implicit function θ as

$$\phi_0^{(\mathrm{R})} = \theta\left(\frac{1-x}{\lambda}; -\mathcal{V}_3\right) + \psi_R\,, \qquad P_0^{(\mathrm{R})} = \exp\left[-\theta\left(\frac{1-x}{\lambda}; -\mathcal{V}_3\right)\right]\,. \tag{5.36}$$

Matched asymptotic expansions for the perovskite layer. Uniformly-valid asymptotic expansions for the leading-order electric potential and iodide ion vacancy density within $0 < x < 1$, in terms of the four undetermined functions of time ψ_a, $\mathcal{V}_2$, $\mathcal{V}_3$, ψ_b, are found via matching across the perovskite Debye layer to be

$$\phi \sim (\psi_a - \mathcal{V}_2)(1-x) + (\psi_b + \mathcal{V}_3)x + \theta\left(\frac{x}{\lambda}; \mathcal{V}_2\right) + \theta\left(\frac{1-x}{\lambda}; -\mathcal{V}_3\right)\,, \tag{5.37}$$

$$P \sim \exp\left[-\theta\left(\frac{x}{\lambda}; \mathcal{V}_2\right)\right] + \exp\left[-\theta\left(\frac{1-x}{\lambda}; -\mathcal{V}_3\right)\right] - 1\,, \tag{5.38}$$

where, from (5.28), $\theta(z;\mathcal{V})$ is defined as the inverse of

$$\begin{cases} z(\theta;\mathcal{V}) = \displaystyle\int_\theta^{\mathcal{V}} \frac{1}{\sqrt{2}}\,\mathrm{sign}(\Theta)\left(\mathrm{e}^{-\Theta} + \Theta - 1\right)^{-\frac{1}{2}}\,\mathrm{d}\Theta\,, \\ \qquad\qquad\qquad\qquad \text{for } 0 < \theta \le \mathcal{V}\,, \text{ or for } \mathcal{V} \le \theta < 0\,, \\ \text{otherwise,} \quad \theta(z;\mathcal{V}) = 0\,. \end{cases} \tag{5.39}$$

5.2.2 Electron transport layer ($-x_E < x < 0$)

ETL bulk (EB). In this region, the electric potential, electron concentration and electron current density are expanded in terms of λ as follows.

$$\phi = \phi_0^{(\mathrm{EB})} + \lambda\phi_1^{(\mathrm{EB})} + \dots\,, \quad n^E = n_0^{(\mathrm{EB})} + \lambda n_1^{(\mathrm{EB})} + \dots\,, \quad j^n = j_0^{(\mathrm{EB})} + \lambda j_1^{(\mathrm{EB})} + \dots\,. \tag{5.40}$$

From (5.6)-(5.7), the leading-order variables are found to be constant in space and therefore equal to their value at the metal contact. Hence, using the boundary conditions (5.8a-c),

$$n_0^{(\mathrm{EB})} = 1\,, \qquad \phi_0^{(\mathrm{EB})} = \frac{\Phi_{bi} - \Phi}{2}\,, \qquad j_0^{(\mathrm{EB})} = J(t)\,, \tag{5.41}$$

As a result of the uniform electric potential across the region, a relationship is found between two as-yet-undetermined functions of time, namely the value of ϕ at $x = 0$,

denoted by ψ_a, and the potential difference $\mathcal{V}_1$, which is given by

$$\psi_a = \frac{\Phi_{bi} - \Phi}{2} - \mathcal{V}_1 \,. \tag{5.42}$$

ETL Debye layer (E). The variables are again expanded in terms of λ as follows.

$$\phi = \phi_0^{(\mathrm{E})} + \lambda\phi_1^{(\mathrm{E})} + \dots\,, \quad n^E = n_0^{(\mathrm{E})} + \lambda n_1^{(\mathrm{E})} + \dots\,, \quad j^n = j_0^{(\mathrm{E})} + \lambda j_1^{(\mathrm{E})} + \dots\,. \tag{5.43}$$

By rescaling the spatial variable using $x = -\lambda_E\eta$, recalling that $\lambda_E = O(\lambda)$ and using the relationship given in (5.42), the governing equations (5.6)-(5.7) and the continuity condition (5.5a) become

$$\frac{\partial j_0^{(\mathrm{E})}}{\partial \eta} = 0\,, \qquad\qquad 0 = \frac{\partial n_0^{(\mathrm{E})}}{\partial \eta} - n_0^{(\mathrm{E})}\frac{\partial \phi_0^{(\mathrm{E})}}{\partial \eta}\,, \tag{5.44}$$

$$\frac{\partial^2 \phi_0^{(\mathrm{E})}}{\partial \eta^2} = n_0^{(\mathrm{E})} - 1\,, \tag{5.45}$$

$$\text{with} \quad \phi_0^{(\mathrm{E})}|_{\eta=0} = \frac{\Phi_{bi} - \Phi}{2} - \mathcal{V}_1\,. \tag{5.46}$$

Hence, by integrating each of the equations in (5.44) and matching to the solutions in the ETL bulk given in (5.41), the leading-order electron concentration and current density are

$$n_0^{(\mathrm{E})} = \exp\left(\phi_0^{(\mathrm{E})} - \frac{\Phi_{bi} - \Phi}{2}\right)\,, \qquad\qquad j_0^{(\mathrm{E})} = J(t)\,. \tag{5.47}$$

By substituting this expression for $n_0^{(\mathrm{E})}$ into (5.45) and transforming the electric potential from $\phi_0^{(\mathrm{E})}$ to $\theta = \frac{\Phi_{bi}-\Phi}{2} - \phi_0^{(\mathrm{E})}$, (5.45)-(5.46) become identical to (5.24)-(5.25) except that $\mathcal{V}_1$ takes the place of $\mathcal{V}_2$. Therefore, in terms of the implicit function θ defined as the inverse of (5.39),

$$\phi_0^{(\mathrm{E})} \sim \frac{\Phi_{bi} - \Phi}{2} - \theta\left(-\frac{x}{\lambda_E}; \mathcal{V}_1\right)\,, \qquad n_0^{(\mathrm{E})} \sim \exp\left[-\theta\left(-\frac{x}{\lambda_E}; \mathcal{V}_1\right)\right]\,. \tag{5.48}$$

Matched asymptotic expansions for the ETL. The corresponding uniformly-valid asymptotic expansions for ϕ and n^E within $-x_E < x < 0$ are found to be

$$\phi \sim \frac{\Phi_{bi} - \Phi}{2} - \theta\left(-\frac{x}{\lambda_E}; \mathcal{V}_1\right)\,, \quad n^E \sim \exp\left[-\theta\left(-\frac{x}{\lambda_E}; \mathcal{V}_1\right)\right]\,, \quad j^n = J(t)\,. \tag{5.49}$$

5.2.3 Hole transport layer ($1 < x < 1 + x_H$)

HTL bulk (HB). Here, the electric potential, hole concentration and hole current density are expanded in terms of λ as follows.

$$\phi = \phi_0^{(\mathrm{HB})} + \lambda\phi_1^{(\mathrm{HB})} + \dots\,, \quad p^H = p_0^{(\mathrm{HB})} + \lambda p_1^{(\mathrm{HB})} + \dots\,, \quad j^p = j_0^{(\mathrm{HB})} + \lambda j_1^{(\mathrm{HB})} + \dots\,. \tag{5.50}$$

From (5.9)-(5.10), the leading-order variables are found to be constant in space and therefore, by applying the boundary conditions (5.11c-d,a),

$$p_0^{(\mathrm{HB})} = 1\,, \qquad \phi_0^{(\mathrm{HB})} = -\frac{\Phi_{bi} - \Phi}{2}\,, \qquad j_0^{(\mathrm{HB})} = J\,. \tag{5.51}$$

As a result, a relationship is found between two as-yet-undetermined functions of time, namely the value of ϕ at $x = 1$, denoted by ψ_b, and the potential difference $\mathcal{V}_4$, given by

$$\psi_b = -\frac{\Phi_{bi} - \Phi}{2} + \mathcal{V}_4\,. \tag{5.52}$$

HTL Debye layer (H). The variables are again expanded in terms of λ as follows.

$$\phi = \phi_0^{(\mathrm{H})} + \lambda\phi_1^{(\mathrm{H})} + \dots\,, \quad p^H = p_0^{(\mathrm{H})} + \lambda p_1^{(\mathrm{H})} + \dots\,, \quad j^p = j_0^{(\mathrm{H})} + \lambda j_1^{(\mathrm{H})} + \dots\,. \tag{5.53}$$

The problem for the HTL Debye layer is equivalent to the problem for the left-hand Debye layer, with the leading-order hole concentration $p_0^{(\mathrm{H})}$ taking the place of the leading-order ion vacancy density $P_0^{(\mathrm{R})}$ and the potential difference $\mathcal{V}_4$ replacing $\mathcal{V}_2$. Hence, calculations equivalent to those for the right-hand Debye layer, combined with matching to the bulk solutions in (5.51), lead to the following solutions.

$$\phi_0^{(\mathrm{H})} \sim -\frac{\Phi_{bi} - \Phi}{2} + \theta\left(\frac{x-1}{\lambda_H}; \mathcal{V}_4\right)\,, \quad p_0^{(\mathrm{H})} \sim \exp\left[-\theta\left(\frac{x-1}{\lambda_H}; \mathcal{V}_4\right)\right]\,, \quad j_0^{(\mathrm{H})} = J(t)\,. \tag{5.54}$$

Matched asymptotic expansions for the HTL. The corresponding leading-order uniformly-valid asymptotic expansions within $1 < x < 1 + x_H$ are

$$\phi \sim -\frac{\Phi_{bi} - \Phi}{2} + \theta\left(\frac{x-1}{\lambda_H}; \mathcal{V}_4\right)\,, \quad p^H \sim \exp\left[-\theta\left(\frac{x-1}{\lambda_H}; \mathcal{V}_4\right)\right]\,, \quad j^p = J(t)\,. \tag{5.55}$$

5.2.4 Summary

Uniformly-valid approximations for the electric potential (ϕ) and the majority species of mobile charge in each of the three layers of a PSC (n^E, P, p^H) have been derived from the decoupled model (5.2)-(5.11). The expressions depend on the as-yet-undetermined potential differences $\mathcal{V}_{1-4}$, the total current density $J(t)$ and the implicit function $\theta(\cdot\,;\mathcal{V})$, which is defined as the inverse of (5.39).

Substituting (5.42) and (5.52) into (5.37) gives

$$\phi \sim \left(\frac{\Phi_{bi}-\Phi}{2} - \mathcal{V}_1 - \mathcal{V}_2\right)(1-x) + \left(-\frac{\Phi_{bi}-\Phi}{2} + \mathcal{V}_4 + \mathcal{V}_3\right)x + \theta\left(\frac{x}{\lambda};\mathcal{V}_2\right) + \theta\left(\frac{1-x}{\lambda};-\mathcal{V}_3\right). \tag{5.56}$$

In the perovskite layer ($0 < x < 1$),

$$P \sim \exp\left[-\theta\left(\frac{x}{\lambda};\mathcal{V}_2\right)\right] + \exp\left[-\theta\left(\frac{1-x}{\lambda};-\mathcal{V}_3\right)\right] - 1\,. \tag{5.38 repeated}$$

In the ETL ($-x_E < x < 0$),

$$\phi \sim \frac{\Phi_{bi}-\Phi}{2} - \theta\left(-\frac{x}{\lambda_E};\mathcal{V}_1\right), \quad n^E \sim \exp\left[-\theta\left(-\frac{x}{\lambda_E};\mathcal{V}_1\right)\right], \quad j^n = J(t)\,. \tag{5.49 repeated}$$

In the HTL ($1 < x < 1 + x_H$),

$$\phi \sim -\frac{\Phi_{bi}-\Phi}{2} + \theta\left(\frac{x-1}{\lambda_H};\mathcal{V}_4\right), \quad p^H \sim \exp\left[-\theta\left(\frac{x-1}{\lambda_H};\mathcal{V}_4\right)\right], \quad j^p = J(t)\,. \tag{5.55 repeated}$$

In addition, it is known that the iodide ion vacancy flux F^P is uniform across the perovskite bulk. From substitution of (5.16), (5.42) and (5.52) into (5.15b), the leading-order ion vacancy flux F^P in the perovskite bulk is determined as

$$\mathcal{F}_0^{P(\mathrm{B})} = \Phi_{bi} - \Phi - \mathcal{V}_1 - \mathcal{V}_2 - \mathcal{V}_3 - \mathcal{V}_4\,. \tag{5.57}$$

The leading-order equation for the ion vacancy flux in the left-hand Debye layer given in (5.18a) (or, equivalently, its counterpart in the right-hand Debye layer) is considered in the next section.

5.3 Evolution of the charge density stored within the Debye layers

In order to determine a uniformly-valid approximation for the electric potential that is consistent across all three layers of the model, the remaining governing equations and continuity conditions must be imposed on the asymptotic approximations for the electric potential ϕ across the ETL, perovskite layer and HTL, given separately in (5.49a), (5.37) and (5.55a), respectively. Following the work of [34], this is achieved by considering the relationship between the charge density stored with the Debye layers and the potential differences across them ($\mathcal{V}_{1-4}$).

Debye layer charge densities. The leading-order ionic charge density $\mathcal{Q}^{(\mathrm{L})}$ stored within the left-hand Debye layer is defined in terms of the rescaled spatial variable $z = x/\lambda$ by

$$\mathcal{Q}^{(\mathrm{L})} = \int_0^\infty \left(P_0^{(\mathrm{L})} - 1 \right) \, \mathrm{d}z \, . \tag{5.58}$$

Transforming from $P_0^{(\mathrm{L})}$ to the shifted potential $\theta = \phi_0^{(\mathrm{L})} - \psi_L$ using (5.29b) gives

$$\mathcal{Q}^{(\mathrm{L})} = \int_0^\infty \left(\mathrm{e}^{-\theta} - 1 \right) \, \mathrm{d}z \, . \tag{5.59}$$

Here, for clarity, let the function $M(\theta)$ be defined as

$$M(\theta) = \mathrm{e}^{-\theta} + \theta - 1 \, , \tag{5.60}$$

so that, from (5.25) and (5.27),

$$\mathcal{Q}^{(\mathrm{L})} = \int_0^{\mathcal{V}_2} \frac{\mathrm{d}M}{\mathrm{d}\theta} \cdot \frac{1}{\sqrt{2}} \, \mathrm{sign}(-\theta) M^{-\frac{1}{2}} \, \mathrm{d}\theta \, . \tag{5.61}$$

Hence, the charge density $\mathcal{Q}^{(\mathrm{L})}$ is related to the potential difference $\mathcal{V}_2$ via

$$\mathcal{Q}^{(\mathrm{L})} = \, \mathrm{sign}(-\mathcal{V}_2) \sqrt{2} \left(\mathrm{e}^{-\mathcal{V}_2} + \mathcal{V}_2 - 1 \right)^{\frac{1}{2}} \, . \tag{5.62}$$

A similar calculation for the right-hand Debye layer yields that the leading-order ionic charge density $\mathcal{Q}^{(\mathrm{R})}$ is related to the potential difference $\mathcal{V}_3$ as follows.

$$\mathcal{Q}^{(\mathrm{R})} = \, \mathrm{sign}(\mathcal{V}_3) \sqrt{2} \left(\mathrm{e}^{\mathcal{V}_3} - \mathcal{V}_3 - 1 \right)^{\frac{1}{2}} \, . \tag{5.63}$$

Hence, the relationships between the charge density and the potential difference for each

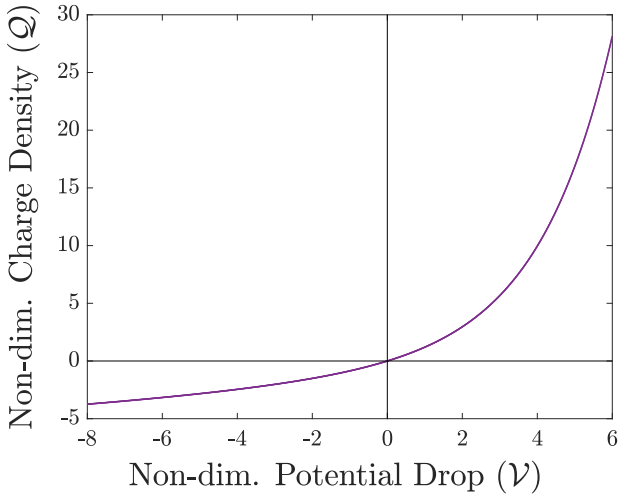

FIGURE 5.2: The non-linear capacitance relation for the right-hand perovskite Debye layer, as given by (5.65) and reproduced from [34].

of the perovskite Debye layers are given by

$$\mathcal{Q}^{(\mathrm{L})} = Q(-\mathcal{V}_2)\,, \qquad\qquad \mathcal{Q}^{(\mathrm{R})} = Q(\mathcal{V}_3)\,, \tag{5.64}$$

where the function $Q(\mathcal{V})$ has been defined as follows and plotted in Figure 5.2.

$$Q(\mathcal{V}) = \ \mathrm{sign}(\mathcal{V})\sqrt{2}\left(\mathrm{e}^{\mathcal{V}} - \mathcal{V} - 1\right)^{\frac{1}{2}}\ . \tag{5.65}$$

An analogous definition for the leading-order charge density stored within the ETL Debye layer in terms of the local variable η is given by

$$\mathcal{Q}^{(\mathrm{E})} = \int_0^\infty \left(1 - n_0^{(\mathrm{E})}\right)\,\mathrm{d}\eta\,. \tag{5.66}$$

Hence, transforming to the shifted potential $\theta = \frac{\Phi_{bi}-\Phi}{2} - \phi_0^{(\mathrm{E})}$ using (5.48b) gives

$$\mathcal{Q}^{(\mathrm{E})} = \int_0^\infty \left(1 - \mathrm{e}^{-\theta}\right)\,\mathrm{d}\eta\,. \tag{5.67}$$

Proceeding as before with the use of the function $M(\theta)$ from (5.60) yields

$$\mathcal{Q}^{(\mathrm{E})} = -Q(-\mathcal{V}_1)\,. \tag{5.68}$$

Similarly, the leading-order charge density stored within the HTL Debye layer is given by

$$\mathcal{Q}^{(\mathrm{H})} = Q(-\mathcal{V}_4)\,. \tag{5.69}$$

Continuity of the displacement field across the interfaces. In order to apply the continuity condition on the gradient of the potential at $x = 0$, it is useful to first note that, from integrating the definition of $\mathcal{Q}^{(\mathrm{L})}$ in (5.58) using (5.19), and from integrating the definition of $\mathcal{Q}^{(\mathrm{E})}$ in (5.66) using (5.45),

$$\mathcal{Q}^{(\mathrm{L})} = \lambda \frac{\partial \phi_0^{(\mathrm{L})}}{\partial x}\Big|_{x=0^+}, \qquad \mathcal{Q}^{(\mathrm{E})} = -\lambda_E \frac{\partial \phi_0^{(\mathrm{E})}}{\partial x}\Big|_{x=0^-}. \tag{5.70}$$

Therefore, the continuity condition (5.8d) can be rewritten as

$$\mathcal{Q}^{(\mathrm{E})} = -\Omega_E \mathcal{Q}^{(\mathrm{L})}, \tag{5.71}$$

where the parameter $\Omega_E = \frac{\lambda_E}{r_E \lambda} = \sqrt{\frac{\varepsilon_p N_0}{\varepsilon_E d_E}}$. In physical terms, this condition ensures that the (dimensional) charge densities either side of the ETL/perovskite interface are equal and opposite.

Similarly, the continuity condition on the gradient of the potential at $x = 1$ (5.11b) requires that the charge densities either side of the perovskite/HTL interface are related by

$$\mathcal{Q}^{(\mathrm{H})} = -\Omega_H \mathcal{Q}^{(\mathrm{R})}, \tag{5.72}$$

where $\Omega_H = \frac{\lambda_H}{r_H \lambda} = \sqrt{\frac{\varepsilon_p N_0}{\varepsilon_H d_H}}$.

Conservation of charge in the perovskite. The conservation of iodide ion vacancies within (and restricted to) the perovskite layer requires that the two perovskite Debye layers also contain equal and opposite charge, *i.e.* that

$$\mathcal{Q}^{(\mathrm{L})} = -\mathcal{Q}^{(\mathrm{R})}. \tag{5.73}$$

Hence, all four of the Debye layer charge densities can be written in terms of one charge density $\mathcal{Q}$, chosen here to equal the charge density $\mathcal{Q}^{(\mathrm{R})}$ stored within the right-hand perovskite Debye layer. So, from (5.71) and (5.72),

$$\mathcal{Q}^{(\mathrm{E})} = \Omega_E \mathcal{Q}, \qquad \mathcal{Q}^{(\mathrm{L})} = -\mathcal{Q}, \qquad \mathcal{Q}^{(\mathrm{R})} = \mathcal{Q}, \qquad \mathcal{Q}^{(\mathrm{H})} = -\Omega_H \mathcal{Q}. \tag{5.74}$$

Hence, from (5.64), (5.68) and (5.69), the potential difference across each of the four Debye layers can be given in terms of the single charge density $\mathcal{Q}$ as follows.

$$\mathcal{V}_1 = -\mathcal{V}(-\Omega_E \mathcal{Q}), \quad \mathcal{V}_2 = -\mathcal{V}(-\mathcal{Q}), \quad \mathcal{V}_3 = \mathcal{V}(\mathcal{Q}), \quad \mathcal{V}_4 = -\mathcal{V}(-\Omega_H \mathcal{Q}), \tag{5.75}$$

where $\mathcal{V}(Q)$ is defined as the inverse of $Q(\mathcal{V})$, defined in (5.65) and plotted in Figure 5.2. As expected, the four potential differences take the same sign at any given time. From these expressions, it can be seen that the dimensionless parameters Ω_E and Ω_H play a key role in determining the relative sizes of the potential differences $\mathcal{V}_{1-4}$ and therefore the distribution of the electric field across the three layers of a PSC. The effects of different values for Ω_E and Ω_H on the distribution of the electric field and hence the performance of a PSC are investigated in the next chapter.

Evolution of the charge density $\mathcal{Q}$. Here, the evolution of the charge density $\mathcal{Q}$ is determined from the relationship between the ion vacancy density and flux in the left-hand Debye layer, given in (5.18a). The rate of change in $\mathcal{Q}$ is given, using (5.74b) and the definition of $\mathcal{Q}^{(\mathrm{L})}$ from (5.58), by

$$\frac{\mathrm{d}\mathcal{Q}}{\mathrm{d}t} = -\int_0^\infty \frac{\partial P_0^{(\mathrm{L})}}{\partial t}\,\mathrm{d}z\,. \tag{5.76}$$

Using the rescaled governing equation (5.18a), this becomes

$$\frac{\mathrm{d}\mathcal{Q}}{\mathrm{d}t} = \int_0^\infty \frac{\partial \mathcal{F}_0^{P(\mathrm{L})}}{\partial z}\,\mathrm{d}z\,. \tag{5.77}$$

Integrating the right-hand side, applying the no-flux boundary condition for $\mathcal{F}_0^{P(\mathrm{L})}$ at $z = 0$ from (5.20a) and matching with the expression for $\mathcal{F}_0^{P(\mathrm{B})}$ in the bulk given in (5.15b) yields

$$\frac{\mathrm{d}\mathcal{Q}}{\mathrm{d}t} = \psi_L - \psi_R\,. \tag{5.78}$$

In physical terms, for the left-hand perovskite Debye layer, this equation states that the rate of change of the total charge density within the layer equals the flux of (positively charged) iodide ion vacancies flowing in from the bulk region. On eliminating ψ_L and ψ_R via (5.16), combined with (5.42) and (5.52), this becomes

$$\frac{\mathrm{d}\mathcal{Q}}{\mathrm{d}t} = \Phi_{bi} - \Phi - \mathcal{V}_1 - \mathcal{V}_2 - \mathcal{V}_3 - \mathcal{V}_4\,. \tag{5.79}$$

As a result, the evolution of the charge density $\mathcal{Q}$ (and, via (5.74), the charge densities stored within all four Debye layers) is described by the following ODE.

$$\frac{\mathrm{d}\mathcal{Q}}{\mathrm{d}t} = \Phi_{bi} - \Phi + \mathcal{V}(-\Omega_E\mathcal{Q}) + \mathcal{V}(-\mathcal{Q}) - \mathcal{V}(\mathcal{Q}) + \mathcal{V}(-\Omega_H\mathcal{Q})\,, \tag{5.80}$$

in which the function $\mathcal{V}(Q)$ is defined as the inverse of $Q(\mathcal{V})$, defined in (5.65) and plotted in Figure 5.2. The solution to this ODE can be obtained numerically, when supplemented

by a suitable initial condition, such as $\mathcal{Q}|_{t=0} = 0$. The reduced model, in which the evolution of the charge distribution within a PSC is described by the ODE in (5.80), is here termed the surface polarisation model.

5.4 Determination of the generated current density

In this section, the asymptotic boundary layer analysis performed in the previous section for the decoupled model (5.2)-(5.11) is extended to the governing equations for the charge carrier concentrations within the perovskite layer from Section 3.5.2. The asymptotic regions are sketched in Figure 5.1. The following analysis leads to a second-order BVP for the electron and hole concentrations with the bulk region of the perovskite layer. The total current density $J(t)$ generated by the PSC can be calculated from numerical solution of this BVP for any given photo-generation and recombination rates (G and R). In Section 5.5, solutions using this combined asymptotic/numeric approach (previously used for the single-layer model in [34]) are compared to numerical solutions of the fully coupled charge transport model.

5.4.1 Charge carrier distributions in the perovskite layer

From Section 3.5.2, the equations for the conservation of charge carriers within the perovskite layer are as follows.

$$\varsigma\frac{\partial n}{\partial t} - \frac{\partial j^n}{\partial x} = G - R(n,p)\,, \qquad j^n = \kappa_n\left(\frac{\partial n}{\partial x} - n\frac{\partial \phi}{\partial x}\right)\,, \tag{3.49 repeated}$$

$$\chi\varsigma\frac{\partial p}{\partial t} + \frac{\partial j^p}{\partial x} = G - R(n,p)\,, \qquad j^p = -\kappa_p\left(\frac{\partial p}{\partial x} + p\frac{\partial \phi}{\partial x}\right)\,. \tag{3.50 repeated}$$

These equations require the application of four boundary conditions. Boundary conditions on each of the charge carrier current densities are given in (3.53a,c). Another two boundary conditions can be determined via substitution of the uniformly-valid approximations for the majority carrier concentration in the TLs, from (5.49) and (5.55), into the continuity conditions (3.61a) and (3.63a) on the ETL/perovskite and perovskite/HTL interfaces, respectively. The boundary conditions are therefore

$$n|_{x=0} = \mathrm{e}^{-\mathcal{V}_1}\,, \qquad j^p|_{x=0} = -R_l\,, \tag{5.81}$$

$$p|_{x=1} = \mathrm{e}^{-\mathcal{V}_4}\,, \qquad j^n|_{x=1} = -R_r\,. \tag{5.82}$$

In addition, two more boundary conditions (dependent on the as-yet-unknown current density $J(t)$) can be determined from, firstly, the continuity condition (3.61b) and the value of the leading-order electron current density within the ETL from (5.49c) and, secondly, the continuity condition (3.63b) and the value of the leading-order hole current density within the HTL from (5.55c). These additional conditions are

$$j^n|_{x=0} = J + R_l\,, \qquad\qquad j^p|_{x=1} = J + R_r\,. \tag{5.83}$$

Left-hand Debye layer (L). Following the same approach as before, space is scaled using $x = \lambda z$ and the variables are expanded in terms of λ as follows.

$$n = n_0^{(\mathrm{L})} + \dots\,, \qquad j^n = j_0^{n(\mathrm{L})} + \dots\,, \qquad p = p_0^{(\mathrm{L})} + \dots\,, \qquad j^p = j_0^{p(\mathrm{L})} + \dots\,. \tag{5.84}$$

From (3.49)-(3.50), (5.81) and (5.83a), the rescaled governing equations and boundary conditions are

$$\frac{\partial j_0^{n(\mathrm{L})}}{\partial z} = 0\,, \qquad\qquad 0 = \frac{\partial n_0^{(\mathrm{L})}}{\partial z} - n_0^{(\mathrm{L})}\frac{\partial \phi_0^{(\mathrm{L})}}{\partial z}\,, \tag{5.85}$$

$$\frac{\partial j_0^{p(\mathrm{L})}}{\partial z} = 0\,, \qquad\qquad 0 = \frac{\partial p_0^{(\mathrm{L})}}{\partial z} + p_0^{(\mathrm{L})}\frac{\partial \phi_0^{(\mathrm{L})}}{\partial z}\,, \tag{5.86}$$

$$\text{with} \quad n_0^{(\mathrm{L})}|_{z=0} = \mathrm{e}^{-\mathcal{V}_1}\,, \qquad j_0^{p(\mathrm{L})}|_{z=0} = -R_l\,, \qquad j_0^{n(\mathrm{L})}|_{z=0} = J + R_l\,. \tag{5.87}$$

From (5.85b) and (5.86b), it is found that the leading-order charge carrier concentrations are Boltzmann-distributed. In particular, by applying (5.87a), the leading-order electron concentration is

$$n_0^{(\mathrm{L})} = \exp\left(\phi_0^{(\mathrm{L})} - \frac{\Phi_{bi} - \Phi}{2}\right)\,. \tag{5.88}$$

From (5.85a) and (5.86a), it is found that the current densities are uniform across the Debye layer and so, from (5.87b-c),

$$j_0^{p(\mathrm{L})} = -R_l\,, \qquad\qquad j_0^{n(\mathrm{L})} = J + R_l\,. \tag{5.89}$$

Right-hand Debye layer (R). As before, in this region, space is rescaled via $x = 1 - \lambda\zeta$ and variables are expanded in terms of λ.

$$n = n_0^{(\mathrm{R})} + \dots\,, \qquad j^n = j_0^{n(\mathrm{R})} + \dots\,, \qquad p = p_0^{(\mathrm{R})} + \dots\,, \qquad j^p = j_0^{p(\mathrm{R})} + \dots\,. \tag{5.90}$$

From (3.49)-(3.50), (5.82) and (5.83b), the rescaled governing equations and boundary conditions are

$$\frac{\partial j_0^{n(\mathrm{R})}}{\partial \zeta} = 0\,, \qquad 0 = \frac{\partial n_0^{(\mathrm{R})}}{\partial \zeta} - n_0^{(\mathrm{R})}\frac{\partial \phi_0^{(\mathrm{R})}}{\partial \zeta}\,, \tag{5.91}$$

$$\frac{\partial j_0^{p(\mathrm{R})}}{\partial \zeta} = 0\,, \qquad 0 = \frac{\partial p_0^{(\mathrm{R})}}{\partial \zeta} + p_0^{(\mathrm{R})}\frac{\partial \phi_0^{(\mathrm{R})}}{\partial \zeta}\,, \tag{5.92}$$

$$\text{with} \quad p_0^{(\mathrm{L})}|_{\zeta=0} = \mathrm{e}^{-\mathcal{V}_4}\,, \qquad j_0^{n(\mathrm{R})}|_{\zeta=0} = -R_r\,, \qquad j_0^{p(\mathrm{R})}|_{\zeta=0} = J + R_r\,. \tag{5.93}$$

As for the right-hand Debye layer, these rescaled equations yield that the leading-order charge carrier concentrations are Boltzmann-distributed and current densities are constant in space. In particular,

$$p_0^{(\mathrm{R})} = \exp\left(-\phi_0^{(\mathrm{R})} - \frac{\Phi_{bi} - \Phi}{2}\right)\,, \qquad j_0^{n(\mathrm{R})} = -R_r\,, \qquad j_0^{p(\mathrm{R})} = J + R_r\,. \tag{5.94}$$

Bulk region (B). The charge carrier concentrations in the perovskite layer are again expanded in terms of λ.

$$n = n_0^{(\mathrm{B})} + \dots\,, \qquad j^n = j_0^{n(\mathrm{B})} + \dots\,, \qquad p = p_0^{(\mathrm{B})} + \dots\,, \qquad j^p = j_0^{p(\mathrm{B})} + \dots\,. \tag{5.95}$$

From (5.56), the leading-order bulk electric potential (E_0) is given by

$$E_0 = -\frac{\partial \phi_0^{(\mathrm{B})}}{\partial x} = \Phi_{bi} - \Phi - \mathcal{V}_1 - \mathcal{V}_2 - \mathcal{V}_3 - \mathcal{V}_4\,. \tag{5.96}$$

Hence, at leading order, the governing equations (3.49) and (3.50) become

$$-\frac{\partial j_0^{n(\mathrm{B})}}{\partial x} = G - R(n_0^{(\mathrm{B})}, p_0^{(\mathrm{B})})\,, \qquad j_0^{n(\mathrm{B})} = \kappa_n\left(\frac{\partial n_0^{(\mathrm{B})}}{\partial x} + n_0^{(\mathrm{B})}E_0\right)\,, \tag{5.97}$$

$$\frac{\partial j_0^{p(\mathrm{B})}}{\partial x} = G - R(n_0^{(\mathrm{B})}, p_0^{(\mathrm{B})})\,, \qquad j_0^{p(\mathrm{B})} = -\kappa_p\left(\frac{\partial p_0^{(\mathrm{B})}}{\partial x} - p_0^{(\mathrm{B})}E_0\right)\,, \tag{5.98}$$

subject to the following matching conditions determined from the Debye layer analysis.

$$n_0^{(\mathrm{B})} \to \exp\left(-\mathcal{V}_1 - \mathcal{V}_2\right)\,, \qquad j_0^{p(\mathrm{B})} \to -R_l\,, \qquad \text{as } x \to 0\,, \tag{5.99}$$

$$p_0^{(\mathrm{B})} \to \exp\left(-\mathcal{V}_3 - \mathcal{V}_4\right)\,, \qquad j_0^{n(\mathrm{B})} \to -R_r\,, \qquad \text{as } x \to 1\,, \tag{5.100}$$

For non-linear recombination rates, the leading-order bulk variables $n_0^{(\mathrm{B})}$ and $p_0^{(\mathrm{B})}$ at a particular time must be obtained from numerical solution of the quasi-steady state BVP described by (5.97)-(5.100) upon extrapolating the matching conditions to the bound-

aries. The interface recombination rates, from (3.66), can be reformulated in terms of the bulk variables using the following relations.

$$R_l(n|_{x=0^+},\, p|_{x=0^+}) = R_l(\mathrm{e}^{-\mathcal{V}_1},\, p_0^{(\mathrm{B})}|_{x\to 0}\mathrm{e}^{-\mathcal{V}_2})\,, \tag{5.101}$$

$$R_r(n|_{x=1^-},\, p|_{x=1^-}) = R_r(n_0^{(\mathrm{B})}|_{x\to 1}\mathrm{e}^{-\mathcal{V}_3},\, \mathrm{e}^{-\mathcal{V}_4})\,. \tag{5.102}$$

Uniformly-valid charge carrier distributions. The preceding analysis yields the following uniformly-valid approximations for the electron and hole concentrations within the perovskite layer ($0 < x < 1$).

$$\begin{aligned} p \sim p_0^{(\mathrm{B})} + p_0^{(\mathrm{B})}|_{x\to 0} \left[\exp\left(-\theta\left(\frac{x}{\lambda};\mathcal{V}_2\right)\right) - 1\right] \\ + \mathrm{e}^{-\mathcal{V}_3-\mathcal{V}_4}\left[\exp\left(-\theta\left(\frac{1-x}{\lambda};-\mathcal{V}_3\right)\right) - 1\right]\,, \end{aligned} \tag{5.103}$$

$$\begin{aligned} n \sim n_0^{(\mathrm{B})} + \mathrm{e}^{-\mathcal{V}_1-\mathcal{V}_2}\left[\exp\left(\theta\left(\frac{x}{\lambda};\mathcal{V}_2\right)\right) - 1\right] \\ + n_0^{(\mathrm{B})}|_{x\to 1}\left[\exp\left(\theta\left(\frac{1-x}{\lambda};-\mathcal{V}_3\right)\right) - 1\right]\,, \end{aligned} \tag{5.104}$$

in which the implicit function $\theta(\cdot\,;\mathcal{V})$ is defined as the inverse of (5.39) and the potential differences $\mathcal{V}_{1-4}$ are defined in terms of the charge density $\mathcal{Q}(t)$ as stated in (5.75). The leading-order bulk variables $n_0^{(\mathrm{B})}$ and $p_0^{(\mathrm{B})}$ can be obtained from numerical solution of the quasi-steady state BVP described by (5.97)-(5.100) upon extrapolating the matching conditions to the boundaries.

5.4.2 Total current density

The leading-order current density $J(t)$ generated by the PSC can be found from the sum of, and the difference between, (5.97a) and (5.98a) as follows.

Upon integration of the difference between (5.97a) and (5.98a), it is found that the total current density $j_0^{n(\mathrm{B})} + j_0^{p(\mathrm{B})}$ is uniform across the perovskite bulk. By matching with the leading-order current densities in the left-hand Debye layer from (5.89), it is found that

$$j_0^{n(\mathrm{B})} + j_0^{p(\mathrm{B})} = J(t)\,. \tag{5.105}$$

Half of the sum of (5.97a) and (5.98a) gives

$$\frac{1}{2}\frac{\partial}{\partial x}\left(j_0^{p(\mathrm{B})} - j_0^{n(\mathrm{B})}\right) = G - R\left(n_0^{(\mathrm{B})}, p_0^{(\mathrm{B})}\right)\,. \tag{5.106}$$

Integrating this expression over the width of the perovskite layer, making use of (5.105) and applying the boundary conditions extrapolated from (5.99b) and (5.100b) gives

$$\int_0^1 \left[G - R\left(n_0^{(\mathrm{B})}, p_0^{(\mathrm{B})}\right)\right] \,\mathrm{d}x = \frac{1}{2}\left[j_0^{p(\mathrm{B})} - j_0^{n(\mathrm{B})}\right]_{x=0}^{x=1} = J + R_l + R_r \,. \tag{5.107}$$

By rearranging this expression, the leading-order current density is obtained:

$$J = \int_0^1 \left[G - R\left(n_0^{(\mathrm{B})}, p_0^{(\mathrm{B})}\right)\right] \,\mathrm{d}x - R_l - R_r \,, \tag{5.108}$$

in which the losses due to interface recombination can be calculated from the bulk charge carrier concentrations $n_0^{(\mathrm{B})}$ and $p_0^{(\mathrm{B})}$ using (5.101)-(5.102). In the general case, the current density must be calculated using numerical integration.

5.5 Verification against numerical solutions

In order to plot the uniformly-valid asymptotic expansions derived from the preceding analysis and stated in Section 5.2.4 and (5.103)-(5.104), a combined asymptotic/numerical approach is needed. The variables which require a numerical treatment are the charge density $\mathcal{Q}(t)$, which satisfies the ODE given in (5.80), and the bulk charge carrier concentrations $n_0^{(\mathrm{B})}$ and $p_0^{(\mathrm{B})}$, which can be computed from the second-order BVP (5.97)-(5.100). This BVP exhibits significantly reduced stiffness compared to the full model since asymptotic expressions have been derived for the solution in the Debye layers and so only the solution in the perovskite bulk needs to be resolved numerically. As a result, a straightforward application of the `bvp4c` routine in MATLAB [91] suffices. The implicit function $\theta(\cdot\,; V)$ and the current density $J(t)$ must also be evaluated numerically from (5.39) and (5.108), respectively. The same combined approach has previously been used in [34].

The combined asymptotic/numerical approach. In summary, the steps are:

1. numerical solution of the ODE given in (5.80) to find the evolution of the Debye layer charge density $\mathcal{Q}(t)$
2. numerical solution of the second-order BVP (5.97)-(5.100) for the bulk charge carrier concentrations $n_0^{(\mathrm{B})}(x,t)$ and $p_0^{(\mathrm{B})}(x,t)$ within the perovskite layer
3. substitution of the numerical results from the previous two steps into the uniformly-valid asymptotic approximations found for the ion vacancy density in the per-

ovskite (5.38); electric potential in the ETL (5.49a), perovskite (5.56) and HTL (5.55a); electron concentrations in the ETL (5.49b) and perovskite (5.104); and hole concentrations in the perovskite (5.103) and HTL (5.55b)

4. calculation of the current density via numerical integration of the bulk recombination rate using (5.108)

Results from the combined asymptotic/numerical approach are here compared to numerical solutions of the full charge transport model from Section 3.5.2 for realistic experimental measurement protocols, namely scans of the applied voltage (from the built-in voltage down to short-circuit or up into forward bias) and current-voltage curves performed after preconditioning in forward bias under illumination. The numerical solutions are obtained using the finite difference scheme presented in both [35] and Section 4.4 and extended to the three layers of a PSC in Section B.1.

5.5.1 Voltage scans

Figures 5.3-5.5 show the internal state of a cell at five evenly-spaced values of time during a linear variation of the applied voltage, in a scenario in which the cell is abruptly illuminated at $t = 0$ after having been preconditioned in the dark with zero potential difference across the cell (*i.e.* $\Phi_{bi} - \Phi = 0$ or, in dimensional terms, at $V = V_{bi}$).

The agreement between the combined asymptotic/numerical and purely numerical results in Figure 5.3 is extremely close for all variables. This agreement indicates that the asymptotically reduced model provides a very good approximation to the full charge transport model for the realistic parameter estimates given in Table 3.2 and under realistic operating conditions. In order to test the sensitivity of the approximations to the size of the parameter λ, Figure 5.4 shows equivalent results for a value that is 10 times larger ($\lambda \approx 0.037$), for which all physical parameter values are kept the same except the mean density of iodide ion vacancies N_0 is reduced from 1.6×10^{25} to 1.6×10^{23} m^{-3}. Very good agreement is again demonstrated for the iodide ion vacancy and electric potential distributions, discrepancies are only clearly visible in the charge carrier concentrations within the perovskite Debye layers (on a logarithmic scale). Hence, it is shown that the asymptotic approach is robust with respect to significant variation in the size of the mean ion vacancy density N_0.

Figure 5.5 shows results for a scenario in which the applied voltage is slowly increased. In forward bias, the cell produces a large reverse current and, as shown, charge carriers accumulate within the perovskite layer. Therefore, at an applied voltage beyond around

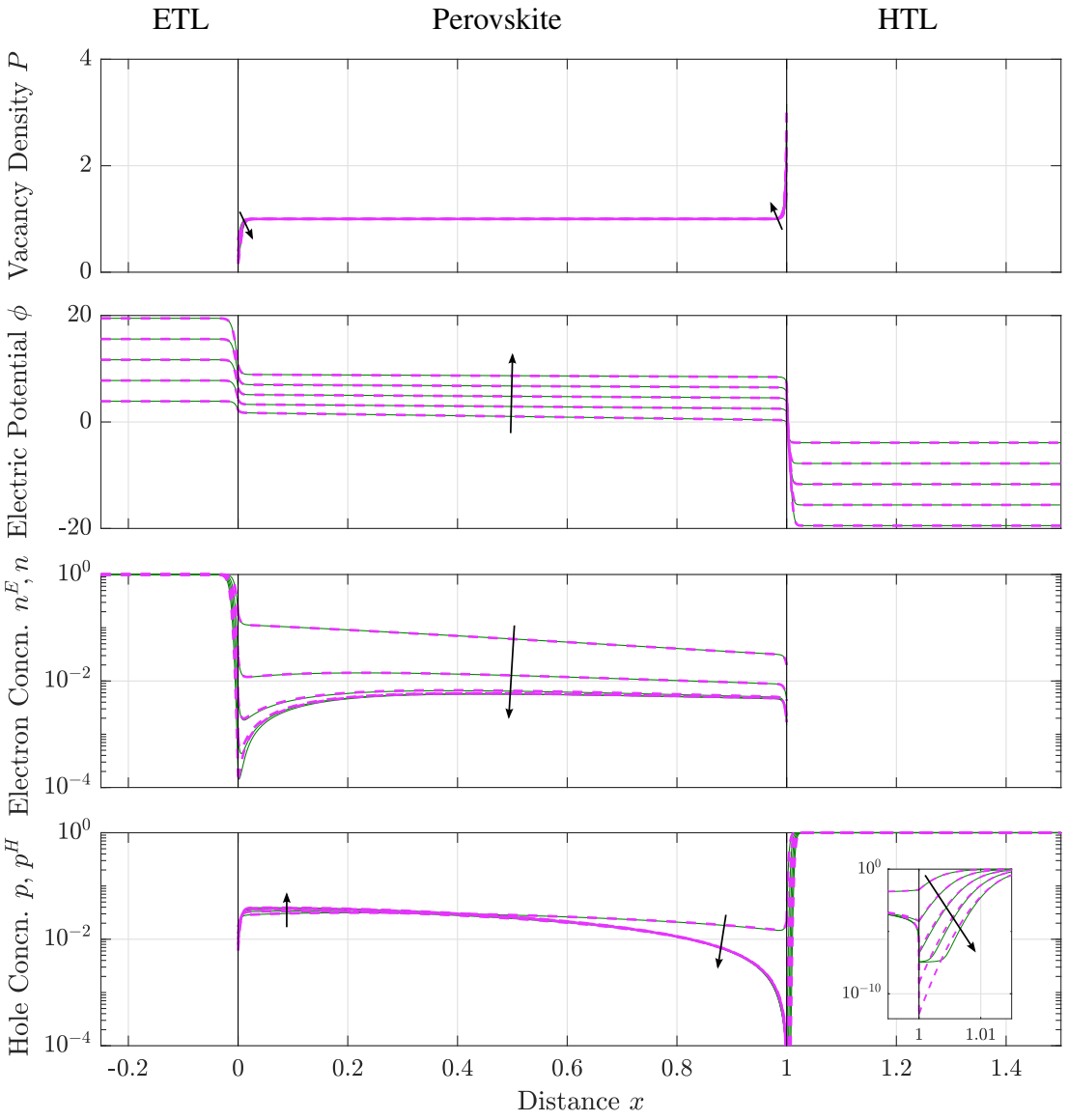

FIGURE 5.3: The dimensionless variable profiles across the three layers of a PSC at five evenly-spaced times between ≈ 0.34 and ≈ 1.7 (corresponding to dimensional times of 2, 4, 6, 8 and 10 s) during a linear decrease in the applied voltage from the built-in voltage (*i.e.* $\Phi - \Phi_{bi} = 0$, or $V = V_{bi} = 1.1$ V in dimensional terms) to ≈ 3.9 (0.1 V). The change in voltage corresponds to a scan rate of ≈ 23 (100 mV/s). The variables shown top to bottom are the ion vacancy density, electric potential, electron concentration and hole concentration. Note that the charge carrier concentrations are shown on a logarithmic scale and are scaled differently in the different material layers (see Section 3.5.1). Solid green lines represent the full numerical solutions while pink dashed lines represent results from the combined asymptotic/numerical approach. The parameter values are those given in Tables 3.2 and 3.3(a), which give a dimensionless Debye length of $\lambda \approx 3.7 \times 10^{-3}$. Arrows indicate the direction of increasing time. The inset shows a magnified view of the hole concentrations near the perovskite/HTL interface at $x = 1$.

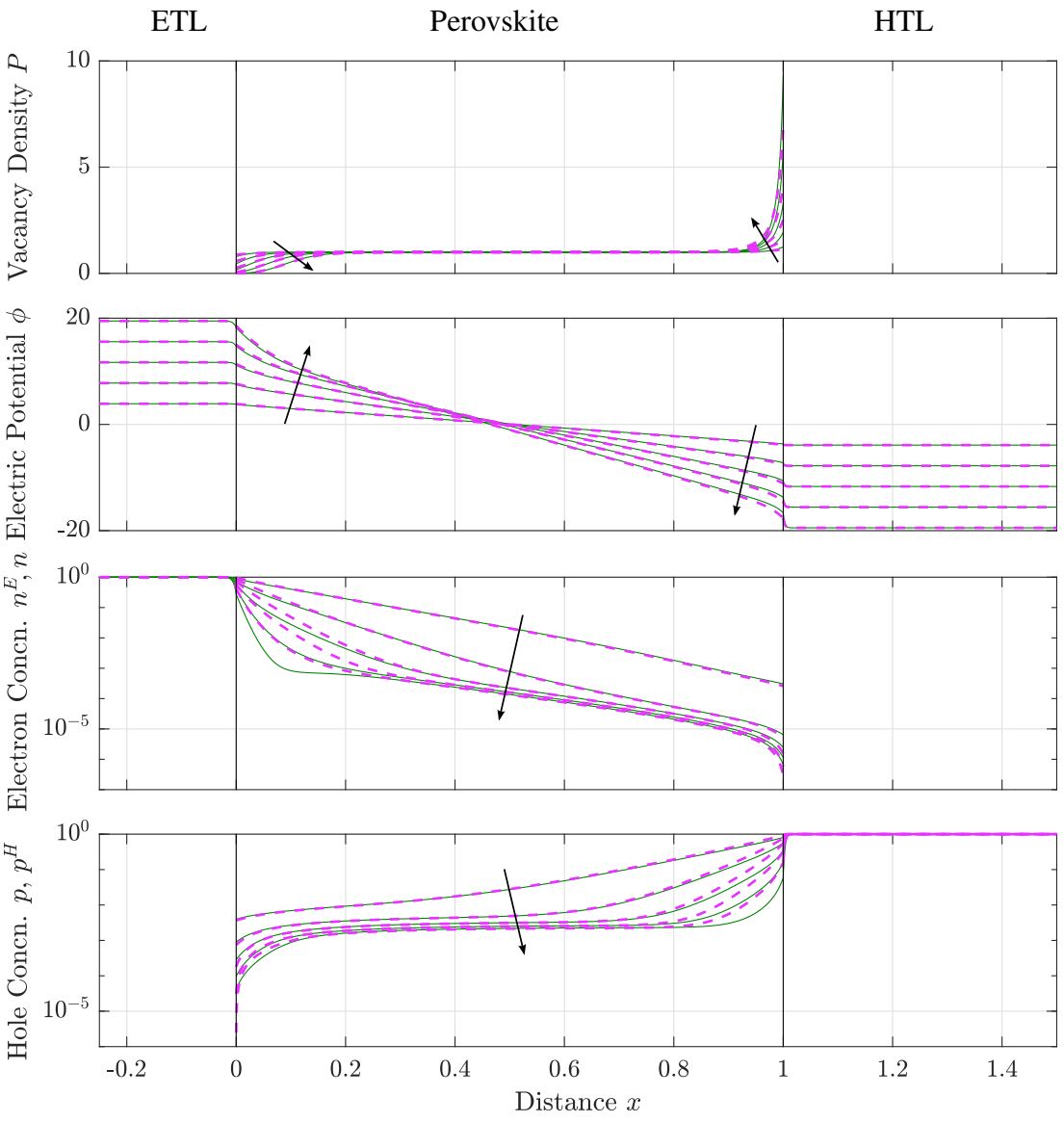

FIGURE 5.4: As for Figure 5.3 but for a mean iodide ion vacancy density that is one hundred times smaller (here, $N_0 = 1.6 \times 10^{23}$ m^{-3}) and hence a Debye length that is ten times larger, corresponding to a dimensional Debye length of $\lambda \approx 0.037$.

51 (1.3 V), the assumption that the charge carrier concentrations in the perovskite bulk are $O(\lambda)$ begins to break down and their effect on the electric potential can no longer be neglected. However, such high applied voltages are outside of the range of normal operation of the cell.

5.5.2 Current-voltage curves

A set of four simulations for J-V curves performed at five scan rates between 50 mV/s and 1 V/s are shown in Figure 5.6. The simulation protocol includes a 5 s preconditioning step at 1.2 V in the light before the J-V curve is measured. The current is calculated at

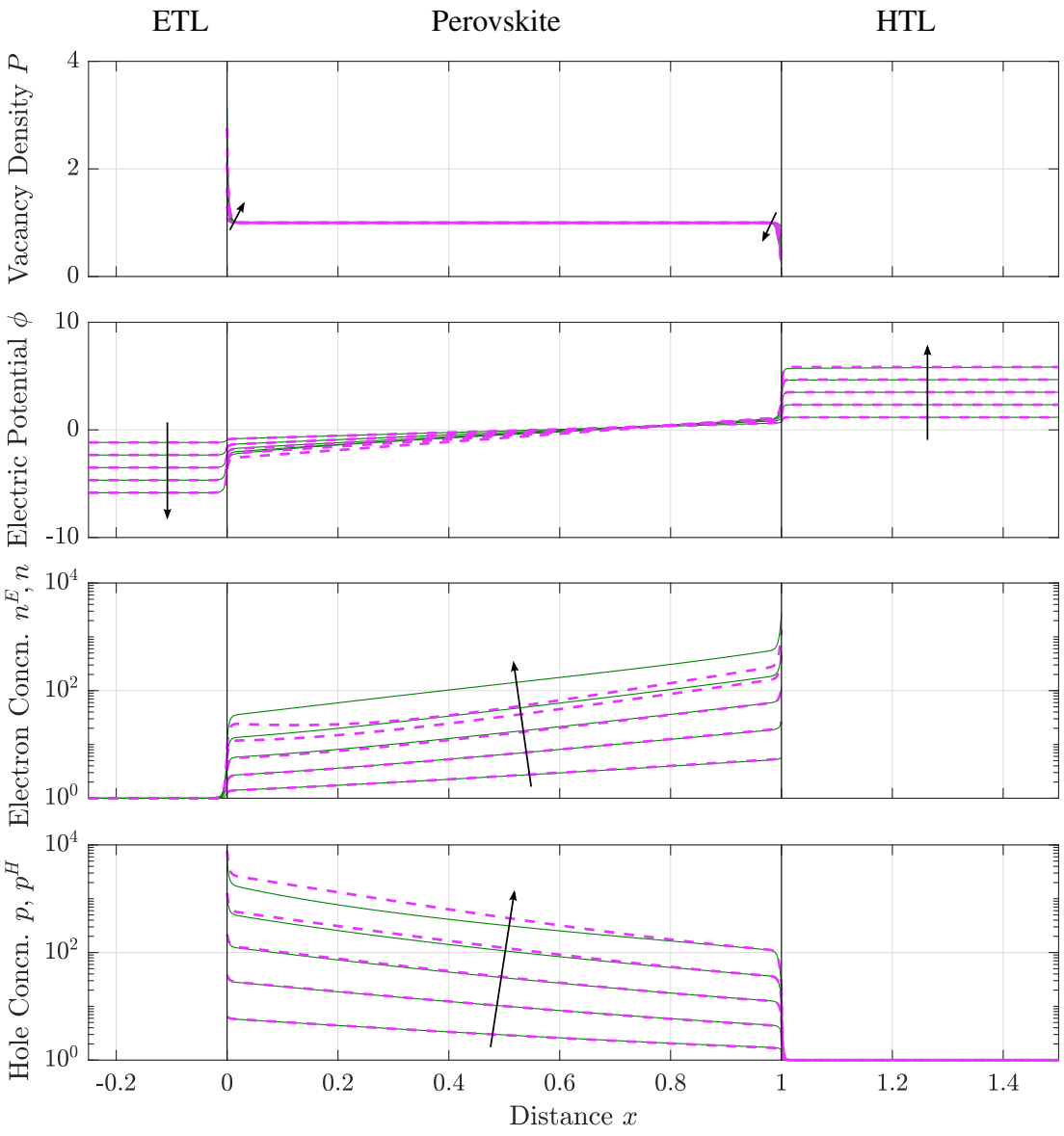

FIGURE 5.5: As for Figure 5.3 but for a linear increase in the applied voltage from the built-in voltage (*i.e.* $\Phi - \Phi_{bi} = 0$, or $V = V_{bi} = 1.1$ V in dimensional terms) to ≈ 54 (1.4 V) over a timespan of ≈ 0.51 (3 s). The change in voltage corresponds to a scan rate of ≈ 23 (100 mV/s).

equally spaced intervals in time as the applied voltage is varied at a constant rate from 1.2 V (forward bias) to 0 V (short-circuit) and back. The resulting curves show very close agreement between the combined asymptotic/numerical approach and the full numerical solutions, in which the only visible discrepancies appear after the switch in scan direction at short-circuit for the fastest scan rates. The colour scheme is chosen for consistency with the single-layer results published in Figure 7 (a) from [34], which model experimental data presented by Richardson *et al.* shown in Figure 7 (b) from [109].

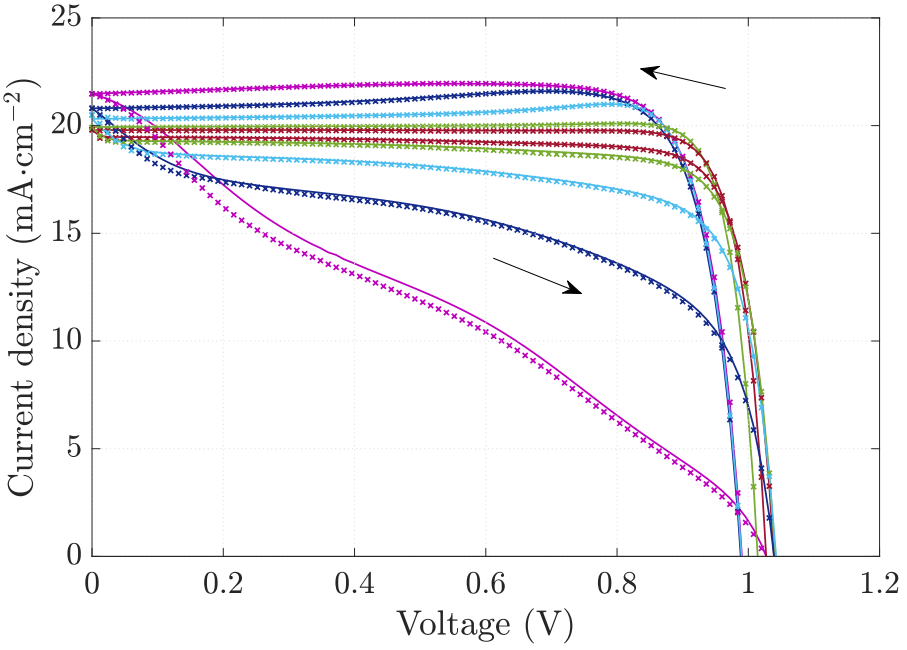

FIGURE 5.6: J-V curves simulated at scan rates of 50 mV/s (red), 100 mV/s (green), 250 mV/s (light blue), 500 mV/s (dark blue) and 1 V/s (pink). Solid lines represent the full numerical solutions while crosses represent results from the combined asymptotic/numerical approach. The parameter values are those given in Tables 3.2 and 3.3(a) and, in particular, these values correspond to a dimensionless Debye length of $\lambda \approx 3.7 \times 10^{-3}$. Arrows indicate the scan direction.

5.6 Discussion and summary

In this chapter, the details of an asymptotic analysis of the charge transport model are presented. This analysis successfully reduces the complexity of the problem to give the surface polarisation model for a PSC. The asymptotic approach reveals the key physical mechanisms and material parameters that control the performance of a PSC. The analysis was performed by taking the limit of the small dimensionless Debye length $\lambda \to 0$. Assumptions on the sizes of the other parameters are stated in (5.1). The asymptotic analysis, analogous to that performed in [34] for the single-layer model, shows that the problem for the electric potential and the majority mobile charge species in each layer is almost completely independent of the charge carrier concentrations within the perovskite layer. Hence, it is found that this decoupled problem is well-approximated by the solution to a single first-order ODE that describes the evolution of charge in the Debye layers, given in (5.80).

A particularly significant feature of this approach is the identification of two dimensionless parameters, Ω_E and Ω_H, which describe how the potential drops are apportioned between the ETL, perovskite and HTL. These two parameters prove to be key in understanding how the choice of materials for the TLs affects not only the dynamic response

of a PSC to changes in applied voltage but also its steady-state performance.

Via the comparison to numerical solutions of the full model made in Section 5.5, it is shown that the asymptotically simplified model provides an accurate approximation within realistic parameter regimes and operating conditions. In particular, a typical experimental protocol for measuring J-V curves is simulated for five different scan rates between 50 mV/s and 1 V/s. The results, shown in Figure 5.6, show minimal deviation from a numerical solution of the full model. Two potential causes of breakdown in the solution are investigated in Figures 5.4 and 5.5. Firstly, the value of the asymptotic parameter λ is increased by a factor of 10, corresponding to a reduction in the mean iodide ion vacancy density by a factor of 100. Figure 5.4 shows that very good agreement persists even for this relatively large value of λ, except for small discrepancies in the charge carrier concentrations within the perovskite Debye layers. Hence, the asymptotic method can be considered robust for the range of iodide ion vacancy densities reported in the literature. Secondly, the assumption that the charge carrier concentrations within the perovskite layer have a negligible effect on the electric potential is tested by simulating the internal state of the cell as the applied voltage is increased into forward bias, *i.e.* into a regime where the cell is using, and not generating, power. While the assumption holds for all applied voltages of practical interest for a PSC, Figure 5.5 shows that it begins to breakdown as the (dimensional) applied voltage is increased beyond approximately 1.3 V (corresponding to a dimensionless potential difference across the cell of $\Phi - \Phi_{bi} \approx 8$).

In summary, it is found that the asymptotic analysis provides a useful tool in the study of PSCs. The extension of the analysis to the three material layers of a PSC is a significant advancement on the single-layer analysis [34] as it enables physical properties of the two TL materials, as well as those of the perovskite, to be investigated. Both experimental and theoretical studies in the literature indicate that the types of TL materials and the quality of the interfaces play a crucial role in determining a cell's behaviour, as described in the next chapter. In particular, this three-layer analysis identifies two dimensionless parameters Ω_E and Ω_H which quantify the effects of the TLs on the internal state of the cell. These parameters highlight that two physical properties of the TLs, namely the permittivity and the effective doping density, have a substantial impact on the charge distribution within the device. A thorough investigation into the effects of varying these properties, based on the role of the parameters Ω_E and Ω_H identified in this chapter, is made in the next chapter.

Chapter 6

Effects of Key Physical Properties on Cell Performance

An open question in the field of PSC development is: how does the choice of material for the two transport layers have such a significant impact on the behaviour of a PSC? The consensus among researchers is that iodide ion vacancy migration is the underlying cause of hysteresis and that the ion vacancies exist only within the perovskite layer. However, experimental studies show that the extent of hysteresis depends strongly on the type of TL material, with PSCs incorporating organic TLs tending to display less hysteresis than PSCs with an inorganic ETL, under standard experimental conditions. To date, theoretical modelling has not been used to explain how the type of TL affects the migration of ion vacancies, intrinsic to the perovskite layer. In this chapter, a theory is put forward to explain the trend of reduced hysteresis for PSCs with organic TLs based upon just two key physical properties, namely the permittivity and effective doping density, of the TL materials.

In addition, the implications of this theory could have important consequences for PSC design in terms of addressing the main challenges that, at present, prevent the development of laboratory-scale PSCs into a viable photovoltaic technology. The first challenge is that of maximising the steady-state power conversion efficiency (PCE) of PSCs. There is a misconception among researchers that the existence of mobile ions in the perovskite layer does not affect the steady-state performance of a PSC. In fact, an uneven distribution of ionic charge has a significant impact on the electric field across a PSC. In turn, the distribution of the electric field proves to be crucial for explaining the complex interplay between ionic accumulation and the rates of charge carrier recombination at the perovskite/TL interfaces. Therefore, the theory is used to suggest strategies for redistributing the electric field in order to reduce losses due to interface recombination and

improve the steady-state performance of a PSC. The second major challenge to overcome is that of degradation. The dominant degradation mechanism varies depending on the specific cell composition under investigation, however the mechanisms can be split into two broad categories. Some degradation pathways depend on external factors (such as the ingress of *e.g.* water or oxygen from the atmosphere) and can be blocked via encapsulation. Other mechanisms are intrinsic to the PSC and are likely to be exacerbated by ionic accumulation. The theory developed in this chapter explains how the choice of TL materials can reduce the amount of ionic accumulation in the perovskite Debye layers adjacent to the TLs, and hence reduce the rate of associated degradation.

The focus of the two preceding chapters is on the development of mathematical methods capable of obtaining solutions, within realistic parameter regimes, to the drift-diffusion model of a PSC presented in Chapter 3. The aim here is to use these mathematical tools to predict the J-V characteristics of a PSC from the charge transport model and investigate the effects of varying a number of different physical properties on a cell's behaviour. The finite difference scheme presented in Section 4.4 (and extended to three layers in Section B.1) is used to generate all the figures in this chapter. To aid in the explanation of our findings, we make use of the approximate results of the asymptotic analysis presented, and validated against numerical solutions of the full model, in Chapter 5.

The chapter is set out as follows. In Section 6.1, there is a discussion of experimental findings from the literature which describe how cell performance is affected by the composition of a PSC. Next, in Section 6.2, the surface polarisation model is restated in dimensional terms. In Section 6.3, the effects of varying physical properties that have a direct impact on the process of iodide ion vacancy migration are investigated. Then, in Section 6.4, the effects of variation in the physical properties of the TLs are studied and it is explained how the type of TL material has a significant (and unexpected) impact on the extent of J-V hysteresis exhibited by a PSC. A summary of the findings is given in Section 6.5.

6.1 Review of experimentally observed trends in cell performance

A planar PSC is typically formed of three thin layers of material, namely the electron transport layer (ETL), perovskite layer and hole transport layer (HTL), sandwiched between two metal contacts, see Figure 3.1. A standard-architecture cell is one in which the light enters through the ETL, while in an inverted-architecture cell, light enters through the HTL. The three core layers of a typical standard-architecture PSC consist of an in-

organic ETL made from titania (TiO_2), a $MAPbI_3$ perovskite layer and an organic HTL made from Spiro-OMeTAD, as discussed previously in Chapter 3. Such cells have been shown to exhibit a photo-current that depends not only on the applied voltage but also its history [128]. The standard method for evaluating the performance of a solar cell, namely by measuring the photo-current (J) generated by the cell as the voltage is scanned between short-circuit ($V = 0$ V) and open-circuit ($V = V_{\mathrm{OC}}$), is hampered by hysteresis, as the measured J-V curve can vary significantly depending on the scan rate and preconditioning of the cell. See, for example, the simulated J-V curves in Figure 5.6. The extent of hysteresis, and sometimes just the term hysteresis, is qualitatively used to mean the difference between the reverse ($V_{\mathrm{OC}} \rightarrow 0$) and forward ($0 \rightarrow V_{\mathrm{OC}}$) scans of a J-V curve. The work of Richardson *et al.* [109] confirmed that the theory of iodide ion vacancy migration provides a plausible explanation for hysteresis and reproduced the shape of a set of J-V curves measured at a range of voltage scan rates for two standard-architecture PSCs. In the last few years, intense research effort has led to improvements in the design and performance of PSCs, however, advancements in our theoretical understanding of how the underlying processes affect the extent of J-V hysteresis have not kept pace with experimental findings [88]. In this section, some of the key developments in the composition of planar PSCs, relevant to the charge transport model, are described.

6.1.1 Reduced hysteresis for cells with organic transport layers

Shao *et al.* [125] were the first to report that the effects of hysteresis are suppressed in PSCs employing organic materials for both TLs. Initially, observed reductions in hysteresis (*i.e.* smaller differences between the reverse and forward J-V scans of a PSC) were attributed to the passivation of interface trap states and hence a reduction in the photo-current losses due to interface recombination. However, in 2015, Bryant *et al.* [18] discovered that a PSC with organic TLs (made from PEDOT:PSS and PCBM), previously considered to be "hysteresis-free", exhibits hysteresis when measured at a lower temperature (175 K). The reappearance of hysteresis at low temperature suggests that the use of organic materials for the TLs affects the underlying mechanism that causes hysteresis.

The proposed mechanism of iodide ion vacancy migration is a thermally-activated process. The temperature dependence of the iodide ion vacancy diffusion coefficient is given by the Arrhenius relation

$$D = D_{\infty} \exp\left(-E_A/k_B T\right) . \qquad \text{(2.3 repeated)}$$

Therefore, it should be expected that the appearance and extent of hysteresis is temperature dependent. However, it is not clear how the type of TL material should affect the mechanism of iodide ion vacancy migration, which is assumed to take place solely within

the perovskite layer. So the question arises: how does the choice of TL materials affect a mechanism that is intrinsic to the perovskite layer?

Experimental results published by Levine *et al.* [81] confirm the findings that the timescale of hysteresis shifts with temperature and that the choice of materials for the TLs is an important factor. The degree of hysteresis exhibited by an inverted-architecture cell with organic TLs (PEDOT:PSS / $MAPbI_3$ / PCBM) is compared to equivalent results for a standard-architecture cell (TiO_2 / $MAPbI_3$ / Spiro-OMeTAD). Measurements are performed under non-standard external conditions that vary temperature, light intensity and scan rate. A qualitative explanation of how the extent of hysteresis depends on temperature and scan rate is given that is based on the theory of ion vacancy migration within the perovskite layer. However, despite using the same type of perovskite ($MAPbI_3$) in both types of cell, it is concluded that the reduced hysteresis displayed at room temperature by the inverted-architecture cell with organic TLs is due to an *effective* ion vacancy diffusion coefficient (D_I) that is three orders of magnitude higher than that in the standard-architecture cells (and that predicted by DFT calculations [45]). A review of theories and open questions on how organic layers reduce the effects of hysteresis has been presented by Fang *et al.* [48].

6.1.2 Studies comparing multiple different architectures

Comparisons between the performances of different $MAPbI_3$-based PSCs, that make use of different TL materials, are made in each of [74] and [167]. The first study, published by Kim *et al.* [74], presents J-V measurements for both standard- and inverted-architecture cells at room temperature. It is shown that the inverted cells exhibit negligible hysteresis in their J-V curves as well as reduced ionic accumulation at the interfaces (indicated by smaller values for the capacitance at low frequency) compared to the standard cells. Zimmermann *et al.* [167] emphasise the need to use a measurement protocol that provides a fair and reliable comparison of performance, given that both hysteresis and degradation often prevent accurate characterisation of PSCs. Such a protocol is suggested and used to obtain experimental results which confirm the finding that inverted cells typically exhibit hysteresis to a much lesser degree than standard cells.

Kegelmann *et al.* [72] provide a systematic comparison of the use of different electron transport materials within a standard cell architecture. In all cases, the $MAPbI_3$ perovskite layer and a Spiro-OMeTAD HTL are deposited using the same processing techniques on top of the different ETLs. By measuring J-V curves at scan rates between 250 mV/s and 2.5 V/s, it is shown that standard cells incorporating TiO_2 as the ETL display a greater degree of hysteresis and lower steady state performance in comparison to those making

use of SnO_2 (first studied in [31]) or an organic material (such as PCBM). It is also found that the extent of hysteresis can be further reduced by the incorporation of a double layer (either SnO_2 / PCBM or TiO_2 / PCBM) as the ETL. Improved performance is attributed to reduced rates of interface recombination.

6.1.3 Effects of varying one of the transport layers or interfaces

Despite the experimental difficulties associated with attempting to vary just one device parameter independently of the other properties of a PSC, some recent papers focus on how a single property of a transport layer or interface affects performance. In this discussion, reported values for the V_{OC} are used as an indicator for the overall performance of a cell.

Belisle *et al.* [11] systematically test standard-architecture PSCs incorporating different organic materials for the HTL, evaporated on top of a PCBM ETL and a $MAPbI_3$ perovskite layer. A correlation between the ionisation potential of the HTL and the open-circuit voltage (V_{OC}) is expected [106], but instead only minimal differences in V_{OC} are measured. This finding implies that the performance of a typical cell is not limited by the energetic band alignment between the perovskite and HTL.

A subsequent investigation into which factors limit the V_{OC} of a PSC is made by Correa-Baena *et al.* [32]. A range of experimental techniques are used to conclude that the HTL, and not the perovskite morphology or ETL, determines the V_{OC} for a PSC consisting of an SnO_2 ETL, a mixed-ion perovskite layer and a Spiro-OMeTAD HTL. A correlation is found between the V_{OC} and the amount of Li-doping added to the Spiro-OMeTAD HTL, in which increases in the HTL doping density cause an increase in the rate of interface recombination, reducing the V_{OC} by up to 0.2 V (for 100 mol% Li-doping).

A similar study is presented by Yin *et al.* [157] in which the doping density within a TiO_2 ETL is varied. In this case, the addition of some (1 mol%) Nb-doping is shown to improve both performance and stability of a standard-architecture cell, however further increases in the doping density (to 2 or 3 mol%) cause the V_{OC} to decrease.

Wolff *et al.* [153] also study the relative importance of energetic band alignment and interface recombination, but this time the focus is on the interface between the perovskite and different organic ETLs in inverted-architecture PSCs. A higher V_{OC} is observed for cells which incorporate an ultra-thin organic layer between the perovskite and the ETL. It is concluded that this improvement is due to the suppression of trap-assisted recombination at the ETL/perovskite interface and therefore that, for these cells, performance is

limited by the rate of interface recombination, and not the energetic band alignment, at the ETL/perovskite interface.

In the work of Tan *et al.* [135], a Cl-capped TiO_2 ETL is incorporated into a standard-architecture cell along with a mixed-ion perovskite and Spiro-OMeTAD. Using DFT, it is shown that the additional chlorine has a passivating effect on the ETL/perovskite interface, reducing the trap state density and hence the rate of interface recombination. This passivation of the ETL/perovskite interface leads to improvements in all-round performance and stability. Despite such reports, significant progress still needs to be made in terms of long-term performance and stability in order for PSCs to fulfil their potential to become a commercial technology.

6.1.4 Proposed degradation mechanisms

A review of the environmental factors that affect the chemical stability of PSCs, including exposure to oxygen, moisture and ultraviolet light, is given by Niu *et al.* [98]. In this review, the nature of the mechanisms by which degradation takes place is highlighted as a key area for future research. Since its publication in 2015, a number of degradation mechanisms have been proposed, some of which are intrinsic to the composition of a PSC and cannot be eliminated via encapsulation of the device.

Iodide ion vacancy migration has been directly linked to degradation of bare $MAPbI_3$ perovskite films in experimental studies [64, 159, 164] which monitor the optical properties of the perovskite as it is exposed to either an electron beam or a varying illumination intensity. Chemical interactions between iodide ions and each of the most common TL materials (TiO_2 and Spiro-OMeTAD) have also been identified in [23]. Degradation via chemical interactions is likely to be exacerbated by ionic accumulation at the perovskite/TL interfaces. For an inverted-architecture cell (PEDOT:PSS / $MAPbI_3$ / PCBM), it has been suggested that iodide ions are able to migrate out of the perovskite and across the organic PCBM layer, resulting in chemical degradation at the adjoining metal contact [63]. A large accumulation of ion vacancies may also lead to structural degradation of the perovskite morphology [154].

Other mobile ionic species originating from any of the layers of a PSC may also cause degradation. For example, the migration of gold from the metal contact into the perovskite has been observed to cause degradation at a temperature of 70°C [37, 39]. Li *et al.* [84] show that small ions such as Li^+, Na^+ and H^+ can migrate into and across the perovskite layer and affect the performance, including the extent of hysteresis, exhibited by a PSC.

So-called reversible degradation, in the form of reversible transients in PCE on a timescale of several hours, has been measured by Domanski *et al.* [40]. This work combines theory and experiment to suggest that the transients are due to the migration of MA^+ cation vacancies within the perovskite. It has recently been shown that so-called reversible degradation occurs within perovskite crystal grains, while irreversible degradation is located along the grain boundaries of a mixed-ion perovskite film [59]. These results are consistent with the theory of ion vacancy migration as the cause of so-called reversible degradation.

6.2 Physical description of the asymptotic results

Within realistic parameter regimes, approximate, yet highly accurate, solutions to the three-layer charge transport model can be generated by using the method based on matched asymptotic expansions described in detail in Chapter 5.

6.2.1 The surface polarisation model

By applying the assumptions listed in Section 5.1, it is shown that:

1. due to their low concentrations, the charge carriers (electrons and holes) in the perovskite layer do not appreciably affect the electric potential;

2. the electric potential is linear across the bulk of the perovskite layer and constant across the bulk of each TL, except in narrow Debye layers around the perovskite/TL interfaces (see Figure 6.1);

3. the ionic charge stored in the Debye layer within the perovskite adjacent to the HTL (density $\mathcal{Q}$ per unit area) is balanced by an equal and opposite charge (density $-\mathcal{Q}$) within the perovskite Debye layer adjacent to the ETL (as a consequence of the conservation of ionic charge);

4. the ionic charge stored in each of the Debye layers within the perovskite is balanced by an equal and opposite charge in the Debye layer within the adjacent TL; and,

5. the evolution of the ionic charge density $\mathcal{Q}$ is controlled by the flow of iodide ion vacancies from the perovskite bulk into the Debye layers and is therefore proportional to the bulk electric field E_0 across the perovskite.

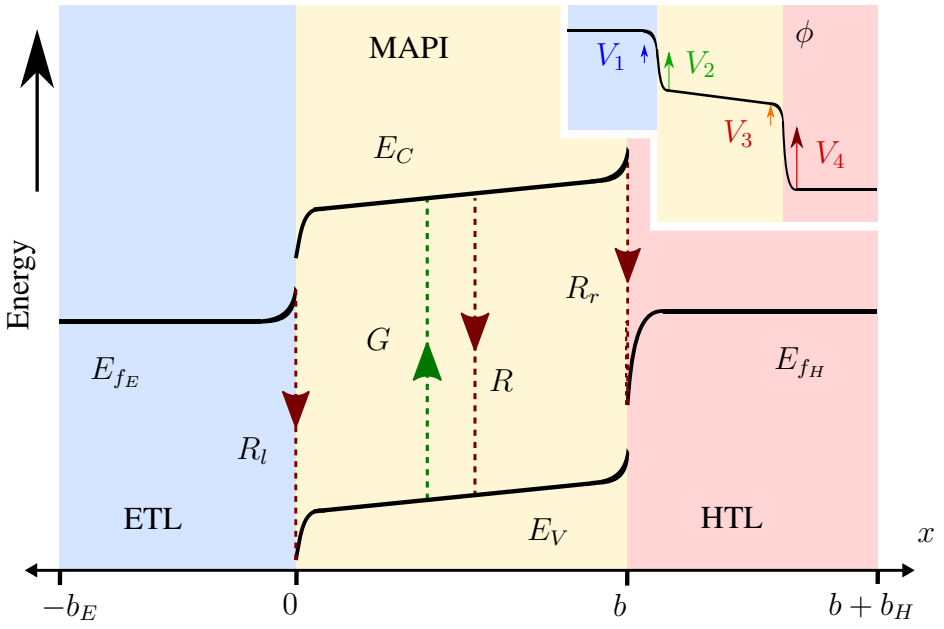

FIGURE 6.1: A schematic band energy diagram of a PSC (not at steady state) with dotted lines showing the recombination and generation pathways. Inset: the corresponding electric potential distribution showing the locations of the four Debye layers described by the surface polarisation model. Not to scale.

In dimensional terms, the relationship between the Debye layer charge density $\mathcal{Q}(t)$ and the bulk electric field $E_0(t)$ is, from (5.80) and (5.96), described by

$$\frac{\mathrm{d}\mathcal{Q}}{\mathrm{d}t} = \frac{qD_I N_0}{V_T} E_0(t)\,. \tag{6.1}$$

in which the bulk electric field $E_0(t)$ is given by

$$E_0(t) = \frac{1}{b}(V_{bi} - V - V_1 - V_2 - V_3 - V_4)\,, \tag{6.2}$$

in which V_{1-4} are the potential differences across the Debye layers as illustrated in the inset to Figure 6.1. It is further found that V_{1-4} are functions of the Debye layer charge density $\mathcal{Q}$, satisfying the following capacitance relations.

$$\begin{aligned} &V_1 = -f(-\Omega_E \mathcal{Q})\,, \quad V_2 = -f(-\mathcal{Q})\,, \quad V_3 = f(\mathcal{Q})\,, \\ &V_4 = -f(-\Omega_H \mathcal{Q})\,, \quad \Omega_E = \sqrt{\tfrac{\varepsilon_p N_0}{\varepsilon_E d_E}}\,, \quad \Omega_H = \sqrt{\tfrac{\varepsilon_p N_0}{\varepsilon_H d_H}}\,, \end{aligned} \tag{6.3}$$

in which the function $f(\mathcal{Q})$ is, from (5.65), the inverse of the function

$$\mathcal{Q}(V) = qN_0 L_D \,\mathrm{sign}(V)\sqrt{2}\left(\mathrm{e}^{V/V_T} - V/V_T - 1\right)^{\frac{1}{2}}\,. \tag{6.4}$$

The capacitance relations for the Debye layer charge density $\mathcal{Q}$ in terms of the potential

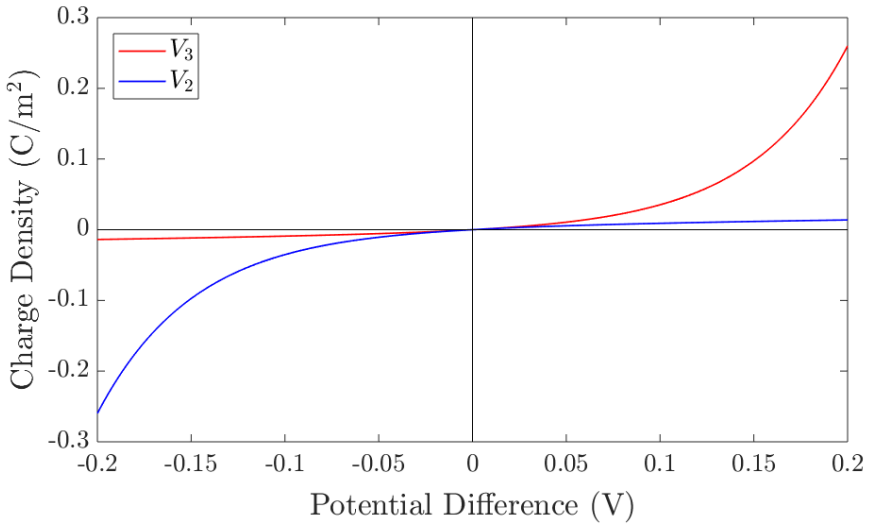

FIGURE 6.2: The relationship between the Debye layer charge density $\mathcal{Q}$ (stored within the perovskite Debye layer adjacent to the HTL) and the potential differences across the two Debye layers within the perovskite (V_2 and V_3), given by (6.3)-(6.4).

differences V_2 and V_3 are displayed in Figure 6.2.

The surface polarisation model is comprised of (6.1)-(6.4). These equations can readily be solved to find $\mathcal{Q}(t)$, from which the evolution of the four potential differences V_{1-4} can also be determined via (6.3)-(6.4). The solution for $\mathcal{Q}(t)$ provides a complete description of the evolution of the electric potential across the three layers of a PSC, via the uniformly-valid asymptotic expression in (5.56). A simplified drift-diffusion model for the charge carrier concentrations in the perovskite bulk, based upon the known electric potential and given in dimensionless terms by (5.97)-(5.100), can then be solved and used to obtain the cell's J-V characteristics. In Section 5.5 and [34], this method of solution is referred to as the combined asymptotic/numerical approach.

6.2.2 Key parameters for the distribution of the electric potential

Two dimensionless parameters, namely Ω_E and Ω_H, identified in the asymptotic derivation of the surface polarisation model and defined in (6.3), play a key role in determining what proportion of the total potential difference occurs within each Debye layer (*i.e.* the relative sizes of V_{1-4}). It follows from (6.3) that the Debye layer potential differences V_{1-4} necessarily take the same sign at any given instant of time. For small $\Omega_E < 1$, most of the potential difference across the ETL/perovskite interface lies within the perovskite (*i.e.* $|V_2| \gg |V_1|$), whereas for large $\Omega_E > 1$ most of the potential difference occurs in the ETL (*i.e.* $|V_2| \ll |V_1|$). Similarly, for small $\Omega_H < 1$, most of the potential difference across the perovskite/HTL interface lies within the perovskite, rather than the HTL (*i.e.* $|V_3| \gg |V_4|$) and vice versa for large $\Omega_H > 1$. In physical terms, decreasing the product

of the permittivity and doping density within the TLs (*i.e.* $\varepsilon_E d_E$ in the ETL and $\varepsilon_H d_H$ in the HTL) increases the proportion of the total potential difference across the cell that lies within the TLs and, correspondingly, decreases the proportion of the potential difference taken up within the perovskite layer. For example, replacing an inorganic TiO_2 ETL (which has a relatively high permittivity and doping density) with an organic PCBM ETL (which has a lower permittivity and doping density) leads to a PSC in which less of the potential difference occurs across the perovskite layer, *i.e.* there is a smaller bulk electric field E_0 across the perovskite. The bulk electric field E_0 is the driving force for both ion vacancy migration and the separation and extraction of photo-generated electrons and holes. Hence, changing the magnitude of E_0 can have a considerable effect on the behaviour, including the degree of J-V hysteresis, exhibited by a PSC. The effects of varying Ω_E and Ω_H are investigated in Section 6.4.

6.3 Modelling hysteresis as an effect of iodide ion vacancy migration

6.3.1 How hysteresis depends on voltage scan rate

The theory of ion vacancy migration explains why hysteresis only occurs within a range of scan rates [81]. At slow scan rates (*i.e.* for slow changes to the applied voltage), there is enough time for the ion vacancy distribution to adjust and remain in quasi-equilibrium. Therefore the generated current is almost independent of the scan direction and depends solely on the applied voltage. At very fast scan rates (*i.e.* for rapid changes to the applied voltage), the ion vacancy distribution does not have time to vary significantly and is therefore approximately fixed in its initial state during the scan. Therefore, again, the current is close to being independent of the scan direction and so no difference is seen between the reverse and forward scans. However, at intermediate scan rates, the history of the scan impacts the distribution of the ion vacancies and electric potential, and hence different values of the current can be measured on the reverse and forwards scans, at the same applied voltage. An example simulation of a J-V curve displaying significant hysteresis is shown in Figure 6.3, for a PSC preconditioned at $V = 1.2$ V for 4 s then scanned down to $V = 0$ V and back at a scan rate of 0.75 V/s. The extent of hysteresis depends on how the electric potential distribution, resulting from different ion vacancy distributions, affects the amount of charge carrier recombination and consequently the current generated by the cell.

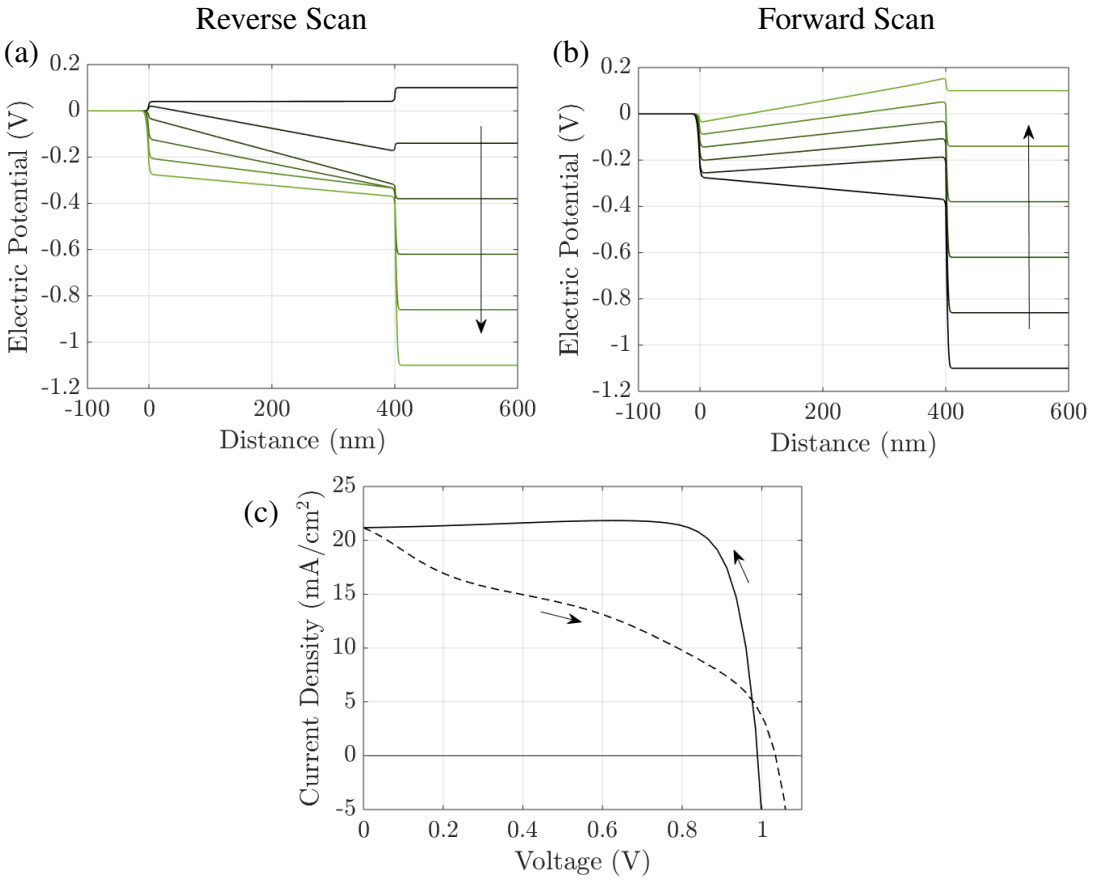

FIGURE 6.3: Simulation of a J-V curve measured at a scan rate of 0.75 V/s, after 4 s preconditioning at $V = 1.2$ V, using the parameter values in Tables 3.2 and 3.3(a). Panels (a) and (b) show the potential distributions across the cell at six evenly-spaced times over the 1.6 s duration of the reverse and forward scans, respectively, of the J-V curve plotted in (c). For clarity, in (a) and (b), the electric potential ϕ is shifted such that $\phi \equiv 0$ at the left-hand side. In (c), the solid line represents the reverse scan, the dashed line is the forward scan. Arrows indicate the direction of scan/increasing time.

6.3.2 Definition of the hysteresis factor

In order to quantify the degree of J-V hysteresis exhibited by a PSC, Levine *et al.* [81] among others have defined a measure called a hysteresis factor or a hysteresis index. Here, the hysteresis factor (H) is defined as the absolute difference between the area under the forward scan and the area under the reverse scan of a J-V curve, normalised by the area under the reverse scan, see Figure 6.3. The formula for H is therefore

$$H = \frac{A(|\mathcal{J}_{\text{rev.}} - \mathcal{J}_{\text{for.}}|)}{A(\mathcal{J}_{\text{rev.}})}\,, \tag{6.5}$$

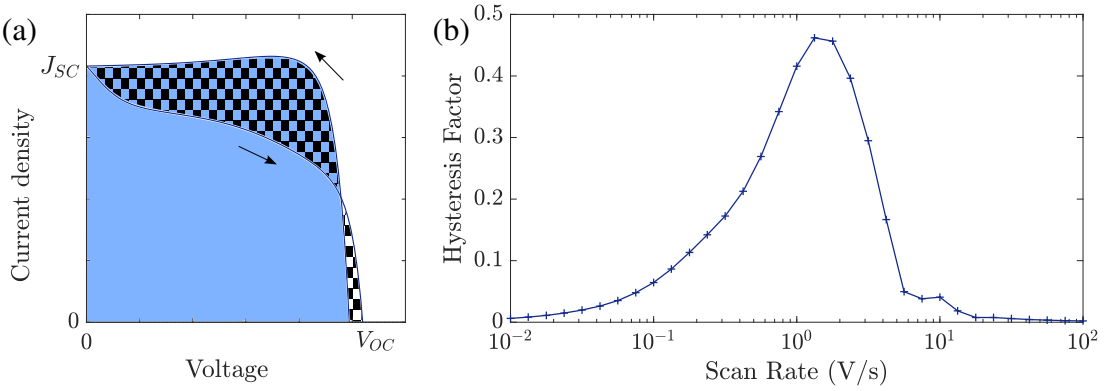

FIGURE 6.4: (a) A diagram showing the definition of the hysteresis factor H, defined in (6.5), as the area between the two J-V scans (checkered) divided by the area below the reverse scan (blue). Arrows indicate the scan direction. (b) The hysteresis factors corresponding to 33 simulations of J-V curves, each measured at a different scan rate between 10 mV/s and 100 V/s. The parameter values in Tables 3.2 and 3.3(a) are used.

in which $\mathcal{J}_{\text{rev.}}$ and $\mathcal{J}_{\text{for.}}$ are the non-negative current densities for the reverse and forward scan, respectively, and $A(\cdot)$ signifies the area under the curve, defined by

$$\mathcal{J}(V) = \max[J(V),\ 0]\,, \qquad A(\mathcal{J}) = \int_{V=0}^{V=V_{\text{OC}}} \mathcal{J}(V)\,\mathrm{d}V\,. \tag{6.6}$$

In the definition of the area $A(\cdot)$, the open-circuit voltage V_{OC} is chosen to be the higher of the two values measured on the reverse and forward scans. This definition is chosen to enable consistent evaluation for J-V curves that show "inverted" hysteresis, *i.e.* when the forward scan crosses or is above the reverse scan of a J-V curve, as reported in experimental works such as [108, 126].

As expected, the plot of the hysteresis factor versus scan rate in Figure 6.4 shows that the extent of hysteresis is very small for both slow and very fast scan rates. However, at the intermediate scan rates commonly used in experiment, ion vacancy migration can cause a PSC to exhibit significant hysteresis.

6.3.3 How the ion vacancy diffusion coefficient affects hysteresis

As suggested by Levine *et al.* [81], the ion vacancy diffusion coefficient D_I has a direct effect on the range of scan rates at which hysteresis appears. This effect is captured by the expression for the characteristic timescale of ion motion τ_{ion}, defined in this work by

$$\tau_{ion} = \frac{b}{D_I}\sqrt{\frac{V_T \varepsilon_p}{q N_0}}\,. \tag{3.48 repeated}$$

In order to explain the reappearance of hysteresis at low temperature, it is suggested in [81] that the ion vacancy diffusion coefficient D_I within the inverted-architecture cells with organic TLs is three orders of magnitude higher than in the standard-architecture cells and, as a result, the timescale of ion vacancy migration τ_{ion} is reduced and the scan rates at which hysteresis appears are increased, also by three orders of magnitude. However, while the ion vacancy diffusion coefficient is likely to vary with the quality of the $MAPbI_3$ perovskite morphology, it is not expected to vary (especially by such a large amount) between two different PSC architectures employing the same perovskite material.

The effects resulting from a change in the temperature T or ion vacancy density N_0 are studied by Cave *et al.* [24] who use the finite difference scheme presented in Section 4.4 and extended to three layers in Section B.1. This work presents the first theoretical investigation of the dependence of hysteresis on scan rate supported by time-dependent numerical solutions of a drift-diffusion model for a PSC within realistic parameter regimes. It is shown that cells with lower rates of recombination display less hysteresis and a higher short-circuit current density than those with higher rates of recombination. The chosen parameter values describe a PSC that is limited by bulk recombination that includes a combination of both bimolecular and SRH recombination mechanisms.

The approximate theoretical results of Neukom *et al.* [96] confirm the expectation that reduced rates of recombination correspond to better performance and reduced hysteresis. However, a reduction in the rates of recombination does not explain why hysteresis reappears at low temperature for PSCs with organic TLs [18, 81].

In the next section, an alternative theory is proposed to explain why hysteresis is reduced under standard operating conditions and why it reappears at low temperature for PSCs with organics TLs.

6.4 Modelling the effects of variation in the transport layer properties

The surface polarisation model provides an accurate approximation of the full charge transport model and hence it is appropriate to discuss recombination losses in terms of this model. Note, however, that all the figures are generated from simulations of the full model obtained using the finite difference numerical method. A key assumption of the surface polarisation model, stated in Section 6.2, is that there is a significant disparity between the ion vacancy density and the (much smaller) charge carrier concentrations

which means that the electric potential distribution within the perovskite layer of a PSC is set predominantly by the ion vacancy distribution. The key quantities determined by the ion vacancy distribution are the electric field within the perovskite bulk E_0 and the potential differences V_{1-4} across the Debye layers (see Figure 6.1). Where $E_0 > 0$, the electric field acts to drive electrons towards the ETL and holes to the HTL and thus reduces the rate of bulk recombination within the perovskite. In addition, positive values of V_1 and V_2 act to drive electrons in the ETL and holes in the perovskite away from the ETL/perovskite interface, respectively, thereby suppressing the rate of interface recombination across this interface. While positive values of V_3 and V_4 similarly suppress the rate of interface recombination across the perovskite/HTL interface. The opposite is true for negative values of E_0 and V_{1-4}, which enhance rather than suppress the associated rates of bulk and interface recombination. As a result, the J-V behaviour of a PSC is heavily influenced by the location of the dominant source of recombination. For both sets of recombination parameters given in Table 3.3, SRH recombination across the ETL/perovskite interface is limited by the perovskite hole concentration and SRH recombination across the perovskite/HTL interface is limited by the perovskite electron concentration, *i.e.* the interface recombination rates from (3.36) and (3.37) are well-approximated by

$$R_l = \nu_{p,E} p|_{x=0^+} , \qquad R_r = \nu_{n,H} n|_{x=1^-} . \tag{6.7}$$

However, the full SRH rates are used in all of the simulations performed for this chapter.

6.4.1 How TL properties affect ion vacancy migration

As previously discussed, the parameter regimes considered here lead to solutions in which the electric potential distribution across a PSC is almost solely determined by the slow motion of ion vacancies within the perovskite layer. In turn, the distribution of the electric potential controls the rates of charge carrier recombination and hence the current generated by the cell. We therefore first seek to understand ion vacancy migration, in isolation from the perovskite charge carriers, before looking at its consequences on perovskite charge carrier distributions and the resulting current extracted from the cell.

The driving force for ion vacancy migration is the almost uniform electric field across the bulk of the perovskite layer. Under the action of this field, ionic charge is redistributed between the two perovskite Debye layers, via the migration of mobile ion vacancies, which in turn affects the potential differences across the Debye layers. For a constant applied voltage, this leads to a progressive screening of the bulk electric field E_0 as the total potential difference across the cell is progressively absorbed into the Debye layers. These processes are well-described by the approximate surface polarisation model (6.1)-

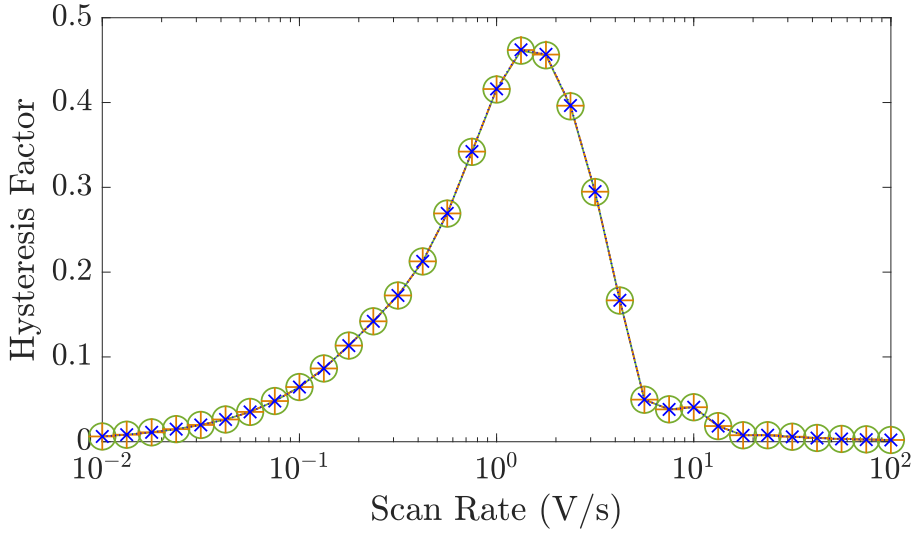

FIGURE 6.5: Hysteresis factor H versus scan rate for three different sets of the ETL effective doping density d_E and permittivity ε_E that give equal values of Ω_E. Precisely, $d_E = [\frac{50}{3}, 5, 1.25] \times 10^{24}$ m^{-3} and $\varepsilon_E = [3, 10, 40]\varepsilon_0$ (in green circles, orange pluses and blue crosses, respectively); all other parameters are fixed equal to the values in Tables 3.2 and 3.3(a).

(6.4).

Essential to understanding the effects of the TLs on ion vacancy motion are the dimensionless parameters Ω_E and Ω_H (given in (6.3) and discussed in Section 6.2.2) which encapsulate the key properties of the ETL and HTL, respectively. In Figure 6.5, we use the full numerical model to demonstrate that the behaviour of the cell depends on the bulk properties of the TLs almost entirely through these parameters by showing that the H versus scan rate curves for three cells with different permittivities ε_E and effective doping densities d_E, but with fixed Ω_E (and Ω_H), are almost identical. The same level of agreement can be found for an equivalent variation of the HTL parameters, d_H and ε_H (but is not shown here). Furthermore our numerical simulations show that, within the range of parameters considered, TL widths and carrier diffusion coefficients do not significantly alter the cell's properties.

The capacitance relations found in (6.3b-c) and (6.4), and plotted in Figure 6.2, show that reduced potential drops in the Debye layers lying within the perovskite (*i.e.* V_2 and V_3 as shown in the inset of Figure 6.1) correspond to a reduced ionic Debye layer charge density $\mathcal{Q}$. Figure 6.6 shows the effect of varying the permittivity of the ETL (ε_E) on the evolution of the Debye layer charge density $\mathcal{Q}$ during the voltage transient plotted on the same figure. This transient starts with a preconditioning step in which the applied voltage is held at the built-in voltage (*i.e.* $V = V_{bi} = 1.1$ V), so that initially the Debye layers are uncharged ($\mathcal{Q} = 0$), before the voltage is stepped up to $V = 1.2$ V and then reduced in steps to $V = 0.4$ V. Here a permittivity of $3\varepsilon_0$ corresponds to an organic material such

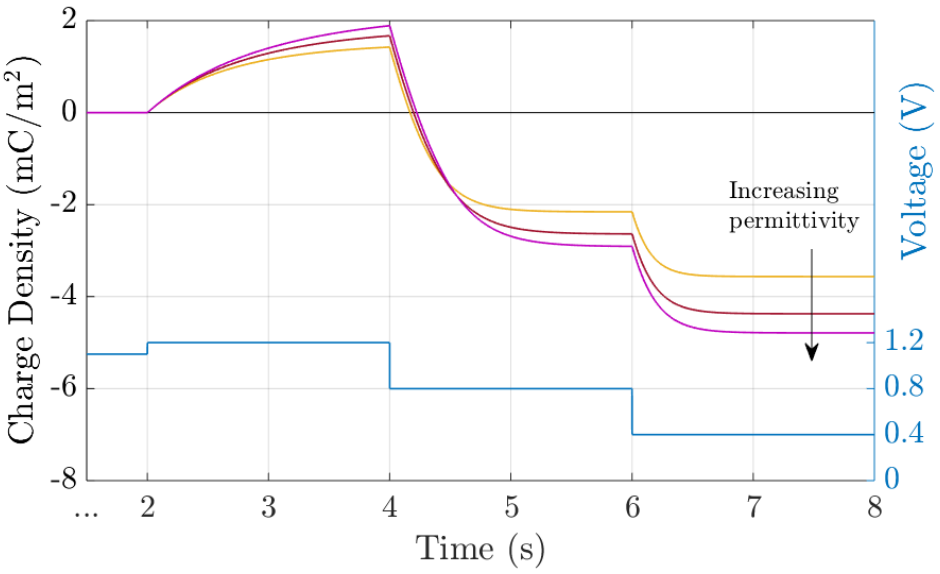

FIGURE 6.6: Evolution of the charge density due to the ionic accumulation within ≈ 10 nm of perovskite adjacent to the ETL during the voltage transient (blue line). Simulations are performed for $\varepsilon_E = [3, 10, 40]\varepsilon_0$ while all other parameters remain fixed, as given in Tables 3.2 and 3.3(a).

as PCBM, while $40\varepsilon_0$ corresponds to a material such as TiO_2. The simulations show that lowering the ETL permittivity reduces the magnitude of the Debye layer charge density $\mathcal{Q}$ throughout the entire transient.

A related effect due to varying both TL doping densities can be seen by comparing Figures 6.7 (a,b) (high TL doping) and (c,d) (low TL doping). Here it can be seen that the magnitude of the electric field E_0 (*i.e.* minus the gradient of the electric potential ϕ) in the perovskite bulk is consistently lower in the low TL doping cell than in the high TL doping cell. This is because in the low TL doping cell a significantly greater fraction of the potential drop across the cell occurs in the TLs (as opposed to across the perovskite) than occurs in the high TL doping cell. These effects can be explained in terms of the dimensionless parameters Ω_E and Ω_H which apportion the potential drop between the Debye layers in the TLs and the perovskite. In particular Ω_E and Ω_H are both larger for the low TL doping cell than they are for the high TL doping cell. Therefore, the potential drops in the TLs of the low TL doping cell are greater than the corresponding potential drops of the high TL doping cell. Notice also that, as expected, in Figures 6.7 (a,b) (high TL doping) most of the potential drop across the Debye layers occurs in the perovskite, whereas in Figures 6.7 (c,d) (low TL doping) most of the potential drop across the Debye layers occurs in the TLs.

The plots of H versus scan rate made in Figure 6.8 demonstrate how observable J-V hysteresis varies with scan rate for different devices, all with significant bulk recombination (using the recombination parameters given in Set (a) of Table 3.3), but with different

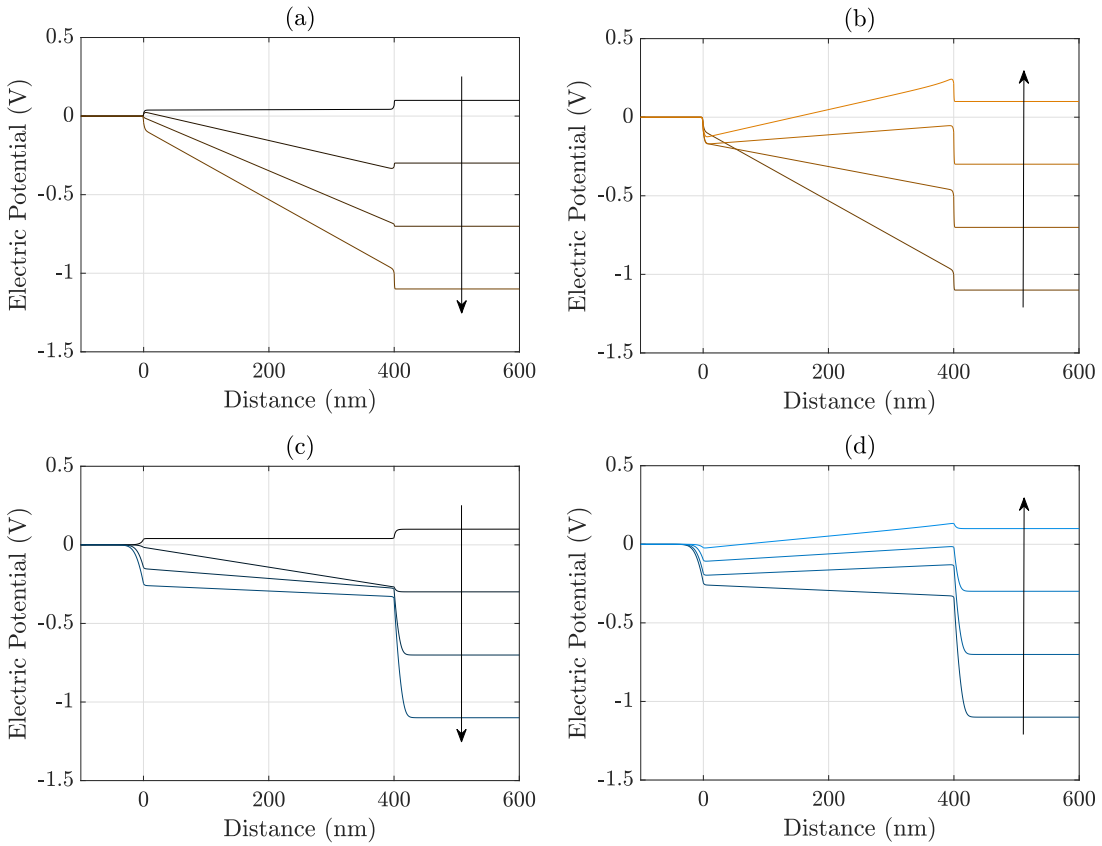

FIGURE 6.7: Effects of varying the TL doping densities on the evolution of the electric potential ϕ. Panels (a) and (b) show the evolution of the potential distribution during the reverse and forward scans, respectively (arrows indicate increasing time) during a 1.78 V/s J-V scan from $V = 1.2$ V to 0 V and back for high TL doping $d_H = d_E = 5 \times 10^{25}$ m^{-3}). Panels (c) (reverse scan) and (d) (forward scan) show the evolution of the electric potential for a cell with low TL doping ($d_H = d_E = 5 \times 10^{23}$ m^{-3}). All other parameters are those given in Tables 3.2 and 3.3(a).

TL doping levels. For the lowest TL doping (5×10^{21} m^{-3}), the maximum H is approximately 0.15. As the TL doping levels are increased, the maximum H reaches over 0.4 and also shifts to lower (measurable) scan rates. The small value of the maximum H for low TL doping is a result of screening of the electric field from the perovskite by the TLs. Thus, for a cell with low TL doping, the strength of the electric field within the perovskite is decreased, in comparison to a cell with high TL doping. Furthermore, if the dominant loss mechanism is bulk recombination within the perovskite, the differences between the current on the reverse and forward scans of a J-V curve (and consequently the hysteresis and corresponding value of H) are smaller for a cell with low TL doping than they are for a cell with high TL doping. As noted at the start of Section 6.4, recombination occurring in the perovskite bulk is very sensitive to the electric field across the perovskite layer which either aids or hinders charge separation depending on its direction. The shift to higher scan rates, as TL doping is decreased, results from a decrease in the size of the Debye layer charge density $\mathcal{Q}$ (comparable to the trend shown in Figure 6.6). It follows

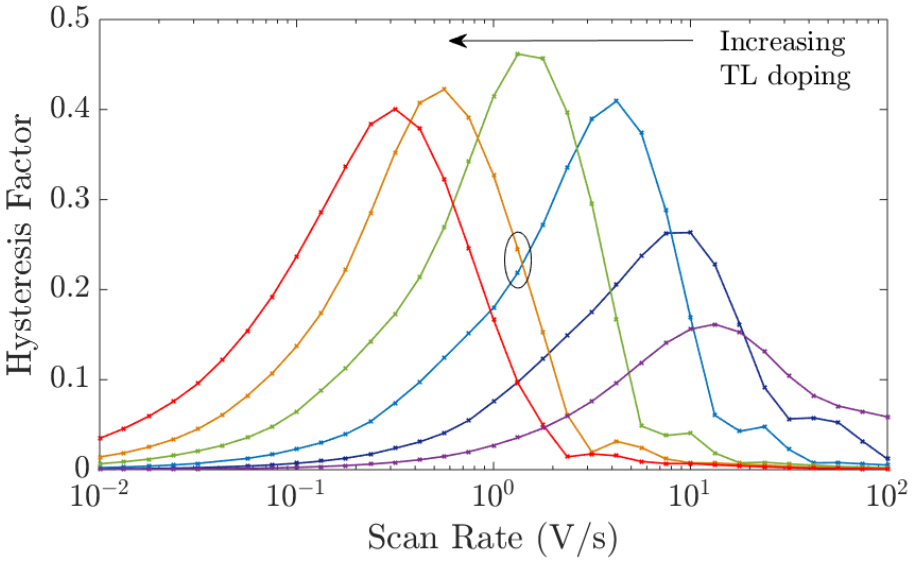

FIGURE 6.8: Effects of varying the TL doping density on the H curve of a cell, showing results for the six different TL doping densities $d_H = d_E = 5 \times [10^{21}, 10^{22}, 10^{23}, 10^{24}, 10^{25}, 10^{26}]$ m^{-3}. All other parameters as in Tables 3.2 and 3.3(a). The oval indicates the data points corresponding to the two simulations plotted in Figure 6.7. In particular, the higher, orange cross corresponds to the high TL doping case (panels (a-b)) and the lower, blue cross corresponds to the low TL doping case (panels (c-d)).

that the scan rate at which maximum hysteresis occurs increases as the TL doping is decreased (indeed the whole curve shifts to the right), as less charge needs to be moved in and out of the Debye layers in order to re-equilibrate the ion vacancy distribution.

In Figure 6.9 we perform a similar investigation of the effects of TL doping on J-V hysteresis to that performed in Figure 6.8 except on a device that is limited by interface (rather than bulk) recombination by taking the recombination parameters from Table 3.3(b). Notably, some features of the trends in the hysteresis factor curves differ from those for the cell with dominant bulk recombination. In particular, for a device limited by interface recombination (Figure 6.9), the photo-current displays a stronger dependence on the potential drops across the Debye layers than the bulk electric field. As noted at the start of Section 6.4, large positive potential drops (*i.e.* V_{1-4}) across these Debye layers efficiently extract electrons to the ETL and holes to the HTL while opposing the motion of holes onto the ETL/perovskite interface and electrons onto the perovskite/HTL interface, where they can recombine in interfacial traps. Thus, in cells dominated by interface recombination, the division of the potential drop between the Debye layers at the ETL/perovskite interface and between those at the perovskite/HTL interface (*i.e.* between V_1, V_2, V_3 and V_4) and the location of the dominant recombination pathway play an important role in determining the degree of hysteresis and the overall level of recombination. As discussed in Section 6.2, the potential is predominantly determined by the ion vacancy distribution, and so is, for practical purposes, independent of the recombination

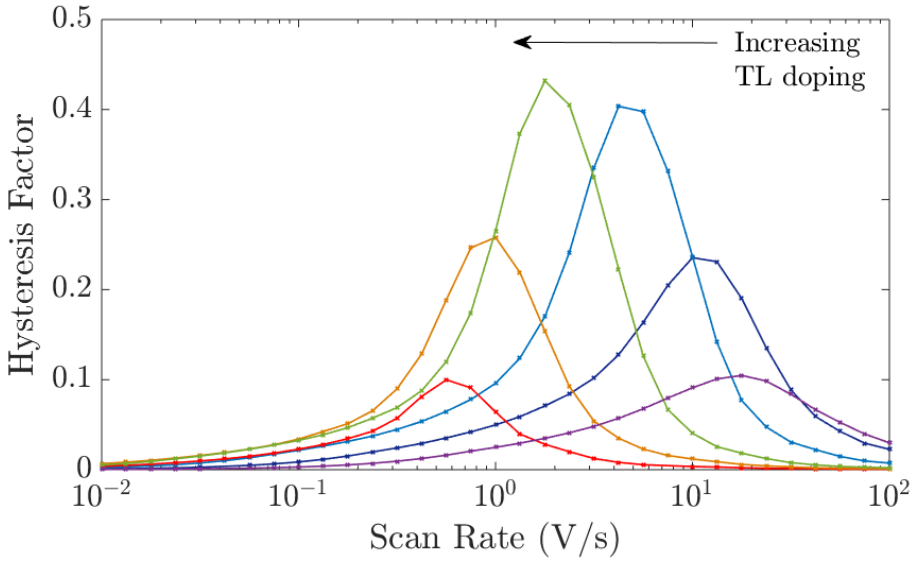

FIGURE 6.9: Equivalent to Figure 6.8 but for the recombination parameters in Table 3.3(b), *i.e.* for a cell limited by interface (rather than bulk) recombination.

mechanisms. Hence, Figure 6.7 is equally applicable to the cell dominated by interface recombination.

One notable difference between the sets of hysteresis factor curves shown in Figure 6.8 and those in Figure 6.9 occurs as the doping density is increased beyond $d_E = d_H = 5 \times 10^{24}$ m^{-3} at which H is most pronounced (green curve). In the former case (dominant bulk recombination), the maximum H remains relatively high even as the TL doping is increased beyond $d_E = d_H = 5 \times 10^{24}$ m^{-3} while in the latter case (dominant interface recombination), H decays rapidly from its maximum value as the TL doping is increased beyond $d_E = d_H = 5 \times 10^{24}$ m^{-3}. The rapid decay in H with increases in doping for the dominant interface recombination case, can be explained by the fact that as doping increases so the potential drops in the perovskite Debye layers (V_2 and V_3) increase (with respect to the other potential drops). This is enough to almost eliminate interface recombination for all applied voltages much below V_{bi}, and in turn this reduces the variations that give rise to hysteresis.

The differences resulting from changes to the recombination parameters highlight the importance of also understanding the dependence of hysteresis on the recombination mechanisms within a particular PSC. This aspect is discussed in the following section.

The trend of H curves being shifted to higher scan rates for cells with lower TL doping densities (shown in both Figures 6.8 and 6.9) or lower permittivities (not shown) is consistent with the reports of low temperature hysteresis for cells with organic TLs made by Bryant *et al.* [18] and Levine *et al.* [81]. At room temperature, the hysteresis is present but only for scan rates much faster than commonly used in practice. At lower temper-

atures, the diffusion coefficient of the ion vacancies is reduced and so the H curves are shifted back to the scan rates which are commonly probed experimentally. This explains why devices that appear hysteresis-free at room temperature demonstrate hysteresis upon cooling.

As discussed in Section 6.1.4, the accumulation of ionic charge at the edges of the perovskite, in the form of the Debye layers, is likely to contribute significantly towards degradation. Hence, it is worth noting that increasing Ω_E and/or Ω_H results in smaller ionic charge densities $\mathcal{Q}$ in the perovskite Debye layers at steady-state and during J-V scans (as in Figure 6.6). Thus, PSCs with TLs that have low permittivities and/or low doping densities, and consequently reduced ionic accumulation at the interfaces, might be expected to show reduced degradation and longer lifetimes.

6.4.2 Detecting the dominant recombination mechanism

The aim of this section is to use the numerical model to consider how different recombination mechanisms affect the J-V hysteresis. The eventual goal of such a study is to develop tools that can be used to assess the type and location of recombination losses. Since these losses depend on the quality of the perovskite crystal structure and the interfacial contacts, such studies have the potential to assess cell degradation and to guide future cell development. Here, for simplicity, we vary only the material parameters associated with electronic charge carrier recombination but otherwise set the material parameters equal to those in Table 3.2. Thus, each simulated cell has an identical predisposition for ion vacancy migration. A common feature of all the simulations that we have performed is that reducing the amount of recombination, via any recombination pathway, improves the performance on both forward and reverse scans, and hence reduces the degree of hysteresis.

In order to illustrate that features of J-V hysteresis can be used to diagnose the dominant recombination pathway, we show J-V curves for two representative cells. The first cell, whose J-V curves are shown in Figure 6.10 (a), has recombination parameters taken from Set (a) of Table 3.3 and losses that are dominated by bulk recombination in the perovskite. The second cell, whose J-V curves are shown in Figure 6.10 (b), has recombination parameters taken from Set (b) of Table 3.3 and losses that are dominated by interface recombination. The experimental protocol for both sets of J-V curves, Figures 6.10 (a-b), is as follows: the device is preconditioned at 1.2 V for 4 s, the voltage is then scanned down to 0 V at a scan rate of 0.2 V/s and immediately back up to 1.2 V. The same procedure of preconditioning for 4 s and then scanning is then repeated for two more scan rates: 0.6 V/s and 1 V/s.

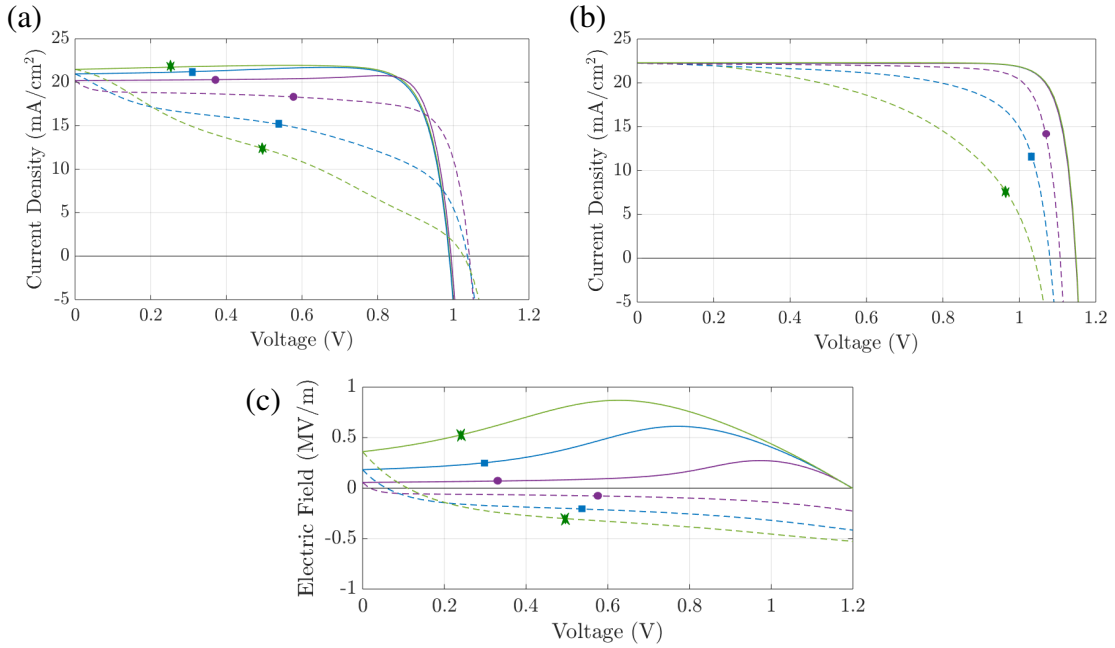

FIGURE 6.10: Simulations using the parameter set in Table 3.2. Panels (a) and (b) show simulated J-V curves at scan rates of 0.2 V/s (purple, circles), 0.6 V/s (blue, squares) and 1 V/s (green, stars) for the recombination parameters given in Table 3.3 Sets (a) and (b), respectively. Solid lines represent the reverse scans; dashed lines the subsequent forward scans. Panel (c) shows the electric field at $x = 200$ nm during the J-V scans.

The first distinct feature is the current maximum (or "bump") on the reverse scans of the two slower J-V curves in Figure 6.10 (a). This feature arises because, as the scan progresses from high applied voltage to low applied voltage, the charging of the Debye layers lags behind the voltage drop across the cell. This lag results in a positive bulk electric field E_0 which, as the scan proceeds, eventually reaches a maximum at $V \approx 0.75$ V for the medium scan rate (blue curve) before slowly decreasing until $V = 0$ V (see Figure 6.10 (c)). Where the dominant recombination pathway is bulk recombination, the positive bulk electric field serves to separate photo-generated charge carriers to their respective contacts and thereby reduce recombination losses. The maximum in the current is thus associated with the maximum in E_0 and the corresponding minimum in bulk recombination. In turn such a maximum in the current on the reverse scan of a J-V curve can be a sign of significant bulk recombination.

Another feature which can be attributed to bulk recombination is that of a noticeable drop-off in current just after the switch in scan direction at short-circuit. This drop in current is associated with the steep decrease in E_0 (see Figure 6.10 (c)) on a slow to mid-rate scan immediately after the reverse in scan direction.

Near open-circuit (V_{OC}), the potential drops across the Debye layers are relatively small but still crucial for interpreting the different behaviour demonstrated by Figures 6.10 (a) and (b). At the start of the reverse scan, the potential drops V_{1-4} are all negative because

the cell is preconditioned at an applied voltage above V_{bi} (but change sign as the reverse scan proceeds and V drops much below V_{bi}). Negative potential differences $V_1 + V_2$ and $V_3 + V_4$ across the ETL/perovskite and perovskite/HTL Debye layers, respectively, act to drive electrons from the ETL, and holes from the HTL, into the perovskite. This influx of charge carriers substantially increases the magnitude of recombination losses in the perovskite layer to the extent that these losses swamp the generated current. This effect is particularly pronounced in cells with large numbers of recombination sites in the perovskite layer, such as the one whose recombination parameters are given by Set (a) of Table 3.3. Hence, such cells, when preconditioned above V_{bi}, show an apparent V_{OC} on the reverse scan that is significantly depressed and often significantly below V_{bi}. In contrast, on the forward scan, the potential drops V_{1-4} are all positive (until the applied voltage is increased beyond V_{bi}) and so act to drive electrons and holes out of the perovskite layer into their respective transport layers. This means that where the dominant form of recombination is bulk recombination (within the perovskite), the performance is particularly adversely affected on the reverse scan, compared to the forward scan, at applied voltages around V_{bi}. As a result, for a cell dominated by bulk recombination, the forward and reverse scans of a J-V curve may cross, as depicted in Figure 6.10 (a). For a cell with significantly smaller numbers of recombination sites in the perovskite layer (*e.g.* the cell described by the recombination parameters in Set (b) of Table 3.3), the apparent V_{OC} on the reverse scan is not significantly depressed, despite the increase in carrier concentrations in the perovskite layer from leakage in from the TLs. Consequently, the forward and reverse scans of the J-V curves do not cross (see Figure 6.10 (b)). This reasoning explains why inverted hysteresis (*i.e.* the crossing of the reverse and forward scans of a J-V curve that can be seen in Figure 6.10 (a) but not Figure 6.10 (b)) can be observed for cells with dominant bulk recombination in the vicinity of V_{OC}.

6.4.3 Improving steady-state performance

We have demonstrated that varying the dimensionless parameters Ω_E and/or Ω_H (by adjusting either the TL doping densities or permittivities) changes the distribution of the electric potential within a PSC during transient measurements. However, the key property of a PSC, its power conversion efficiency, is measured under steady-state conditions. In this section, we suggest how the TL doping can be tuned to improve the steady-state photo-current, for a given density of trap states (*i.e.* fixed recombination velocities). It is commonly assumed in the literature that reduced hysteresis is associated with better steady-state performance. In the work of Cave *et al.* [24] (which is based upon the same charge transport model and finite difference code as this chapter), it is shown that reducing the rate of bulk recombination does indeed lead to reduced hysteresis. However,

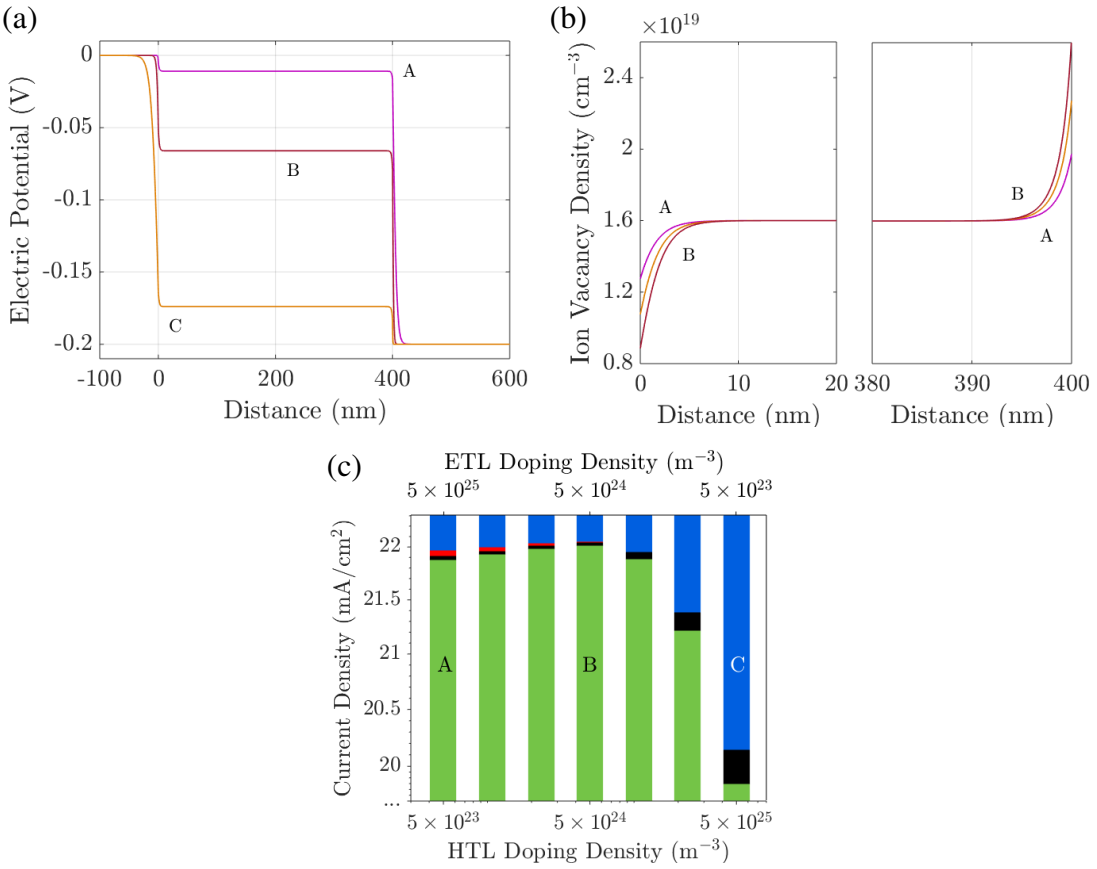

FIGURE 6.11: Steady-state profiles for (a) the electric potential and (b) the iodide ion vacancy density, for differently-doped TLs, held at 0.9 V. The TL doping densities are A: $d_E = 5 \times 10^{25}$ m^{-3}, $d_H = 5 \times 10^{23}$ m^{-3}; B: $d_E = d_H = 5 \times 10^{24}$ m^{-3}; and, C: $d_E = 5 \times 10^{23}$ m^{-3}, $d_H = 5 \times 10^{25}$ m^{-3}. All other parameters are as in Tables 3.2 and 3.3(b). Panel (c) shows the photo-current density (J, green) and losses due to bulk (R, black) and interface (R_r, red; R_l, blue) recombination for a range of TL doping densities including cases A-C above.

here we show that, although lowering the TL doping densities can help to reduce hysteresis, this does not necessarily improve the steady-state performance of a PSC limited by interface recombination.

Recent experimental work on PSCs with a $MAPbI_3$ perovskite absorber layer indicates that, for high performing cells, recombination at one of the interfaces (rather than in the bulk) is the performance-limiting mechanism [72, 153]. In Figure 6.11, we consider the case where interface recombination, and in particular recombination at the ETL/perovskite interface, dominates by using the recombination parameters in Table 3.3(b), in which the recombination velocities are given by $\nu_{p,E} = 10$ ms^{-1} and $\nu_{n,H} = 0.1$ ms^{-1}.

At steady-state, charge is distributed so that the electric field has been screened throughout the PSC except in the narrow Debye layers about the interfaces. Consequently, at steady-state, the bulk electric field is flat ($E_0 = 0$) and the electric potential is split between the four Debye layers. Figure 6.11 (a) shows three possible steady-state potential

distributions for three different pairs of TL doping densities (d_E and d_H) for cells operating near maximum power point at $V = 0.9$ V (*i.e.* $V = V_{bi} - 0.2$ V). At this applied voltage, the potential drops across the Debye layers (V_{1-4}) are all positive and so provide energetic barriers to charge injection from the TLs into the perovskite. Figure 6.11 shows the corresponding distributions of ion vacancies. Note that scenario B (with doping densities equal to 5×10^{24} m^{-3}) displays the highest levels of ionic accumulation adjacent to the interfaces.

In Figure 6.11 (c), we investigate the effects of varying the effective TL doping densities (simultaneously) on the performance of a cell primarily controlled by recombination across the ETL/perovskite interface (R_l). This type of recombination depends both on the electron concentration in the ETL and on the hole concentration in the perovskite. Note that the potential drops V_{1-4} are not independent (see equations (6.3)). For example, increasing d_H leads to a shift in potential out of the HTL Debye layer into the other Debye layers, increasing V_{1-3} (comparable to the trend from A to B). Moving from left to right in Figure 6.11 (c), reductions in ETL doping and increases in HTL doping (which both increase V_1 while decreasing V_4) initially result in an improvement in performance over cell A, by suppressing the electron concentration on the ETL/perovskite interface. However, further decreasing the ETL doping while increasing the HTL doping beyond scenario B results in a decrease in V_2 (which can be identified from the corresponding decrease in ionic accumulation near the ETL/perovskite interface shown in Figure 6.11 (b)). A smaller V_2 causes an increase in the number of holes reaching the ETL/perovskite interface, which results in increased interfacial recombination and poorer performance. There is thus an optimal point along this line of changing doping densities, represented by best-performing cell B. This is because, after the optimal point, the reduction in recombination brought about by further decreases in the electron concentration in the ETL are more than offset by the increases in hole concentration in the perovskite.

The situation is reversed for a cell whose performance is limited by recombination at the perovskite/HTL interface (R_r). It can be seen in Figure 6.11 (c) that losses due to this type of recombination increase from scenario B to A, due to an increasing concentration of electrons in the perovskite.

An important conclusion from this section is that significant potential drops in the perovskite (V_2 and V_3) are required to improve performance. Large potential drops in the perovskite Debye layers enhance charge carrier collection efficiencies and hence the photocurrent, by keeping holes in the perovskite from recombining across the ETL/perovskite interface and electrons in the perovskite from recombining across the perovskite/HTL interface. However, large potential drops within the perovskite (which correspond to small potential drops within the TLs) also allow for a large electric field across the bulk of the

perovskite layer during transient measurements. So, in contrast, large potential drops within the perovskite are also associated with potentially harmful levels of ionic accumulation at the edges of the perovskite and also significant ion vacancy migration, and hence hysteresis, during transient measurements. This finding, for cells limited by interface recombination, runs counter to the usual assumption that hysteresis is associated with poor efficiency. The optimal amount of doping of the TLs must therefore be a balance between creating large energy barriers in the perovskite Debye layers (to prevent recombination at the interfaces) and screening the potential drop across the perovskite layer (to reduce the bulk electric field during transients and hence reduce ion vacancy migration).

6.5 Summary

In this chapter, we demonstrate how ion vacancy migration affects the performance of PSCs and that the observable effects are strongly dependent on the permittivity and the effective doping density of the transport layers. While ion vacancy migration is now commonly accepted as the cause of J-V hysteresis, we find that ion vacancy migration plays a significant role even for steady-state device performance, through the resulting accumulation of ionic charge and band bending in narrow layers adjacent to the interfaces between the perovskite and the TLs. We show that the distribution of the electric potential is key in determining both the transient and steady-state behaviour of a cell. Further to this, we suggest that the doping density and/or permittivities of each TL may be tuned to reduce losses due to interface recombination.

Numerical simulations of the charge transport model reproduce a number of experimental trends, including reduced hysteresis for PSCs with organic TLs and the reappearance of observable hysteresis at low temperature, via the adjustment of just a few significant material parameters. The results are explained in terms of the surface polarisation model stated in Section 6.2.1. Understanding how and which TL properties affect cell performance is vital for informing future cell design. In particular, we demonstrate that the replacement of standard TL materials (Spiro-OMeTAD and TiO_2) with materials that have a lower permittivity and/or doping density leads to a shift in the scan rates at which J-V hysteresis is most pronounced to rates that are higher than those commonly used in experiment. Thus, this chapter provides a cogent explanation for why organic ETLs can yield seemingly "hysteresis-free" devices which nevertheless exhibit hysteresis at low temperature. In such devices, the decrease in the ion vacancy mobility with temperature compensates for the increase in the scans rates at which hysteresis occurs due to the use of low permittivity/doping organic TLs. Furthermore, we postulate that cells fabricated using TLs with a low permittivity and doping density are more stable with regard

to degradation, than those made using TLs with a high permittivity and doping density. The reason for this is that such cells show reduced ion vacancy accumulation within the perovskite Debye layers, which has been linked to chemical degradation at the edges of the perovskite.

In addition, simulations are used to classify features of a J-V curve that distinguish between cells in which charge carrier recombination occurs predominantly within the bulk of the perovskite and those where it occurs predominantly at the perovskite/TL interfaces. Once the rate-limiting recombination mechanism has been identified, the results of the last section provide suggestions for how to tune the TL properties to enhance performance. The relationship between the steady-state photo-current and material parameters, such as the TL doping density, for a PSC limited by interface recombination is analysed further in Chapter 7.

Chapter 7

An Analytic Expression for the Current Density

In all areas of solar cell research, it is common practice to compare experimental data to the standard Shockley diode equation in order to determine the performance-limiting recombination mechanism occurring within a cell. However, in the case of thin-film, perovskite cells, this approach has led to some unexpected results which cast doubt on its validity. This chapter addresses this issue and outlines the first steps towards the development of a new framework for understanding the potential of PSCs. By extending the asymptotic analysis of the non-dimensional drift-diffusion model performed in Chapter 5, a modified relationship between the current density J and the applied voltage V is derived and used to explain the anomalous findings for PSCs.

Firstly, analytic solutions for the charge carrier concentrations are derived by assuming that the three rates of recombination included in the charge transport model can be well-approximated by relevant monomolecular recombination rates, *i.e.* rates that depend on just one type of charge carrier. Simplification of the bulk recombination rate R is necessary to allow for analytic solutions of the (usually nonlinear) boundary value problem for the electron and hole concentrations across the perovskite bulk to be found, as in [34]. From the uniformly-valid approximations for the charge carrier concentrations, analytic expressions for the rates of recombination and hence the current density J are derived.

Secondly, the case of a steady-state J-V curve is considered, *i.e.* the case where the changes in applied voltage are sufficiently slow that the ion vacancies are in equilibrium with the experimental conditions and the electric field in the bulk of the perovskite layer is zero. Three physically justifiable assumptions are then applied to the analytic expression for the steady-state current density. The result of this analysis is a steady-state current density for a PSC limited by interface recombination which can be expressed simply in

terms of the four Debye layer potential drops $\mathcal{V}_{1-4}$ (see Figure 5.1). These potential drops may in turn be expressed in terms of the Debye layer charge density $\mathcal{Q}(t)$ obtained from the solution of a single ODE, that in (5.80). The final, simplified expression separates into a generation term (that depends only on the light intensity) subtracted by an expression for the dark current (which depends only on the recombination). As a result, this expression represents an improvement over the standard Shockley diode equation for describing the J-V curves of PSCs, held at steady state (the results are also valid for J-V scans conducted at sufficiently slow rates).

In Section 7.1, an overview of the use of the standard diode equation in the literature relating to PSCs is given. Analytic expressions for the charge carrier concentrations and current density are derived and compared to numerical solutions of the full model in Section 7.2. In this chapter, the numerical solutions are computed using the finite element scheme described in Section 4.3 and extended to three layers in Section B.2. The solutions are computed on a "tanh" grid with $N = 800$ and with temporal tolerances set with $\texttt{RelTol} = 10^{-10}$ and $\texttt{AbsTol} = 10^{-10}$. In Section 7.3, the steady-state current density is considered and a series of three approximations are used to derive an alternative to the standard Shockley diode equation. Finally, a summary and outlook for this work is given in Section 7.4.

7.1 Review of the diode theory for perovskite solar cells

Within the standard diode theory for solar cells, the J-V characteristics of a cell are approximated as those of a simple p-n junction [95]. A p-n junction is a device formed from a layer of a positively-doped material in contact with a layer of negatively-doped material. When an external voltage is applied across a p-n junction, the potential difference is dropped across a narrow region around the interface between the two materials. The ideal diode equation is derived from the drift-diffusion equations for a p-n junction in which the dominant recombination mechanism is a band-to-band process (occurring away from the interface). The non-ideal version of the diode equation takes the same form but introduces a fitting parameter n_{id} termed the ideality factor and is given (in dimensional terms) by

$$J = J_{\text{SC}} - J_{\text{dark}}(V)\,, \qquad J_{\text{dark}}(V) = J_0\left[\exp\left(\frac{V}{n_{\text{id}}V_T}\right) - 1\right], \tag{7.1}$$

in which J_{SC} is the short-circuit current density (which gives a good measure of the current generated in the cell by solar radiation), J_0 is the saturation current density in the dark and $V_T = k_BT/q$ is the thermal voltage. For $n_{\text{id}} = 1$, the equation reduces to the

ideal case in which band-to-band recombination dominates. Higher values of n_{id} indicate that another recombination mechanism is dominant. In particular, $n_{\mathrm{id}} = 2$ is typically interpreted to correspond to trap-assisted recombination across the interface, while $n_{\mathrm{id}} = 3$ signifies Auger recombination, see Figure 3.5. Other interpretations of the value of n_{id} are summarised in the Supplementary Information of [4]. The value of the ideality factor for a real cell can be estimated via the fitting of experimental J-V data to the non-ideal diode equation. Ideality factors can also be estimated from experimental measurements of the open-circuit voltage (V_{OC}) versus illumination intensity, electro-luminescence versus illumination intensity, or J-V curves measured in the dark, see [141].

In order to model a complete photovoltaic device, two additional terms are often included in the diode equation to account for the effects of series and shunt resistance, which may originate from elsewhere in the device (*e.g.* at other material interfaces). See, for example, [95]. With these additions, the non-ideal diode equation is able to provide an accurate description of the J-V characteristics of a typical inorganic (*e.g.* silicon) solar cell. However, these additional terms provide little information about the location of the associated recombination losses and do not account for the anomalous values of the ideality factor observed for PSCs. Therefore, the effects of both series and shunt resistance are not considered here.

Prior to the recognition of the importance of ion vacancy migration for explaining the J-V characteristics of a PSC, Agarwal *et al.* [2] made use of the standard diode theory to investigate the dominant form of recombination limiting the performance of five different PSC architectures fabricated in five different laboratories. It is reported that the value of the ideality factor is around 2 for all of the cells. However, more recent papers have reported anomalous ideality factors that are lower than 1 [33, 163] and some that are higher than 5 [104]. Such values are outside of the range predicted for a p-n junction and therefore cannot reliably be interpreted using the standard diode theory. In addition, ideality factors calculated from the derivative of a J-V curve are strongly voltage-dependent, as observed in [141, 150] and the Supporting Information of [4].

Almora *et al.* [3, 4] note that J-V hysteresis can interfere with estimations of the ideality factor from experimental J-V data and propose that the expression for the dark current density J_{dark}, given in (7.1), should be supplemented by the current loss due to shunt resistance and two new terms: a capacitive and a non-capacitive current. The capacitive current is defined to be proportional to the scan rate, while the non-capacitive current is chosen to satisfy an empirical formula. However, in the later work, these terms are neglected in order to find values of the ideality factor (defined as before) between 1.5 and 3, which are interpreted using the standard diode theory.

A different approach is taken in the following sections. The asymptotic analysis detailed

in Chapter 5 shows that the electric potential within the perovskite layer of a PSC is dominated by the ion vacancy distribution. As a result, the distribution of the electric potential evolves on a slower timescale than that of the charge carrier dynamics and has a notably different profile compared to a p-n junction, as shown by the simulation results in Figures 5.3-5.5. The electric potential across the three layers of a PSC displays a linear profile across the bulk of each layer and rapid changes across the narrow Debye layers either side of each interface, in contrast to the single potential drop across a p-n junction. As discussed in Chapter 6, the proportion of the total potential difference across each Debye layer (for a given Debye layer charge density $\mathcal{Q}$) depends on the relative values of the permittivity and majority carrier density of each material layer (via the values of Ω_E and Ω_H). The current losses (due to either bulk or interface recombination) depend on both the Debye layer potential differences $\mathcal{V}_{1-4}$ and the local charge carrier concentrations, which in turn also depend on the distribution of the electric potential across the cell. In the following sections, an expression for the current density in terms of the Debye layer potential differences is derived in order to examine the meaning of the ideality factor for J-V curves of PSCs measured at sufficiently slow scan rates.

7.2 Analysis based on monomolecular recombination rates

Here, we simplify the three rates of charge carrier recombination, in line with the parameter estimates given in Tables 3.2 and 3.3(b), to the following monomolecular rates.

$$R(n,p) = \gamma p\,, \qquad R_l = \gamma_l p|_{x=0^+}\,, \qquad R_r = \gamma_r n|_{x=1^-}\,. \tag{7.2}$$

Based on the findings of an experimental study of bulk recombination performed by Stranks *et al.* [131], an analogous approximation for the bulk recombination rate was previously made in Section 3.3 of [34] for the single-layer model. In order to substitute these monomolecular rates into the steady-state charge carrier BVP given by (5.97)-(5.100), the expressions are rewritten in terms of the leading-order bulk electron and hole concentrations ($n_0^{(\mathrm{B})}$ and $p_0^{(\mathrm{B})}$, respectively) as follows.

$$R(n_0^{(\mathrm{B})}, p_0^{(\mathrm{B})}) = \gamma p_0^{(\mathrm{B})}\,, \qquad R_l = \gamma_l \mathrm{e}^{-\mathcal{V}_2} p_0^{(\mathrm{B})}|_{x=0}\,, \qquad R_r = \gamma_r \mathrm{e}^{-\mathcal{V}_3} n_0^{(\mathrm{B})}|_{x=1}\,. \tag{7.3}$$

Fortuitously, as noted in [34], due to this physically relevant selection of recombination rates, the leading-order equations for the bulk hole concentration (5.98) decouple from those for the bulk electron concentration (5.97) and lead to a linear equation for the hole concentration $p_0^{(\mathrm{B})}$ in the perovskite layer. As a result, it is possible to derive the bulk hole concentration $p_0^{(\mathrm{B})}$ and, in turn, the bulk electron concentration $n_0^{(\mathrm{B})}$ as well as an

analytic expression for the total current density $J(t)$, as has previously been done for a single-layer model with zero interfacial recombination in [34] Section 3.3. The analysis is carried out in Sections 7.2.1-7.2.3 and verified against numerical solutions to the full charge transport model in Section 7.2.4.

7.2.1 Hole distribution

The leading-order bulk hole concentration $p_0^{(\mathrm{B})}$ is found from the steady-state BVP given by (5.98) along with boundary conditions extrapolated from (5.99)-(5.100), *i.e.* from

$$\frac{\partial j_0^{p(\mathrm{B})}}{\partial x} = I_s \bar{G}_l \mathrm{e}^{-l\Upsilon x} - \gamma p_0^{(\mathrm{B})}\,, \qquad j_0^{p(\mathrm{B})} = -\kappa_p \left(\frac{\partial p_0^{(\mathrm{B})}}{\partial x} - E_0 p_0^{(\mathrm{B})} \right), \tag{7.4}$$

$$\text{with} \quad j_0^{p(\mathrm{B})}|_{x=0} = -\gamma_l \mathrm{e}^{-\mathcal{V}_2} p_0^{(\mathrm{B})}|_{x=0}\,, \qquad p_0^{(\mathrm{B})}|_{x=1} = \mathrm{e}^{-\mathcal{V}_3-\mathcal{V}_4}\,, \tag{7.5}$$

in which the term $I_s \bar{G}_l \mathrm{e}^{-l\Upsilon x}$ is the dimensionless photo-generation rate (obeying the Beer-Lambert Law of light absorption) and E_0 is the constant value of the electric field across the bulk of the perovskite. In the boundary conditions, the exponential factors account for the rapid changes in the hole concentration across the Debye layers. The equations in (7.4) combine to give the following steady-state, second-order ODE.

$$\frac{\partial^2 p_0^{(\mathrm{B})}}{\partial x^2} - E_0 \frac{\partial p_0^{(\mathrm{B})}}{\partial x} - \frac{\gamma}{\kappa_p} p_0^{(\mathrm{B})} = -\frac{I_s \bar{G}_l}{\kappa_p} \mathrm{e}^{-l\Upsilon x}\,. \tag{7.6}$$

The general solution is as follows.

$$p_0^{(\mathrm{B})} = A_+ \mathrm{e}^{m_+ x} + A_- \mathrm{e}^{m_- x} - G_p \mathrm{e}^{-l\Upsilon x}\,, \tag{7.7}$$

where, after application of the two boundary conditions,

$$\begin{aligned} A_\pm &= \frac{(l\Upsilon + E_0 + d_l) G_p \mathrm{e}^{m_\mp} - (m_\pm + d_l)(\mathrm{e}^{-\mathcal{V}_3-\mathcal{V}_4} + G_p \mathrm{e}^{-l\Upsilon})}{(m_\mp + d_l)\mathrm{e}^{m_\mp} - (m_\pm + d_l)\mathrm{e}^{m_\pm}}\,, \\ d_l &= \frac{\gamma_l \mathrm{e}^{-\mathcal{V}_2}}{\kappa_p}\,, \qquad\qquad m_\pm = \frac{1}{2}\left(E_0 \pm \sqrt{E_0^2 + \frac{4\gamma}{\kappa_p}} \right), \\ G_p &= \frac{I_s \bar{G}_l}{\kappa_p \Upsilon(\Upsilon + lE_0) - \gamma}\,. \end{aligned} \tag{7.8}$$

The values of these parameters are dependent on the illumination intensity $I_s(t)$ and the evolution of the Debye layer charge density $\mathcal{Q}(t)$ via the time-dependent potential differences $\mathcal{V}_{1-4}$ and E_0.

7.2.2 Electron distribution

The steady-state BVP for the bulk electron concentration $n_0^{(\mathrm{B})}$, from (5.98)-(5.100), is

$$\frac{\partial j_0^{n(\mathrm{B})}}{\partial x} = -\left(I_s \bar{G}_l \mathrm{e}^{-l\Upsilon x} - \gamma p_0^{(\mathrm{B})}\right), \quad j_0^{n(\mathrm{B})} = \kappa_n \left(\frac{\partial n_0^{(\mathrm{B})}}{\partial x} + E_0 n_0^{(\mathrm{B})}\right), \tag{7.9}$$

$$\text{with} \quad n_0^{(\mathrm{B})}|_{x=0} = \mathrm{e}^{-\mathcal{V}_1-\mathcal{V}_2}, \qquad j_0^{n(\mathrm{B})}|_{x=1} = -\gamma_r \mathrm{e}^{-\mathcal{V}_3} n_0^{(\mathrm{B})}|_{x=1}. \tag{7.10}$$

Given that the bulk hole concentration $p_0^{(\mathrm{B})}$ takes the form given in (7.7), the problem for the electrons is again reduced to finding the solution to one second-order ODE. From (7.9), the relevant ODE is

$$\frac{\partial^2 n_0^{(\mathrm{B})}}{\partial x^2} + E_0 \frac{\partial n_0^{(\mathrm{B})}}{\partial x} = \frac{\gamma}{\kappa_n} p_0^{(\mathrm{B})} - \frac{I_s \bar{G}_l}{\kappa_n} \mathrm{e}^{-l\Upsilon x}. \tag{7.11}$$

Hence, the general solution for the bulk electron concentration is

$$n_0^{(\mathrm{B})} = \mathrm{e}^{-\mathcal{V}_1-\mathcal{V}_2} - \frac{B(\mathrm{e}^{-E_0 x}-1)}{d_r(\mathrm{e}^{-E_0}-1)-E_0} + A'_+(\mathrm{e}^{m_+ x}-1) + A'_-\mathrm{e}^{m_- x} - G_n \mathrm{e}^{-l\Upsilon x}, \tag{7.12}$$

where

$$\begin{aligned}
A'_\pm &= \frac{\gamma A_\pm}{\kappa_n m_\pm (m_\pm + E_0)}, \\
d_r &= \frac{\gamma_r \mathrm{e}^{-\mathcal{V}_3}}{\kappa_n}, \qquad\qquad G_n = \frac{\kappa_p(\Upsilon + lE_0)G_p}{\kappa_n(\Upsilon - lE_0)}, \\
B &= (E_0 + d_r)[A'_+(\mathrm{e}^{m_+}-1) + A'_-(\mathrm{e}^{m_-}-1) + G_n(e^{-l\Upsilon}-1) + \mathrm{e}^{-\mathcal{V}_1-\mathcal{V}_2}] \\
&\quad + A'_+ m_+ \mathrm{e}^{m_+} + A'_- m_- \mathrm{e}^{m_-} + l\Upsilon G_n \mathrm{e}^{-l\Upsilon}.
\end{aligned} \tag{7.13}$$

As before, the values of these parameters depend on the illumination intensity $I_s(t)$ and the evolution of the Debye layer charge density $\mathcal{Q}(t)$ via the time-dependent potential differences $\mathcal{V}_{1-4}$ and E_0.

7.2.3 Total current density

From (5.108), the leading-order current density generated by the PSC is given by

$$J = \int_0^1 \left[G - R\left(n_0^{(\mathrm{B})}, p_0^{(\mathrm{B})}\right)\right] \mathrm{d}x - R_l - R_r.$$

Simplifying the recombination rates to the monomolecular rates given in (7.3) leads to

$$J = I_s - \gamma \int_0^1 p_0^{(\mathrm{B})} \,\mathrm{d}x - \gamma_l \mathrm{e}^{-\mathcal{V}_2} p_0^{(\mathrm{B})}|_{x=0} - \gamma_r \mathrm{e}^{-\mathcal{V}_3} n_0^{(\mathrm{B})}|_{x=1} \,. \tag{7.14}$$

Substituting in the expressions for the bulk hole and electron concentrations from (7.7) and (7.12) gives

$$\begin{aligned} J = I_s &- \gamma \left(\frac{A_+(\mathrm{e}^{m_+} - 1)}{m_+} + \frac{A_-(\mathrm{e}^{m_-} - 1)}{m_-} + \frac{G_p(\mathrm{e}^{-l\Upsilon} - 1)}{l\Upsilon} \right) \\ &- \gamma_l \mathrm{e}^{-\mathcal{V}_2} \left(A_+ + A_- - G_p \right) \\ &- \gamma_r \mathrm{e}^{-\mathcal{V}_3} \left(\mathrm{e}^{-\mathcal{V}_1 - \mathcal{V}_2} - \frac{B(\mathrm{e}^{-E_0} - 1)}{d_r(\mathrm{e}^{-E_0} - 1) - E_0} \right. \\ &\qquad \left. + A'_+(\mathrm{e}^{m_+} - 1) + A'_-(\mathrm{e}^{m_-} - 1) - G_n(\mathrm{e}^{-l\Upsilon} - 1) \right) \,. \end{aligned} \tag{7.15}$$

This result provides the leading order current density generated by the PSC in terms of the time-dependent variables I_s, $\mathcal{V}_{1-4}$ and E_0. The illumination intensity $I_s(t)$ is an input variable, while the potential differences $\mathcal{V}_{1-4}$ and the constant bulk electric field E_0 are determined, using (5.75) and (5.96), in terms of the Debye layer charge density $\mathcal{Q}(t)$. The evolution of $\mathcal{Q}(t)$ must be found numerically from the ODE given in (5.80) and depends on the second input variable, namely the applied voltage.

7.2.4 Verification of the choice of monomolecular rates

Here, the accuracy of analytic solutions, derived using the monomolecular recombination rates given in (7.3) is demonstrated, via comparison to numerical solutions of the full charge transport model, for the parameters given in Tables 3.2 and 3.3(b) (which describe a PSC limited by interface recombination).

The uniformly-valid approximations for the electron and hole concentrations, plotted in Figure 7.1, are obtained from substituting the expressions given in (7.7) and (7.12) for the bulk region into (5.103) and (5.104), respectively. The asymptotic results derived from the assumption of monomolecular recombination rates show excellent agreement to numerical solutions of the full charge transport model for the chosen parameter set during a linear decrease of the applied voltage.

Figure 7.2 shows the reverse and forward scans of J-V curves measured at different scan rates for the two sets of recombination parameters that are studied in Chapter 6, *i.e.* Sets (a) and (b) in Table 3.3. The crosses represent the asymptotic expressions derived from the monomolecular recombination rates, while the solid lines correspond to the current density computed from numerical solutions of the full charge transport model. The results

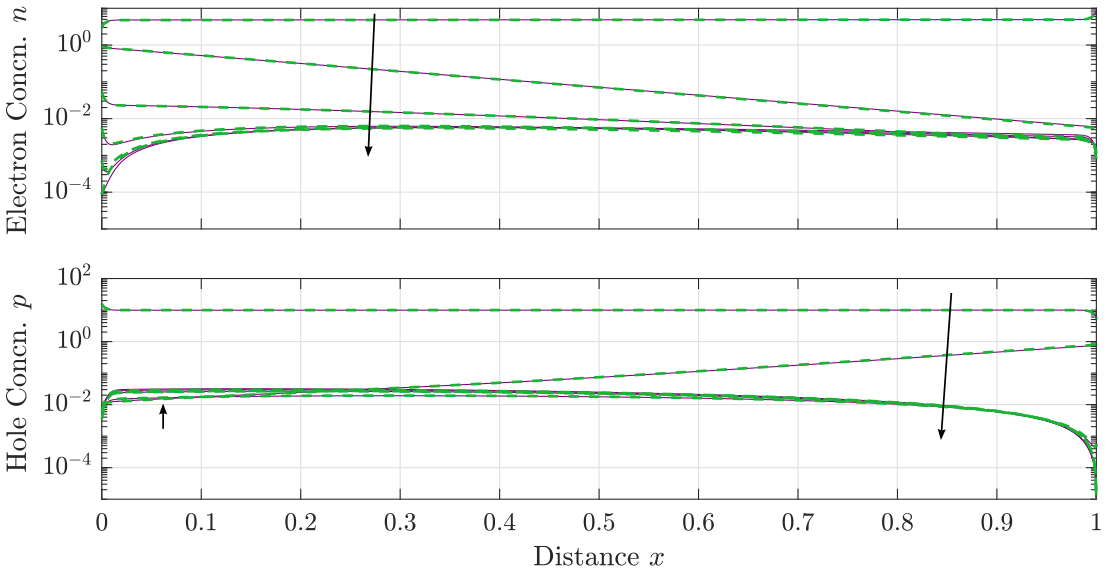

FIGURE 7.1: Comparison between the uniformly-valid approximations (green dashed lines) and numerical solutions of the full charge transport model (purple solid lines) for the dimensionless electron concentration (top) and hole concentration (bottom) across the perovskite layer of a three-layer PSC during a linear decrease in applied voltage from 1.2 V to 0 V over 4.8 s (corresponding to a scan rate of 250 mV/s), after preconditioning at 1.2 V for 5 s. Plots correspond to six evenly-spaced times between (and including) 0 and 4.8 s through the voltage scan. The parameters from Tables 3.2 and 3.3(b) are used. Arrows show the direction of increasing time.

compare very well for the range of scan rates commonly used in experiment. In panel (a), good agreement is demonstrated for the J-V curves corresponding to a PSC dominated by bulk recombination, up to a scan rate of around 250 mV/s. At faster scan rates (not shown), the monomolecular bulk recombination rate overestimates the amount of bulk recombination because the rate is not limited when the concentration of the opposite type of charge carrier (the electrons) becomes very small. However, the simplification of the bulk recombination rate to a monomolecular rate is shown to be a valid and accurate approximation for realistic voltage scan rates. This is in agreement with the conclusions of the analysis of the single-layer model in [34]. In panel (b), in which the J-V curves are dominated by interface (rather than bulk) recombination, good agreement is shown up to a higher scan rate of around 1 V/s. On a closer inspection of the J-V curves corresponding to the slowest scan rate in each case, the uniformly-valid asymptotic expansions are a very good approximation of the full numerical solutions. In the following sections, the expression for the current density J in (7.14) is investigated and simplified further in the case of scan rates that are sufficiently slow that the ion vacancy distribution remains in quasi-equilibrium with the applied voltage throughout the measurement (and hence there is no difference between the forward and reverse scans of the J-V curve).

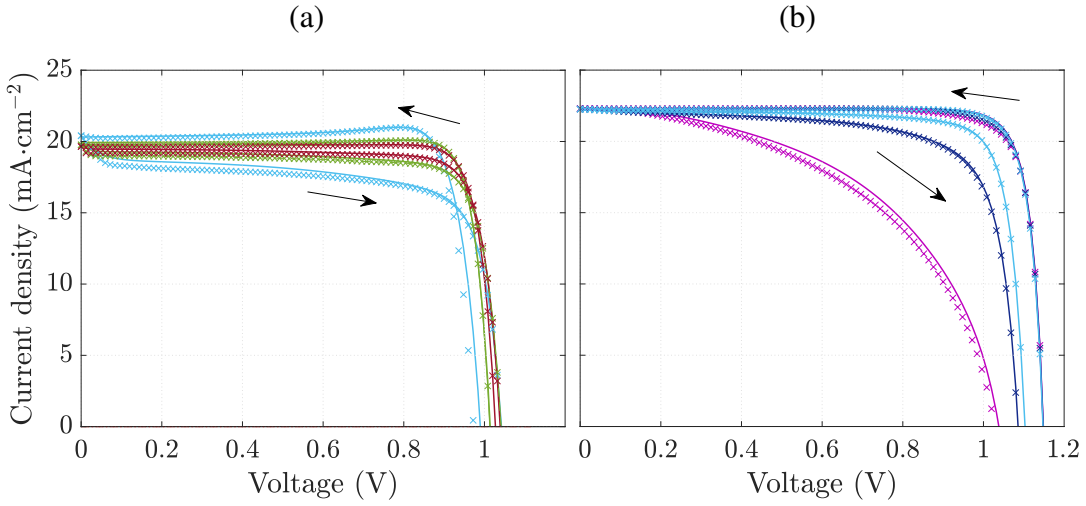

FIGURE 7.2: Comparison between J-V curves calculated from the asymptotic expressions based on monomolecular rates (crosses) and from numerical solution of the full charge transport model (solid lines). (a) J-V curves simulated at 50 mV/s (red), 100 mV/s (green) and 250 mV/s (light blue), using the bulk-dominated recombination parameters in Table 3.3(a). (b) J-V curves simulated at 250 mV/s (light blue), 500 mV/s (dark blue) or 1 V/s (pink), using the interface-dominated recombination parameters in Table 3.3(b). The simulation protocol includes a 5 s preconditioning step at 1.2 V before the J-V scan is simulated. Other parameters are as in Table 3.2. Arrows indicate the direction of scan.

7.3 Simplified expressions for the current density

In this section, a series of approximations are applied to the analytic expression for the current density J given in (7.15). Each approximation and corresponding expression for the current density is detailed at every step to allow for further analysis and interrogation of these results in future work. The approximations are consistent with parameter estimates for a PSC limited by interface recombination. As noted in Chapter 6, recent experimental work on PSCs with a $MAPbI_3$ perovskite layer indicates that interface, rather than bulk, recombination is now the performance-limiting mechanism [72, 153]. The result of the simplifications is an expression that takes a similar form to that of the standard diode equation (see Section 7.1) but which shows some important modifications relating to the effect of the distribution of the electric potential across a PSC resulting from the accumulation of ion vacancies. The simplified expression for J is compared to a numerical solution of the full transport model in Section 7.3.4 for a range of parameter values.

7.3.1 The steady state limit

The first simplification is to restrict this analysis to the simulation of steady state J-V curves. The steady state simplification is encapsulated in the assumption that the bulk

electric field E_0 is zero. Substituting the limit $E_0 = 0$ into the definition of the bulk electric field given in (5.96) gives

$$0 = \Phi_{bi} - \Phi(t) - \mathcal{V}_1 - \mathcal{V}_2 - \mathcal{V}_3 - \mathcal{V}_4 \,, \tag{7.16}$$

in which the non-dimensional applied voltage is denoted by Φ. This equation is an implicit equation for the steady-state Debye layer charge density $\mathcal{Q}$ at any given time t, from which the potential differences $\mathcal{V}_{1-4}$ can be determined directly using (5.75).

Applying the limit $E_0 = 0$ to the expression for the steady-state current density J in (7.15) gives

$$\begin{aligned} J = I_s &- \gamma \left(\frac{A_+(\mathrm{e}^{M} - 1)}{M} - \frac{A_-(\mathrm{e}^{-M} - 1)}{M} + \frac{G_p(\mathrm{e}^{-l\Upsilon} - 1)}{l\Upsilon} \right) \\ &- \gamma_l \mathrm{e}^{-\mathcal{V}_2} \left(A_+ + A_- - G_p \right) \\ &- \gamma_r \mathrm{e}^{-\mathcal{V}_3} \left(\mathrm{e}^{-\mathcal{V}_1 - \mathcal{V}_2} - \frac{B}{d_r + 1} + A'_+(\mathrm{e}^{M} - 1) + A'_-(\mathrm{e}^{-M} - 1) \right. \\ &\qquad \left. - G_n(\mathrm{e}^{-l\Upsilon} - 1) \right) \,, \end{aligned} \tag{7.17}$$

in which $M = \sqrt{\gamma/\kappa_p}$ and, from (7.8) and (7.13),

$$\begin{aligned} A_\pm &= \frac{\mp(l\Upsilon + d_l) G_p \mathrm{e}^{\mp M} \pm (d_l \pm M)(\mathrm{e}^{-\mathcal{V}_3 - \mathcal{V}_4} + G_p \mathrm{e}^{-l\Upsilon})}{(d_l + M)\mathrm{e}^{M} - (d_l - M)\mathrm{e}^{-M}} \,, \\ A'_\pm &= \frac{\kappa_p A_\pm}{\kappa_n} \,, \qquad d_l = \frac{\gamma_l \mathrm{e}^{-\mathcal{V}_2}}{\kappa_p} \,, \qquad d_r = \frac{\gamma_r \mathrm{e}^{-\mathcal{V}_3}}{\kappa_n} \,, \\ G_p &= \frac{I_s \bar{G}_l}{\kappa_p(\Upsilon^2 - M^2)} \,, \qquad G_n = \frac{\kappa_p G_p}{\kappa_n} \,, \\ B &= d_r[A'_+(\mathrm{e}^{M} - 1) + A'_-(\mathrm{e}^{-M} - 1) + G_n(e^{-l\Upsilon} - 1) + \mathrm{e}^{-\mathcal{V}_1 - \mathcal{V}_2}] \\ &\quad + A'_+ M \mathrm{e}^{M} - A'_- M \mathrm{e}^{-M} + l\Upsilon G_n \mathrm{e}^{-l\Upsilon} \,. \end{aligned} \tag{7.18}$$

7.3.2 Further simplifying approximations

1) Assumption that diffusion across the perovskite dominates over the trapping of charge carriers in interfacial trap states ($d_l,\ d_r \to 0$). The parameter d_l is the ratio between the dimensionless rate of trapping of holes near the ETL/perovskite interface ($\gamma_l \mathrm{e}^{-\mathcal{V}_2}$), see (7.3b), and the dimensionless diffusion coefficient for holes in the perovskite (κ_p). Similarly, the parameter d_r is the ratio between the dimensionless rate of trapping of electrons near the perovskite/HTL interface ($\gamma_r \mathrm{e}^{-\mathcal{V}_3}$), see (7.3c), and the dimensionless diffusion coefficient for electrons in the perovskite (κ_n). Here, it is assumed that, for

a cell operating in its power generating regime (*i.e.* $0 \leq V \leq V_{\mathrm{OC}}$), the process of diffusion dominates over the rate of recombination via interfacial trap states, for both holes and electrons within the perovskite, *i.e.* that $\kappa_p \gg \gamma_l \mathrm{e}^{-\mathcal{V}_2}$ and $\kappa_n \gg \gamma_r \mathrm{e}^{-\mathcal{V}_3}$. In particular, for an applied voltage that is around the built-in voltage, $\mathcal{V}_2$ and $\mathcal{V}_3$ are small and so $\mathrm{e}^{-\mathcal{V}_2}$, $\mathrm{e}^{-\mathcal{V}_3} = O(1)$. Using the parameter estimates in Tables 3.2 and 3.3(b) gives $d_l \approx 0.024$ and $d_r \approx 2.4 \times 10^{-4}$. Formally taking the limits d_l, $d_r \to 0$ in the previous expression for the steady-state current density J gives

$$\begin{aligned} J = I_s &- \gamma \left(\frac{A_+(\mathrm{e}^M - 1)}{M} - \frac{A_-(\mathrm{e}^{-M} - 1)}{M} + \frac{G_p(\mathrm{e}^{-l\Upsilon} - 1)}{l\Upsilon} \right) \\ &- \gamma_l \mathrm{e}^{-\mathcal{V}_2} \left(A_+ + A_- - G_p \right) \\ &- \gamma_r \mathrm{e}^{-\mathcal{V}_3} \left(\mathrm{e}^{-\mathcal{V}_1 - \mathcal{V}_2} - B + A'_+(\mathrm{e}^M - 1) + A'_-(\mathrm{e}^{-M} - 1) \right. \\ &\qquad \left. - G_n(\mathrm{e}^{-l\Upsilon} - 1) \right) , \end{aligned} \tag{7.19}$$

in which

$$\begin{aligned} A_\pm &= \frac{\mp l\Upsilon G_p \mathrm{e}^{\mp M} + M(\mathrm{e}^{-\mathcal{V}_3 - \mathcal{V}_4} + G_p \mathrm{e}^{-l\Upsilon})}{M(\mathrm{e}^M + \mathrm{e}^{-M})} , \qquad A'_\pm = \frac{\kappa_p A_\pm}{\kappa_n}, \\ G_p &= \frac{I_s \bar{G}_l}{\kappa_p(\Upsilon^2 - M^2)} , \qquad G_n = \frac{\kappa_p G_p}{\kappa_n} , \\ B &= A'_+ M \mathrm{e}^M - A'_- M \mathrm{e}^{-M} + l\Upsilon G_n \mathrm{e}^{-l\Upsilon} . \end{aligned} \tag{7.20}$$

2) Limit of ideal extraction ($M \to 0$). To simplify this expression still further, the next limit that is taken is $M \to 0$. In terms of physical properties, the non-dimensional parameter $M = b/\sqrt{\tau_p D_p}$ is the ratio between the perovskite width (b) and the hole diffusion length ($\sqrt{\tau_p D_p}$). Thus, the limit $M \to 0$ describes a cell in which the likelihood of a hole being extracted from the perovskite layer is significantly greater than that of it recombining via the capture of a free electron; a reasonable assumption for a high performing PSC. It should be noted that taking this limit does not eliminate the bulk recombination term, but means that it is not the dominant form of recombination. Using the parameter estimates in Tables 3.2 and 3.3(b), for a cell dominated by interface recombination, $M \approx 0.056$.

Upon taking $M \to 0$, the terms involving $A'_\pm$ cancel out, leaving

$$\begin{aligned} J = I_s &- \gamma \left(\mathrm{e}^{-\mathcal{V}_3 - \mathcal{V}_4} + G_p \left(\mathrm{e}^{-l\Upsilon} + \frac{l\Upsilon}{2} + \frac{\mathrm{e}^{-l\Upsilon} - 1}{l\Upsilon} \right) \right) \\ &- \gamma_l \mathrm{e}^{-\mathcal{V}_2} \left(\mathrm{e}^{-\mathcal{V}_3 - \mathcal{V}_4} + G_p \left(l\Upsilon + \mathrm{e}^{-l\Upsilon} - 1 \right) \right) \\ &- \gamma_r \mathrm{e}^{-\mathcal{V}_3} \left(\mathrm{e}^{-\mathcal{V}_1 - \mathcal{V}_2} + G_n(1 - \mathrm{e}^{-l\Upsilon} - l\Upsilon \mathrm{e}^{-l\Upsilon}) \right) , \end{aligned} \tag{7.21}$$

in which

$$G_p = \frac{I_s \bar{G}_l}{\kappa_p \Upsilon^2}\,, \qquad G_n = \frac{I_s \bar{G}_l}{\kappa_n \Upsilon^2}\,. \tag{7.22}$$

3) Assumption of moderate illumination (G_p, $G_n \to 0$). The values of G_p and G_n corresponding to the equivalent of 1 Sun illumination are estimated, respectively, to be 0.013 and 7.1×10^{-5} for a standard architecture PSC (with $l = 1$) and 9.2×10^{-3} and 5.1×10^{-5} for an inverted-architecture PSC (with $l = -1$). Therefore, it is here assumed that these terms are also small in comparison to the other terms for applied voltages near V_{bi}. Neglecting G_p and G_n from the previous expression for the steady-state current density J gives

$$J = I_s - \gamma \mathrm{e}^{-\mathcal{V}_3 - \mathcal{V}_4} - \gamma_l \mathrm{e}^{-\mathcal{V}_2 - \mathcal{V}_3 - \mathcal{V}_4} - \gamma_r \mathrm{e}^{-\mathcal{V}_1 - \mathcal{V}_2 - \mathcal{V}_3}\,. \tag{7.23}$$

Notably, this expression takes a similar form to that of the standard diode equation, in that I_s is independent of the applied voltage, while the following three terms are independent of the photo-generation parameters and constitute the current density in the dark (due to recombination).

7.3.3 Dimensional steady-state current density

By rescaling according to the non-dimensionalisation in Section 3.5.1, the simplified expression for the steady-state current density in (7.23) becomes

$$J^{\text{dim}}(V) = J_s - J_{\text{dark}}(V)\,, \tag{7.24}$$

where

$$J_s = qG_0 b I_s = qI_s F^{ph}(1 - \mathrm{e}^{-\alpha b})\,, \tag{7.25}$$

$$\begin{aligned} J_{\text{dark}}(V) = J_b \exp\left(\frac{V - V_{bi} + V_1 + V_2}{V_T}\right) + J_l \exp\left(\frac{V - V_{bi} + V_1}{V_T}\right) \\ + J_r \exp\left(\frac{V - V_{bi} + V_4}{V_T}\right)\,, \end{aligned} \tag{7.26}$$

in which the dimensional potential differences V_{1-4} and the dimensional constants J_b, J_l and J_r are as follows, while all other dimensional parameters are defined, along with estimated values taken from the literature, in Tables 3.2 and 3.3. The dimensional constants

with the units of a current density are defined by

$$J_b = qG_0 b\gamma = \frac{qbN_V}{\tau_p} \exp\left(\frac{E_V - E_{f_H}}{qV_T}\right), \tag{7.27}$$

$$J_l = qG_0 b\gamma_l = q\nu_{p,E} N_V \exp\left(\frac{E_V - E_{f_H}}{qV_T}\right), \tag{7.28}$$

$$J_r = qG_0 b\gamma_r = q\nu_{n,H} N_C \exp\left(-\frac{E_C - E_{f_E}}{qV_T}\right). \tag{7.29}$$

In contrast, the Debye layer potential differences V_{1-4} must be determined numerically via the solution of an implicit equation for the Debye layer charge density $\mathcal{Q}$ which, from (7.16), is given by

$$V_{bi} - V(t) = V_1 + V_2 + V_3 + V_4\,, \tag{7.30}$$

where

$$\begin{aligned} &V_1 = -f(-\Omega_E \mathcal{Q})\,, \quad V_2 = -f(-\mathcal{Q})\,, \quad V_3 = f(\mathcal{Q})\,, \\ &V_4 = -f(-\Omega_H \mathcal{Q})\,, \quad \Omega_E = \sqrt{\tfrac{\varepsilon_p N_0}{\varepsilon_E d_E}}\,, \quad \Omega_H = \sqrt{\tfrac{\varepsilon_p N_0}{\varepsilon_H d_H}}\,, \end{aligned} \tag{6.3 repeated}$$

in which the function $f(\mathcal{Q})$ is the inverse of the function

$$\mathcal{Q}(V) = qN_0 L_D \,\mathrm{sign}(V)\sqrt{2}\left(\mathrm{e}^{V/V_T} - V/V_T - 1\right)^{\frac{1}{2}}. \tag{6.4 repeated}$$

Note that there are two important outcomes from this section. Firstly, via careful application of approximations, the task of simulating a steady-state J-V curve of a PSC has been reduced to finding the numerical solution to a single implicit equation for the charge density $\mathcal{Q}$, followed by substitution into (7.24). Secondly, the definitions of the dimensional parameters that appear the expression for the current density in (7.24) provide a vital link between physical properties of the materials that comprise the three core layers of a PSC and its overall performance as a solar cell during steady-state operation.

7.3.4 Verification of approximations

The first verification of the simplified expression for the steady-state current density J given in (7.24)-(7.29) is to confirm that the shape of a steady state J-V curve, for a PSC dominated by interface recombination, is approximately independent of the illumination intensity. In Figure 7.3, steady-state J-V curves for light intensities of 0.25, 0.5, 0.75 and 1 times the equivalent of 1 Sun illumination are shown. The close agreement between the approximate expression (crosses) and numerical simulations of the full model (solid

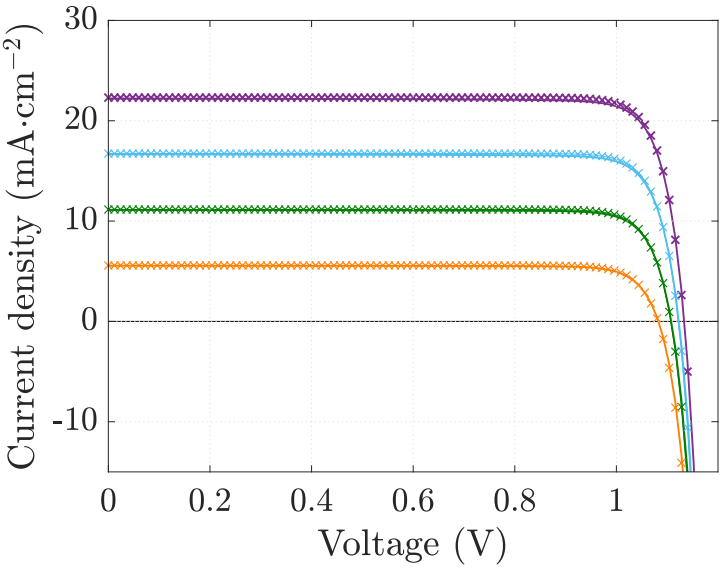

FIGURE 7.3: A comparison between the steady-state current density calculated from the simplified expression given in (7.24)-(7.29) (crosses) and a numerical solution of the full model for a slow scan measured at 1 mV/s (solid lines) for different values of the illumination intensity. Lowest to highest: $I_s = 0.25$, 0.5, 0.75 and 1 Sun equivalent. Parameter values are those given in Tables 3.2 and 3.3(b), which describe a PSC limited by interface recombination.

lines) indicate that the approximations applied in Section 7.3 are valid for the parameter set given in Tables 3.2 and 3.3(b).

The example curves in Figure 7.3 display the particularly high fill factors achieved by state-of-the-art PSCs in recent experimental reports *e.g.* [19, 102, 129, 135, 157]. The unusually high fill factors, compared to other solar cell technologies, are a sign of the promising potential of PSCs. However, in reality, the effects of series and shunt resistance (arising, for example, from contact resistances and short circuits caused by imperfections in the cell's construction) reduce the performance of any photovoltaic device below its ideal behaviour, as investigated here.

Next, the validity of the approximations for a wider set of parameter values is tested. In particular, the effects of variation in the TL effective doping densities, interface recombination velocities and the Fermi levels of the TLs are investigated. The results are shown in Figure 7.4. The assumptions made in Section 7.3 are again shown to lead to a good approximation for the steady-state current density J in the parameter regimes of interest and capture the effects of changing each of the physical parameters, particularly in the region near open-circuit. These results indicate that the simplified expression is able to provide an accurate prediction of the open-circuit voltage for a PSC in terms of key physical properties.

Notably, one commonly-used way to calculate the standard ideality factor is based on

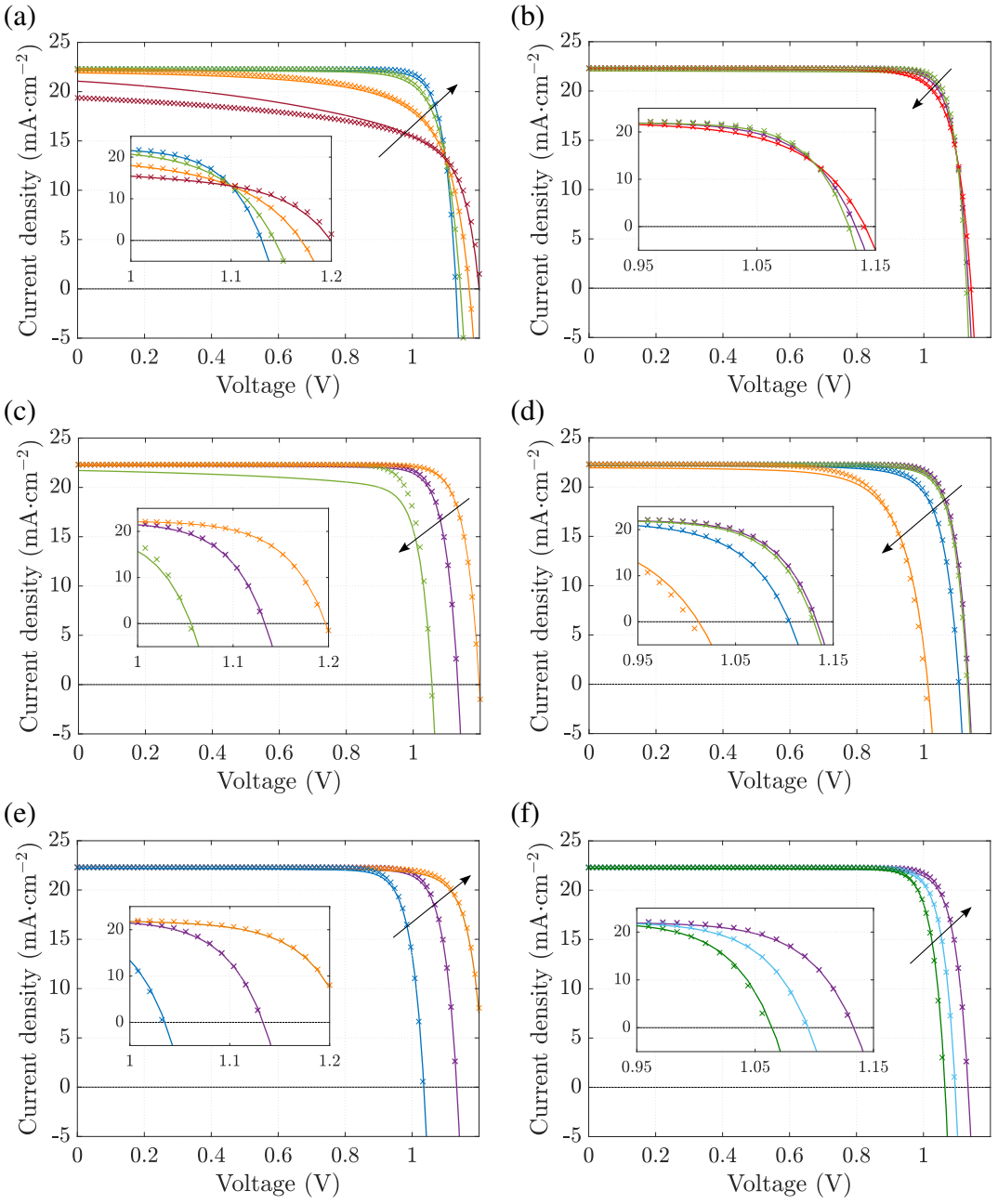

FIGURE 7.4: As for Figure 7.3 but for variations in (a) the effective doping density in the ETL: $d_E = 10^{[22,\,23,\,24,\,25]}$ m^{-3}; (b) the effective doping density in the HTL: $d_H = 5 \times 10^{[23,\,24,\,25]}$ m^{-3}; (c) the hole recombination velocity towards the ETL/perovskite interface: $\nu_{p,E} = [1,\ 10,\ 100]$ ms^{-1}; (d) the electron recombination velocity towards to the perovskite/HTL interface: $\nu_{n,H} = [0.1,\ 1,\ 10,\ 100]$ ms^{-1}; (e) the Fermi level of the ETL: $E_{f_E} = [-4.1,\ -4.0,\ -3.9]$ eV; and, (f) the Fermi level of the HTL: $E_{f_H} = [-5.3,\ -5.2,\ -5.1]$ eV. Arrows indicate the direction in which the value of the varied parameter increases. All other parameters are those for a PSC with dominant interface recombination given in Tables 3.2 and 3.3(b). Insets show a magnified view of the region near the open-circuit voltages.

the relationship between the open-circuit voltage and illumination intensity. Figures 7.3 and 7.4 show that the new expression derived in this chapter is able to accurately predict the V_{OC} for a range of cells limited by interface recombination. These results provide motivation for further work in this area.

7.4 Summary and outlook

In summary, the surface polarisation model derived in Chapter 5 can be further analysed to obtain a simple, but informative, result for the theoretical potential of a PSC. Following on from the discovery of the importance of two particular material properties in Chapters 5 and 6, the simplified steady-state current density derived here reveals the dominant effect of each model parameter on the theoretical power output of a PSC. As a result, the relationship between adjustable physical properties and the predicted power output could be used to help PSC researchers identify the location of the limiting recombination mechanism in a particular cell architecture and to optimise cell design for maximum power output. It is interesting to note that, according to the simplified expression, there is theoretically no intrinsic difference between standard- and inverted architecture cells. This observation lends support to the diversified approach taken by the perovskite solar cell community in studying both kinds of PSC architecture.

In this chapter, firstly, a set of analytic expressions for the charge carrier concentrations in the perovskite bulk and hence the rates of recombination and resulting photo-current density are derived for the case of monomolecular rates. By comparison to numerical simulations, it is shown that these analytic solutions are accurate for J-V curves measured at slow scan rates for the same two sets of cell parameters as studied in Chapter 6. Further to this, the case of a steady-state J-V curve is analysed. A series of three simplifications to the analytic expression for the steady-state current density is used to derive an alternative expression to the standard Shockley diode equation for PSCs. In the new expression for the dark current density J_{dark}, the effects of ionic accumulation are incorporated via the values of the potential drops V_{1-4}, which depend on the Debye layer charge density $\mathcal{Q}$ and the two key dimensionless parameters discussed in Chapter 6 (namely, Ω_E and Ω_H).

The appearance of the potential drops V_{1-4} in the alternative expression for the dark current density provides a reason why the standard diode theory does not fit experimental measurements of PSCs. An alternative interpretation of the ideality factor based on the results of this chapter could explain the experimental measurements of ideality factors outside the range predicted by the standard diode theory. A simple analytic expression,

such as (7.24), could be a valuable and practical tool for researchers in the field of PSCs, to use alongside detailed numerical modelling, to quantify the effects of ionic accumulation and interface recombination on the steady-state performance of PSCs.

Chapter 8

Conclusions and Future Directions

Charge-transport modelling is a useful tool which can be used to guide the future development of the emerging technology of perovskite solar cells in a thorough and sustainable way. The methods of solution developed in this work provide a step forward that has the potential to make a significant contribution to the research field by unravelling the complex interplay between ion vacancy migration and the electrical behaviour exhibited by a PSC. In this final chapter, the conclusions of this work are drawn together and possible future research directions are discussed.

In this study, complementary use is made of two distinct mathematical methods of solution. Both asymptotic analysis and numerical techniques are used to investigate ion vacancy migration as the cause of hysteresis in the current-voltage curves of PSCs. This combined approach has successfully led to a number of important advances in the development of methods able to obtain accurate solutions to the drift-diffusion model (set out in Chapter 3) for realistic values of the parameters and within realistic operating regimes. The method of matched asymptotic expansions is used to systematically reduce the problem to a much simplified model, termed the surface polarisation model. In this way, the asymptotic analysis is able to highlight the key mechanisms and physical parameters that control the performance of a PSC. In particular, the asymptotic analysis (which follows the analysis of a single-layer model presented by Richardson *et al.* [34, 109]) shows that rapid changes in solution occur within narrow boundary layers, termed Debye layers, adjacent to the interfaces between the perovskite and each transport layer. This knowledge informed the choice to test two non-uniform spatial grids for the calculation of numerical solutions. The choice of a non-uniform grid, in which points are clustered within the Debye layers, turns out to be crucial for maintaining accuracy in a numerical solution as it is evolved forward in time. In Section 4.5, the performances of three different numerical schemes on two different non-uniform grids are tested. It is shown that, independent of

the numerical method, the tanh grid defined in (4.76) outperforms the Chebyshev grid in terms of numerical accuracy versus computation time.

The numerical scheme based upon finite differences (presented in Section 4.4 and extended to three layers in Section B.1) has already contributed to a combined theoretical and experimental study published by Idígoras *et al.* [67]. In this paper, the finite difference code is used to qualitatively reproduce and explain the main features of two J-V curves corresponding to different types of PSC, in which only the structure of the electron transport layer is modified. The different behaviour displayed by the cells is explained by a shift from dominant bulk to dominant interface recombination. The finite difference method was also used to acquire the simulation results presented in Chapters 5 and 6. However, the more recently developed finite element scheme (presented in Section 4.3 and extended to three layers in Section B.2) shows improved accuracy versus run time over the finite difference scheme. Indeed, the finite element method takes only a few seconds to simulate a typical voltage protocol, namely a J-V curve, on a standard personal computer. At present, the finite element scheme is the fastest published method for solving PSC models, that incorporate both ion vacancy motion and charge carrier transport, within realistic parameter regimes [35].

While asymptotic results guided the development of the numerical methods, in turn, the ability to obtain accurate numerical solutions is useful for verifying the validity of the asymptotic results derived from the surface polarisation model in Chapter 5. Very good agreement is found, in Section 5.5, between the uniformly-valid asymptotic expansions and numerical solutions of the full model for a set of typical measurement protocols. This agreement provides the justification for using the surface polarisation model (described in dimensional terms in Section 6.2.1) to interpret the simulation results presented in Chapter 6. The results also highlight the importance of studying a model that explicitly describes the three layers of a PSC, as it is found that the distribution of the electric potential across the three layers plays a crucial role in determining both the transient and steady-state performance of a PSC. In particular, the analysis identifies two key dimensionless parameters that control the proportion of the electric potential that falls across each region of a PSC (see Figure 5.1). The two dimensionless parameters are:

$$\Omega_E = \sqrt{\frac{\varepsilon_p N_0}{\varepsilon_E d_E}}, \qquad \Omega_H = \sqrt{\frac{\varepsilon_p N_0}{\varepsilon_H d_H}}, \tag{8.1}$$

in which N_0 is the mean density of iodide ion vacancies within the perovskite layer, $d_{E,H}$ are the effective doping densities of the electron/hole transport layers and ε denotes the permittivity of the layer indicated by the subscript. Crucially, the permittivity and doping density of each transport layer are physical properties which may be varied experimentally via the choice of different transport layer materials and level of doping.

The ways in which ion vacancy migration affects the J-V characteristics of a PSC are studied in Chapter 6. Numerical simulations of the full model confirm that the extent of J-V hysteresis is strongly affected by the values of Ω_E and Ω_H. In particular, variations in these parameters shift the scan rates at which J-V hysteresis appears. This finding offers the first plausible explanation of the experimental observation that devices with organic transport layers typically exhibit a lower degree of hysteresis than those with inorganic transport layers. Devices with organic transport layers have previously been incorrectly labelled "hysteresis-free" cells in the literature due to the absence of hysteresis observed using standard experimental protocols. In fact, the effects of hysteresis reappear at the standard scan rates if the cell is cooled to very low temperatures ($\sim 175 - 225$ K) [18, 81]. Cells that do not exhibit hysteresis have been the target of intense research and the explanation offered in this work is the first satisfactory physical explanation of how the choice of transport layer materials affects the degree of hysteresis. The charge transport model studied in this work is also able to explain why hysteresis reappears in apparently "hysteresis-free" cells at low temperature [24].

In the literature, ion vacancy migration is often attributed as the cause of transient behaviour, such as hysteresis, however comments on its effects on steady-state performance are rare. It is shown in this work that ion vacancy migration also has a dominant effect on the steady-state performance of PSC. The distribution of the electric field, resulting from ionic accumulation in the perovskite Debye layers adjacent to each of the transport layers, controls the rate of charge carrier recombination across each interface. Simulations indicate that increasing the doping density of a transport layer may help to reduce the amount of recombination occurring at the interface between that layer and the perovskite, and hence lead to an increase the photo-current. Understanding the effects of variation in different material parameters is vital for guiding the future development of PSCs. The approximate expression for the steady-state current density derived in Chapter 7 describes how key properties of a PSC influence the performance of an ideal PSC.

Although no specific degradation pathways are included in the model, it is suspected that chemical degradation is enhanced by ionic accumulation at the interfaces. Therefore, it is suggested that PSCs incorporating TLs that have a lower permittivity and doping density, which show reduced ionic accumulation in the perovskite Debye layers, may also show improved long-term stability as a result.

Future directions. This theoretical study has begun to unravel the complex interplay between material properties and the processes of ion vacancy migration and charge carrier transport that occur within a PSC. The next step is to validate the findings, and investigate the limitations, of the charge transport model via comparison to experimental data.

In order to investigate the underlying cause, and not just the effects, of ion migration, it is preferable to make a direct comparison between the predicted and measured internal state of a PSC. The evolution of the internal state of a PSC is difficult to measure experimentally but one promising technique has recently been developed by Weber *et al.* [147]. The technique is based upon Kelvin Probe Force Microscopy (KPFM) and is able to measure the electric potential across all layers of a device (with a lateral resolution of 10-50 nm) within a very short timescale (sub-millisecond). As a result, repeated measurements can be pieced together to show dynamic changes in the electric potential. The images in [147] show close resemblance to the simulated potential profiles presented in this work, except at the interface between the perovskite and the hole transport layer, in this instance Spiro-OMeTAD. One hypothesis to explain this discrepancy is that, in the measured cells, ions are able to migrate out of the perovskite and into the hole transport layer. There is experimental evidence indicating that iodide ions are able to move within the hole transport material Spiro-OMeTAD [71]. Alternatively, there is also evidence that lithium (Li^+) and other ions (that are added to Spiro-OMeTAD as dopants) can migrate from the hole transport layer into the perovskite [84]. An extension of the charge transport model to include mobile ions in the hole transport layer could be used to test whether a transfer of ions between the layers can explain the discrepancy and to find out what other effects the mechanism has on the J-V characteristics of a PSC.

Another avenue for future research involves the addition of a second type of mobile ion vacancy in the perovskite layer *e.g.* the methyl ammonium cation vacancies. Cation vacancies are orders of magnitude less mobile than the iodide ion vacancies. As a result, the presence of mobile cation vacancies has previously been suggested as an explanation for so-called reversible degradation which occurs on a timescale of hours [40]. This paper demonstrates qualitative agreement between simulation and experiment; however, the work used only the single-layer model with charge carrier recombination taking place only within the bulk of the perovskite layer. The limiting recombination mechanism in high quality PSCs is now considered to be that of interface recombination rather than bulk. Therefore, the aim of future work should be to obtain quantitative comparison with experimental data and to uncover the location of the dominant recombination mechanism.

The solution techniques developed in this work can be adapted to similar models of ion vacancy migration and charge carrier transport that also account for the effects of other processes, such as those described above. In fact, there are numerous other applications and possible extensions of the model that merit further research. Thorough investigation of more advanced models may be able to answer the outstanding questions about how to optimise the design of PSCs for both high performance and long-term stability.

Appendix A

Ion flux with volume exclusion effects

The aim of this appendix is to justify the use of the standard drift-diffusion equation, as given in (3.4b), to describe the motion of iodide ion vacancies within the perovskite layer. In semiconductor device models, drift-diffusion equations are often used to describe the motion of electronic charge carriers, however it is not immediately clear whether the same description can be applied to the migration of an ionic species through a crystal lattice. In the field of electrolytes, classical drift-diffusion theory breaks down for high surface charges or high potentials where space constraints are important in limiting the density of ions to the maximum physical density of close packing [13, 73]. In this appendix, a modified drift-diffusion equation for the vacancy-assisted migration of iodide ions, that incorporates volume exclusion effects, is derived using two methods.

The first method, presented in Section A.1, treats the ions as point particles hopping on a fixed one-dimension lattice, in the direction of current through the cell and perpendicular to the material interfaces. A similar derivation for a general case in which there are an arbitrary number of particle species has been given by Burger *et al.* [20]. The second approach, detailed in Section A.2, arises from thermodynamic considerations and follows similar work regarding the accumulation of electrolytes by Borukhov *et al.* [13] and Kilic *et al.* [73]. Note that direct ion-ion interactions are neglected in all cases. In Section A.3, the resulting modified Poisson-Nernst-Planck equations are considered and a justification is given for presenting and analysing an unmodified model in the main text.

A.1 Lattice hopping model

Here, it is assumed that iodide ions within the perovskite layer are located on a fixed lattice of ion sites, as illustrated in one spatial dimension in Figure A.1 as a row of N

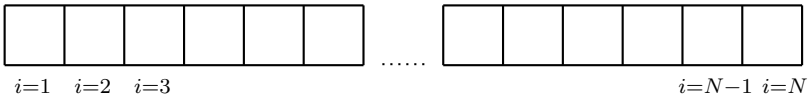

FIGURE A.1: One-dimensional lattice of N ion sites (of width Δx).

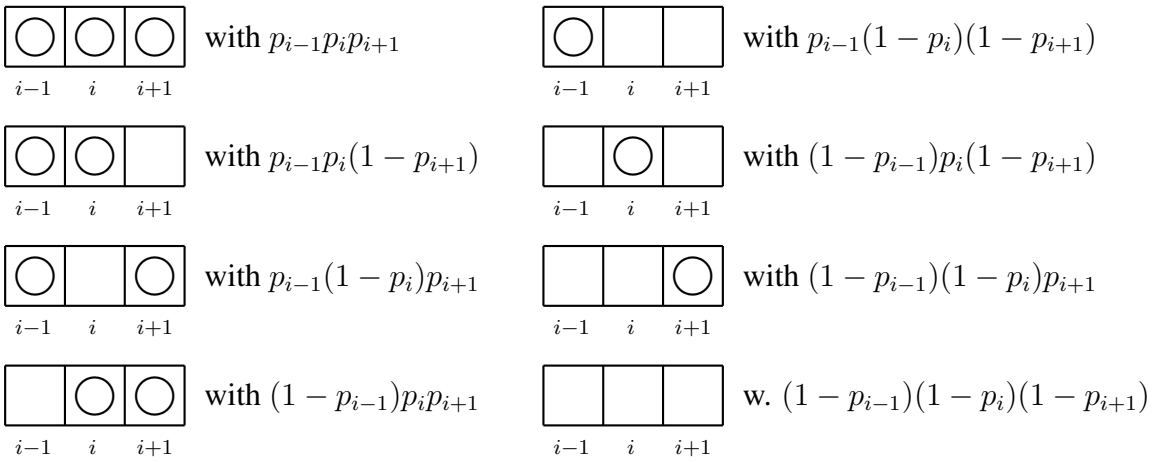

FIGURE A.2: The eight possible arrangements of ions across three lattice sites with the associated probability.

boxes of width Δx. Let $p_i(t)$ be the probability that site i is filled by an ion at time t, and hence $[1 - p_i(t)]$ is the probability that it is vacant. In this derivation, use is made of the closure assumption that these occupational probabilities are independent from one another. In addition, let $W_{i,j}\Delta t$ be the transition probability for an ion to move from site i to an adjacent and vacant site j in an infinitesimal time Δt.

The first step is to consider the probability $p_i(t + \Delta t)$, that is, the probability that site i ($\neq 1, N$) is filled after a short time interval, Δt. The 8 possible arrangements for the state of site i and its two immediate neighbours, sites $i - 1$ and $i + 1$, is given with its associated probability in Figure A.2. By considering the possible transition events for an ion either staying or moving into site i and assuming that only one transition event may take place (*i.e.* neglecting terms of $O(\Delta t^2)$),

$$\begin{aligned} p_i(t+\Delta t) = {} & p_{i-1}p_ip_{i+1} \times 1 + p_{i-1}p_i(1-p_{i+1}) \times (1 - W_{i,i+1}\Delta t) \\ & + p_{i-1}(1-p_i)p_{i+1} \times (W_{i-1,i}\Delta t + W_{i+1,i}\Delta t) \\ & + (1-p_{i-1})p_ip_{i+1} \times (1 - W_{i,i-1}\Delta t) \\ & + p_{i-1}(1-p_i)(1-p_{i+1}) \times (W_{i-1,i}\Delta t) \\ & + (1-p_{i-1})p_i(1-p_{i+1}) \times (1 - W_{i,i-1}\Delta t - W_{i,i+1}\Delta t) \\ & + (1-p_{i-1})(1-p_i)p_{i+1} \times (W_{i+1,i}\Delta t) \\ & + (1-p_{i-1})(1-p_i)(1-p_{i+1}) \times 0\,. \end{aligned} \tag{A.1}$$

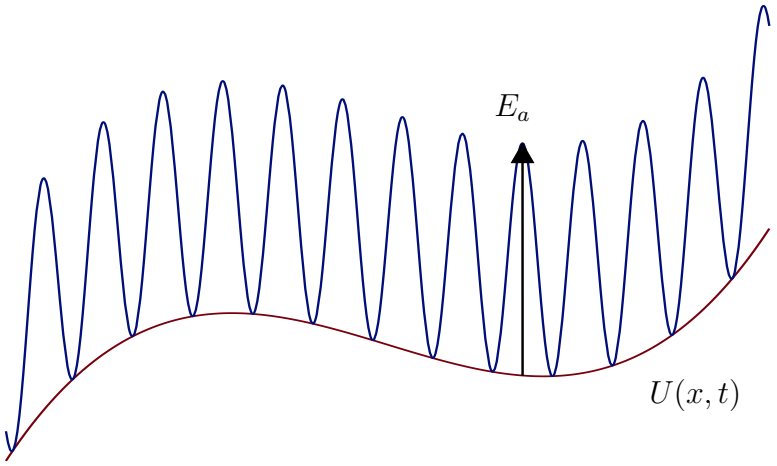

FIGURE A.3: A diagram of the potential energy landscape in which the iodide ions exist, where each trough represents an iodide ion site, E_a is the energy barrier between each lattice site and $U(x,t)$ is a smoothly varying potential.

This expression simplifies to

$$p_i(t+\Delta t) = p_i + \Delta t\big[W_{i+1,i}p_{i+1}(1-p_i) - W_{i,i-1}p_i(1-p_{i-1}) + W_{i-1,i}p_{i-1}(1-p_i) - W_{i,i+1}p_i(1-p_{i+1})\big]\,. \tag{A.2}$$

By taking the limit $\Delta t \to 0$, the master equation is given by

$$\frac{\mathrm{d}p_i}{\mathrm{d}t} = W_{i+1,i}p_{i+1}(1-p_i) - W_{i,i-1}p_i(1-p_{i-1}) + W_{i-1,i}p_{i-1}(1-p_i) - W_{i,i+1}p_i(1-p_{i+1})\,, \tag{A.3}$$

for all sites ($i = 1, ..., N$) provided that the following boundary conditions are applied:

$$W_{0,1} = W_{1,0} = W_{N,N+1} = W_{N+1,N} = 0\,. \tag{A.4}$$

Such conditions are termed reflecting boundary conditions and are the appropriate choice for perovskite/TL interfaces which are impermeable to the ions.

Next, it is assumed that the transition probabilities take the commonly-used Arrhenius form:

$$W_{i,i-1} = K\exp\left(-\frac{E_{i,i-1}}{k_BT}\right)\,, \qquad W_{i,i+1} = K\exp\left(-\frac{E_{i,i+1}}{k_BT}\right)\,. \tag{A.5}$$

where K is a constant of proportionality and $E_{i,j}$ is the energy required to move an iodide ion from site i to site j. The potential energy landscape is assumed to take the form shown schematically in Figure A.3. Hence, the energies $E_{i,j}$ are given as follows by the sum of the energy barrier, of magnitude E_a, between each pair of neighbouring lattice sites and

the change in the smoothly varying potential $U(x,t)$.

$$E_{i,i-1} = U\left(x - \frac{\Delta x}{2}, t\right) - U(x,t) + E_a\,, \tag{A.6}$$

$$E_{i,i+1} = U\left(x + \frac{\Delta x}{2}, t\right) - U(x,t) + E_a\,. \tag{A.7}$$

Therefore the transition probabilities can be rewritten in terms of the constant $C = K\exp\left(-\frac{E_a}{k_BT}\right)$ as

$$W_L = C\exp\left(-\frac{U\left(x-\frac{\Delta x}{2},t\right) - U(x,t)}{k_BT}\right)\,, \tag{A.8}$$

$$W_R = C\exp\left(-\frac{U\left(x+\frac{\Delta x}{2},t\right) - U(x,t)}{k_BT}\right)\,. \tag{A.9}$$

In order to apply the continuum approximation, both the occupational and transition probabilities are re-defined as functions of space, as well as time, as follows. This approach is valid provided that Δx is small compared to the length-scale over which $p(x,t)$ varies.

$$p_i(t) = p(x,t)\,, \qquad W_{i,i-1}(t) = W_L(x,t)\,, \qquad W_{i,i+1}(t) = W_R(x,t)\,. \tag{A.10}$$

Therefore the master equation (A.3) becomes

$$\begin{aligned}\frac{\partial p}{\partial t} = {} & W_L(x+\Delta x)p(x+\Delta x)[1-p] - W_L p[1-p(x-\Delta x,t)] \\ & + W_R(x-\Delta x,t)p(x-\Delta x,t)[1-p] - W_R p[1-p(x+\Delta x,t)]\,.\end{aligned} \tag{A.11}$$

Here, and in the following derivation, expressions are evaluated at (x,t) unless otherwise indicated. Note that the first two terms have the same form but are evaluated at points shifted by Δx, and that the same is true of the second pair of terms. Therefore, Taylor expansions can be used to obtain

$$\begin{aligned}\frac{\partial p}{\partial t} = {} & \Delta x\frac{\partial}{\partial x}\Big(W_L p[1-p(x-\Delta x,t)] - W_R p[1-p(x+\Delta x,t)]\Big) \\ & + \frac{1}{2}(\Delta x)^2\frac{\partial^2}{\partial x^2}\Big(W_L p[1-p(x-\Delta x,t)] + W_R p[1-p(x+\Delta x,t)]\Big) \\ & + O\left(C(\Delta x)^3\right)\,.\end{aligned} \tag{A.12}$$

The expressions for W_R and W_L can also be expanded using Taylor series to give

$$W_L = C\left[1 + \frac{\Delta x}{2k_BT}\frac{\partial U}{\partial x}\right] + O\left(C(\Delta x)^2\right) , \tag{A.13}$$

$$W_R = C\left[1 - \frac{\Delta x}{2k_BT}\frac{\partial U}{\partial x}\right] + O\left(C(\Delta x)^2\right) . \tag{A.14}$$

Substituting these expressions, along with Taylor expansions for $p(x-\Delta x,t)$ and $p(x+\Delta x,t)$ about x, into (A.12), gives

$$\begin{aligned}\frac{\partial p}{\partial t} = \Delta x\frac{\partial}{\partial x}\left(C\left[2\Delta x p\frac{\partial p}{\partial x} + \frac{\Delta x}{k_BT}\frac{\partial U}{\partial x}p(1-p)\right]\right)\\ + \frac{1}{2}(\Delta x)^2\frac{\partial^2}{\partial x^2}\Big(2Cp[1-p]\Big) + O\left(C(\Delta x)^3\right) .\end{aligned} \tag{A.15}$$

Hence, the leading-order governing equation for the density of ions is

$$\frac{\partial p}{\partial t} = (\Delta x)^2\frac{\partial}{\partial x}\left(C\left[\frac{\partial p}{\partial x} + \frac{p(1-p)}{k_BT}\frac{\partial U}{\partial x}\right]\right) . \tag{A.16}$$

Here, it is assumed that the potential U is due solely to the mean-field electric potential ϕ. Hence, for the negatively charged iodide ions,

$$U(x,t) = -q\phi(x,t) . \tag{A.17}$$

Then, by replacing the probability $p(x,t)$ by the expected occupation $\frac{c_-}{\rho}$, where $c_-(x,t)$ is the density of ions and ρ is the constant and uniform density of ion sites, we arrive at the following modified drift-diffusion equation:

$$\frac{\partial c_-}{\partial t} = \frac{\partial}{\partial x}\left(D_I\frac{\partial c_-}{\partial x} - M(c_-)c_-\frac{\partial \phi}{\partial x}\right) , \tag{A.18}$$

where D_I is the diffusion coefficient and $M(c_-)$ is the density-dependent mobility, given by

$$D_I = K(\Delta x)^2\exp\left(-\frac{E_a}{k_BT}\right) , \qquad M(c_-) = \frac{qD_I}{k_BT}\left(1 - \frac{c_-}{\rho}\right) . \tag{A.19}$$

For a low fractional occupancy ($c_- \ll \rho$), the mobility reduces to the constant mobility expected from the Einstein relation, $M = \frac{qD_I}{k_BT}$. However, for the relevant case of high occupancy, it is clear that the mobility is strongly dependent on the density of vacant ion sites and decreases to zero for the case where there are no neighbouring vacancies.

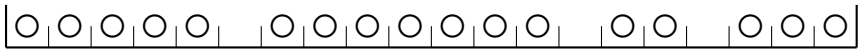

FIGURE A.4: Lattice of N ion sites partially filled by m ions.

A.2 Thermodynamic approach

For comparison, another simple model for the vacancy-assisted migration of iodide ions across the perovskite layer is constructed following the statistical mechanical approach used by Borukhov *et al.* [13] and Kilic *et al.* [73] among others. Here, we consider a lattice of N iodide ion sites, partially filled by m ions, as shown schematically in Figure A.4. It is assumed that this lattice fills a volume δV which is small enough to be considered to be in thermodynamic equilibrium. Let a be the distance between iodide ion sites, then the volume occupied by an ion site is a^3 ($\ll \delta V$). The constant and uniform density of ion sites is denoted by ρ ($= N/\delta V = 1/a^3$) and the density of negatively-charged iodide ions is c_- ($= m/\delta V$).

The Helmholtz free energy in this system, denoted by δF, depends on the electrostatic energy δU, the temperature T (assumed to be constant and in equilibrium with the surroundings, *i.e.* the system is considered to be a canonical ensemble) and the entropy δS as follows [58]:

$$\delta F = \delta U - T\delta S\,. \tag{A.20}$$

In the mean-field approximation, the electrostatic energy density depends on the mean-field electric potential, ϕ, and the distribution of charge as follows,

$$\delta U = \left(-\frac{1}{2}\varepsilon_p|\nabla\phi|^2 + qc_+\phi - qc_-\phi\right)\delta V\,, \tag{A.21}$$

where ε_p is the permittivity of the perovskite and c_+ is the density of immobile, positively-charged ions, assumed to be constant and uniformly distributed throughout the perovskite layer. The first term on the right-hand side is the self-energy of the electric field, while the second and third terms are the electrostatic energies of the positive and negative ions, respectively [13].

In statistical mechanics [58], the entropy S of a system is calculated in terms of the probability of the different possible states from

$$S = k_B \ln\Omega\,, \tag{A.22}$$

where k_B is Boltzmann's constant and Ω is the total number of possible states, *i.e.* the

number of ways in which m ions can fill N states:

$$\Omega = \frac{N!}{m!(N-m)!}\,. \tag{A.23}$$

Both N and m are assumed to be large and so, using Stirling's formula, the entropy is approximated as

$$S = k_B[N\log(N) - (N-m)\log(N-m) - m\log(m)]\,. \tag{A.24}$$

In order to calculate the entropy δS of a volume δV, the above formula is rewritten in terms of densities, *i.e.* by substituting $N = \rho\delta V$ and $m = c_-\delta V$. Hence,

$$\delta S = k_B[\rho\delta V\log(\rho\delta V) - (\rho - c_-)\delta V\log((\rho - c_-)\delta V) - c_-\delta V\log(c_-\delta V)]\,. \tag{A.25}$$

This expression simplifies to

$$\delta S = -k_B\left[(\rho - c_-)\log\left(1 - \frac{c_-}{\rho}\right) + c_-\log\left(\frac{c_-}{\rho}\right)\right]\delta V\,. \tag{A.26}$$

It follows from (A.20) that

$$\begin{aligned}\delta F = \Bigg\{ &-\frac{1}{2}\varepsilon_p|\nabla\phi|^2 + qc_+\phi - qc_-\phi \\ &+k_BT\left[(\rho - c_-)\log\left(1 - \frac{c_-}{\rho}\right) + c_-\log\left(\frac{c_-}{\rho}\right)\right]\Bigg\}\delta V\,,\end{aligned} \tag{A.27}$$

and, hence, the free energy density $\mathcal{F}$ is given by

$$\mathcal{F} = -\frac{1}{2}\varepsilon_p|\nabla\phi|^2 + qc_+\phi - qc_-\phi + k_BT\left[(\rho - c_-)\log\left(1 - \frac{c_-}{\rho}\right) + c_-\log\left(\frac{c_-}{\rho}\right)\right]\,. \tag{A.28}$$

The flux of ionic charge, denoted by $\mathcal{J}_-$, can now be found from Fick's First Law:

$$\mathcal{J}_- = -Mc_-\frac{\partial\mu^-}{\partial x}\,, \tag{A.29}$$

where μ^- is the chemical potential of the iodide ions, which equals the partial molar Helmholtz free energy density (using the assumptions that the temperature, volume and total number of ions are all constant) [58], given by

$$\mu^- = \frac{\partial\mathcal{F}}{\partial c_-} = -q\phi + k_BT\left[\log\left(\frac{c_-}{\rho}\right) - \log\left(1 - \frac{c_-}{\rho}\right)\right]\,. \tag{A.30}$$

Hence, the flux of ionic charge is

$$\mathcal{J}_- = -M\left[k_B T\left(\frac{\rho}{\rho - c_-}\right)\frac{\partial c_-}{\partial x} - qc_-\frac{\partial \phi}{\partial x}\right]. \tag{A.31}$$

Assuming that the mobility M takes the density-dependent form derived in Section A.1 and stated in (A.19b), we arrive at an expression that is equivalent to the modified drift-diffusion equation derived from the lattice hopping model and given in (A.18).

A.3 Modified Possion-Nernst-Planck equations

The modified drift-diffusion equation for the vacancy-assisted migration of iodide ions through the perovskite lattice can be rewritten in terms of the ion vacancy density $P(x,t)$ and flux $\mathcal{F}_P(x,t)$ via

$$P = \rho - c_-\,, \qquad\qquad F^P = -\frac{1}{q}\mathcal{J}_-\,. \tag{A.32}$$

Applying these transformations to (A.18) leads to

$$\frac{\partial P}{\partial t} + \frac{\partial F^P}{\partial x} = 0\,, \qquad F^P = -D_I\left(\frac{\partial P}{\partial x} + \frac{P}{V_T}\left(1 - \frac{P}{\rho}\right)\frac{\partial \phi}{\partial x}\right). \tag{A.33}$$

The following self-consistent Poisson equation (in which the charge density is dominated by the distribution of ionic charge) is derived by minimising the Helmholtz free energy density $\mathcal{F}$ given in (A.28) with respect to the electric potential ϕ, *i.e.* by substitution of $\mathcal{F}(x, \phi, \frac{\partial \phi}{\partial x})$ into the Euler-Lagrange equation:

$$\frac{\partial^2 \phi}{\partial x^2} = -\frac{q}{\varepsilon_p}(c_+ - c_-) = -\frac{q}{\varepsilon_p}(P - N_0)\,, \tag{A.34}$$

in which $N_0 = \rho - c_+$ is a constant and uniform density of negative charge due to the existence of cation vacancies. In order to ensure (ionic) charge neutrality within the perovskite layer, N_0 is also, as in the main text, the mean density of iodide ion vacancies. Note that this modified Poisson equation is equivalent to the (dimensionless) leading-order Poisson equation in (5.3), which forms part of the decoupled model that is analysed in Chapter 5.

The modified Poisson-Nernst-Planck equations (A.33)-(A.34) form a complete description for the motion of iodide ion vacancies within the perovskite layer. These equations incorporate the effects of volume exclusion and therefore remain valid in the limit of

close-packing. The accumulation of charge in the perovskite Debye layers adjacent to each perovskite/TL interface is key to the performance of a PSC. Therefore, the question is: do volume exclusion effects play a role in the performance of a PSC under standard operating conditions?

DFT calculations performed by Walsh *et al.* [145] indicate that around 0.4% of iodide ion sites are vacant at room temperature. Using this estimate, the density of lattice sites $\rho = N_0/0.004$. Hence, using the same non-dimensionalisation as set out in Section 3.5.1, the dimensionless form of (A.33) is

$$\frac{\partial P}{\partial t} + \lambda \frac{\partial F^P}{\partial x} = 0\,, \qquad F^P = -\left(\frac{\partial P}{\partial x} + P\left(1 - 0.004P\right)\frac{\partial \phi}{\partial x}\right)\,, \tag{A.35}$$

in which λ ($\approx 3.7 \times 10^{-3}$) is the dimensionless Debye length. It can be seen, therefore, that for the set of parameter values considered in this work (see Table 3.2), the incorporation of volume exclusion effects leads to the addition of a term of $O(\lambda)$ to the standard expression for the dimensionless iodide ion flux F^P, given in (3.51). The asymptotic boundary layer analysis of the charge transport model, performed in Chapter 5, is made in the limit $\lambda \to 0$. Therefore, it is consistent to neglect the effects of volume exclusion in this analysis. In addition, the simulation results in Figures 5.3-5.5 indicate that the dimensionless ion vacancy density P is typically less than 10, far below the maximum dimensionless density of 250 for the estimate that 0.4% of lattice sites are vacant.

In the case of the single-layer model (for PSCs in which the TLs are so highly doped that they can be considered to act as "quasi-metals"), larger Debye layer potential differences and, correspondingly, larger ion vacancy densities are possible. The maximum value of the dimensionless ion vacancy density P in the single-layer simulation results shown in Figure 4.8 is around 40. However, this value is still well below the limit of close-packing and so the effects of volume exclusion are not expected to have any significant impact on the ionic distribution and, in turn, the performance of a PSC. Hence, it is concluded that the standard form of the drift-diffusion equation is valid for the simulation of iodide ion vacancy migration within PSCs during typical measurement protocols.

Appendix B

Extension of Numerical Schemes to the Three-Layer Model

In this appendix, the details of the extension to three layers of both the finite difference and the finite element schemes, presented and compared in Chapter 4, are given. The three layers of a PSC are the electron transport layer (ETL), the perovskite absorber layer and the hole transport layer (HTL). In the charge transport model set out in Chapter 3, the ETL contains only one type of mobile charge, namely the electrons; the perovskite absorber layer contains iodide ion vacancies, electrons and holes; and, the HTL contains only holes. See Figures 3.3 and 3.4.

B.1 Finite difference scheme

The finite difference scheme for the single-layer model is described in Section 4.4. Here, the extension of this scheme onto a three-layer Chebyshev grid is given.

B.1.1 Three-layer Chebyshev grid

The three-layer computational grid is made up of three sub-grids; one for each of the three layers: the ETL, the perovskite layer and the HTL. As before the equations in the perovskite layer are discretised onto $N+1$ grid points, denoted by $x = x_i$ for $i = 0, ..., N$, which partition the domain $x \in [0, 1]$ into N subintervals. To ensure that computational effort is expended where it is needed most (in the Debye layers) the grid points are posi-

tioned according to a Chebyshev distribution as follows.

$$x_i = \frac{1}{2}\left\{1 + \cos\left[\pi\left(\frac{i}{N} - 1\right)\right]\right\}, \qquad \text{for} \quad i = 0, ..., N\,. \tag{B.1}$$

Here, similar grids are introduced for treatment of the equations in the ETL (of dimensionless width x_E) and the HTL (of dimensionless width x_H) and these are defined by

$$x_i^E = \frac{x_E}{2}\left\{\cos\left[\pi\left(\frac{i}{N_E} - 1\right)\right] - 1\right\}, \qquad \text{for} \quad i = 0, ..., N_E\,, \tag{B.2}$$

$$x_i^H = 1 + \frac{x_H}{2}\left\{\cos\left[\pi\left(\frac{i}{N_H} - 1\right)\right] + 1\right\}, \qquad \text{for} \quad i = 0, ..., N_H\,. \tag{B.3}$$

where $N_E = \text{round}\left(\sqrt{x_E}N\right)$ and $N_H = \text{round}\left(\sqrt{x_H}N\right)$. These values of N_E and N_H are chosen to give approximately equal spacing either side of the interfaces (at $x = 0$ and $x = 1$). For the results presented in Chapters 5 and 6, a value of $N = 400$ is used, and hence $N_E = 200$ and $N_H = 283$. For each of the three sub-grids, a set of half-points, which lie midway between the grid points, is defined by

$$x_{i+1/2} = \frac{x_{i+1} + x_i}{2}\,, \qquad \text{for} \quad i = 0, ..., N - 1\,, \tag{B.4}$$

for the perovskite layer, with analogous definitions for the sets of half-points within the ETL and HTL.

B.1.2 Extension of finite difference discretisation

Within the ETL, the governing equations for the conservation of electrons (3.54) and Poisson's equation (3.55), along with the left-hand boundary conditions (3.56) imposed at the metal contact are discretised in a precisely analogous way to those for the perovskite layer, as described in Section 4.3.1. The same is done to discretise the HTL equations, for the conservation of holes (3.57), Poisson's equation (3.58) and right-hand boundary conditions (3.59) at the metal contact. Note that it is assumed in this work that ion vacancies are restricted to the perovskite layer and therefore do not need to be accounted for within the TLs.

In order to preserve the second-order accuracy of the single-layer spatial discretisation, it is important to choose discretisations for the continuity conditions, given by (3.60)-(3.63), that also exhibit second order accuracy. Finding such discrete approximations is trivial for the conditions on the continuity of the potential and the prescribed ratios between the carrier concentrations on either side of the respective interfaces. However, the electric field (E) and carrier current densities (j^n, j^p) are only defined on the half-

points (*i.e.* not directly on the interface where the conditions are to be applied) as follows

$$E_{i+1/2} = -\mathfrak{D}_{i+1/2}\left(\phi_{i+1}, \phi_i\right), \tag{B.5}$$

$$j^n{}_{i+1/2} = \kappa_n\left(\mathfrak{D}_{i+1/2}(n_{i+1}, n_i) + \mathfrak{I}_{i+1/2}(n_{i+1}, n_i)E_{i+1/2}\right), \tag{B.6}$$

$$j^p{}_{i+1/2} = -\kappa_p\left(\mathfrak{D}_{i+1/2}(p_{i+1}, p_i) - \mathfrak{I}_{i+1/2}(p_{i+1}, p_i)E_{i+1/2}\right), \tag{B.7}$$

for $i = 0, ..., N-1$. Equivalent expressions for the electric field and the relevant carrier current density in each TL follow from identical considerations. The location of the half-points (away from the interfaces) necessitates extrapolating the relevant quantities, namely the electric field and carrier current densities, to the interfaces at which the continuity conditions (3.60)-(3.63) are applied. The chosen extrapolation is linear and based on the values of the variables at the two nearest half-points on either side of the interface.

Hence, the continuity conditions at the ETL/perovskite interface at $x = 0$, given in (3.60)-(3.61), are imposed using the following equations.

$$\phi^E_{N_E} = \phi_0\,, \tag{B.8}$$

$$\begin{aligned} r_E\,&\left[E^E_{N_E-\frac{1}{2}} + \mathfrak{D}_{N_E-1}\left(E^E_{N_E-\frac{1}{2}},\, E^E_{N_E-\frac{3}{2}}\right)\left(1 - x^E_{N_E-\frac{1}{2}}\right)\right] \\ &= \left[E_{\frac{1}{2}} - \mathfrak{D}_1\left(E_{\frac{3}{2}},\, E_{\frac{1}{2}}\right)x_{\frac{1}{2}}\right], \end{aligned} \tag{B.9}$$

$$n^E_{N_E} = n_0\,, \tag{B.10}$$

$$\begin{aligned} &j^{n,E}{}_{N_E-\frac{1}{2}} + \mathfrak{D}_{N_E-1}\left(j^{n,E}{}_{N_E-\frac{1}{2}},\, j^{n,E}{}_{N_E-\frac{3}{2}}\right)\left(1 - x^E_{N_E-\frac{1}{2}}\right) \\ &\qquad = j^n{}_{\frac{1}{2}} - \mathfrak{D}_1\left(j^n{}_{\frac{3}{2}},\, j^n{}_{\frac{1}{2}}\right)x_{\frac{1}{2}} - R_l\left(n_0, p_0\right). \end{aligned} \tag{B.11}$$

Similarly, at the perovskite/HTL interface at $x = 1$, the continuity conditions from (3.62)-(3.63) are imposed using

$$\phi_N = \phi^H_0\,, \tag{B.12}$$

$$\begin{aligned} &\left[E_{N-\frac{1}{2}} + \mathfrak{D}_{N-1}\left(E_{N-\frac{1}{2}},\, E_{N-\frac{3}{2}}\right)\left(1 - x_{N-\frac{1}{2}}\right)\right] \\ &\qquad = r_H\left[E^H_{\frac{1}{2}} - \mathfrak{D}_1\left(E^H_{\frac{3}{2}},\, E^H_{\frac{1}{2}}\right)x^H_{\frac{1}{2}}\right], \end{aligned} \tag{B.13}$$

$$p_N = p^H_0\,, \tag{B.14}$$

$$\begin{aligned} &j^p{}_{N-\frac{1}{2}} + \mathfrak{D}_{N-1}\left(j^p{}_{N-\frac{1}{2}},\, j^p{}_{N-\frac{3}{2}}\right)\left(1 - x_{N-\frac{1}{2}}\right) - R_r\left(n_N, p_N\right) \\ &\qquad = j^{p,H}{}_{\frac{1}{2}} - \mathfrak{D}_1\left(j^{p,H}{}_{\frac{3}{2}},\, j^{p,H}{}_{\frac{1}{2}}\right)x^H_{\frac{1}{2}}. \end{aligned} \tag{B.15}$$

B.1.3 Implementation

The extended system of $2N_E + 4N + 3 + 2N_H$ DAEs, incorporating the eight boundary conditions and eight continuity conditions, is implemented into a MATLAB routine that makes use of the built-in solver `ode15s` in an analogous way to the single-layer system, as described in Section 4.4.2. This is the method that is used to obtain numerical results for comparison to uniformly-valid asymptotic approximations in Chapter 5 and to investigate the effects of key material parameters in Chapter 6.

B.2 Finite element scheme

As shown in Chapter 4, the finite element scheme outperforms all other methods that have been tested to date. Typical computation times are within the range of seconds to minutes on a modern personal computer for any realistic measurement protocol, including the simulation of J-V curves including a preconditioning step. The single-layer scheme is described in Section 4.3. Here, the extension of the scheme to the three layers of a PSC is presented along with an extension of the tanh grid defined in Section 4.5.2.

B.2.1 Three-layer tanh grid

The three-layer computational grid is comprised of $N + N_E + N_H + 1$ non-uniformly positioned grid points which partition the (non-dimensional) domain $x \in [-x_E, 1 + x_H]$ into $N + N_E + N_H$ subintervals. The perovskite layer (including the interfaces) contains $N+1$ grid points located at $x = x_i$ for $i = 0, ..., N$ with subintervals denoted by $\Delta_{i+1/2} = x_{i+1} - x_i$. The transport layer domains (excluding the interfaces) contain N_E and N_H grid points, respectively, with grid points located at $x = x_i^E$ for $i = 0, ..., N_E - 1$ and $x = x_i^H$ for $i = 1, ..., N_H$, respectively, with analogous notation for the corresponding subintervals. The three-layer tanh grid is the set of points described by

$$x_i = \frac{1}{2}\left(\frac{\tanh\left[s\left(\frac{2i}{N} - 1\right)\right]}{\tanh(s)} + 1\right), \quad \text{for} \quad i = 0, ..., N, \tag{B.16}$$

$$x_i^E = \frac{x_E}{2}\left(\frac{\tanh\left[s\left(\frac{2i}{N_E} - 1\right)\right]}{\tanh(s)} - 1\right), \quad \text{for} \quad i = 0, ..., N_E - 1, \tag{B.17}$$

$$x_i^H = 1 + \frac{x_H}{2}\left(\frac{\tanh\left[s\left(\frac{2i}{N_H} - 1\right)\right]}{\tanh(s)} + 1\right), \quad \text{for} \quad i = 1, ..., N_H. \tag{B.18}$$

An appropriate value for the parameter s is calculated by choosing to have 20% of the perovskite layer grid points $\{x_i\}$ fall within one Debye length of each interface (*i.e.* within the intervals $x \in [0, \lambda]$ and $x \in [1-\lambda, 1]$) and the remaining 60% within the bulk of the perovskite layer (*i.e.* within $x \in [\lambda, 1-\lambda]$). The value is found via numerical solution of

$$\lambda = \frac{1}{2}\left(\frac{\tanh(0.6)}{\tanh(s)} + 1\right) . \tag{B.19}$$

The number of grid points within each of the TLs (N_E and N_H) are chosen from the number of perovskite layer grid points (N) to give approximately equal spacing immediately either side the interface using the following expressions.

$$N_E = \text{round}\left(\frac{2}{1 - \frac{1}{s}\tanh^{-1}[A(x_E)]}\right) , \quad N_H = \text{round}\left(\frac{2}{1 - \frac{1}{s}\tanh^{-1}[A(x_H)]}\right) ,$$
$$\text{where} \qquad A(x) = \frac{1}{x}\left\{\tanh\left[s\left(1 - \frac{2}{N}\right)\right] - (1-x)\tanh(s)\right\} . \tag{B.20}$$

B.2.2 Extension of finite element discretisation

The three discrete operators defined in (4.26)-(4.28) are used to discretise the electric field and carrier current densities in the TLs in an analogous way to the equivalent variables in the perovskite, which are discretised in (4.29), (4.31) and (4.32). Hence, the equations describing the conservation of electrons (3.54) and Poisson's equation (3.55) in the ETL, those describing the conservation of holes (3.57) and Poisson's equation (3.58) in the HTL and the two boundary conditions imposed at each of the two metal contacts given in (3.56) and (3.59) can be discretised in an identical way to their counterparts for the perovskite layer in the single-layer case. In addition, eight continuity conditions (four on each interface) are required.

The continuity conditions on the charge carrier concentrations and the electric potential across the interfaces, given in (3.60)-(3.63), are imposed using

$$\phi^E_{N_E} = \phi_0 , \qquad n^E_{N_E} = n_0 , \tag{B.21}$$
$$\phi_N = \phi^H_0 , \qquad p_N = p^H_0 . \tag{B.22}$$

The continuity of the displacement field across each interface is ensured via

$$0 = \mathfrak{D}_{1/2}(\phi) - r_E \mathfrak{D}^E_{N_E-1/2}(\phi^E) - \frac{\Delta_{1/2}}{\lambda^2}\left(\frac{1}{2} - \frac{P_1}{3} - \frac{P_2}{6} + \delta\left[\frac{n_1}{3} + \frac{n_2}{6} - \frac{p_1}{3} - \frac{p_2}{6}\right]\right) - r_E \frac{\Delta^E_{N_E-1/2}}{\lambda_E^2}\left(\frac{n^E_{N_E-1}}{6} + \frac{n_0}{3} - \frac{1}{2}\right), \tag{B.23}$$

$$0 = r_H \mathfrak{D}^H_{1/2}(\phi^H) - \mathfrak{D}_{N-1/2}(\phi) - r_H \frac{\Delta^H_{1/2}}{\lambda_H^2}\left(\frac{1}{2} - \frac{p_N}{3} - \frac{p^H_1}{6}\right) - \frac{\Delta_{N-1/2}}{\lambda^2}\left(\frac{1}{2} - \frac{P_{N-1}}{6} - \frac{P_N}{3} + \delta\left[\frac{n_{N-1}}{6} + \frac{n_N}{3} - \frac{p_{N-1}}{6} - \frac{p_N}{3}\right]\right). \tag{B.24}$$

Lastly, the continuity of carrier current densities (including losses due to interface recombination) is imposed using

$$\frac{\sigma_E}{6}\Delta^E_{N_E-1/2}\frac{\mathrm{d}n^E_{N_E-1}}{\mathrm{d}t} + \left(\frac{\sigma_E}{3}\Delta^E_{N_E-1/2} + \frac{\sigma}{3}\Delta_{1/2}\right)\frac{\mathrm{d}n_0}{\mathrm{d}t} + \frac{\sigma}{6}\Delta_{1/2}\frac{\mathrm{d}n_1}{\mathrm{d}t} = -\left[j^{n,E}{}_{N_E-1/2} - j^n{}_{1/2}\right] + \frac{\Delta_{1/2}}{2}\left[G_{1/2} - R_{1/2}\right] - R_l(n_0, p_0), \tag{B.25}$$

$$\frac{\sigma\chi}{6}\Delta_{N-1/2}\frac{\mathrm{d}p_{N-1}}{\mathrm{d}t} + \left(\frac{\sigma\chi}{3}\Delta_{N-1/2} + \frac{\sigma_H}{3}\Delta^H_{1/2}\right)\frac{\mathrm{d}p_N}{\mathrm{d}t} + \frac{\sigma_H}{6}\Delta^H_{1/2}\frac{\mathrm{d}p^H_1}{\mathrm{d}t} = j^p{}_{N-1/2} - j^{p,H}{}_{1/2} + \frac{\Delta_{N-1/2}}{2}\left[G_{N-1/2} - R_{N-1/2}\right] - R_r(n_N, p_N). \tag{B.26}$$

B.2.3 Implementation

The set of $2N_E + 4N + 4 + 2N_H$ discretised DAEs is evolved in time using MATLAB's built-in solver `ode15s` using an analogous method to that described in Section 4.3.2.

B.3 Initial conditions

In most cases, the following piecewise linear initial conditions provide a suitable starting point for the solver, despite not satisfying all of the equations and boundary conditions.

$$P = 1, \qquad \text{for } 0 \le x \le 1, \tag{B.27}$$

$$n^E = 1, \qquad \text{for } -x_E \le x < 0, \tag{B.28}$$

$$n = \chi x + (1 - x), \qquad \text{for } 0 \le x \le 1, \tag{B.29}$$

$$\phi = 0, \qquad \text{for } -x_E \le x \le 1 + x_H, \tag{B.30}$$

$$p = x + (1 - x)/\chi, \qquad \text{for } 0 \le x \le 1, \tag{B.31}$$

$$p^H = 1, \qquad \text{for } 1 < x \le 1 + x_H. \tag{B.32}$$

References

[1] Advanpix Multiprecision Computing Toolbox for MATLAB 4.3.2.12144, 2017.

[2] S. Agarwal, M. Seetharaman, N. K. Kumawat, A. S. Subbiah, S. K. Sarkar, D. Kabra, M. A. G. Namboothiry, and P. R. Nair. On the uniqueness of ideality factor and voltage exponent of perovskite-based solar cells. *The Journal of Physical Chemistry Letters*, 5(23):4115–4121, 2014.

[3] O. Almora, C. Aranda, I. Zarazua, A. Guerrero, and G. Garcia-Belmonte. Noncapacitive hysteresis in perovskite solar cells at room temperature. *ACS Energy Letters*, 1(1):209–215, 2016.

[4] O. Almora, K. T. Cho, S. Aghazada, I. Zimmermann, G. J. Matt, C. J. Brabec, M. K. Nazeeruddin, and G. Garcia-Belmonte. Discerning recombination mechanisms and ideality factors through impedance analysis of high-efficiency perovskite solar cells. *Nano Energy*, 48:63–72, 2018.

[5] O. Almora, I. Zarazua, I. Mas-Marza, E.and Mora-Sero, J. Bisquert, and G. Garcia-Belmonte. Capacitive dark currents, hysteresis, and electrode polarization in lead halide perovskite solar cells. *The Journal of Physical Chemistry Letters*, 6(9):1645–1652, 2015.

[6] E. H. Anaraki, A. Kermanpur, M. T. Mayer, L. Steier, T. Ahmed, S.-H. Turren-Cruz, J. Seo, J. Luo, S. M. Zakeeruddin, W. R. Tress, T. Edvinsson, M. Grätzel, A. Hagfeldt, and J.-P. Correa-Baena. Low-temperature Nb-doped SnO_2 electron-selective contact yields over 20% efficiency in planar perovskite solar cells. *ACS Energy Letters*, 3(4):773–778, 2018.

[7] E. H. Anaraki, A. Kermanpur, L. Steier, K. Domanski, T. Matsui, W. Tress, M. Saliba, A. Abate, M. Grätzel, A. Hagfeldt, and J.-P. Correa-Baena. Highly efficient and stable planar perovskite solar cells by solution-processed tin oxide. *Energy & Environmental Science*, 9(9):3128–3134, 2016.

[8] T. Baikie, Y. Fang, J. M. Kadro, M. Schreyer, F. Wei, S. G. Mhaisalkar, M. Grätzel, and T. J. White. Synthesis and crystal chemistry of the hybrid perovskite

$CH_3NH_3PbI_3$ for solid-state sensitised solar cell applications. *Journal of Materials Chemistry A*, 1(18):5628, 2013.

[9] J. M. Ball, S. D. Stranks, M. T. Horantner, S. Huttner, W. Zhang, E. J. W. Crossland, I. Ramirez, M. Riede, M. B. Johnston, R. H. Friend, and H. J. Snaith. Optical properties and limiting photocurrent of thin-film perovskite solar cells. *Energy & Environmental Science*, 8:602–609, 2015.

[10] J. Beilsten-Edmands, G. E. Eperon, R. D. Johnson, H. J. Snaith, and P. G. Radaelli. Non-ferroelectric nature of the conductance hysteresis in $CH_3NH_3PbI_3$ perovskite-based photovoltaic devices. *Applied Physics Letters*, 106(17):173502, 2015.

[11] R. A. Belisle, P. Jain, R. Prasanna, T. Leijtens, and M. D. McGehee. Minimal effect of the hole-transport material ionization potential on the open-circuit voltage of perovskite solar cells. *ACS Energy Letters*, 1(3):556–560, 2016.

[12] T. A. Berhe, W.-N. Su, C.-H. Chen, C.-J. Pan, J.-H. Cheng, H.-M. Chen, M.-C. Tsai, L.-Y. Chen, A. A. Dubale, and B.-J. Hwang. Organometal halide perovskite solar cells: Degradation and stability. *Energy & Environmental Science*, 9:323–356, 2016.

[13] I. Borukhov, D. Andelman, and H. Orland. Steric effects in electrolytes: A modified Poisson-Boltzmann equation. *Physical Review Letters*, 79(3):435–438, 1997.

[14] T. M. Brenner, D. A. Egger, L. Kronik, G. Hodes, and D. Cahen. Hybrid organic-inorganic perovskites: Low-cost semiconductors with intriguing charge-transport properties. *Nature Reviews Materials*, 1(15007), 2016.

[15] D. Brinkman, K. Fellner, P. A. Markowich, and M.-T. Wolfram. A drift-diffusion-reaction model for excitonic photovoltaic bilayers: Asymptotic analysis and a 2D HDG finite element scheme. *Mathematical Models and Methods in Applied Science*, 23(05):839–872, 2013.

[16] F. Brivio, K. T. Butler, A. Walsh, and M. van Schilfgaarde. Relativistic quasiparticle self-consitent electronic structure of hybride halide perovskite photovoltaic absorbers. *Physical Review B*, 89(15):155204, 2014.

[17] F. Brivio, A. B. Walker, and A. Walsh. Structural and electronic properties of hybrid perovskites for high-efficiency thin-film photovoltaics from first-principles. *APL Materials*, 1(4):042111, 2013.

[18] D. Bryant, S. Wheeler, B. C. O'Regan, T. Watson, P. R. F. Barnes, D. Worsley, and J. R. Durrant. Observable hysteresis at low temperature in "hysteresis

free" organic-inorganic lead halide perovskite solar cells. *The Journal of Physical Chemistry Letters*, 6(16):3190–3194, 2015.

[19] T. Bu, X. Liu, Y. Zhou, J. Yi, X. Huang, L. Luo, J. Xiao, Z. Ku, Y. Peng, F. Huang, Y.-B. Cheng, and J. Zhong. A novel quadruple-cation absorber for universal hysteresis elimination for high efficiency and stable perovskite solar cells. *Energy & Environmental Science*, 10:2509–2515, 2017.

[20] M. Burger, B. Schlake, and M.-T. Wolfram. Nonlinear Poisson-Nernst-Planck equations for ion flux through confined geometries. *Nonlinearity*, 25(4):961, 2012.

[21] J. Burschka, N. Pellet, S.-J. Moon, R. Humphry-Baker, P. Gao, M. K. Nazeeruddin, and M. Grätzel. Sequential deposition as a route to high-performance perovskite-sensitized solar cells. *Nature*, 499:316, 2013.

[22] P. Calado, A. M. Telford, D. Bryant, X. Li, J. Nelson, B. C. O'Regan, and P. R. F. Barnes. Evidence for ion migration in hybrid perovskite solar cells with minimal hysteresis. *Nature Communications*, 7(13831):13831, 2016.

[23] J. Carrillo, A. Guerrero, S. Rahimnejad, O. Almora, I. Zarazua, E. Mas-Marza, J. Bisquert, and G. Garcia-Belmonte. Ionic reactivity at contacts and aging of methylammonium lead triiodide perovskite solar cells. *Advanced Energy Materials*, 6(9), 2016.

[24] J. M. Cave. *Modelling Novel Photovoltaic Devices*. PhD thesis, University of Bath, 2018.

[25] B. Chen, M. Yang, X. Zheng, C. Wu, W. Li, Y. Yan, J. Bisquert, G. Garcia-Belmonte, K. Zhu, and S. Priya. Impact of capacitive effect and ion migration on the hysteretic behavior of perovskite solar cells. *The Journal of Physical Chemistry Letters*, 6(23):4693–4700, 2015.

[26] H.-W. Chen, N. Sakai, M. Ikegami, and T. Miyasaka. Emergence of hysteresis and transient ferroelectric response in organo-lead halide perovskite solar cells. *The Journal of Physical Chemistry Letters*, 6(1):164–169, 2015.

[27] J. A. Christians, J. S. Manser, and P. V. Kamat. Best practices in perovskite solar cell efficiency measurements. Avoiding the error of making bad cells look good. *The Journal of Physical Chemistry Letters*, 6(5):852–857, 2015.

[28] L. Cojocaru, S. Uchida, P. V. V. Jayaweera, S. Kaneko, J. Nakazaki, T. Kubo, and H. Segawa. Origin of the hysteresis in I-V curves for planar structure perovskite solar cells rationalized with a surface boundary-induced capacitance model. *Chemistry Letters*, 44(12):1750–1752, 2015.

[29] L. Cojocaru, S. Uchida, P. V. V. Jayaweera, S. Kaneko, Y. Toyoshima, J. Nakazaki, T. Kubo, and H. Segawa. Simulation of current-voltage curves for inverted structure perovskite solar cells using equivalent circuit model with inductance. *Applied Physics Express*, 10(5):059102, 2017.

[30] J.-P. Correa-Baena, A. Abate, M. Saliba, W. Tress, T. Jesper Jacobsson, M. Grätzel, and A. Hagfeldt. The rapid evolution of highly efficient perovskite solar cells. *Energy & Environmental Science*, 10(3):710–727, 2017.

[31] J. P. Correa Baena, L. Steier, W. Tress, M. Saliba, S. Neutzner, T. Matsui, F. Giordano, T. J. Jacobsson, A. R. Srimath Kandada, S. M. Zakeeruddin, A. Petrozza, A. Abate, M. K. Nazeeruddin, M. Grätzel, and A. Hagfeldt. Highly efficient planar perovskite solar cells through band alignment engineering. *Energy & Environmental Science*, 8(10):2928–2934, 2015.

[32] J.-P. Correa-Baena, W. Tress, K. Domanski, E. H. Anaraki, S.-H. Turren-Cruz, B. Roose, P. P. Boix, M. Grätzel, M. Saliba, A. Abate, and A. Hagfeldt. Identifying and suppressing interfacial recombination to achieve high open-circuit voltage in perovskite solar cells. *Energy & Environmental Science*, 10:1207–1212, 2017.

[33] J.-P. Correa-Baena, S.-H. Turren-Cruz, W. Tress, A. Hagfeldt, C. Aranda, L. Shooshtari, J. Bisquert, and A. Guerrero. Changes from bulk to surface recombination mechanisms between pristine and cycled perovskite solar cells. *ACS Energy Letters*, 2(3):681–688, 2017.

[34] N. E. Courtier, J. M. Foster, S. E. J. O'Kane, A. B. Walker, and G. Richardson. Systematic derivation of a surface polarisation model for planar perovskite solar cells. *European Journal of Applied Mathematics*, 30(3):427–457, 2019.

[35] N. E. Courtier, G. Richardson, and J. M. Foster. A fast and robust numerical scheme for solving models of charge carrier transport and ion vacancy motion in perovskite solar cells. *Applied Mathematical Modelling*, 63:329 – 348, 2018.

[36] D. W. de Quilettes, S. M. Vorpahl, S. D. Stranks, H. Nagaoka, G. E. Eperon, M. E. Ziffer, H. J. Snaith, and D. S. Ginger. Impact of microstructure on local carrier lifetime in perovskite solar cells. *Science*, 348(6235):683–686, 2015.

[37] D. W. de Quilettes, W. Zhang, V. M. Burlakov, D. J. Graham, T. Leijtens, A. Osherov, V. Bulović, H. J. Snaith, D. S. Ginger, and S. D. Stranks. Photo-induced halide redistribution in organic-inorganic perovskite films. *Nature Communications*, 7:11683, 2016.

[38] S. De Wolf, J. Holovsky, S.-J. Moon, P. Löper, B. Niesen, M. Ledinsky, F.-J. Haug, J.-H. Yum, and C. Ballif. Organometallic halide perovskites: Sharp optical absorption edge and its relation to photovoltaic performance. *The Journal of Physical Chemistry Letters*, 5(6):1035–1039, 2014.

[39] K. Domanski, J.-P. Correa-Baena, N. Mine, M. K. Nazeeruddin, A. Abate, M. Saliba, W. Tress, A. Hagfeldt, and M. Grätzel. Not all that glitters is gold: Metal-migration-induced degradation in perovskite solar cells. *ACS Nano*, 10(6):6306–14, 2016.

[40] K. Domanski, B. Roose, T. Matsui, M. Saliba, S.-H. Turren-Cruz, J.-P. Correa-Baena, C. R. Carmona, G. Richardson, J. M. Foster, F. D. Angelis, J. M. Ball, A. Petrozza, N. Mine, M. K. Nazeeruddin, W. Tress, M. Grätzel, U. Steiner, A. Hagfeldt, and A. Abate. Migration of cations induces reversible performance losses over day/night cycling in perovskite solar cells. *Energy & Environmental Science*, 10(2):604–613, 2017.

[41] K. Domanski, W. Tress, T. Moehl, M. Saliba, M. K. Nazeeruddin, and M. Grätzel. Working principles of perovskite photodetectors: Analyzing the interplay between photoconductivity and voltage-driven energy-level alignment. *Advanced Functional Materials*, 25(44):6936–6947, 2015.

[42] Q. Dong, F. Liu, M. K. Wong, H. W. Tam, A. B. Djurišić, A. Ng, C. Surya, W. K. Chan, and A. M. C. Ng. Encapsulation of perovskite solar cells for high humidity conditions. *ChemSusChem*, 9(18):2597–2603, 2016.

[43] T. A. Driscoll, N. Hale, and L. N. Trefethen. *Chebfun Guide*. Panufty Publications, Oxford, 2014.

[44] A. Dualeh, T. Moehl, N. Tétreault, J. Teuscher, P. Gao, M. K. Nazeeruddin, and M. Grätzel. Impedance spectroscopic analysis of lead iodide perovskite-sensitized solid-state solar cells. *ACS Nano*, 8(1):362–373, 2014.

[45] C. Eames, J. M. Frost, P. R. F. Barnes, B. C. O'Regan, A. Walsh, and M. S. Islam. Ionic transport in hybrid lead iodide perovskite solar cells. *Nature Communications*, 6:7497, 2015.

[46] J. Emara, T. Schnier, N. Pourdavoud, T. Riedl, K. Meerholz, and S. Olthof. Impact of film stoichiometry on the ionization energy and electronic structure of $CH_3NH_3PbI_3$ perovskites. *Advanced Materials*, 28(3):553–559, 2016.

[47] G. E. Eperon, V. M. Burlakov, P. Docampo, A. Goriely, and H. J. Snaith. Morphological control for high performance, solution-processed planar heterojunction perovskite solar cells. *Advanced Functional Materials*, 24(1):151–157, 2014.

[48] Y. Fang, C. Bi, D. Wang, and J. Huang. The functions of fullerenes in hybrid perovskite solar cells. *ACS Energy Letters*, 2(4):782–794, 2017.

[49] D. W. Ferdani, A. L. Johnson, S. E. Lewis, P. J. Baker, and P. J. Cameron. Opposites attract, muons as direct probes for iodide diffusion in methyl ammonium lead iodide. *arXiv:1801.03845v2*, 2018.

[50] D. Forgcs, M. Sessolo, and H. J. Bolink. Lead acetate precursor based p-i-n perovskite solar cells with enhanced reproducibility and low hysteresis. *Journal of Materials Chemistry A*, 3:14121–14125, 2015.

[51] J. M. Foster, J. Kirkpatrick, and G. Richardson. Asymptotic and numerical prediction of current-voltage curves for an organic bilayer solar cell under varying illumination and comparison to the Shockley equivalent circuit. *Journal of Applied Physics*, 114(10):104501, 2013.

[52] J. M. Foster, H. J. Snaith, T. Leijtens, and G. Richardson. A model for the operation of perovskite based hybrid solar cells: Formulation, analysis, and comparison to experiment. *SIAM Journal on Applied Mathematics*, 74(6):1935–1966, 2014.

[53] G. Friesen and H. A. Ossenbrink. Capacitance effects in high-efficiency cells. *Solar Energy Materials and Solar Cells*, 48(1):77 – 83, 1997.

[54] J. M. Frost, K. T. Butler, and A. Walsh. Molecular ferroelectric contributions to anomalous hysteresis in hybrid perovskite solar cells. *APL Materials*, 2(8):081506, 2014.

[55] J. M. Frost and A. Walsh. What is moving in hybrid halide perovskite solar cells? *Accounts of Chemical Research*, 49(3):528–535, 2016.

[56] C. W. Gear. *Numerical Initial Value Problems in Ordinary Differential Equations*. Prentice Hall PTR, Upper Saddle River, NJ, USA, 1971.

[57] S. George, J. M. Foster, and G. Richardson. Modelling in vivo action potential propagation along a giant axon. *Journal of Mathematical Biology*, 70(1-2):237–263, 2015.

[58] M. Glazer and J. Wark. *Statistical Mechanics: A Survival Guide*. Oxford University Press, 2001.

[59] A. Gomez, S. Sanchez, M. Campoy-Quiles, and A. Abate. Topological distribution of reversible and non-reversible degradation in perovskite solar cells. *Nano Energy*, 45:94–100, 2018.

[60] R. Gottesman, E. Haltzi, L. Gouda, S. Tirosh, Y. Bouhadana, A. Zaban, E. Mosconi, and F. De Angelis. Extremely slow photoconductivity response of $CH_3NH_3PbI_3$ perovskites suggesting structural changes under working conditions. *The Journal of Physical Chemistry Letters*, 5(15):2662–2669, 2014.

[61] R. Gottesman, P. Lopez-Varo, L. Gouda, J. A. Jimenez-Tejada, J. Hu, S. Tirosh, A. Zaban, and J. Bisquert. Dynamic phenomena at perovskite/electron-selective contact interface as interpreted from photovoltage decays. *Chem*, 1(5):776–789, 2016.

[62] G. Grancini, C. Roldán-Carmona, I. Zimmermann, E. Mosconi, X. Lee, D. Martineau, S. Narbey, F. Oswald, F. De Angelis, M. Grätzel, and M. K. Nazeeruddin. One-year stable perovskite solar cells by 2D/3D interface engineering. *Nature Communications*, 8:1–8, 2017.

[63] A. Guerrero, J. You, C. Aranda, Y. S. Kang, G. Garcia-Belmonte, H. Zhou, J. Bisquert, and Y. Yang. Interfacial degradation of planar lead halide perovskite solar cells. *ACS Nano*, 10(1):218–224, 2016.

[64] O. Hentz, Z. Zhao, and S. Gradeak. Impacts of ion segregation on local optical properties in mixed halide perovskite films. *Nano Letters*, 16(2):1485–1490, 2016.

[65] J. H. Heo, H. J. Han, D. Kim, T. K. Ahn, and S. H. Im. Hysteresis-less inverted $CH_3NH_3PbI_3$ planar perovskite hybrid solar cells with 18.1% power conversion efficiency. *Energy & Environmental Science*, 8:1602–1608, 2015.

[66] L. M. Herz. Charge-carrier dynamics in organic-inorganic metal halide perovskites. *Annual Review of Physical Chemistry*, 67:65–89, 2016.

[67] J. Idígoras, L. Contreras-Bernal, J. M. Cave, N. E. Courtier, A. Barranco, A. Borras, J. R. Sánchez-Valencia, J. A. Anta, and A. B. Walker. The role of surface recombination on the performance of perovskite solar cells: Effect of morphology and crystalline phase of TiO_2 contact. *Advanced Materials Interfaces*, 5:1801076, 2018.

[68] D. Jacobs, Y. Wu, H. Shen, C. Barugkin, F. Beck, T. White, K. Weber, and K. Catchpole. Hysteresis phenomena in perovskite solar cells: The many and varied effects of ionic accumulation. *Physical Chemistry Chemical Physics*, 19:3094–3103, 2017.

[69] T. J. Jacobsson, J.-P. Correa-Baena, M. Pazoki, M. Saliba, K. Schenk, M. Grätzel, and A. Hagfeldt. Exploration of the compositional space for mixed lead halogen perovskites for high efficiency solar cells. *Energy & Environmental Science*, 9:1706–1724, 2016.

[70] N. J. Jeon, H. Na, E. H. Jung, T.-Y. Yang, Y. G. Lee, G. Kim, H.-W. Shin, S. I. Seok, J. Lee, and J. Seo. A fluorene-terminated hole-transporting material for highly efficient and stable perovskite solar cells. *Nature Energy*, 3:682–689, 2018.

[71] Y. Kato, L. K. Ono, M. V. Lee, S. Wang, S. R. Raga, and Y. Qi. Silver iodide formation in methyl ammonium lead iodide perovskite solar cells with silver top electrodes. *Advanced Materials Interfaces*, 2(13):1500195, 2015.

[72] L. Kegelmann, C. M. Wolff, C. Awino, F. Lang, E. L. Unger, L. Korte, T. Dittrich, D. Neher, B. Rech, and S. Albrecht. It takes two to tango - Double-layer selective contacts in perovskite solar cells for improved device performance and reduced hysteresis. *ACS Applied Materials & Interfaces*, 9(20):17245–17255, 2017.

[73] M. S. Kilic, M. Z. Bazant, and A. Ajdari. Steric effects in the dynamics of electrolytes at large applied voltages. II. Modified Poisson-Nernst-Planck equations. *Physical Review E - Statistical, Nonlinear, and Soft Matter Physics*, 75(2):1–11, 2007.

[74] H.-S. Kim, I. H. Jang, N. Ahn, M. Choi, A. Guerrero, J. Bisquert, and N.-G. Park. Control of I-V hysteresis in $CH_3NH_3PbI_3$ perovskite solar cell. *The Journal of Physical Chemistry Letters*, 6(22):4633–4639, 2015.

[75] H.-S. Kim, C.-R. Lee, J.-H. Im, K.-B. Lee, T. Moehl, A. Marchioro, S.-J. Moon, R. Humphry-Baker, J.-H. Yum, J. E. Moser, M. Grätzel, and N.-G. Park. Lead iodide perovskite sensitized all-solid-state submicron thin film mesoscopic solar cell with efficiency exceeding 9%. *Scientific Reports*, 2(7436):591, 2012.

[76] T. Kirchartz, B. E. Pieters, J. Kirkpatrick, U. Rau, and J. Nelson. Recombination via tail states in polythiophene:fullerene solar cells. *Physical Review B*, 83(11):115209, 2011.

[77] A. Kojima, K. Teshima, Y. Shirai, and T. Miyasaka. Organometal halide perovskites as visible-light sensitizers for photovoltaic cells. *Journal of the American Chemical Society*, 131(17):6050–6051, 2009.

[78] I. B. Koutselas, L. Ducasse, and G. C. Papavassiliou. Electronic properties of three- and low-dimensional semiconducting materials with Pb halide and Sn halide units. *Journal of Physics: Condensed Matter*, 8(9):1217–1227, 1996.

[79] M. M. Lee, J. Teuscher, T. Miyasaka, T. N. Murakami, and H. J. Snaith. Efficient hybrid solar cells based on meso-superstructured organometal halide perovskites. *Science*, 338(6107):643–647, 2012.

[80] T. Leijtens, K. Bush, R. Cheacharoen, R. Beal, A. Bowring, and M. D. McGehee. Towards enabling stable lead halide perovskite solar cells; interplay between structural, environmental, and thermal stability. *Journal of Materials Chemistry A*, 5:11483–11500, 2017.

[81] I. Levine, P. K. Nayak, J. T. W. Wang, N. Sakai, S. van Reenen, T. M. Brenner, S. Mukhopadhyay, H. J. Snaith, G. Hodes, and D. Cahen. Interface-dependent ion migration/accumulation controls hysteresis in $MAPbI_3$ solar cells. *The Journal of Physical Chemistry C*, 120(30):16399–16411, 2016.

[82] C. Li, S. Tscheuschner, F. Paulus, P. E. Hopkinson, J. Kießling, A. Köhler, Y. Vaynzof, and S. Huettner. Iodine migration and its effect on hysteresis in perovskite solar cells. *Advanced Materials*, 28(12):2446–2454, 2016.

[83] X. Li, N. P. Hylton, V. Giannini, K.-H. Lee, N. J. Ekins-Daukes, and S. A. Maier. Multi-dimensional modeling of solar cells with electromagnetic and carrier transport calculations. *Progress in Photovoltaics: Research and Applications*, 21(1):109–120, 2013.

[84] Z. Li, C. Xiao, Y. Yang, S. P. Harvey, D. H. Kim, J. A. Christians, M. Yang, P. Schulz, S. U. Nanayakkara, C.-S. Jiang, J. M. Luther, J. J. Berry, M. C. Beard, M. M. Al-Jassim, and K. Zhu. Extrinsic ion migration in perovskite solar cells. *Energy & Environmental Science*, 10(5):1234–1242, 2017.

[85] W. Liao, D. Zhao, Y. Yu, N. Shrestha, K. Ghimire, C. R. Grice, C. Wang, Y. Xiao, A. J. Cimaroli, R. J. Ellingson, N. J. Podraza, K. Zhu, R.-G. Xiong, and Y. Yan. Fabrication of efficient low-bandgap perovskite solar cells by combining formamidinium tin iodide with methylammonium lead iodide. *Journal of the American Chemical Society*, 138(38):12360–12363, 2016.

[86] M. Liu, M. B. Johnston, and H. J. Snaith. Efficient planar heterojunction perovskite solar cells by vapour deposition. *Nature*, 501(7467):395–398, 2013.

[87] P. Löper, M. Stuckelberger, B. Niesen, J. Werner, M. Filipič, S.-J. Moon, J.-H. Yum, M. Topič, S. De Wolf, and C. Ballif. Complex refractive index spectra of $CH_3NH_3PbI_3$ perovskite thin films determined by spectroscopic ellipsometry and spectrophotometry. *The Journal of Physical Chemistry Letters*, 6(1):66–71, 2015.

[88] P. Lopez-Varo, J. A. Jimnez-Tejada, M. Garca-Rosell, S. Ravishankar, G. Garcia-Belmonte, J. Bisquert, and O. Almora. Device physics of hybrid perovskite solar cells: Theory and experiment. *Advanced Energy Materials*, 8(14):1702772, 2018.

[89] G. Lozano. The role of metal halide perovskites in next-generation lighting devices. *The Journal of Physical Chemistry Letters*, 9(14):3987–3997, 2018.

[90] D. J. C. MacKay. *Sustainable Energy - without the hot air*. UIT Cambridge Ltd., 2009.

[91] MATLAB version 9.3.0.713579 (R2017b), 2017.

[92] F. Matteocci, L. Cinà, E. Lamanna, S. Cacovich, G. Divitini, P. A. Midgley, C. Ducati, and A. D. Carlo. Encapsulation for long-term stability enhancement of perovskite solar cells. *Nano Energy*, 30:162–172, 2016.

[93] T. Miyasaka. Perovskite photovoltaics: Rare functions of organo lead halide in solar cells and optoelectronic devices. *Chemistry Letters*, 44(6):720–729, 2015.

[94] National Renewable Energy Laboratory (NREL) research cell record efficiency chart. http://www.nrel.gov/pv/assets/images/efficiency-chart.png, 2018.

[95] J. Nelson. *The Physics of Solar Cells*. Imperial College Press, London, UK, 2003.

[96] M. T. Neukom, S. Züfle, E. Knapp, M. Makha, R. Hany, and B. Ruhstaller. Why perovskite solar cells with high efficiency show small IV-curve hysteresis. *Solar Energy Materials and Solar Cells*, 169:159–166, 2017.

[97] W. Nie, H. Tsai, R. Asadpour, J.-C. Blancon, A. J. Neukirch, G. Gupta, J. J. Crochet, M. Chhowalla, S. Tretiak, M. A. Alam, H.-L. Wang, and A. D. Mohite. High-efficiency solution-processed perovskite solar cells with millimeter-scale grains. *Science*, 347(6221):522–525, 2015.

[98] G. Niu, X. Guo, and L. Wang. Review of recent progress in chemical stability of perovskite solar cells. *Journal of Materials Chemistry A*, 3(17):8970–8980, 2015.

[99] S. E. J. O'Kane, G. Richardson, A. Pockett, R. G. Niemann, J. M. Cave, N. Sakai, G. E. Eperon, H. J. Snaith, J. M. Foster, P. J. Cameron, and A. B. Walker. Measurement and modelling of dark current decay transients in perovskite solar cells. *Journal of Materials Chemistry C*, 5(2):452–462, 2017.

[100] Oxford PV. https://www.oxfordpv.com/news/oxford-pv-collaborates-hzb-move-peroskite-solar-cells-closer-commercialisation. 9th January 2018.

[101] N. Pellet, P. Gao, G. Gregori, T.-Y. Yang, M. K. Nazeeruddin, J. Maier, and M. Grätzel. Mixed-organic-cation perovskite photovoltaics for enhanced solar-light harvesting. *Angewandte Chemie International Edition*, 53(12):3151–3157, 2014.

[102] J. Peng, Y. Wu, W. Ye, D. A. Jacobs, H. Shen, X. Fu, Y. Wan, T. Duong, N. Wu, C. Barugkin, H. T. Nguyen, D. Zhong, J. Li, T. Lu, Y. Liu, M. N. Lockrey, K. J. Weber, K. R. Catchpole, and T. P. White. Interface passivation using ultrathin polymer-fullerene films for high-efficiency perovskite solar cells with negligible hysteresis. *Energy & Environmental Science*, 10(8):1792–1800, 2017.

[103] C. P. Please. An analysis of semiconductor PN junctions. *IMA Journal of Applied Mathematics*, 28(3):301–318, 1982.

[104] A. Pockett, G. E. Eperon, T. Peltola, H. J. Snaith, A. Walker, L. M. Peter, and P. J. Cameron. Characterization of planar lead halide perovskite solar cells by impedance spectroscopy, open-circuit photovoltage decay, and intensity-modulated photovoltage/photocurrent spectroscopy. *The Journal of Physical Chemistry C*, 119(7):3456–3465, 2015.

[105] A. Pockett, G. E. Eperon, N. Sakai, H. J. Snaith, L. M. Peter, and P. J. Cameron. Microseconds, milliseconds and seconds: Deconvoluting the dynamic behaviour of planar perovskite solar cells. *Physical Chemistry Chemical Physics*, 19(8):5959–5970, 2017.

[106] L. E. Polander, P. Pahner, M. Schwarze, M. Saalfrank, C. Koerner, and K. Leo. Hole-transport material variation in fully vacuum deposited perovskite solar cells. *APL Materials*, 2(8):081503, 2014.

[107] C. Quarti, G. Grancini, E. Mosconi, P. Bruno, J. M. Ball, M. M. Lee, H. J. Snaith, A. Petrozza, and F. De Angelis. The Raman spectrum of the $CH_3NH_3PbI_3$ hybrid perovskite: Interplay of theory and experiment. *The Journal of Physical Chemistry Letters*, 5(2):279–284, 2014.

[108] S. Ravishankar, O. Almora, C. Echeverría-Arrondo, E. Ghahremanirad, C. Aranda, A. Guerrero, F. Fabregat-Santiago, A. Zaban, G. Garcia-Belmonte, and J. Bisquert. Surface polarization model for the dynamic hysteresis of perovskite solar cells. *The Journal of Physical Chemistry Letters*, 8(5):915–921, 2017.

[109] G. Richardson, S. E. J. O'Kane, R. G. Niemann, T. A. Peltola, J. M. Foster, P. J. Cameron, and A. B. Walker. Can slow-moving ions explain hysteresis in the current-voltage curves of perovskite solar cells? *Energy & Environmental Science*, 9(4):1476–1485, 2016.

[110] G. Richardson, C. Please, J. Foster, and J. Kirkpatrick. Asymptotic solution of a model for bilayer organic diodes and solar cells. *SIAM Journal on Applied Mathematics*, 72(6):1792–1817, 2012.

[111] G. Richardson, C. P. Please, and V. Styles. Derivation and solution of effective medium equations for bulk heterojunction organic solar cells. *European Journal of Applied Mathematics*, 28(2017):1–42, 2017.

[112] G. Richardson and A. Walker. Drift diffusion modelling of charge transport in photovoltaic devices. In *Unconventional Thin Film Photovoltaics*, pages 297–331. Royal Society of Chemistry (RSC), 2016.

[113] M. Sajedi Alvar, M. Kumar, P. W. M. Blom, G.-j. A. H. Wetzelaer, and K. Asadi. Absence of ferroelectricity in methylammonium lead iodide perovskite. *AIP Advances*, 7(9):095110, 2017.

[114] M. Saliba, T. Matsui, K. Domanski, J.-Y. Seo, A. Ummadisingu, S. M. Zakeeruddin, J.-P. Correa-Baena, W. R. Tress, A. Abate, A. Hagfeldt, and M. Grätzel. Incorporation of rubidium cations into perovskite solar cells improves photovoltaic performance. *Science*, 354(6309):206–209, 2016.

[115] M. Saliba, T. Matsui, J.-Y. Seo, K. Domanski, J.-P. Correa-Baena, M. K. Nazeeruddin, S. M. Zakeeruddin, W. Tress, A. Abate, A. Hagfeldt, and M. Grätzel. Cesium-containing triple cation perovskite solar cells: Improved stability, reproducibility and high efficiency. *Energy & Environmental Science*, 9(6):1989–1997, 2016.

[116] R. S. Sanchez, V. Gonzalez-Pedro, J.-W. Lee, N.-G. Park, Y. S. Kang, I. Mora-Sero, and J. Bisquert. Slow dynamic processes in lead halide perovskite solar cells. Characteristic times and hysteresis. *The Journal of Physical Chemistry Letters*, 5(13):2357–2363, 2014.

[117] D. L. Scharfetter and H. K. Gummel. Large-signal analysis of a silicon Read diode oscillator. *IEEE Transactions on Electron Devices*, 16(1):64–77, 1969.

[118] C. Schmeiser and A. Unterreiter. The derivation of analytic device models by asymptotic methods. In *Semiconductors Part II*, pages 343–363. Springer New York, 1994.

[119] D. Schroeder. *Modelling of Interface Carrier Transport for Device Simulation*. Computational Microelectronics. Springer-Verlag Wien, New York, 1994.

[120] P. Schulz, E. Edri, S. Kirmayer, G. Hodes, D. Cahen, and A. Kahn. Interface energetics in organo-metal halide perovskite-based photovoltaic cells. *Energy & Environmental Science*, 7(4):1377–1381, 2014.

[121] J.-Y. Seo, T. Matsui, J. Luo, J.-P. Correa-Baena, F. Giordano, M. Saliba, K. Schenk, A. Ummadisingu, K. Domanski, M. Hadadian, A. Hagfeldt, S. M. Zakeeruddin, U. Steiner, M. Grätzel, and A. Abate. Ionic liquid control crystal growth

to enhance planar perovskite solar cells efficiency. *Advanced Energy Materials*, 6(20):1600767, 2016.

[122] L. F. Shampine and M. W. Reichelt. The MATLAB ODE Suite. *SIAM Journal on Scientific Computing*, 18(1):1–22, 1997.

[123] L. F. Shampine, M. W. Reichelt, and J. A. Kierzenka. Solving index-1 DAEs in MATLAB and Simulink. *SIAM Review*, 41(3):538–552, 1999.

[124] Y. Shao, Y. Fang, T. Li, Q. Wang, Q. Dong, Y. Deng, Y. Yuan, H. Wei, M. Wang, A. Gruverman, J. Shield, and J. Huang. Grain boundary dominated ion migration in polycrystalline organic-inorganic halide perovskite films. *Energy & Environmental Science*, 9:1752–1759, 2016.

[125] Y. Shao, Z. Xiao, C. Bi, Y. Yuan, and J. Huang. Origin and elimination of photocurrent hysteresis by fullerene passivation in $CH_3NH_3PbI_3$ planar heterojunction solar cells. *Nature Communications*, 5:5784, 2014.

[126] H. Shen, D. A. Jacobs, Y. Wu, T. Duong, J. Peng, X. Wen, X. Fu, S. K. Karuturi, T. P. White, K. Weber, and K. R. Catchpole. Inverted hysteresis in $CH_3NH_3PbI_3$ solar cells: Role of stoichiometry and band alignment. *The Journal of Physical Chemistry Letters*, 8(12):2672–2680, 2017.

[127] R. D. Skeel and M. Berzins. A method for the spatial discretization of parabolic equations in one space variable. *SIAM Journal on Scientific and Statistical Computing*, 11(1):1–32, 1990.

[128] H. J. Snaith, A. Abate, J. M. Ball, G. E. Eperon, T. Leijtens, N. K. Noel, S. D. Stranks, J. T.-W. Wang, K. Wojciechowski, and W. Zhang. Anomalous hysteresis in perovskite solar cells. *The Journal of Physical Chemistry Letters*, 5(9):1511–1515, 2014.

[129] M. Stolterfoht, C. M. Wolff, Y. Amir, A. Paulke, L. Perdigon-Toro, P. Caprioglio, and D. Neher. Approaching the fill factor Shockley Queisser limit in stable, dopant-free triple cation perovskite solar cells. *Energy & Environmental Science*, 10(6):1530–1539, 2017.

[130] C. C. Stoumpos, C. D. Malliakas, and M. G. Kanatzidis. Semiconducting tin and lead iodide perovskites with organic cations: Phase transitions, high mobilities, and near-infrared photoluminescent properties. *Inorganic Chemistry*, 52(15):9019–9038, 2013.

[131] S. D. Stranks, V. M. Burlakov, T. Leijtens, J. M. Ball, A. Goriely, and H. J. Snaith. Recombination kinetics in organic-inorganic perovskites: excitons, free charge, and subgap states. *Physical Review Applied*, 2(3):034007, 2014.

[132] S. D. Stranks, G. E. Eperon, G. Grancini, C. Menelaou, M. J. P. Alcocer, T. Leijtens, L. M. Herz, A. Petrozza, and H. J. Snaith. Electron-hole diffusion lengths exceeding 1 micrometer in an organometal trihalide perovskite absorber. *Science*, 342(6156):341–344, 2013.

[133] S. D. Stranks and H. J. Snaith. Metal-halide perovskites for photovoltaic and light-emitting devices. *Nature Nanotechnology*, 10(5):391–402, 2015.

[134] T. C. Sum, S. Chen, G. Xing, X. Liu, and B. Wu. Energetics and dynamics in organic-inorganic halide perovskite photovoltaics and light emitters. *Nanotechnology*, 26(34):342001, 2015.

[135] H. Tan, A. Jain, O. Voznyy, X. Lan, F. P. G. de Arquer, J. Z. Fan, R. Quintero-Bermudez, M. Yuan, B. Zhang, Y. Zhao, F. Fan, P. Li, L. N. Quan, Y. Zhao, Z.-H. Lu, Z. Yang, S. Hoogland, and E. H. Sargent. Efficient and stable solution-processed planar perovskite solar cells via contact passivation. *Science*, 355(6326):722–726, 2017.

[136] N. Taylor. Guidelines for PV power measurement in industry. *JRC Scientific and Technical Reports, Joint Research Centre-European Commission, Itália*, 2010.

[137] T. Todorov, O. Gunawan, and S. Guha. A road towards 25% efficiency and beyond: Perovskite tandem solar cells. *Molecular Systems Design & Engineering*, 1(4):370–376, 2016.

[138] W. Tress. Metal halide perovskites as mixed electronic-ionic conductors: Challenges and opportunities - From hysteresis to memristivity. *The Journal of Physical Chemistry Letters*, 8(13):3106–3114, 2017. PMID: 28641009.

[139] W. Tress, N. Marinova, O. Inganäs, M. K. Nazeeruddin, S. M. Zakeeruddin, and M. Grätzel. Predicting the open-circuit voltage of $CH_3NH_3PbI_3$ perovskite solar cells using electroluminescence and photovoltaic quantum efficiency spectra: The role of radiative and non-radiative recombination. *Advanced Energy Materials*, 5(3):1400812, 2015.

[140] W. Tress, N. Marinova, T. Moehl, S. M. Zakeeruddin, M. K. Nazeeruddin, and M. Grätzel. Understanding the rate-dependent J-V hysteresis, slow time component, and aging in $CH_3NH_3PbI_3$ perovskite solar cells: The role of a compensated electric field. *Energy & Environmental Science*, 8(3):995–1004, 2015.

[141] W. Tress, M. Yavari, K. Domanski, P. Yadav, B. Niesen, J. P. Correa Baena, A. Hagfeldt, and M. Grätzel. Interpretation and evolution of open-circuit voltage, recombination, ideality factor and subgap defect states during reversible light-soaking and irreversible degradation of perovskite solar cells. *Energy & Environmental Science*, 11(1):151–165, 2018.

[142] K. Tvingstedt, L. Gil-Escrig, C. Momblona, P. Rieder, D. Kiermasch, M. Sessolo, A. Baumann, H. J. Bolink, and V. Dyakonov. Removing leakage and surface recombination in planar perovskite solar cells. *ACS Energy Letters*, 2(2):424–430, 2017.

[143] E. L. Unger, E. T. Hoke, C. D. Bailie, W. H. Nguyen, A. R. Bowring, T. Heumüller, M. G. Christoforo, and M. D. McGehee. Hysteresis and transient behavior in current-voltage measurements of hybrid-perovskite absorber solar cells. *Energy & Environmental Science*, 7(11):3690–3698, 2014.

[144] S. van Reenen, M. Kemerink, and H. J. Snaith. Modeling anomalous hysteresis in perovskite solar cells. *The Journal of Physical Chemistry Letters*, 6(19):3808–3814, 2015.

[145] A. Walsh, D. O. Scanlon, S. Chen, X. G. Gong, and S.-H. Wei. Self-regulation mechanism for charged point defects in hybrid halide perovskites. *Angewandte Chemie International Edition*, 54(6):1791–1794, 2015.

[146] D. Walter, A. Fell, Y. Wu, T. Duong, C. Barugkin, N. Wu, T. P. White, and K. Weber. Transient photovoltage in perovskite solar cells: Interaction of trap-mediated recombination and migration of multiple ionic species. *The Journal of Physical Chemistry C*, 122(21):11270–11281, 2018.

[147] S. Weber, I. M. Hermes, S. H. Turren Cruz, C. Gort, V. W. Bergmann, L. Gilson, A. Hagfeldt, M. Grätzel, W. Tress, and R. Berger. How the formation of interfacial charge causes hysteresis in perovskite solar cells. *Energy & Environmental Science*, 2018.

[148] J. Wei, Y. Zhao, H. Li, G. Li, J. Pan, D. Xu, Q. Zhao, and D. Yu. Hysteresis analysis based on the ferroelectric effect in hybrid perovskite solar cells. *The Journal of Physical Chemistry Letters*, 5(21):3937–3945, 2014.

[149] J. Werner, C.-H. Weng, A. Walter, L. Fesquet, J. P. Seif, S. De Wolf, B. Niesen, and C. Ballif. Efficient monolithic perovskite/silicon tandem solar cell with cell area >1 cm^2. *The Journal of Physical Chemistry Letters*, 7(1):161–166, 2016.

[150] G.-J. A. H. Wetzelaer, M. Scheepers, A. M. Sempere, C. Momblona, J. Ávila, and H. J. Bolink. Trap-assisted non-radiative recombination in organic-inorganic perovskite solar cells. *Advanced Materials*, 27(11):1837–1841, 2015.

[151] L. D. Whalley, J. M. Frost, Y.-K. Jung, and A. Walsh. Perspective: Theory and simulation of hybrid halide perovskites. *Journal of Chemical Physics*, 146(22), 2017.

[152] K. Wojciechowski, S. D. Stranks, A. Abate, G. Sadoughi, A. Sadhanala, N. Kopidakis, G. Rumbles, C.-Z. Li, R. H. Friend, A. K.-Y. Jen, and H. J. Snaith. Heterojunction modification for highly efficient organicinorganic perovskite solar cells. *ACS Nano*, 8(12):12701–12709, 2014.

[153] C. M. Wolff, F. Zu, A. Paulke, L. P. Toro, N. Koch, and D. Neher. Reduced interface-mediated recombination for high open-circuit voltages in $CH_3NH_3PbI_3$ solar cells. *Advanced Materials*, 29:1700159, 2017.

[154] M. Xiao, F. Huang, W. Huang, Y. Dkhissi, Y. Zhu, J. Etheridge, A. Gray-Weale, U. Bach, Y.-B. Cheng, and L. Spiccia. A fast deposition-crystallization procedure for highly efficient lead iodide perovskite thin-film solar cells. *Angewandte Chemie*, 126(37):10056–10061, 2014.

[155] K. Yan, M. Peng, X. Yu, X. Cai, S. Chen, H. Hu, B. Chen, X. Gao, B. Dong, and D. Zou. High-performance perovskite memristor based on methyl ammonium lead halides. *Journal of Materials Chemistry C*, 4:1375–1381, 2016.

[156] D. Yang, X. Zhou, R. Yang, Z. Yang, W. Yu, X. Wang, C. Li, S. F. Liu, and R. P. H. Chang. Surface optimization to eliminate hysteresis for record efficiency planar perovskite solar cells. *Energy & Environmental Science*, 9:3071–3078, 2016.

[157] G. Yin, J. Ma, H. Jiang, J. Li, D. Yang, F. Gao, J. Zeng, Z. Liu, and S. F. Liu. Enhancing efficiency and stability of perovskite solar cells through Nb-doping of TiO_2 at low temperature. *ACS Applied Materials & Interfaces*, 9(12):10752–10758, 2017.

[158] X. Yin, M. Que, Y. Xing, and W. Que. High efficiency hysteresis-less inverted planar heterojunction perovskite solar cells with a solution-derived NiO_x hole contact layer. *Journal of Materials Chemistry A*, 3:24495–24503, 2015.

[159] H. Yuan, E. Debroye, K. Janssen, H. Naiki, C. Steuwe, G. Lu, M. Moris, E. Orgiu, H. Uji-i, F. De Schryver, P. Samorì, J. Hofkens, and M. Roeffaers. Degradation of methylammonium lead iodide perovskite structures through light and electron beam driven ion migration. *The Journal of Physical Chemistry Letters*, 7:561–566, 2016.

[160] Y. Yuan and J. Huang. Ion migration in organometal trihalide perovskite and its impact on photovoltaic efficiency and stability. *Accounts of Chemical Research*, 49(2):286–293, 2016.

[161] H. Zhang, C. Liang, Y. Zhao, M. Sun, H. Liu, J. Liang, D. Li, F. Zhang, and Z. He. Dynamic interface charge governing the current-voltage hysteresis in perovskite solar cells. *Physical Chemistry Chemical Physics*, 17(15):9613–9618, 2015.

[162] Y. Zhang, M. Liu, G. E. Eperon, T. C. Leijtens, D. McMeekin, M. Saliba, W. Zhang, M. de Bastiani, A. Petrozza, L. M. Herz, M. B. Johnston, H. Lin, and H. J. Snaith. Charge selective contacts, mobile ions and anomalous hysteresis in organic-inorganic perovskite solar cells. *Materials Horizons*, 2:315–322, 2015.

[163] D. Zhao, M. Sexton, H.-Y. Park, S. Liu, G. Baure, J. C. Nino, and F. So. High-efficiency solution-processed planar perovskite solar cells with a polymer hole transport layer. *Advanced Energy Materials*, 5(6):1401855, 2014.

[164] J. Zhao, Y. Deng, H. Wei, X. Zheng, Z. Yu, Y. Shao, J. E. Shield, and J. Huang. Strained hybrid perovskite thin films and their impact on the intrinsic stability of perovskite solar cells. *Science Advances*, 3(11), 2017.

[165] H. Zhou, Q. Chen, G. Li, S. Luo, T.-b. Song, H.-S. Duan, Z. Hong, J. You, Y. Liu, and Y. Yang. Interface engineering of highly efficient perovskite solar cells. *Science*, 345(6196):542–546, 2014.

[166] Z. Zhu, Y. Bai, X. Liu, C.-C. Chueh, S. Yang, and A. K.-Y. Jen. Enhanced efficiency and stability of inverted perovskite solar cells using highly crystalline SnO_2 nanocrystals as the robust electron-transporting layer. *Advanced Materials*, 28(30):6478–6484, 2016.

[167] E. Zimmermann, K. K. Wong, M. Müller, H. Hu, P. Ehrenreich, M. Kohlstädt, U. Würfel, S. Mastroianni, G. Mathiazhagan, A. Hinsch, T. P. Gujar, M. Thelakkat, T. Pfadler, and L. Schmidt-Mende. Characterization of perovskite solar cells: Towards a reliable measurement protocol. *APL Materials*, 4(9):091901, 2016.